Nanostructure evolution of Cu films deposited on Mo(110)

a study using Molecular Dynamics simulations

Masters thesis

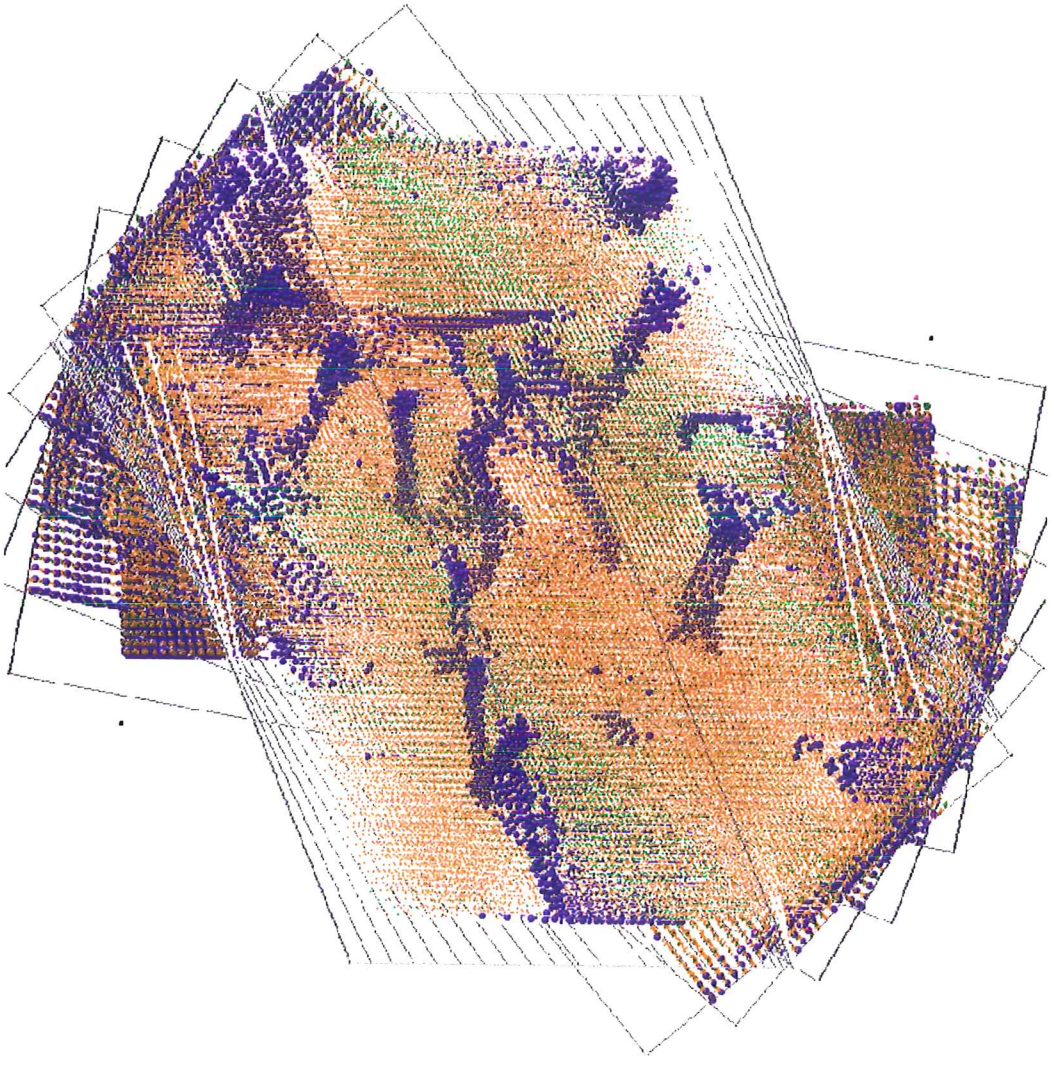

Bouke Sybren Bunnik

The cover picture is the result of artifacts due to the conversion of an animation from the Quicktime[1]-format to the "flic" file-format by the Apple Quicktime[1] Player program. When playing this flic backwards with "xanim", the window is not properly refreshed, with the result shown.

The animation is made from the same configuration as shown in figure 81 on page 148, it displays the same atoms and uses the same colouring scheme as this figure. The blue dots are atoms with bcc local crystal symmetry which form threading dislocations, the small green and orange dots are atoms with fcc and hcp local crystal symmetry, respectively. The gray lines are the simulation box edges, with small black dots at the corners.

This picture expresses the complexity of the developing nanostructure. The animation rotates the configuration over several axes, so that it is visible from all sides, thus giving an even better understanding of the film and its nanostructure than static images are able to provide. The motion is nicely illustrated by the remnants of the rotation from previous frames of the animation that are visible in the picture.

Part of this work has already been published:

[29] Edwin F.C Haddeman, Bouke S. Bunnik, and Barend J. Thijsse, *Thin film growth and ion-beam modification: MD simulations going beyond simple systems*, Fundamental mechanics of low-energy-beam-modified surface growth and processing (Steven C. Moss, Eric H. Chason, Barbara H. Cooper, James E. Harper, Thomas Diaz de la Rubia, and M.V. Ramava Murty, eds.), Mat. Res. Soc. Conf. Proc., vol. 585, 2000, pp. 103–108.

[15] Bouke S. Bunnik, Carin de Hoog, Edwin F.C. Haddeman, and Barend J. Thijsse, *Molecular dynamics study of Cu deposition on Mo and the effects of low-energy ion irradiation*, Nucl. Instr. Meth. B **accepted for publication** (2000–2001).

[1]Quicktime is a trademark of Apple Computer, Inc., registered in the U.S. and other countries.

Nanostructure evolution of Cu films deposited on Mo(110)

a study using Molecular Dynamics simulations

Bouke Sybren Bunnik

Masters thesis

Supervisor: Dr. B.J. Thijsse

Delft Technical University
Applied Sciences
Department for Materials Science and Engineering
Section of Physical and Chemical Materials Science

13th June 2001
Minor emends 4th July 2001

Contents

1 Introduction

1.1 Purpose of this work

In this work we study the (semi-)epitaxial PVD growth of Cu on Mo(110) using Embedded Atom Method (EAM) MD simulations, both with, and without ion beam assistance (IBAD). Currently available computer power makes it possible to study more complex systems than previously possible [62, 47, 49, 34, 33] on a realistic scale, in which a complex structure consisting of nanocristalline grains and stacking-faults can form. Fundamental insight in processes underlying film growth and microstructural evolution of these multi-element films are greatly enhanced by adding this extra complexity to the model systems.

First we will present the technological and scientific reasons for undertaking this study. The section concludes with an outline of the content of this thesis.

1.2 Integrated Circuits

Computers, and more general, Integrated Circuits (ICs), are becoming more and more important in our daily lives. To enable this, and to meet growing demand for computing power in a wide range of applications, there is a constant drive towards cheaper, faster and less power drawing components.

In order to reduce the cost of ICs by lowering the silicon waver surface needed per IC and thus reducing the cost of the Si used per IC, nowadays ICs are made up of several levels. For example, current desktop computer CPU's like the AMD Athlon™/Duron™, Intel® Celeron or Pentium® III/4, and PowerPC[2] G4 consist of 6 levels of IC layers.

Currently, there is a clear need for reducing heat dissipation and electro-migration induced degradation of the IC interconnects between the Si components (the "wires" of the electronic circuit) and IC levels. This has to be achieved under the conditions of ever higher currents and smaller interconnect dimensions. To make all this possible, the industry is currently switching from the use of aluminium (Al) or aluminium-copper (Al(Cu)) alloys to copper for the ≤ 0.18 μm generations IC interconnects.

Figure 1 shows both a Cu "trench" which is the earlier mentioned wire (next to point 4 in the figure) and an interconnect "via" (next to 2) between two levels of an IC. Both the via and the trench have to be constructed in Cu. The bulk Cu "fill" of the via and trench (7) is electro-plated into a previously created IC interconnect+level structure (1–4). The trench and via are subsequently made by etching away part of the IC level dielectric (4) up to the "etch stop" (3), thereby creating the trench, followed by etching away of the inter-level dielectric (2) up to the underlying etch stop (1), thus creating a via. This process might superficially seem quite similar in appearance to the processes used for other, earlier generation, interconnects. However, it is a very different process.

[2]PowerPC is a trademark of International Business Machines Corporation, registered in the U.S. and other countries.

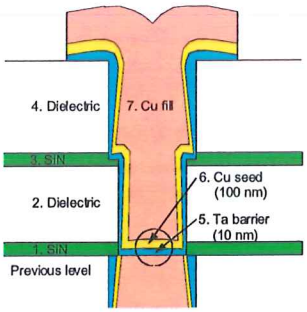

Figure 1: IC interconnect via and trenches in two different levels of the IC, with a Cu "seed" layer on a Ta diffusion barrier. From bottom to top, one can identify the "trench" (Cu) of the previous level, (1) the first SiN "etch stop" layer separating this previous level from the interconnect, (2) the interconnect dielectric containing and surrounding the interconnect via, (3) the second SiN layer, separating the interconnect layer from the next IC level, (4) the dielectric of this next level, containing a trench, then (5) the 10 nm Ta barrier, (6) the 100 nm Cu seed layer and (7) the electro-plated Cu "fill" of the via and next-level trench. To complete the level, the Cu (and Ta) "spilling out" over the top of the trench is removed using a chemical mechanical polishing (CMP) planarisation step.

1.3 Processing Cu interconnects

The main difference between the production processes used for earlier generations of interconnects and the production process utilized for Cu interconnects is that for the last Cu is laid into the pre-formed via or trench, while in earlier generations the Al (Al(Cu) alloy) was deposited on a flat wafer surface. After this part of the Al would be etched away and the IC components is built up around the Al interconnects. As Cu cannot be conveniently etched, it is not possible to do this with Cu. For this reason, the previously sketched "Damascene" process (see the caption of figure 1) for Cu interconnects has been developed. The difficulty here is that the texture(s) of the surroundings can have a strong influence on the grain orientation of the electro-plated Cu film (7) [82]. Therefore, care has to be taken to obtain the most favourable orientation of this Cu fill. A correctly oriented seed layer (6) can help in achieving this.

Some orientations of the interconnect material, be it Al or Cu, are more favoured than others. This is related to the electro-migration stability. Research has led to the conclusion that a metal with a strong fcc(111) texture leads to the least electro-migration. In copper thin films some grains are found to have (100) or (110) orientations and twins. Also, the grain size distribution sometimes shows a large spread after annealing, with many grains substantially larger than the average grain size. Annealing to 400 °C is a common procedure in the production of IC devices, so this may pose a problem [44, 18, 32].

A further unfortunate fact is that Cu readily diffuses into silicon (Si) and silicon (di-)oxide (SiO_2) (see for example [74, 73, 64]), so that between the via or trench and the surroundings, a diffusion barrier has to be inserted to prevent such fatal intermixing. Materials that are often mentioned as being suitable for use in a barrier layer between the Cu and surrounding materials are tantalum

(Ta), and tantalum nitride (TaN) [73, 64]. These are deposited as a thin layer on the via walls using PVD or CVD techniques, often with plasma assistance.

To obtain a good adhesion of the electro-plated Cu fill to these (Ta) diffusion barriers, first a seed layer is deposited, followed by electro-plating the fill on top of it. The seed layer is used to enhance adhesion to Ta and to set a template for the fill. The way in which this Cu seed film begins to grow on the Ta, and how the microstructure then develops, will affect the properties of the Cu fill electro-plated onto it. Which (physical) processes are involved in the improved characteristics of the fill when using such a seed layer is not clear from the literature. However, it is widely accepted that a seed layer is necessary for a good adhesion. It may be that the high energy with which the seed layer is deposited creates better adhesion, possibly due to some intermixing of the Ta and Cu layers. It is also not fully clear what the most favourable conditions are for the Cu seed layer and thus for the process/deposition conditions. The mechanism of the enhanced adhesion, especially, needs more research before the underlying principles will be fully understood [18]. One of the purposes of this work is to provide fundamental information on the Cu seed layer growth.

1.4 The Cu/Mo model system

The Cu/Mo system is an appropriate model system for the first stage of studying the growth of a Cu seed film on Ta, because Mo is very similar to Ta in several respects, but lacks the complicating tetragonal crystal structure that can form under certain circumstances in Ta (β-Ta). As mentioned, what those circumstances are is not fully known at this time. The metastable β-Ta has been found to grow in an epitaxial relationship with the $Cu[2\bar{2}0]_{(111)}$ parallel to $Ta[3\bar{3}0]_{(002)}$ when it was grown on such a Cu{111} surface under (ultra-high) vacuum (UHV) conditions [64, 37] (the use of non-Miller indices indicates the coincidence of the two structures for these crystal directions). In addition to α-Ta, β-Ta has also been reported for Cu/Ta multilayers and for Ta sputter-deposited onto SiO_2 [37]. The thickness of the layer seems to have some influence on its formation. Currently, there is a generally accepted structure for β-Ta, but the evidence [56, 21] is not conclusive. Additionally, there is some confusion on the use of the term β-Ta as some older papers use the term to describe a bcc Ta with a superstructure, formed in the presence of oxygen or nitrogen atoms. It is found for instance when Ta is grown on a SiO_2 substrate.

Apart from the above described interest in Cu/Ta and the subsequent link to the Cu/Mo system, the Cu/Mo system itself offers some fundamentally interesting aspects of film growth, namely growth in the presence of mismatching lattices of substrate and adsorbate (bcc/fcc). It is also also interesting because the Cu/Mo system has a large negative heat of mixing (0.27 eV) so that under normal circumstances virtually no intermixing between Cu and Mo would take place, thus maintaining an atomically sharp interface.

Often, it is desirable to obtain smooth surfaces. One of the methods used to achieve this is Ion Beam Assisted Deposition (IBAD), where a small amount of 25–250 eV ions are introduced along with the deposited atoms. The idea is

that the extra energy of the ions enhances diffusion by the film atoms creating a more smooth surface and lowering the (point) defect concentration. A problem with IBAD is the fact that the ions may themselves create defects, for example when ions are trapped in the film.

Thermal Desorption Spectroscopy (TDS) can be used as a method to study the amount and energy of defects introduced during growth by recording desorption peaks when heating a sample. An extensive study on TDS on deposited Mo samples (using both evaporation deposition (EVAP) and IBAD) has been performed by van der Kuur and others [36, 75, 76]. Recently TDS has been applied to the deposition of Cu as well, and an attempt has been made to combine TDS experiments with a simulation of the initial phase of the technique using some of the deposited films of this study, as well as the Cu-Cu and Cu-Mo EAM interactions developed in the current study [15, 19].

A second goal of this study is to help in understanding the experimental IBAD and TDS experiments on Cu and Cu/Mo that are performed in our group. The problem with TDS lies in attributing peak positions to desorption from the sample. Determining which structures and defects can be identified in the simulated films helps this process.

1.5 Contents of this thesis

Section two addresses the simulation method used (Molecular Dynamics) and the special points of our implementation thereof, as well as the used interaction tyupes, pair potentials and the Embedded Atom Method (EAM). The section continues with the subjects of (surface) diffusion and considerations concerning a trade-off between simulation time versus simulation temperature. The section discusses several aspects of layer growth, such as epitaxy, growth modes (conditions), stresses in the film and Ion Beam Assisted Deposition (IBAD).

In section three, the interaction potentials used for copper and molybdenum as well as the potentials for interactions with argon (used in IBAD) are discussed. The section then presents the visualization and analysis methods and conventions we use, such as atomic planes and neighbour-counting, spherical harmonics symmetry analysis, the film roughness parameter, stresses in the film, plane-filling and "atom history", and introduces the definitions of nominal deposition rate and thickness of the film. At the end of the section, the most important parameters of the simulations runs are listed in tabular form, and several of the principles behind them are explained.

In section four the results are presented, starting with some of the system properties that follow from our interactions. After that, the results of Cu deposition on Cu (EVAP) and of Cu on Mo (both EVAP and IBAD) are given.

The discussion in section five includes a comparison with a related TDS simulation study [15, 19]. A comparison between the EVAP and IBAD results is particularly interesting as the IBAD is reminiscent of the plasma deposition, utilizing high energy. In this respect, comparing EVAP with IBAD may give some clues about the origin of the enhanced adhesion when using a Cu seed layer on Ta, as mentioned above. In section six, the results are summarized. Section seven gives recommendations and ideas for future simulations.

2 Theory

In this section, the principles of the molecular dynamics simulation method will be discussed, as well as the more special aspects of implementation. The general philosophy behind the interaction types we use is discussed and briefly compared with other interaction types in §2.1. The specific parameters of the interaction potentials will be postponed until the first part of the next section (§3.1).

After the interactions and the simulation method have been described, the general aspects of film growth, diffusion and stresses in thin films will be discussed in §2.5. The topics of that subsection can be seen as a background for the analysis methods and visualization tools described in §3.2, and will be useful for interpreting the results.

This section will end with a discussion about the trade-off between simulation temperature, simulation duration and deposition rate (§2.4), a factor that should be considered before performing simulations, as it prescribes how one should choose most of the simulation parameters.

2.1 Molecular Dynamics

Molecular dynamics (MD) simulation involves solving Newton's equations of motion for all individual atoms in a system [5, Allen and Tildesley]. For systems containing more than two particles (the simulations in the present study involve systems with up to $\sim 10^5$ atoms) an analytical solution is infeasible and equations have to be solved numerically. Foiles [25, Foiles] has shown that using a classical description instead of a description using quantum mechanics is in a lot of cases justified when one only looks at non-electronic properties of the system.

In general there are two applicability regions for MD. The first is obtaining atomic trajectories for times comparable with correlation times that are of interest in the simulations performed. This enables a calculation of time correlation functions. In the first part of section 4, this is essentially what we will do when studying surface diffusion by looking at "jump" movements of individual atoms (§4.1.7). The second application of MD is generating states sampled from the canonical ensemble that applies to the situation studied. In order for this to work we do not necessarily need the exact classical trajectories; what we do need however, is that the particle trajectories remain close to appropriate constant-temperature in phase space. In most of the current study, this second application of MD is used.

Knowing the positions and velocities of the individual particles at a particular time, ie. having a *configuration* of the system, paired with a description of the interaction between those particles, one can retrieve the macroscopic properties of the system at that time, such as temperature, density and pressure, from the combined states of the individual particles.

To obtain this macroscopic behaviour alone, it may seem as if we could have used Monte Carlo (MC) methods instead of MD, with a large reduction in the time needed to obtain these results [63]. However, we are also interested in the

dynamics of the individual atoms in time. For instance, after a deposited atom has arrived on the surface, we want to know if it changes its position within the deposited film, and if so, in what way and by how much. In addition, our systems are locally often far from equilibrium — Monte Carlo methods are not appropriate for studying the relaxation towards equilibrium.

The interests and objects described above could be achieved using Lattice MC methods, except that we would have to restrict ourselves to predefined processes and provide input information about activation energies and their rate of change or their frequency of occurring. Apart from the desire to avoid such restrictions, a related problem is that knowledge of processes involved in growth of the Cu layers presented here is lacking, which is one of the reasons for conducting this study in the first place. In addition, the numbers may vary with time, as the film evolves.

While MC could be used in between impacts to allow for more time for relaxation of the lattice, during impacts, we have to use MD. There are some efforts in our group to use (dynamic) MC in between impacts, but this is currently not a widely adopted practice. In the future, this method is a candidate for further study.

In MD, the time evolution of the individual atoms, and thus that of the whole system, can be found from (a many-body expression for) the force on an atom i:

$$\vec{F}_i = -\frac{\partial U}{\partial \vec{r}_i}, \quad i = 1 - N, \tag{1}$$

with r_i the position vector of atom i, U the total potential energy of the system, resulting from the interaction between the atoms, and N the number of atoms in the system.

Classical molecular dynamics uses Newton's equations of motion, which relate the acceleration of an atom i, $\vec{a}_i$, to the force $\vec{F}_i$ acting on it, and to the mass of the atom, m_i:

$$\vec{a}_i = \frac{\vec{F}_i}{m_i}. \tag{2}$$

To do a simulation we need a first *configuration*, a list of the position, velocity and element type of each atom. From the positions and the element types of the atoms U can be calculated, so that the forces can be determined using equation (1), which are then used to obtain the accelerations of the atoms with equation (2). The velocities are used together with the acceleration to compute the time evolution of the system.

2.1.1 Time evolution

Starting from the initial configuration, we can integrate Newton's equations of motion (equations (1), (2)). Here, the time comes into play. We perform this integration using a finite difference method. The algorithm we use for evaluating the evolution of a configuration is the velocity Verlet algorithm [5,

Allen and Tildesley,§3.2.1, p. 82], which is symmetric in time and utilizes a multiple stage method for getting from t to $t+\delta t$, lowering (numerical) errors:

$$\vec{r}(t+\delta t) = \vec{r}(t) + \delta t\,\vec{v}(t) + \frac{1}{2}(\delta t)^2\vec{a}(t), \tag{3}$$

$$\vec{v}(t+\frac{1}{2}\delta t) = \vec{v}(t) + \frac{1}{2}\delta t\,\vec{a}(t), \tag{4}$$

$$\vec{v}(t+\delta t) = \vec{v}(t+\frac{1}{2}\delta t) + \frac{1}{2}\delta t\,\vec{a}(t+\delta t). \tag{5}$$

Determining the accelerations $a(t+\delta t)$ from the advanced positions $r(t+\delta t)$, in the last stage of the algorithm, is the most time consuming part as this uses equation (2), which involves evaluating equation (1) for each atom using the functions describing the interactions (see below, in §2.1.2, and the next section, §3.1, for these equations).

Using a finite integration time (*time-step*) δt with this velocity Verlet algorithm introduces an error of order $\mathrm{O}\big((\delta t)^2\big)$ for the velocities, and an error of order $\mathrm{O}\big((\delta t)^3\big)$ for the positions. It is important that the distance an atom traverses per step is small enough to ensure that the energy does not experience a sudden jump (and a discontinuity in derived quantities as a result of this). In our systems we use a maximum allowed distance of $r_{max} = 0.020$ Å, which is of the order of 1% of an atomic radius.

For the size of the time-step we use either a fixed value of δt, which is only done at low temperatures for stability reasons, or an adaptive value, in all other cases. This variable time-step is automatically determined at each step and is such that no atom experiencing a force can move more than r_{max} in a single step.

The variable time-step is computationally efficient, because a fixed time-step would have to be selected such that the fastest atom of the *entire* simulation would travel no further than r_{max}. A variable time-step adapts to the instantaneous conditions.

Especially in simulations where a large range ("spread") of highest atom velocities can occur in time, such as in deposition and in IBAD simulations, using a variable time-step results in significantly shorter (real- and CPU-) time needed for the simulation due to the larger average time-step. A practical problem encountered here is that δt will generally have to decrease with N, as the probability of a high(er) velocity atom increases with N (As an example: $\mathrm{EVAP}_{\mathrm{b2}}$ begins at $N_i \sim 12 \cdot 10^3$, $\langle \delta t \rangle = 1.023$ fs — $N \sim 60 \cdot 10^3$, $\langle \delta t \rangle = 0.99$ fs — $N_f \sim 115 \cdot 10^3$, $\langle \delta t \rangle = 0.97$ fs, a decrease of 5.5% for $N_f = 10N_i$).

In the determination of the fastest atom, only atoms experiencing a force, or expected to experience a force within δt, called "bound" or "quasi-bound" atoms respectively, are taken into account. Other, so called "free" atoms may limit δt for another reason: a special free-flight algorithm checks if a collision is impending (ie. if the atom would become a quasi-bound atom within δt). If this is the case, δt is limited accordingly.

To improve the accuracy of the time-step determination, accelerations are taken into account for testing an atom's (impending) displacement against the distance limit. A detailed description and a code-fragment of the actual algorithm used can be found in [47].

2.1.2 General remarks on interactions

In addition to a list of positions and velocities (and atom type) of the particles in the system, and a mechanism for time evolution, an interaction potential is needed for all elements involved. The choice of these potentials is important, because it determines to a large extent the physical accuracy of the simulation ("reality-value"). This choice also sets many of the limits of the simulation and influences the number of calculations per time-step and thus the speed. This in itself limits the number of, and the complexity of the simulations that can be performed in the available time.

We use many atoms and look at complex systems which are of considerable size, both in space and in time, so *ab initio* electronic structure calculations cost too much computing (real) and CPU-time. The simplest and fastest interaction description consists of (effective) pair potential interactions for all individual atom pairs. For gases or (nearly) perfect crystals, pair potentials are adequate. However, this description of the interaction is not very well applicable to the behaviour of atoms in a crystal structure with defects [5, Allen and Tildesley], as it uses an average electron density for the entire system, instead of the local electron density of (combinations of) wave functions.

A reasonable compromise between accuracy and speed is the Embedded Atom Method (EAM). This method is more realistic then pair potentials in describing systems of atoms in dense matter. The method allows for a more valid simulation of systems of metals containing pronounced defects such as vacancies, vacancy clusters, and free surfaces [5, 25, Allen and Tildesley, Foiles, Baskes]. In the EAM, a local electron density is used which has a radial distribution around the atoms. This electron density is derived from the distances to the surrounding atoms, without actually calculating electron wave-functions. No angular dependence of the electron density is incorporated in the EAM, so that it is especially suitable to noble or fcc metals, metals with a nearly-filled d-band, but the method can also be applied with success to bcc metals [47, 49, 48, 29, 15, 62, 61].

In the present study copper (Cu) is deposited on Cu and on molybdenum (Mo), so we need to describe the interaction of Cu with Cu, of Mo with Mo and of Cu with Mo. For argon (Ar) Ion Beam Assisted Deposition (IBAD), we also need the interaction potential of Ar with Cu and with Mo.

2.1.3 Pair potentials

Pair potentials look at interacting pairs of atoms (or "bonds") for the calculation of the energy of the system. For pair potentials the total energy U can be described as:

$$U = \frac{1}{2} \sum_i \sum_{j \neq i} \phi_{ij}\left(r_{ij}\right) + D\left(\Omega\right), \tag{6}$$

with $\phi_{ij}\left(r_{ij}\right)$ the pair potential, which is a function of the distance r_{ij} between two atoms i and j. The function D is zero when the pair potentials totally describe U, but is non-zero when the pair potentials describe only part of the

total energy. D is a function of Ω, the average atomic volume in the system, thus providing an average electron density value for all atoms in the system. The more deviations from the average density are present, and the higher in magnitude these deviations are, the less adequate will pair potentials be for describing the energy of a system.

There is an exception however for high energy situations, in which the interacting atoms have very short distances to each other, only two atoms interact at the same time, so that in this area pair potentials are a valid and useful interaction description.

In the present work the Screened Coulomb pair potential with Molière weight factors and Firsov screening length (Fi-Mo potential, FM) [24, Eckstein] is used for the high-energy/short-distance regime of the interactions. This purely repulsive pair potential $\phi_{IJ}^{FM}(r)$, which depends on the atom numbers Z_I and Z_J of the interacting particles i and j, has the form:

$$\phi_{IJ}^{FM}(r_{ij}) = \frac{Z_I Z_J e^2}{4\pi\varepsilon_0 r_{ij}} \gamma_{IJ}^{FM}\left(\frac{r_{ij}}{a_{IJ}^{FM}}\right), \tag{7}$$

in which the function γ_{IJ}^{FM} is given by

$$\gamma_{IJ}^{FM}\left(\frac{r_{ij}}{a_{IJ}^{FM}}\right) = \sum_{\iota}^{3} c_\iota e^{-d_\iota \frac{r_{ij}}{a_{IJ}^{FM}}}, \tag{8}$$

with factor a_{IJ}^{FM} being

$$a_{IJ}^{FM} = \left(\frac{9\pi^2}{128}\right) a_{\mathrm{B}} \left(Z_I^{\frac{1}{2}} + Z_J^{\frac{1}{2}}\right)^{-\frac{2}{3}}, \tag{9}$$

where e is the elementary charge, ε_0 is the vacuum permittivity, γ_{IJ}^{FM} is the screening function, a_{IJ}^{FM} is the Firsov screening length, c_ι and d_ι are constants, and a_{B} is the Bohr radius. The Molière values for c_ι and d_ι are given in table I.

Table I: Molière's values for constants c_ι and d_ι used in the Screened Coulomb pair potential screening function γ_{IJ}^{FM}, equations (7,8). The values are taken from [24].

ι	c_ι	d_ι
1	0.35	0.3
2	0.55	1.2
3	0.10	6.0

2.1.4 Embedded atom method for transition metals

As mentioned above, in the EAM the potential energy of an atom i does not just consist of pair potential contributions from its surrounding atoms. Instead, as the EAM is related to density-functional theory, an additional part of the potential energy comes from a so-called embedding energy F_i. This energy

term can be seen as caused by the atom being embedded in the electron density caused by its surrounding atoms. The value of F_i depends on the *local* electron density at the position of atom i and not on the *average* electron density (equivalent to Ω) like in the case of pair potentials ($D(\Omega)$ from equation (6)).

This local electron density ρ_i is calculated from the positions of the surrounding atoms j relative to atom i and depends on the element types J of atoms j. Using the EAM, the total potential energy of the system, U, is

$$U = \sum_{i=1}^{N} F_I(\rho_i) + \frac{1}{2}\sum_{i=1}^{N}\sum_{j\neq i}^{N} \phi_{IJ}^{EAM}(r_{ij}), \tag{10}$$

in which I and J are the element types of atoms i and j. Equivalently, U is

$$U = \sum_{atoms} F_{atom}(\rho_{atoms}) + \sum_{bonds} \phi_{bond}^{EAM}(r_{bond}). \tag{11}$$

for all N atoms and $N(N-1)/2$ bonds between the atoms.

The electron density contributed by an individual atom to the total electron density ρ_i is derived from atomic wave functions, with some important simplifications. For instance, as already briefly mentioned above, the angular dependence of the electron wave functions is presumed to average out, leaving a rotationally invariant electron density function. Consequently, the local electron density that an atom experiences depends on the distances to other atoms, but not on the directions of the distance vectors between them. This approximation is more appropriate for noble metals, or for transition metals with nearly filled d-bands, such as Cu, than for metals with only partly filled d-bands, for which not all of the directional components of the p- and d- orbitals are equally represented, as is the case for bcc transition metals like Mo.

Nevertheless, the EAM can be used for the case of Mo and other bcc metals, as is shown by a comparison of several EAM bcc potentials with experimental and *ab initio* calculation results for vanadium [22]. In this study a melting temperature of 2163–2183 K was found, consistent with the experimental results for vanadium. Further confirmation of the applicability of the EAM to Mo is found in [29, 47, 48, 49] and [61, 62].

The local electron density at the position of atom i is calculated by adding up the individual contributions from all atoms surrounding atom i:

$$\rho_i = \sum_{j=1;j\neq i}^{N} k_J f_J(r_{ij}), \tag{12}$$

where $f_J(r_{ij})$ is the contribution by atom j to the electron density at the position of atom i and k_J is a factor that cancels out for single-element potentials. The reason for this is the special form of the embedding functions (as will be shown in section §3.1):

$$F_I(\rho_i) = F_I\left(\frac{\rho_i}{\rho_I^{eq}}\right) \overset{eqn.(12)}{=} F_I\left(\frac{\sum_{j\neq i}^{N} k_J \cdot f_J(r_{ij})}{\sum_{j\neq i}^{N_I} k_I \cdot f_I\left(r_{ij}^{eq}\right)}\right), \tag{13}$$

with ρ_I^{eq} the local electron density of atom i in its own equilibrium crystal structure, where all the atoms are at their equilibrium distance $\bar{r}_{II}^{eq}$. If all J are the same as I, then the k_J's cancel out against the k_I's in equation (13). The embedding energy of an atom depends only on the value of ρ_i, not on the element types J of atoms j contributing to that local electron density.

In a perfect single-element crystal at equilibrium and at 0 K, due to the symmetry of the crystal, the pair potential part of the EAM, Φ^{EAM}, is:

$$\Phi^{EAM} = \sum_{i=1}^{N} \sum_{\kappa} C_\kappa \phi_{II} \left(r_{II,\kappa}^{eq} \right), \tag{14}$$

and the equilibrium electron density ρ_I^{eq} is:

$$\rho_I^{eq} = k_I \sum_{\kappa} C_\kappa f_I \left(r_{II,\kappa}^{eq} \right), \tag{15}$$

with $r_{II,\kappa}^{eq}$ the distance to the atoms in the κ^{th} neighbour shell of a particular atom at equilibrium and C_κ the coordination number of that shell. For bcc materials we have to use at the least $\kappa = 1, 2$. For close-packed structures, $\kappa = 1$–3 should be used as a minimum in order to be able to differentiate between fcc and hcp in the (non-directional) EAM, as the first two neighbour shells are equal in spacing and number of neighbours. Simple cubic materials only need $\kappa = 1$. The embedding energy for the equilibrium situation is $F_I^{eq} = F_I \left(\rho_I^{eq} / \rho_I^{eq} \right) = F_I \left(1 \right)$. The equations for $\phi_{IJ}^{EAM}(r)$, $F_I(r)$ and $\rho_I(r)$ used in this work as well as numerical values for the parameters are given in the first part of the next section, §3.1.

2.1.5 Combining high-energy pair potentials with the EAM

The EAM, which is defined for the low/thermal energy regime, is not appropriate for high energies, as it is too "soft" at short interatomic distances. Therefore, we use the above descried Fi-Mo pair potential in this high energy regime, as these are circumstances for which it is very well applicable.

Two things have to be done to go smoothly from the EAM to the Fi-Mo pair potential. Firstly, in the r-range where the values for the Fi-Mo pair potential ϕ^{FM} and the pair potential part of the EAM, ϕ^{EAM}, are very close to each other, the two functions are smoothly connected to each other by using a spline, which is fitted to the two functions and replaces them between certain distances r_{sp}^{FM} and r_{sp}^{EAM}. The values of r_{sp}^{FM} and r_{sp}^{EAM} depend on several factors. For one, the "switching" range should clearly be within $r_{I,1}^{eq}$, to avoid using the Fi-Mo pair potential in the thermal energy regime, where we want to use EAM. In most cases there will be an area in this region where the two pair potential functions are close together or where they cross, so that the choice of the values of r_{sp}^{FM} and of r_{sp}^{EAM} is governed by the smoothness of the transition from ϕ^{FM} to a spline and then from the spline to ϕ^{EAM}.

Secondly, to go from the EAM N-particle interaction to the FM pair-interaction, the embedding contribution to the energy should vanish. This

is not part of the standard EAM formulation. A way to bring this about is to modify the electron density function $f(r)$ at short distances. In our case, this is done by multiplying $f(r)$ with the Fermi-Dirac like function $h(r)$,

$$h(r) = \frac{1}{e^{\frac{r_z - r}{\Delta r_z}} + 1} \tag{16}$$

where r_z and Δr_z are constants that determine respectively the position of the half-height of this cut-off function and how steeply function h falls of from 1 to 0, and thus how steeply the electron density goes to zero from its full EAM value when moving towards the atom core. By using h, the electron density, and hence the embedding energy, is practically zero near the atom core where the pair-interaction takes over.

The range where this fall-off takes place, has to be at about the same range as where the switch between ϕ^{FM} and ϕ^{EAM} takes place, so that r_z typically lies between r_{sp}^{FM} and r_{sp}^{EAM}. The tuning of the electron density function fall-off with the pair potential spline to obtain a smooth and "tidy" transition is actually a trial-and-error process.

The values for r_{sp}^{FM}, r_{sp}^{EAM}, r_z and Δr_z used in this work, and a figure showing their positions relative to r_1^{eq}, can be found in section §3.1.

2.1.6 Calculating the forces

In calculating the forces, the separation distances are not used as r but as r^2, because we want to avoid taking a square root every time the distance has to be evaluated.

An additional method to save time is to create prepared tables for looking up the interaction function values, instead of evaluating the functions as needed. We therefore store a table of the function values at intervals of $\Delta\left(r^2\right)$ in "potential-", "electron density-" and "embedding energy-files". Actually, as the forces are calculated from the derivative of the potential energy, see equation (1), we store the derivative of ϕ_{IJ} as the *virial* of the potential function:

$$w_{IJ}(r) = \frac{\mathrm{d}\phi_{IJ}(r)}{\mathrm{d}r} r \tag{17}$$

in addition to the value of the potential function itself. The electron density function f_I and its derivative are stored in the same manner, using ω_I^{el}. For the EAM embedding function we store the function values of F_I and $F_I^{d\rho} = \mathrm{d}F_I(\rho)/\mathrm{d}\rho$ at intervals of $\Delta\rho$. When the value of an interaction function at a specific value of r^2 (or of ρ, for use with F) is needed during the simulation, it is calculated from a linear interpolation of the tabulated values. The force follows from the virial of the internal energy $\omega_{IJ}^U(r)$, which for EAM is

$$\omega_{IJ}^U = \omega_{IJ}(r_{ij}) + F_I^{d\rho}(\rho_i)\,\omega_J^{el}(r_{ij}) + F_J^{d\rho}(\rho_j)\,\omega_I^{el}(r_{ij}). \tag{18}$$

To restrict the computational effort, interactions generally are given a maximum distance, the cutoff distance over which they operate. This limits the number of forces that have to be calculated. The use of a cutoff-distance is in general only a viable method when using short-range interactions like metal atoms in a crystal, and is more problematic for ionic bonding.

2.1.7 Bookkeeping of the atoms

Periodic Boundary Conditions The simulations are performed inside a rectangular simulation box. This box determines the volume available to the atoms in the system. To prevent boundary artifacts near the sides of the box, we use periodic boundary conditions to simulate an infinite number of "images" around the central simulation box, which are exact copies of this central box [5, Allen and Tildesley §1.5 pp. 23–32]. Atoms in the system can move freely between the central box and its images, allowing for diffusion.

When looking at bulk materials, periodic boundary conditions in all three Cartesian directions should be used (three-dimensional). For deposition, and generally when looking at surfaces, periodic boundary conditions can and should only be applied to the two lateral Cartesian directions that lie in the surface plane, with the third Cartesian directions perpendicular to them being "free".

When periodic boundary conditions are used, the length-scale of any phenomenon that may arise is restricted by the box size. This imposes a restriction on our simulations and the phenomena that can be studied. Periodic phenomena will artificially be forced to observe this periodicity, using a repeat length that fits an integer number of times into the box. Examples of effects for which this may be a concern are surface undulations, (misfit) dislocations and also the orientation of an epitaxial film (see §2.5.1). The crystal structure itself is also influenced by this.

In addition, when performing simulations with (highly) energetic particles, the disturbance of the system should not be larger than the box size, as this would lead to an interference with the identical disturbance of (one of) the images.

Bottom atoms As the periodic boundary conditions for systems with a free surface are imposed only in the two lateral Cartesian directions, without further actions, the system would have two surfaces. To effectively simulate a much larger (underlying) substrate, and to absorb energy and momenta $\vec{p}$ in the direction normal to the bottom surface, we tie the atoms in the lowest part of the simulation box (2 atomic planes in this study) harmonically to anchor points. These are located at the equilibrium positions of the atoms. The atoms thus considered are called "bottom atoms".

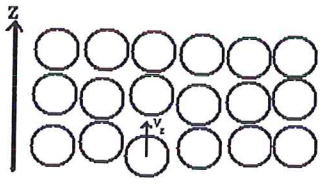

Figure 2: Diagram showing how the "bottom-atom" snapping works. The atom with velocity v_z in the positive z-direction is a candidate for snapping.

When v_z is positive (i.e. when it is an inward velocity) and

$$\frac{1}{2}mv_z^2 > \sigma\left(\frac{1}{2}k_{\mathrm{B}}T\right), \tag{19}$$

where σ is the "snapfactor", the harmonic binding force is set to zero for the duration of one time-step. In this way it can be prevented that too much momentum and kinetic energy is reflected at the bottom surface. Initially we used $\sigma = 1$. In later simulations $\sigma = 1000$ was used, effectively deactivating the "force-snapping" mechanism.

Efficiently searching the interacting pairs of atoms If in the MD algorithm a double loop over *all* atoms would be used when searching for the interaction pairs in the simulation box, only a very small portion of these pairs would be lie within the cutoff distance and actually interact. For a (homogeneous) system with volume V and simulation box edges L_α, where α denotes any of the three Cartesian axes x, y, z, only a fraction

$$\frac{\frac{4}{3}\pi r_c^3}{L_x L_y L_z}, \tag{20}$$

of all the pairs addressed are sufficiently close to interact. For example, lets take a material which has an atomic volume of $\Omega = 11.8$ Å^3, and for which the cutoff distance is $r_c = 5$ Å. Now assume that we perform simulations in two different cubic boxes, one with $L_\alpha = 50$ Å and $N = 10,625$ atoms, the other with $L_\alpha = 100$ Å, and $N = 85,000$ atoms. Equation (20) tells us that of the total number of pairs

$$N_P = N(N-1)/2, \tag{21}$$

only $\simeq 0.42$ % for the smaller and 0.052 % for the larger system are interacting pairs.

The time needed to find the interacting pairs scales with $\mathrm{O}(N^2)$ for this method, which is a problem for large N, but is especially undesirable when doing layer growth simulations, as N strongly increase during the simulation leading to a large increase in CPU-time as the simulation progresses.

To increase the efficiency, several methods have been devised to limit the number of times that the search for interacting pairs has to be conducted, and additionally, to limit the number of pairs that have to be needlessly searched through to find the interacting pairs.

The cell method One method to limit the number of pairs to be searched is the linked cell method [5, §5.3.2, pp. 149–152]. This method divides the box in the three Cartesian directions into m_α^{CM} ($\alpha = x, y, z$) parts at the start of the simulation, thus creating cells dividing up the simulation box. The cells have edge sizes d_α^{CM}:

$$d_\alpha^{CM} = \frac{L_\alpha}{m_\alpha^{CM}}, \tag{22}$$

such that m_α is as large as possible, provided that a cell edge is at least as large as r_c:

$$m_\alpha^{CM} < \frac{L_\alpha}{r_c}. \tag{23}$$

This creates $m_x^{CM} m_y^{CM} m_z^{CM}$ cells, each containing on average

$$N_{CM} = \frac{N}{m_x^{CM} m_y^{CM} m_z^{CM}} \tag{24}$$

atoms (for a homogeneously filled simulation box). For each cell, only atoms in this *central* cell and in the $3^3 - 1 = 26$ neighbouring cells, the *external* interaction volume, can possibly interact with an atom i in the central cell. In other words: for all N_{CM} atoms in the central cell, interaction partners need only to be searched in the central cell itself and in the external interaction volume. To avoid checking the cells two times, only half of the cells in the external interaction volume is checked for each central cell. A minimum value of $m_\alpha^{CM} = 3$, which is equal to the "width" of the interaction volume, is needed to make this method work, giving a lower limit to the size of the simulation box that can be used with the linked list. We call this minimum value m_c^{CM}. By using this cell division, at each step only

$$\frac{m_x^{CM} m_y^{CM} m_z^{CM} N_{CM}}{2} \left(N_{CM} m_{c,CM}^3 - 1 \right) = \frac{N}{2} \left(\frac{N m_{c,CM}^3}{m_x^{CM} m_y^{CM} m_z^{CM}} - 1 \right) \tag{25}$$

pairs will be checked (with O(N) dependency) instead of all pairs (equation (21)).

For each cell, the neighbouring cells have to be indexed once, at the start of the simulation (and every time the volume changes). This "mapping" has an O(N) dependency as well. After that, for each step, the cells are "filled-up" with atoms, where a cell number is assigned to each atom. This is done by a linked list method, where essentially one starts with one atom in the cell which identifies the next atom, etc., creating a chain through all the atoms in a cell. See [5] or [47] for a more detailed description of the method. The filling-up is a rapid process with a O(N) dependency. For a rough calculation of the efficiency of the linked list, these two extra O(N) steps can be neglected.

In our two example systems, we would have $m_{CM} = 9$ and $m_{CM} = 19$. From equation (25), in combination with equation (20) and equation (21), we find that of the checked pairs, 11.3%, respectively 13.3% would be interacting pairs, rendering the search process 27 and 255 times as efficient as a double loop.

Although the linked list is much more efficient than a double loop, the problem remains that the pairs have to be identified in each time-step. The use of a neighbour table can improve this considerably, see below (§2.1.7).

Because r_c, and thus the conditions for the best cell division (equations (26) and (27)) is different for every interaction, a different cell division should be used for each of the $M(M-1)/2$ bond-types. This does mean that introducing a new particle type may introduce a large increase in the memory requirement, because a cell list has to be created for the interaction with each of the previous particles, a $O(M^2)$ memory requirement dependency.

The double layer cell method In our group, an improved version of the linked cells is used, which uses smaller cells, and has two layers of cells in the external interaction volume [61, Robbemond Mast. thesis; in Dutch]. This

leads to a cell division according to:

$$m_\alpha^{2LCM} < \frac{2L_\alpha}{r_c}, \tag{26}$$

$$diag_{2LCM} < r_c, \tag{27}$$

where the second condition ensures that all atoms in the central cell form bonds with the other atoms in the central cell, leading to a small decrease in the time needed to check if the pairs interact.

The external interaction volume now consists of $(5^3 - 1) = 124$ cells, which each have a volume $2^{-3} = 0.125$ times that of the previous cell division for a cubic simulation box. Another change in the requirement with this new double layer cell method is that m_α^{2LCM} should be at least equal to $m_c^{2LCM} = 5$, instead of the previous condition of $m_c = 3$. This finer division of the simulation box leads to a reduction of the pairs that are (needlessly) to be checked, which can be seen from equation (25) combined with either equation (23) or equation (26).

In our two example systems, we would now have $m_{2LCM} = 19$ and $m_{2LCM} = 39$. Using equations (21, 20) and equation (25) with the new cell division leads to an efficiency of respectively 23.1% and 25.0% which is roughly twice as efficient as the normal cell method.

The neighbour table We currently use a neighbour table to limit the number of times that the cell list has to be checked [5, 27, [5]: §5.3.1, pp. 147–149]. This neighbour table contains the pairs ij that are within a distance of $r_c + r_s$ from each other. In the "skin" of thickness r_s, pairs are present that are not currently interacting but that could do so within several steps. The table only needs to be updated at intervals, thereby reducing the time spent evaluating which atoms interact. For each time-step, only the pairs ij that are in the neighbour-pair table of atom i have to be checked to determine if they are within r_c of each other.

The condition for updating the neighbour table is taken from [27]:

$$\Delta r_{max\text{-}NT}^2 > f_u \left(1 - \frac{1}{\Delta s_u + 1}\right) r_s^2, \tag{28}$$

in which $\Delta r_{max\text{-}NT}$ is the largest displacement of a single atom since the time-step of the last update, Δs_u is the number of time-steps after the last update, and f_u is an update frequency tuning factor.

The "skin" thickness r_s has to be chosen carefully, so that the interval between refreshing the list is as large as possible (requiring a large r_s) but the list itself does not become too large. In addition to the skin thickness, the update factor can also be used to alter the refreshing frequency. Tests with the two have indicated that a value of r_s in the range 0.27–0.54 Å is a good choice for systems containing Cu, Mo, Ar, and He. The update factor should be in the range 0.6–0.9 [27]. We use the values $r_s = 0.27$ Å and $f_u = 0.8$.

This neighbour table itself is built using a slightly modified version of the above described double layer cell method. For the neighbour table construction, the size of the cells has to increase, as the cell edge length, d_α^{NT}, is now

determined by

$$2d_\alpha^{NT} > r_c + r_s, \tag{29}$$

instead of by equation (26), so that instead of the number of pairs interacting, equations (21,20), a larger number of pairs is listed in the neighbour table, namely the fraction

$$\frac{\frac{4}{3}\pi(r_c + r_s)^3}{L_x L_y L_z}, \tag{30}$$

of all possible pairs. The extra condition (27) for the double layer cell method is dropped as it is no longer guaranteed that all atoms in a central cell interact with each other.

Only the pairs in the neighbour table are evaluated at each time-step (equation (30)), leading to an efficiency per time-step η_{NT},

$$\eta_{NT} = \frac{r_c^3}{(r_c + r_s)^3}, \tag{31}$$

the ratio of equations (20) and (30).

Using the above quoted value $r_s = 0.27$ Å with equation (31), the two example systems both have an efficiency of $\eta_{NT} = 85.4\%$ at each time-step. The efficiency of generating the table itself is actually higher than for a normal double neighbour shell linked list method, due to the use of $r_c + r_s$, by a factor $1/\eta_{NT}$ (which is equal to 1.17 in the material of the two example systems and using $r_s = 0.27$ Å).

The overall efficiency of this method can only be determined when the update interval is known. As the maximum possible displacement of any atom is $r_{max\text{-}NT} = r_{max}\Delta s_u$ (see §2.1.1), using equation (28), we can determine a minimum amount of steps $\Delta s_{u,min}$ between updates

$$\Delta s_{u,min} = \text{int}(\sqrt{\frac{f_u r_s^2}{\Delta r_{max}^2} + \frac{1}{4}} - \frac{1}{2}). \tag{32}$$

Note however, that this minimum value is only applicable in the absence of other influences that make make it necessary to update the table. For our $r_{max} = 0.02$ Å, $r_s = 0.27$ Å and $f_u = 0.8$, equation (32) leads to $\Delta s_{u,min} = 11$ time-steps. Per time-step, an average efficiency is reached of

$$\eta = \frac{(\eta_{2LCM} + \eta_{NT}(\Delta s_{u,min} - 1))}{\Delta s_{u,min}},$$

being $\eta = 79.7\%$ and $\eta = 79.9\%$ for the two example systems, which is ~ 3.5 and 3.2 times as efficient as the double layer cell method in finding the interaction pairs.

We have observed in our simulations reductions of 60% in the required CPU-time with the neighbour table as compared to CPU-time with only the double layer cell method (leaving 40% of the CPU-time), a perceived efficiency gain

(2.5 times) that is lower than could be expected from the above calculations of efficiency for a cubic and homogeneously filled simulation box with a fixed volume. One of the reasons for this is that, disregarding the efficiency of finding the interaction pairs, with all described methods we should end up with the same number of interacting pairs for which the forces have to be calculated at each step (for the example systems there would be about $236.5 \cdot 10^3$ and $1900 \cdot 10^3$ pairs). Therefore, the calculated efficiencies in identifying the interaction pairs do not compare directly to the overall needed CPU-time.

When using the neighbour table, for each interaction type, the same cell division is used, namely the largest cell required (largest r_c), thus reducing the memory requirement. This can be done without loss in computing time, as the condition (29) does not guarantee that all atoms in the cell are within r_c of each other, so that this has to be checked regardless of the cell division that is used for an interaction type.

Effect of changing density on the searching for pairs Special care has to be taken during the bookkeeping stage because of the possibilities of introduction of atoms by ion bombardment or by layer growth and removal of atoms by sputtering or by evaporation. These events make it necessary to rebuild the neighbour table and recalculate the temperature (§2.1.8, below) and pressure (§2.1.8) of the system (as well as the system density).

When the volume of the simulation box changes in response to pressure regulation, it becomes necessary to check if the cell division is still correct, which is possibly followed by a re-map and filling of the new cells, in turn making it necessary to rebuild the neighbour table.

Normally, free atoms, ie. atoms that feel no interaction, would not be included in the neighbour table. To determine the time-step length however, all free atoms have to be taken into account (see §2.1.1), using the full interaction volume instead of just the active part, to check if they become "quasi-bound" and should limit the time-step. For his check, the free atoms are first included in an extra "free-atoms" section of the neighbour table. This section also stores all free atoms that are within $r_c + r_s$ of (an) other atom(s). A quasi-bound atom will be bound in the next step, so that the atom and its neighbours are added to the normal neighbour table. To make all of this work correctly, the filling of the cells is done at each step instead of at intervals. As this is a rapid process, it poses no important performance problems.

2.1.8 Temperature and Pressure control

Temperature The temperature is derived from the kinetic energy K using:

$$T = \frac{2\langle K \rangle_N}{3k_B} = \frac{\sum_{atoms} m_i v_i^2}{3Nk_B}, \tag{33}$$

with k_B the Boltzmann constant.

Controlling the temperature involves two steps, namely, using equation (33) to determine T_{sense} for a monitored group of atoms, the "sensing-group", checking if this temperature is equal to a certain required temperature $T_{required}$ and,

if this is not the case, scaling the velocities of the atoms in a "scaling-group" according to:

$$\vec{v}_i^{\,scalers} = \vec{v}_i^{\,scalers}\left[1 + \frac{\delta t}{\tau_T}\left(\frac{T_{required}}{T_{sense}} - 1\right)\right]^{\frac{1}{2}}, \tag{34}$$

where τ_T is the characteristic coupling time. In this way the system is weakly coupled to a "temperature bath", as described by Berendsen *et al.* [11].

At the start of this study, the "sensing-group" consisted of the whole system, while the "scaling-group" contained the bottom atoms when depositing, or the whole system otherwise. It turned out that because of the too weak thermal coupling between the bottom atoms and the other bound atoms in the film (caused by ignoring the electronic thermal conductivity), this could result in situations where the bottom atoms were much hotter/cooler than the rest of the system when heating/cooling, with the other atoms in the sensing-group lagging behind.

Currently we have several options for the sensing- and scaling groups: all atoms, the bound atoms (ie. the atoms experiencing an interaction), the bottom atoms (ie. the atoms that have anchor points), or the non-bottom bound atoms (atoms that have no anchor but are experiencing a force, called "other-bound" atoms). When depositing we mostly use the bound atoms as both the sensing group and the scaling group. The characteristic coupling time τ_T is usually 17.7 fs in our simulations.

During atom or ion impacts, ie. during local disturbances of the system, immediate scaling of the velocities (of the atoms in the scaling group) would be unrealistic, as this would in effect mimic infinite heat diffusion. In these cases temperature control is suspended. After the local disturbance has subdued, subdued, the temperature control is resumed. Determining when such an event takes place and when it has ended should be done automatically, without requiring user interaction.

To this end, an additional requirement is built into the temperature control to determine if velocity scaling should be done. The kinetic energy distribution of the atoms is calculated and tested on being sufficiently Maxwellian. We do this by looking at the Skewness, the Kurtosis, and the width (Σ) of the kinetic energy, as well as the factor by which the maximum kinetic energy is larger than the average kinetic energy.

If the distribution is not sufficiently Maxwellian, no velocity scaling is performed. The critical values for determining the Maxwellian character of the kinetic energy distribution have been tuned so that in thermal equilibrium in approximately 2% of the time-steps velocity scaling is suspended. Table II lists the values used in the current simulations. For faster/better quenching of our systems, we also set a temperature T_{BWAS} below which velocity scaling should always be done, irrespective of the shape of the temperature distribution. This temperature is listed in the table as well.

Usually, when "cooling" our systems to low temperatures for visualization purposes and determination of potential energies, we use a specialized temperature control, or "kinetic energy removal mode" (static relaxation). The

Table II: Values of the critical boundaries for the kinetic energy distribution of the atoms in the system. When any of the boundaries is exceeded, the kinetic energy distribution is considered non-Maxwellian, and no velocity scaling is done. The temperature T_{BWAS}, below which velocity scaling should always be done, is given in Kelvin.

criteria		value
Skewness	high	$1 + 12.73/\sqrt{N}$
	low	$1 - 7.81/\sqrt{N}$
Kurtosis	high	$1 + 61.1/\sqrt{N}$
	low	$1 - 20.4/\sqrt{N}$
Width/Average	high	$1 + 2.615/\sqrt{N}$
	low	$1 - 2.275/\sqrt{N}$
Highest Kinetic Energy /	$k_B T$	$4.657 + 0.687 \ln N$
T_{BWAS}	(K)	101.2

mechanism works as follows. If the acceleration and velocity of an atom i are related by

$$\vec{a}_i \cdot \vec{v}_i < 0, \tag{35}$$

then the velocity is set to zero. The requirement (35) can be applied either to the velocity as a whole, or to each of the three Cartesian directions separately. The last option is the one used here.

Pressure The pressure is derived separately in the three Cartesian directions from the virial theorem, using the diagonal elements $P_\alpha = \sigma_{\alpha\alpha}$ of the *pressure tensor* $\boldsymbol{\sigma}$,

$$\begin{aligned} P_\alpha &= \frac{1}{V} \sum_i^{N_{bound}} \left(m_i v_{\alpha,i}^2 - \sum_{j \neq i} r_{ji}^\alpha \omega_{IJ}^U(r_{ji}) \frac{r_{ji}^\alpha}{r_{ji}^2} \right), (\alpha = x, y, z) \\ &\text{and} \\ P &= \frac{1}{3}(P_x + P_y + P_z), \end{aligned} \tag{36}$$

where $\omega_{IJ}^U(r)$ is the virial of the internal energy U, equation (18).

The pressure is controlled in a similar manner as the temperature. Adjusting the pressure is done by scaling the simulation box, which involves scaling the edge-lengths and the atom positions as well as the anchor points of the special bottom atoms by a factor

$$f_\alpha^P = \left[1 - \frac{\delta t}{\tau_P} (P_{required} - P_\alpha) \right]^{\frac{1}{3}}, \tag{37}$$

where τ_P is not a true time, but instead is really time × pressure, as it also contains the isothermal compressibility. The pressure-control is thus done seperately in all three Cartesian directions. If direction α is non-periodic $P_{required}$ in equation (37) is replaced with 0.0. In our systems, we usually have $\tau_P = 13.77 \cdot 10^{-12}$ Pa s. Rescaling the box may make it necessary to rebuild the cell lists and the neighbour table, see §2.1.7.

Stress tensor From the above, it follows that all of the elements of the stress-tensor (the *negative* of the pressure tensor) can be calculated in the same way as the three pressure components using the stress-tensor elements $\sigma_i^{\alpha\zeta}$ of the atoms:

$$-\sigma_i^{\alpha\zeta} = \frac{1}{\Omega_{II}} \left(m_i v_i^\alpha v_i^\zeta - \sum_{j \neq i} r_{ji}^\zeta \omega_{JI}^U(r_{ji}) \frac{r_{ji}^\alpha}{r_{ji}^2} \right), (\alpha, \zeta = x, y, z), \tag{38}$$

with Ω_{II} the atomic volume. This stress-tensor calculation has been implemented in our simulation code during the time-span of the current study, see [15].

2.2 Stresses

Stresses will develop as a result of mismatch and of temperature (differences in thermal expansion coefficients of substrate and film). The presence of defects will in general introduce local stresses as well. Elastic constants c_{11}, c_{12}, c_{44} are used here to describe the elastic behaviour of the system. The following equations link the macroscopic Bulk modulus B, the Voigt average shear modulus G_V, the Young's modulus E, the anisotropy ratio A, and the Poisson ratio ν_P to these elastic constants:

$$\text{ratio} = \frac{c_{44}}{c_{11}} \tag{39}$$

$$B = \frac{c_{11} + 2c_{12}}{3} = \frac{1}{K} \tag{40}$$

$$G_\mathrm{V} = \frac{3c_{44} + c_{11} - c_{12}}{5} \tag{41}$$

$$A = \frac{2c_{44}}{c_{11} - c_{12}} \tag{42}$$

$$\nu_\mathrm{P} = \frac{c_{12}}{c_{12} + c_{11}} \tag{43}$$

$$E = 2c_{44}\,(1 + \nu_\mathrm{P}) \tag{44}$$

2.3 Diffusion

Diffusion data, and especially the values of activation energies that are of interest for the evolution of the deposited film, are important for deciding on the simulation conditions and for correctly interpreting the simulation results.

In our simulations, there are two main cases of atom movement by diffusion. One is bulk diffusion, which may occur in the deposited film during growth and can result in structure and density changes in parts of the film that are well below the surface. The other is surface diffusion, either over a flat substrate, or over the surface of a growing film, resulting in a displacement of the atoms after they have just found a position on the surface.

Bulk diffusion Bulk (self-)diffusion in a crystal involves a vacancy motion. Assuming that the process follows a Boltzmann (Arrhenius) behaviour with an activation energy for vacancy migration Q_c and that diffusion takes place

according to a random-jump model, together with the Einstein equation, the diffusion coefficient follows from:

$$D_{vac} = \frac{\lambda^2}{6}\nu_{vac} = \frac{\lambda^2}{6}\nu_0\, e^{\frac{-Q_c}{k_B T}} = \frac{1}{6}\lim_{t\longrightarrow\infty}\frac{\mathrm{d}\langle|\Delta\vec{r}|^2\rangle}{\mathrm{d}t} \rightsquigarrow \frac{1}{6}\frac{\langle\Delta r^2\rangle_{N_{vac}}}{\Delta t}, \tag{45}$$

where $\langle\Delta r^2\rangle_{N_{vac}}$ is the mean square drift of a vacancy, λ is the elementary jump length, ν_0 is the attempt frequency, Q_c is the jump activation energy and Δt is the observation time. Note however, that equation (45) is strictly valid only for stationary isotropic systems, so that its use in as deposited thin films such as simulated here requires some caution (see [19] for a discussion on the effects of this).

Surface diffusion on a flat substrate surface One aspect of diffusion in (deposited) films such as the ones simulated here is that in addition to bulk diffusion through the film, surface diffusion may play a large role as well, and increasingly so with smaller film thickness.

Surface diffusion differs from bulk diffusion as it is essentially a two-dimensional process, although in some cases an exchange takes place. This is however, not considered here. Here, surface diffusion occurs as the motion of (an) individual adatom(s) over a flat crystal surface by jumps with a characteristic length λ_{surf}. The surface diffusion coefficient then is:

$$D_{surf} = \frac{\lambda_{surf}^2}{4}\nu_0\, e^{\frac{-Q_c}{k_B T}} = \frac{1}{4}\lim_{t\longrightarrow\infty}\frac{\mathrm{d}\langle|\vec{r}|^2\rangle}{\mathrm{d}t} \rightsquigarrow \frac{1}{4}\frac{\langle\Delta r^2\rangle_N}{\Delta t}, \tag{46}$$

see [12] for more information.

2.4 Temperature and time

2.4.1 Simulation-time problem

A general problem in computer simulation experiments using techniques like MD is that the simulated times are often extremely short compared to the duration of a regular experiment. Simulations typically reach times in the order of ps to a few ns, while regular experimental durations are of the order of seconds to hours (kilo-seconds).

This problem is due to the finite CPU-time required per atom per time-step. With the MD code we use, "camelion" in its current incarnation, the deposition simulations done in the course of this study lasted several months for the smaller systems, and over a year for the deposition of a 50 Å thick Cu film on Mo (on a Pentium III 500 MHz machine).

As a consequence of the short times simulated, the effect of thermally activated processes is lower than would be seen in regular experiments, especially for processes that have higher activation energies. This can be understood from a simple Arrhenius argument. Lets look at figure 3, which shows the number of events N, with activation energy Q_c, which is expected to occur at a certain temperature T within a given time period t

$$N\left(Q_c\right) = \nu_0\, t\, e^{\frac{-Q_c}{k_B T}}, \tag{47}$$

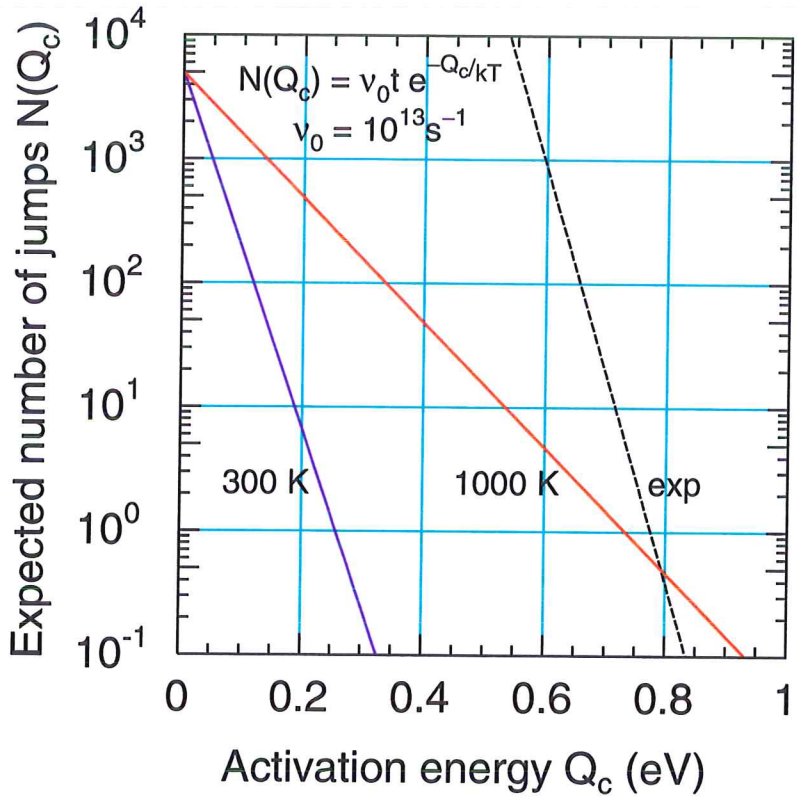

Figure 3: Number of jump events in a typical experiment (line "exp") where a coverage of $\Theta = 1$ monolayer takes $t_{mono} = 1$ s, and in a simulated deposition (line 300 K) with $t_{mono} = 0.5$ ns, both at 300 K. The third line gives the number of jumps for the same simulated deposition, but now at 1000 K.

where ν_0 the attempt frequency, for which 10^{13} s^{-1} is a reasonable value. Only processes that have $N(Q_c) > 1$ are activated in a time t. The figure compares a typical deposition experiment at 300 K, with a monolayer deposition time of $t_{mono} = 1$ s, and a simulated deposition, also at 300 K, for which $t_{mono} = 0.5$ ns. This figure clearly shows that in the simulation, thermal activation is comparatively low for processes with a small activation energy, below $Q_c \simeq 0.8$ eV, and that processes with a larger activation energy, above this "critical" Q_c, will not be active in the timeframe of t_{mono} at all.

2.4.2 Simulation at elevated temperatures

A possible solution for the sketched problem of low activation of thermal processes, is using higher temperatures in the deposition simulation experiments. The effect that this has is shown in figure 3. The line $N(Q_c)$ now has a much smaller slope, which has the effect that Q_c is increased. Moreover, by choosing an appropriate temperature (we used $T = 1012$ K, see §3.4), a situation is reached where the simulation conditions are not very far from the experimental deposition conditions in the Q-range for which the number of jumps in t_{mono} matters, say $Q_c = 0.2$–0.8 eV.

Increasing the temperature is also done in some experiments in order to activate (more) high energy processes and obtain smoother and defect free films, much in the same way as IBAD. A difference with IBAD is that the temperature changes the energy in the system on a global scale, increasing the average kinetic energy of the atoms, and increasing the amount of lower energy processes as well. Of course, there is a thermodynamic limit in the temperature that can be used when looking at solids, namely the melting temperature of the material. It is not wise to go too close to the melting temperature when studying crystalline metals.

2.4.3 Parallel computing as a partial solution for the time problem

A very different solution to increase the time that a simulation can cover is to use parallel computing. This divides the system into multiple parts that are processed in parallel. For Monte Carlo simulations and some *ab initio* calculations the system can be divided into individual slices of time or space that can be individually computed, leading to an almost linear increase in time covered with the number of CPU's used.

With MD, the results of previous time-steps are needed before a next time-step can be calculated, so that the simulation can not be divided into multiple time-intervals that are computed in parallel. It is only possible to divide the system into multiple spatial parts, so that the workload per CPU decreases. As the atoms interact with each other, the different parts need to have up-to-date information about the surroundings, so that the parts are not independent, and a time-step is finished only after all parts of the system are there. The necessary communication between the parts is relatively slow, depending on the hardware used. This introduces and extra computation and communication overhead for parallelized MD simulations. To quantify this we can define the relative efficiency $\nu_{P,relative}$ as

$$\nu_{P,relative} = \frac{t_1}{P\, t_P}, \tag{48}$$

with t_P the time needed to complete the simulation when using P CPU's. We have (in our current MD environments) $\nu_{4,relative} = 0.62$ for $P = 4$, going down to $\nu_{16,relative} = 0.45$ for 16 CPU's. The ultimate consequence of this overhead is that as the volume of the individual parts diminishes, one reaches a point where using more CPU's does not lead to any time being gained, and, eventually, may even lead to a time loss.

Parallel computing does make it possible to perform simulations that would not be possible otherwise, both by reducing the needed time, thus allowing longer times to be simulated, and by allowing simulations to handle larger systems. This first effect will be illustrated by the difference in thickness of two of the deposition simulations, EVAP_{b1} and EVAP_{b2} (see §3.4 and §4.3) which both lasted for about a year. The second effect is utilized in the current study but is also well illustrated in [48] and, to some degree, also in [29, 15] and in [19]. Both of these effects help to reduce the time limitation somewhat.

2.5 Film growth

This subsection will describe some theory concerning growth of a film using PVD techniques, which is what we will simulate in our deposition simulations. First, in §2.5.1 we describe some of the epitaxial relations that are found for fcc/hcp-bcc systems. This information is used near the end of the section to attempt to predict the structure that can be expected for the Cu/Mo deposition. Describing some of the growth modes described in literature (§2.5.2) will help us understand and recognize the growth mode(s) seen in the simulations.

2.5.1 Epitaxy

Epitaxy can occur during growth of a crystalline layer on top of another crystalline layer. It involves a structural relationship between the two layers often consisting of a rotation of the lattices with respect to each other, such that a (semi-)coherent interface can form, ie., the atoms on both sides of the interface are in partial registry with each other, despite possible differences in their crystal lattices. This enables a rather smooth structural transition between the two layers.

When a layer is grown on another layer epitaxially, this usually means the adhesion between the two layers is enhanced, as the total energy that the interface introduces into the system is lowered.

In this subsection, we list some of the epitaxial relationships found experimentally for fcc-bcc interfaces, to make an inventory of what sort of epitaxial relation(s) we can expect to find for the Cu/Mo system. Near the end of this subsection, a first attempt is made to predict what to expect in this system.

Homo-epitaxy If the crystal structure and crystal directions of the underlying substrate are continued in the deposited film, (obviously) only one crystal structure exists. The interface will likely not be visible after growth of the film. Sometimes multiple domains and stacking faults may occur, but stresses will generally be due to thermal and kinetic effects. For an fcc{111}/hcp{0001} close-packed surface, due to the geometry, there are initially two different atom positions, one of which results in a stacking fault. The two have only a very small energy difference between them. Due to this, it is possible, especially at high deposition rates, to find stacking faults parallel to the surface plane. Depending on the growth mode, see §2.5.2, the layer may have a varying number of defects and levels of stress. This form of epitaxy is expected to be found in our case for Cu deposition on a Cu(111) substrate, section 4: §4.2.

Pseudomorphism When one element is grown onto a substrate of another element, the crystal structure of the substrate can be continued across the (usually coherent) hetero-interface into the deposited layer, even when the equilibrium bulk structures of the adsorbate differs from that of the substrate. This is known as pseudomorphism.

Pseudomorphism usually occurs at the onset of growth of a film, at a time when the adsorbate atoms only feel the substrate lattice and the coverage is so

low that they do not see other adsorbate atoms, resulting in an energetically favourable position at the site where the next substrate layer atoms would be. A pseudomorphic epitaxial relation is commensurate in all directions, with all rows in substrate and adsorbate in registry, ie. all atoms lie on the most favourable positions. This does however introduce stresses in the adsorbate layer, which is not in its equilibrium bulk lattice structure.

Randler, Dieterle and Kolb [60] report *in situ* growth of Cu on Au(100) studied by STM, noting that this is related to a so-called under-potential region which generally occurs if the deposit-substrate interaction is stronger than the deposit-deposit interaction.

As the coverage increases and the adsorbate atoms begin to "see" each other, becoming surrounded by other adsorbate atoms, this is increasingly unfavourable, introducing strains of up to 10%, so that pseudomorphism can usually only last up to coverages Θ of several monolayers (MLs). At higher coverages, hetero-epitaxial orientation relations may occur. In this case, it is relatively easy to form orientation relations that require no or only a small rotation and few atomic movements compared to orientations that do require substantial rotation.

Hetero-epitaxy at the bcc{110}-fcc{111}interface Several orientation relationships are possible between an fcc structured material and a bcc structured material. Which orientation relation will occur in a specific case depends for a large amount on the ratio r_{m} between the diameters of the adsorbate and substrate atoms, or the ratio of the sizes of the fcc and the bcc atoms [17]:

$$r_{\mathrm{m}} = \frac{r_{Adsorbate}}{r_{Substrate}} \overset{\text{here}}{=} \frac{r_{fcc}}{r_{bcc}}, \tag{49}$$

giving the mismatch between the atoms in the two structures.

Figure 4 shows the topic of this subsection, the two-dimensional rhombic unit cells of an fcc{111} (or hcp{0001}) monolayer (adsorbate) and a bcc{110} substrate, positioned on top of each other. The Cartesian axes x ($\parallel [\bar{2}11]_{fcc} \parallel [\bar{1}10]_{bcc}$) and y ($\parallel [0\bar{1}1]_{fcc} \parallel [001]_{bcc}$) are shown, as well as the relevant crystal directions, the nearest-neighbour distances a and b of respectively bcc and fcc, the lengths of the diagonals,

$$a_x = d\langle 011\rangle_{bcc} = \sqrt{2}\, l_{bcc} = \sqrt{\frac{8}{3}}\, a, \tag{50}$$

and

$$b_x = d\langle 211\rangle_{fcc} = \sqrt{\frac{2}{3}}\, l_{fcc} = \sqrt{3}\, b, \tag{51}$$

and the angles $\alpha = \arctan\sqrt{2} \simeq 57.74°$ between a and the x axis, and $\beta = \arctan\sqrt{3} = 60°$ between b and the x axis.

The mismatch is expressed in the figure as the ratio of $b/a = r_{\mathrm{m}}$. Not shown in the figure is the orientation angle θ, defined as the (positive) rotation between bcc[001] and fcc[$0\bar{1}1$] or, equivalently, between bcc[$\bar{1}10$] and fcc[$\bar{2}11$] (a_x and b_x). Angle θ is zero in the figure.

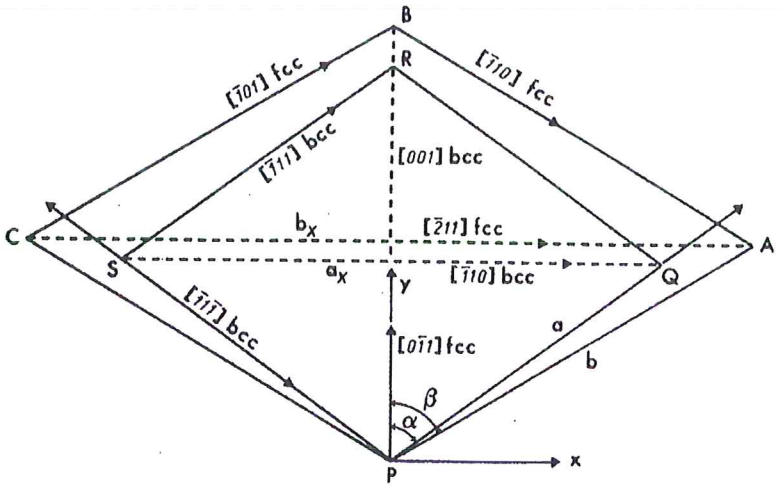

Figure 4: Two-dimensional rhombic unit cells of an fcc{111} (or hcp{0001}) monolayer (adsorbate, PQRS) and a bcc{110} substrate (ABCP), with Cartesian axes, some relevant crystal directions, angles $\alpha = \arctan\sqrt{2}$ and $\beta = 60°$, nearest-neighbour distances a and b of respectively the bcc and fcc structure, and the lengths of the diagonals, $a_x = d[1\bar{1}0]_{bcc}$ and $b_x = d[\bar{2}10]_{fcc}$. Not shown is the orientation is the orientation angle between the adsorbate and substrate unit cells, θ, which is zero in the shown case. The mismatch will be expressed as the ratio b/a, r_m. The bcc and fcc lattice constants are $l_\mathrm{bcc} = 2a\sqrt{3}$ and $l_\mathrm{fcc} = \sqrt{2}b$. The figure is reproduced from [9].

Note that if the atoms on the two sides of the interface overlap as is the case for atom(s) P in the figure this will generally be an unfavourable site for an atom to be in. The most favourable sites for the adsorbate atoms during growth will initially be the pseudomorphism sites, in other words, the sites where the atoms of the "next" substrate layer would be situated.

The two orientations mentioned here, the Nishiyama-Wasserman orientation relation and the Kurdjumov-Sachs orientation relation, are the ones found most often, and until recently, the only categories of orientation relations seen for fcc{111} on bcc{110}. The reason for this is that these two are the only orientations expected on the basis of energy considerations based solely on geometrical considerations, without allowing for relaxation due to stresses. Then only the mismatch r_m determines which of the two orientations is found.

Both the KS and NW orientation relation are commensurate only in one direction. The atoms in that one direction are equally spaced in both the adsorbate and the substrate, with alternating favourable and unfavourable regions in the other crystal directions.

Kurdjumov-Sachs Orientation Relation With the Kurdjumov-Sachs (KS) orientation relation, an fcc$\langle\bar{1}01\rangle$ direction lies parallel to a bcc$\langle111\rangle$ direction, while both directions lie in the closest packed planes of the structure, the fcc(111) plane and the bcc(110) plane. The fcc$[0\bar{1}1]$ direction and the bcc[001] direction make an angle of $\theta = 60° - \arctan\sqrt{2} \simeq \pm 5.26°$ with each other. Because of the possibility of both a positive and a negative angle, two different domains can form. In figure 5, the KS relation is illustrated for an fcc{111}

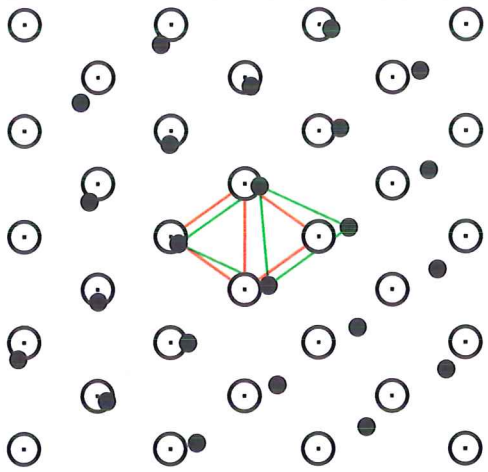

Figure 5: An fcc{111} adsorbate (•) on a bcc{110} substrate (⊙) displaying the Kurdjumov-Sachs orientation relation. The green and red diamonds are the fcc{111} and bcc{110} two-dimensional unit cells. See figure 4 for the crystal directions. The mismatch is such that $3/2d\langle\bar{2}11\rangle_{fcc} = d\langle 110\rangle_{bcc}$, which occurs for a mismatch of $r_{\mathrm{m}} = 4/3\sqrt{3} \simeq 1.0887$.

adsorbate (•) on a bcc{110} substrate (⊙). Note that the angle θ is not explicitly shown, but can be seen between the bcc[001] and the fcc[0$\bar{1}$1] directions, the "bars" in the green (fcc) and red (bcc) diamonds.

The KS orientation is presumably the most likely when:

$$\frac{1}{2}\sqrt{3}\,b = \frac{2}{3}\sqrt{2}\,a \text{ or } r_{\mathrm{m}} = 4/3\sqrt{3} \simeq 1.0887, \tag{52}$$

so that the distances between the corresponding close-packed rows are equal in the two crystals [9].

The KS orientation exhibits a pattern of rotational Moiré fringes, originating from an interplay between the non-aligned close-packed bcc and fcc rows. The angle of the rotational fringes is strongly dependent on the mismatch. Also, when the mismatch is not exactly equal to the ideal r_{m} for KS, a set of parallel fringes is found in addition to these rotational fringes, see Bruce and Jaeger [14].

Figure 6 shows the Moiré pattern for the KS orientation relation at the most favourable mismatch. In this figure, the "light" areas are unfavourable regions, as the atoms of the top substrate layer and those of the first adsorbate layer are positioned on top of each other, while the darker areas have the adsorbate atoms lying in between the top substrate layer x, y-positions. Figure 11 (bottom) shows a pattern for a KS orientation with a mismatch that is not the ideal mismatch for KS, namely the pattern for an undeformed fcc{110} Cu monolayer on Mo{110}.

Nishiyama-Wasserman Orientation Relation The Nishiyama-Wasserman (NW) orientation is rotated in the interface plane with respect to the KS orientation relationship, so that a (close-packed) fcc$\langle 0\bar{1}1\rangle$ direction lies parallel to

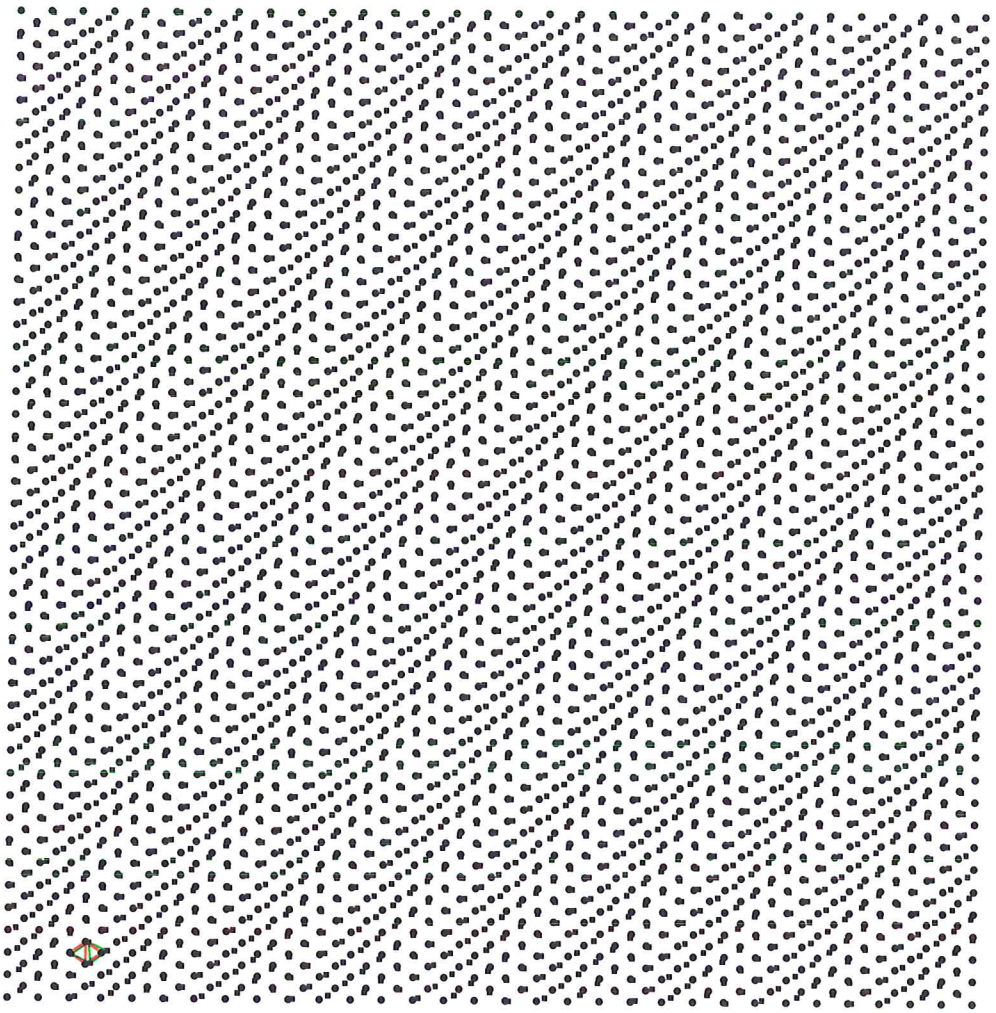

Figure 6: An fcc{111} adsorbate (▪) on a bcc{110} substrate (•) displaying the Kurdjumov-Sachs orientation relation. The green and red diamonds are the fcc{111} and bcc{110} two-dimensional unit cells. See figures 4 and 4. The mismatch is $r_{\mathrm{m}} = 4/3\sqrt{3} \simeq 1.0887$. The pattern formed by the rotational Moiré fringes is clearly visible. Figure 5 is a small selection from the lower left corner of this picture, but uses different symbols for the fcc and bcc atoms.

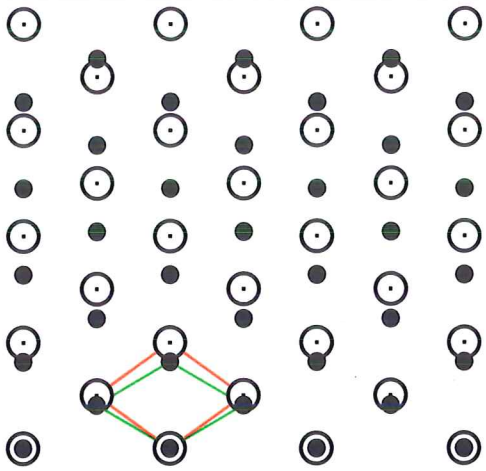

Figure 7: An fcc{111} adsorbate (•) on a bcc{110} substrate (⊙) displaying the Nishiyama-Wasserman-x orientation, where the close-packed directions $[0\bar{1}1]_{fcc(111)} \parallel [001]_{bcc(110)}$. The green and red diamonds are the fcc (111) and bcc (110) two-dimensional unit cells, compare figure 4. The mismatch is such that $b\sqrt{3}/2 = \sqrt{2/3}\,a$, equal to a mismatch of $r_{\mathrm{m}} = 0.9428$.

a bcc$\langle 001\rangle$ direction ($\theta = 0°$), which is not a close packed direction in bcc. In figure 7 this orientation relation is illustrated for an fcc{111} adsorbate (•) on a bcc{110} substrate (⊙). The ideal mismatch for the shown orientation relation is such that $b\sqrt{3}/2 = \sqrt{2/3}\,a$, equal to a mismatch of $r_{\mathrm{m}} = 0.9428$.

There actually are two different NW orientation relations known, which have in common that the close-packed rows in the fcc and bcc structure are not aligned while none-close-packed rows are aligned (see [14]). One of the two is the NW-x orientation, which is the orientation relation shown in figure 7, and which has $r_{\mathrm{m}} = 0.9428$, see above,so the fcc atoms are smaller than the bcc atoms. In this orientation, the distances between the close packed rows are unequal but the distances between the non-close-packed rows $\langle\bar{2}11\rangle_{\mathrm{fcc}\{111\}}$ and $\langle 110\rangle_{\mathrm{bcc}\{110\}}$ are related by:

$$\frac{3}{2}\, d\langle\bar{2}11\rangle_{fcc\{111\}} = d\langle 011\rangle_{bcc\{110\}}. \tag{53}$$

This orientation relation has Moiré fringes along the x (fcc$\langle\bar{2}11\rangle$) direction of figure 4:

$$_{fringe\parallel} \parallel [11\bar{2}]_{fcc(111)} \parallel [1\bar{1}0]_{bcc(110)}. \tag{54}$$

Figure 8 shows this interference pattern of fcc (▪) and bcc (•) atoms for the NW-x orientation relation. Just as in for the pattern of the previously described KS orientation, the "light" areas are unfavourable, and the darker areas are energetically favoured areas.

The second favourable mismatch value for the NW orientation results in the NW-y orientation. For this orientation relation, the distances between

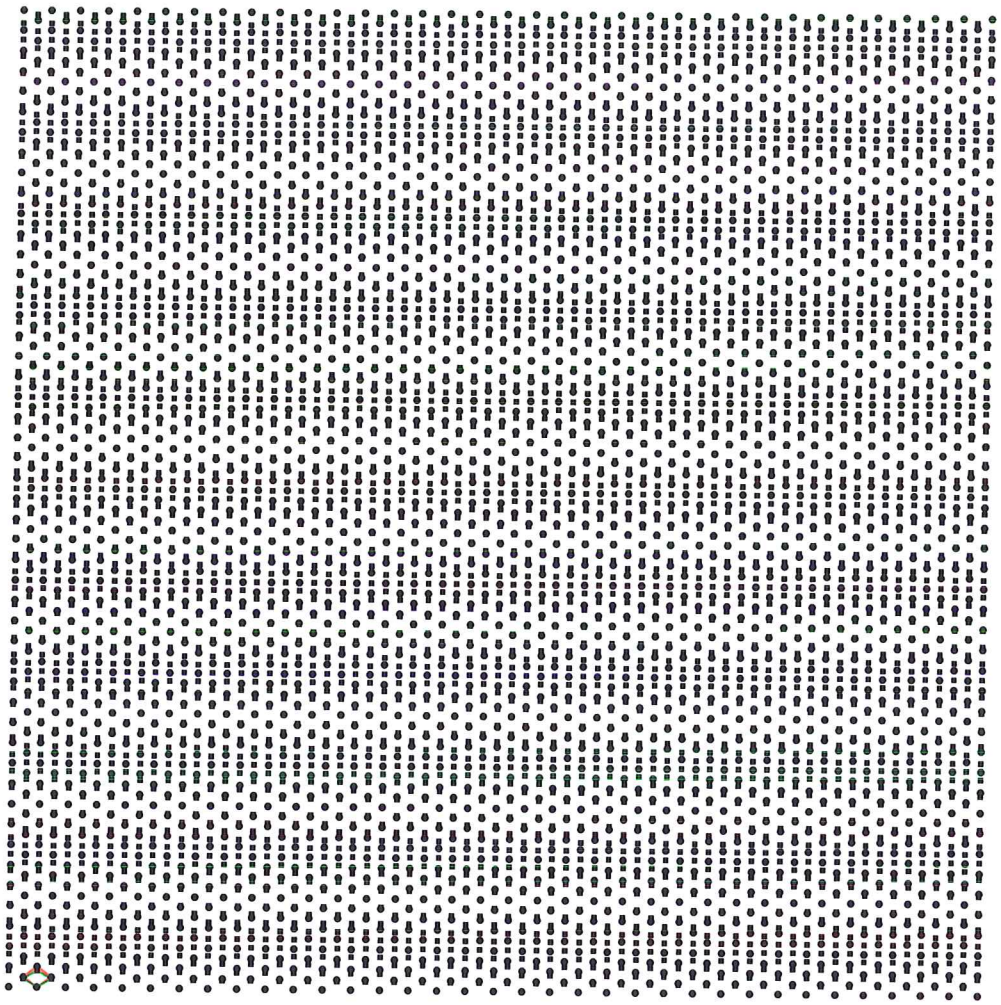

Figure 8: An fcc{111} adsorbate (▪) on a bcc{110} substrate (•) displaying the Nishiyama-Wasserman-x orientation, where the close-packed directions $[0\bar{1}1]_{fcc(111)} \parallel [001]_{bcc(110)}$, possible with $\sqrt{3}/2\,b = \sqrt{2/3}\,a$, equal to a mismatch of $r_{\mathrm{m}} = 0.9428$. The green and red diamonds are the fcc (111) and bcc (110) two-dimensional unit cells, see also figure 4 and figure 7. The pattern formed along the x-axis by parallel Moiré fringes can clearly be seen. Figure 7 is the lower left corner of the pattern shown here.

the (parallel) close-packed rows $\langle 110 \rangle_{fcc}\{111\}$ and $\langle 100 \rangle_{bcc}\{110\}$ are the same, occurring when the mismatch is $r_{\mathrm{m}} = 1.1547$. This results in sets of parallel Moiré fringes along the y-axis instead of along the x-axis.

When the mismatch is close, but not equal, to one of these two mismatch values, a more complicated pattern results for the NW orientation, resulting in a chevron pattern of intermixing x- and y-fringes, see again [14] for a more elaborate description. The effect described here is what would be seen for the Cu/Mo system in this orientation, as the mismatch is close to, but somewhat larger than for the ideal NW-x orientation relation (see figure 11, top).

Calculation of orientation as a function of mismatch A theoretical study by Grey and Bohr [28] revealed a mechanism through which finite-size effects of features on the surface, as well as of the sample, may stabilize an orientation relation. They have calculated the minimum energy surface that an fcc{111} adsorbate monolayer "sees" in a periodic substrate potential formed by the three fundamental Fourier components of a bcc{110} plane. The adsorbate is allowed to relax by a small amount, proportional to the local gradient of the substrate potential. This results in figure 9.

The figure shows that the KS as well as the NW orientation may be stabilized over a large range of misfits r_{m}. Note however, that the model by Grey and Bohr depends only on the relaxation induced by the substrate potential geometry, not taking into account the magnitude of interactions between substrate and adsorbate relative to the adsorbate-adsorbate and substrate-substrate interactions. This factor will however influence the magnitude of the effect that the substrate potential geometry has on the geometry of the adsorbate.

Influence of the interaction strength of adsorbate and substrate According to Bauer and van der Merwe [9], who continued on the work by Stoop and van der Merwe earlier [68, 69, 70, 71, 77, 78, 79], taking into account the relative strength of the materials can be done for epitaxy in non-rigid crystalline monolayers of atoms interacting with each other, and being exposed to the competing periodic substrate field when:

1. Only homogeneous strains are allowed ([9] and [77, 78, 79]); or
2. Homogeneous mismatch strains *and* oscillatory strains in the form of mismatch dislocations — also called solitons or walls — are taken into consideration ([9] and [68, 69, 70, 71]).

If one of these two approaches is taken, the equilibrium configuration is determined by $\min(\bar{\varepsilon} + \Delta V) = E_{min}$, where $\bar{\varepsilon}$ is the mean (elastic) strain energy increase per adatom as compared to the unstrained monolayer ($\bar{\varepsilon} = 0$), and ΔV is the change of the mean potential energy increase per atom, relative to the substrate potential minimum. In this model, E_{min} essentially depends upon the geometry (mismatch) parameter r_{m}, on the relative strength of the intralayer and the adsorbate-substrate interaction, ℓ, and on the chosen strain mode. The relations used in [9] for the elastic constants c_{11}, c_{12} and c_{44} are S, the Poisson

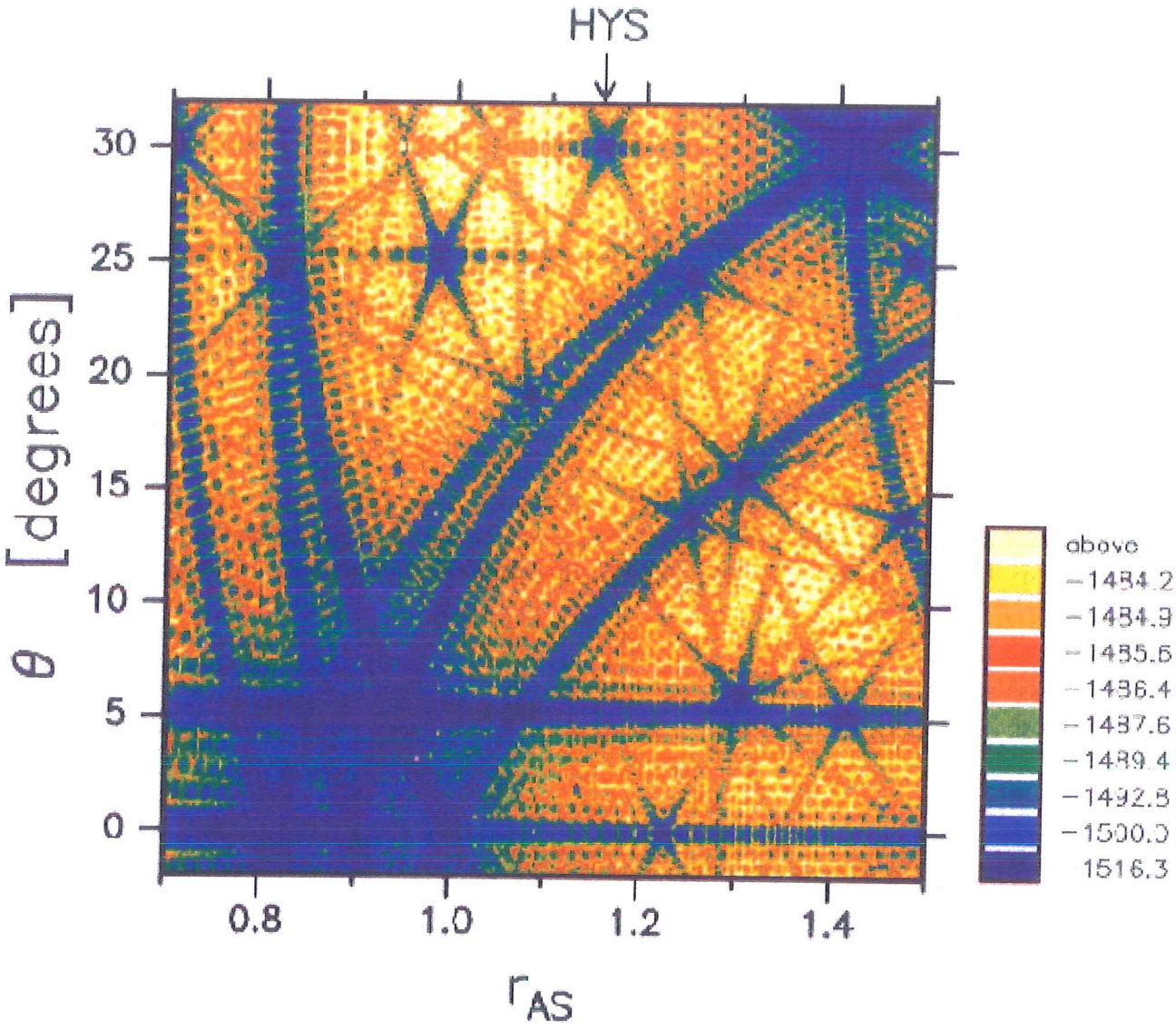

Figure 9: Energy surface for the relaxed fcc{111} adsorbate coordinates. Low-order commensurate structures appear as local energy valleys. Energy surface for adsorbate atom positions in a substrate potential formed from three bcc{110} fundamental Fourier components, as a function of mismatch $r_{AS} = 2r_{\mathrm{m}}/\sqrt{3}$, and adsorbate rotation θ. The colour-contours are such that each colour covers an equal percentile of the energy surface. The energy indicated by the scale is that of the whole adsorbate array. This figure is reproduced from Grey and Bohr [28].

ratio ν_{P}, and R:

$$S = \frac{c_{11}^2 - c_{12}^2}{2c_{11}} \tag{55}$$

$$R = \frac{c_{11}\, c_{44}}{c_{11}^2 - c_{12}^2}. \tag{56}$$

The relative interaction strength ℓ is:

$$\ell = \frac{1.2\,\Omega S}{E_{diff} {r_{\mathrm{m}}}^2}, \tag{57}$$

with E_{diff} the adatom surface migration energy on the substrate surface and Ω the atomic volume of the adatom. The elastic strain energy per atom now is

$$\begin{aligned} \varepsilon &= \frac{E_{diff}}{1.2} \ell^2 {r_{\mathrm{m}}}^2 \left(e_x^2 + e_y^2 + 2\nu_{\mathrm{P}} e_x e_y + R e_{xy}^2\right), \\ &\text{or} \\ \varepsilon &= S\Omega\ell \left(e_x^2 + e_y^2 + 2\nu_{\mathrm{P}} e_x e_y + R e_{xy}^2\right), \end{aligned} \tag{58}$$

where the e_α's are the strain components. Using this, for a strong adsorbate-substrate interaction (small ℓ) the KS orientation is replaced with pseudomorphism. Only homogeneous strains are taken into account, as mismatch dislocations caused no major shift in the stability regions, just a minor correction. The homogeneous strains used in [9] are performed with values corresponding to Cu (see table III on page 43).

The mismatch ranges for which the different orientations are expected depend strongly on the relative strength of the adsorbate-substrate interactions. For each (r, ℓ) combination, the orientation that has the smallest E_{min} value compared to other orientations, can be determined. The phase diagram that can be constructed from these calculations is shown in figure 10. For the Cu/Mo system, where $r_{\mathrm{m}} < 1$, this means that coherency is more easily possible than would be expected from geometric considerations alone.

Allowing mismatch dislocations displaces the stability limits for 1D NW-x, (dashed line LM), and the occurrence of this orientation is extended into an adjacent region when mismatch dislocations and mismatch strains coexist. A similar situation is found for the NW-y and KS orientations. The assumption of crystallinity of the monolayers and the use of elasticity constants equal to the bulk values only effect the precise values of the mismatch r_{m} and the ℓ value for which an orientation is most favourable, not the global picture of the zones shown as shown in the figure. Introducing anharmonicity in the potentials makes coherency possible for a wider range of mismatches $r_{\mathrm{m}} < 1$ than for mismatches $r_{\mathrm{m}} > 1$, causing some minor displacements in figure 10.

Assuming a rigid substrate becomes less valid with increasing film thickness. Therefore, Bauer and van der Merwe make the assumption that the rigidity modulus is n times the monolayer elastic constant for a n layers thick film, so that the ℓ-axis of figure 10 changes to $\sqrt{n}\,\ell$, allowing for an immediate prediction of the evolution of film structure with thickness, provided kinetic limitations do not suppress otherwise possible transitions. In making such a prediction, the (degree of) crystallinity of the film becomes becomes an important factor.

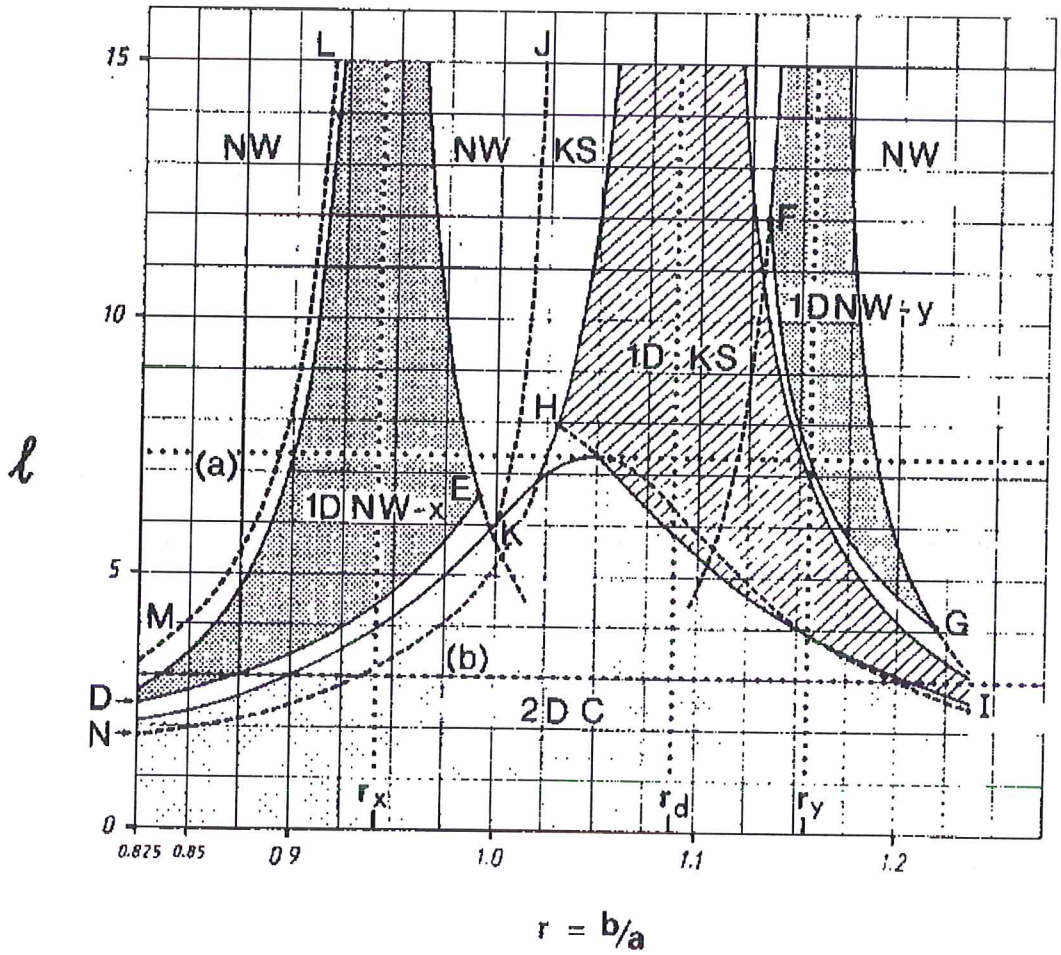

Figure 10: Stability ranges ($\sim$ phases) for pseudomorphy (2D, C), 1D coherency in the NW orientation (1D NW-x, NW-y) and 1D coherency in the KS orientation (1D KS) of homogeneously strained fcc{111} monolayers ($\sim$ Cu) on bcc{110} substrates as a function of mismatch parameter $r = r_m$ and interaction parameter ℓ. In the corridor DE, 2D C has the lower energy but is itself unstable, so that mismatch dislocation formation transforms it into the NW orientation. In the corridor FG, KS would be more stable. However, which of the orientations will prevail is less certain in this corridor than in other corridors. The figure is reproduced from Bauer and van der Merwe [9].

Cu on Mo: what to expect Using the literature values for the lattice constants, the mismatch between Cu and Mo *bulk* atoms at 300 K is $r_{\mathrm{m}} = 0.93785$(with $r_{AS} = 1.083$ Å). This is close to the value for the NW-x orientation relation. An extension of a little more than 8% is needed to make the KS orientation possible instead of the NW-x orientation, which is unlikely. As the mismatch is not too far from unity and as the Cu-Mo interaction is likely stronger (locally) than Cu-Cu, pseudomorphy may also be an option, especially at the start of the deposition, as $\sqrt{N}$ is still small (see figure 10). Also, the growth mode may change the orientation relations that can occur.

Figure 11 shows patterns for Cu on Mo in the NW-x (top) and KS orientations (bottom). Both figures are constructed in the so-called "rigid approximation", ie., the atoms are in the bulk lattice positions, not taking into account. In our simulations, we would expect some relaxation of the Cu film, somewhat altering the pattern, so that the lighter, unfavourable, areas, see above, become smaller or vanish, with the darker areas "prevailing". For pseudomorphy, the pattern would be that of a regular bcc{110} plane, with the Cu strained to be coherent with the underlying Mo substrate.

The relative interaction parameter ℓ for Cu and Mo can be calculated from equations (43) through (57). In section §4.1 this will be done, enabling a prediction of the epitaxial relationship that would be expected based on the theory depicted in figure 10. From the literature values for the atomic volume Ω (and the above given value for r_{m}), and using a value of 0.11 eV (see page 86) for the surface diffusion energy, we can calculate a literature value for ℓ of:

$$\ell = \frac{1.2\,\Omega_{\mathrm{Cu}}\,S}{Q_{\mathrm{diff}}\,{r_{\mathrm{m}}}^2} = \frac{1.2 \cdot 11.8100\text{Å}^3\,(168^2 - 121^2)/(2 \cdot 168)\,\mathrm{MPa}}{0.11\,\mathrm{eV}\;0.93785^2} = 5.88, \tag{59}$$

predicting that Cu starts growing as a pseudomorphic layer for low coverage ($\Theta < 0.58$), and then switches to a NW-x orientation (as found above from the mismatch r_{m}).

2.5.2 Models for growth modes

Growth mode as a function of surface energy and mismatch Three general mechanisms are found for growth of thin films near equilibrium. Which of the three growth "modes" is realized depends on the relative magnitudes of the surface energies of the substrate, γ_s, and of the thin film, γ_f, as well as on the interfacial energy γ_{in}. This interfacial energy also incorporates the strain energy, which is thickness (or n-)dependent — with n the number of monolayers in the thin film. The interfacial energy generally depends on the mismatch r_{m} between the substrate and the adsorbate atoms. The values of γ_s and of γ_f usually are take as the surface energy values for semi-infinite crystals.

The three growth modes are:

- The Frank—van der Merwe growth mode (FM mode, or mode I), also known as layer-by-layer growth. For Frank—van der Merwe growth the

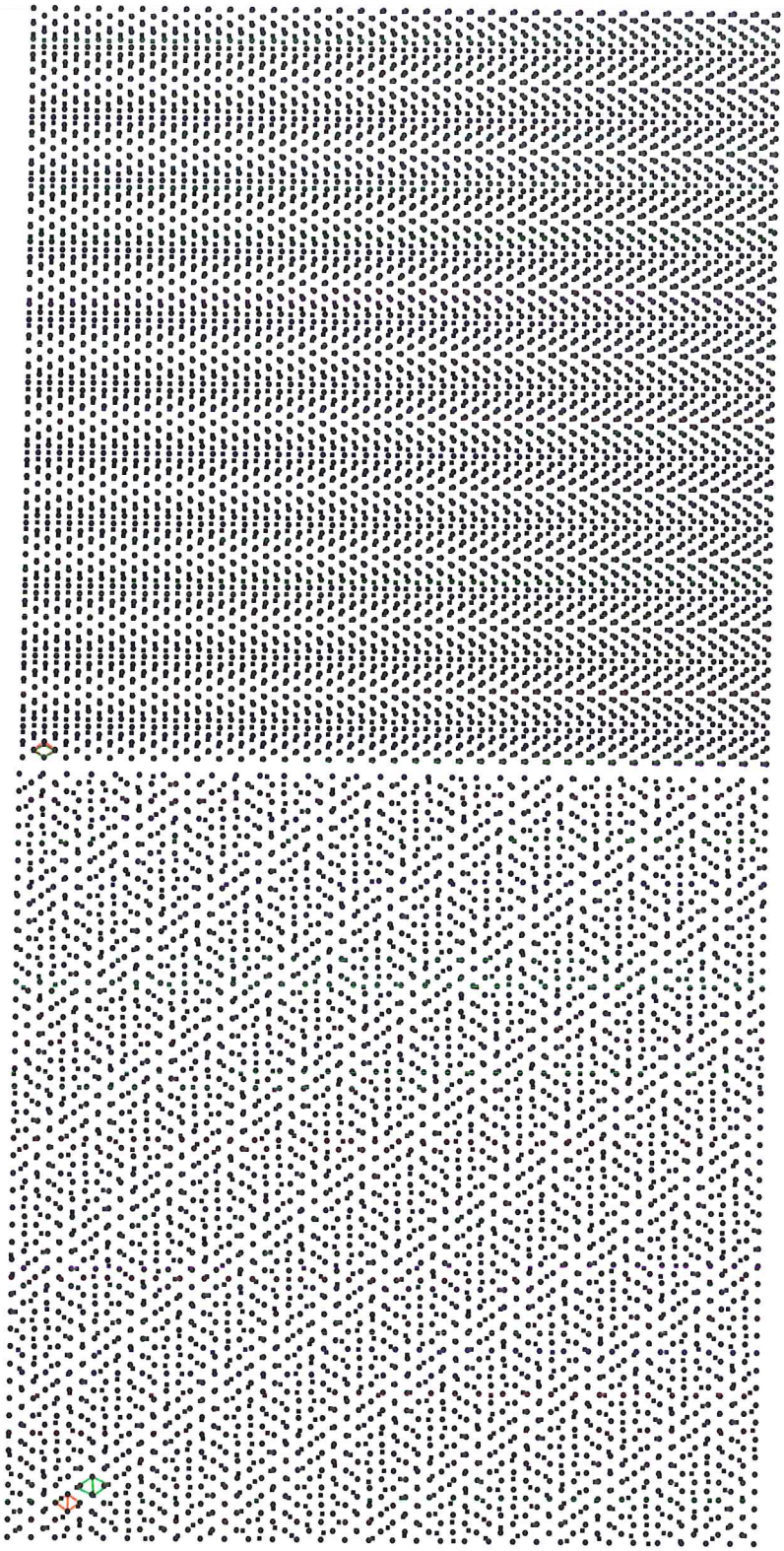

Figure 11: Patterns that can be expected on the basis of the mismatch between bulk Cu and Mo when ignoring relaxation, for a perfectly fcc{111} Cu adsorbate (▪) on a perfect bcc{110} substrate (•) in NW-x (top) and KS orientation (bottom).

conditions are, independent of film thickness (n):

$$\Delta\gamma_n = \gamma_{fn} + \gamma_{in} - \gamma_s \leq 0, \tag{60}$$

where γ_{fn} differs from γ_f due to the n-dependent surface strain. For $\gamma_f < \gamma_s$, Frank—van der Merwe growth can only be achieved when γ_{in} is small. Furthermore, the condition (60) is only fully fulfilled for zero mismatch between the film and substrate atoms, otherwise, the second growth mode develops;

- The Stranski—Krastanov growth mode (SK, or mode II). This mode starts with the growth of one or more monolayers , but the strain energy increases with thickness, until at a given critical value $n = n^*$ the condition (60) is not fulfilled any longer and three dimensional crystal growth develops;

- The Volmer—Weber growth mode (VW, or mode III), also called three-dimensional (island) growth. If the condition for Frank—van der Merwe growth , equation (60), is not fulfilled from the first onset of growth, the layer grows by the Volmer—Weber growth mode, with three dimensional islands growing on the substrate surface.

Whenever the two values of the surface energies differ strongly, the metal with the larger value for γ will tend to grow by either the Stranski—Krastanov growth mode or by the Volmer—Weber growth mode. By going away from quasi-equilibrium conditions it may be still possible to grow continuous monolayers, even when the conditions (60) are not strictly met. This can be done by going to higher super-saturations of the chemical potential $\Delta\mu = \mu - \mu_0$ by increasing the deposition rate or decreasing the substrate temperature. Both of these have the effect that the nucleation rate is lowered so that the crystals never fully develop. Some aspects of the second option will be explored further in §2.4. Furthermore, the interface energy drives a move to smoother (and thus a smaller area) interfaces, when conditions enable atomic scale rearrangements (or diffusion, see §2.3) during interface formation.

Mismatch based explanation for the established growth mode A phenomenological explanation to determine the type of deposit for a (metallic) adsorbate A on a foreign substrate S, is based on the differences in interaction energy between the two, namely the vertical interaction energy ψ_{A-S} of A with the substrate and of A with atoms of the same type ψ_{A-A}, and the crystallographic misfit r_{m}. If $\psi_{A-S} \ll \psi_{A-A}$, then crystal growth is expected via the three-dimensional growth (Volmer—Weber growth) mode. On the other hand, if $\psi_{A-S} \gg \psi_{A-A}$, it depends on the mismatch if Frank—van der Merwe growth occurs, when $r_{\mathrm{m}} \sim 1$, or three-dimensional growth on top of (a) redeposited monolayer(s) (Stranski—Krastanov growth) should occur, which is the case when $r_{\mathrm{m}} \not\sim 1$ [20].

For the deposition of Cu on Mo, the interaction energy ψ_{A-S} is not known yet. However, as $E_c^{Mo} > E_c^{Cu}$, we might expect that the second possibility

mentioned, where the mismatch decides on the growth mode, is the one found in this system.

2.5.3 IBAD

Ion Assisted Deposition (IBAD) changes the deposition conditions by adding energy to the system. The difference with adding energy by using higher temperatures is that IBAD introduces a very local energy increase, at the surface of the growing film, where atoms can diffuse [66]. By these means, already formed structures like columnar structures, cavities and other defects can be flattened and removed. This would decrease the roughness in cases where it is higher than a few (2 or 3) plane distances. If the roughness is already very low without IBAD, then IBAD is not very useful in this respect, although it may still be useful for reducing defects like stacking faults in fcc/hcp materials and other lower energy defects.

The choice of the ion energy used is dependent on the nature of the deposited material. A direct collision between an ion and a (several) adsorbate atom(s) should not result in creating a large molten pool of atoms, which means that lower ion energies must be used when the ion and atom masses are nearly equal. If the objective is to remove columnar structures, the energy needs to be high enough to break these structures down, for instance by 'forward sputtering'. Otherwise, a higher diffusivity is sufficient to remove most vacancies and protrusions from the surface.

Another factor in IBAD is the Ion-to-Atom Ratio (IAR), which is the amount of ions that is introduced per deposited atom. Obviously, the higher the IAR, the higher the energy added to the system. A higher IAR can be used together with a lower ion energy to obtain the same added energy. In our experiments the IAR is about 0.1. Another important, but in general non-adjustable, parameter is the fraction of ions that is neutralized. These atoms are not slowed down as they reach the substrate and consequently arrive with a high energy (velocity) on the substrate. In the experimental setup that we use this fraction is 0.1.

A problem with IBAD can be that it may itself induce defects, both by occasional high energy impacts of neutralized ions in the film, and by incorporation of the ions themselves into the film. Because of this problem, recently an alternative approach is being investigated which involves the use of energetic clusters of atoms of the type which should be deposited (ionized cluster beam deposition). This method is however not without controversy, as no agreement exists that indeed clusters are formed in the current setup [84].

3 Tools

At this point we leave the general theories behind and start discussing the more specific methods and tools used. In subsection 3.1, we will look in detail at the interactions used in this work.

Then we will continue in subsection 3.2, with an inspection of several analysis methods used in this work, which have been applied to study the growth mode and epitaxial relations (see also §2.5), the diffusion behaviour (see also §2.3) and the stresses in the deposited films (see also §2.2). This subsection is concluded with a description of some of the conventions used in our group.

In subsection 3.4 details of the simulation runs are given, including the method used to derive a quantity, system size, simulation duration etc.

3.1 The different particle interactions

3.1.1 Cu-Cu

As described in the previous section (§2.1.2), for the metal-metal interactions, we use EAM in the thermal energy range combined with the Fi-Mo pair potential (see §2.1.3) in the high-energy/short-distance regime.

We have decided to use the EAM interaction potential proposed by Oh and Johnson [57, 58, Oh Johnson 1,2], a choice which is based on previous experience with the Mo-Mo potential proposed by these authors [42, 47, 49, 48, 15]. In addition, the choice is based on a comparison between EAM potentials in fcc and bcc materials by Doyama and Kogure [23, Doyama Kogure pot.].

The Oh-Johnson version of the EAM (OJ-EAM) for a number of fcc transition metals including Cu [57, Oh Johnson 1] uses, in addition to equation (10) for the total energy, the following expressions: the embedding function F_I for atom i of type I

$$F_I(\rho_i) = a_I \left(\frac{\rho_i}{\rho_I^{eq}}\right)^{n_I} + b_I \left(\frac{\rho_i}{\rho_I^{eq}}\right), \tag{61}$$

the base electron density function

$$f_I^{base}(r_{ij}) = k_I e^{-\beta_I \left(\frac{r_{ij}}{r_{II,1}^{eq}} - 1\right)}, \tag{62}$$

which is used together with equation (12) to obtain the local electron density of atom i, and the base EAM pair potential of a pair of atoms i and j, both of type I,

$$\phi_{II}^{base}(r_{ij}) = \phi_{II}^{e} e^{-\gamma_{II} \left(\frac{r_{ij}}{r_{II,1}^{eq}} - 1\right)}. \tag{63}$$

In these equations ρ_I^{eq} is, as mentioned earlier, the equilibrium electron density, k_I is the electron density scaling factor that cancels out for single-element systems, and $r_{II,1}^{eq}$ is the first equilibrium neighbour distance of atoms of type I (in the equilibrium crystal structure, fcc).

The base electron density and base pair potential functions $f_I^{base}(r_{ij})$ and $\phi_{II}^{base}(r_{ij})$ are modified to obtain smooth cutoff exponentials at the cutoff distance $r_{II,c}$, resulting in

$$f_I(r_{ij}) = f_I^{base}(r_{ij}) - f_I^c(r_{ij}), \tag{64}$$

and

$$\phi_{II}^{EAM}(r_{ij}) = \phi_{II}^{base}(r_{ij}) - \phi_{II}^c(r_{ij}), \tag{65}$$

where

$$f_I^c(r_{ij}) = f_I^{base}(r_{II,c}) + g_I(r_{ij}) \frac{f_I'^{base}(r_{II,c})}{g_I'(r_{II,c})}, \tag{66}$$

and

$$\phi_{II}^c(r_{ij}) = \phi_I^{base}(r_{II,c}) + g_I(r_{ij}) \frac{\phi_{II}'^{base}(r_{II,c})}{g_I'(r_{II,c})}, \tag{67}$$

with

$$g_I(r_{ij}) = 1 - e^{-\delta_I \left(\frac{r_{ij} - r_{II,c}}{r_{II,1}^{eq}} \right)}. \tag{68}$$

There are seven parameters in the above equations: a_I, b_I, n_I, β_I, γ_{II}, and the two cutoff parameters δ_I, $r_{II,c}$. Although β_I could be fitted from free (isolated) atom densities, Oh and Johnson use it as an adjustable parameter with a value $\beta_{Cu} = 6.0$ [58, Oh Johnson 2]. Likewise, γ_{CuCu}, which determines the "strength" of the Cu-Cu EAM pair potential, has a value of 8.5 [58]. The cutoff function parameter δ is a constant which determines how steep the functions ϕ_{II} and f_I fall to zero at $r_{II,c}$. To be able to make a distinction between fcc and hcp it is required to take up to third neighbours into account. This choice of cutoff ensures that this is the case. Oh and Johnson use values of $\delta_{Cu} = 20.0$ and $r_{Cu,c}/r_{CuCu,1}^{eq} = c_{Cu} = 1.9$, from which we do not deviate.

Table III gives values for the cohesive energy E_c, the three elastic constants c_{11}, c_{12}, and c_{44} (used in the form of the bulk modulus B and Voigt average shear modulus G_v), the atomic volume Ω and the unrelaxed mono-vacancy formation energy E_{1V}^{UF} of bulk Cu. The table also gives the mass of Cu and some other elastic moduli. The remaining four potential parameters, a_{Cu}, b_{Cu}, n_{Cu} and ϕ_{CuCu}^e, are found by fitting equations (10, 12, 61, 64, 65) to the values in table III, also using β_{Cu}, γ_{CuCu}, c_{Cu}, and δ_{Cu}. In table IV, all parameters used for constructing the Cu interaction are summarized.

As explained in §2.1.5, the EAM is too soft for unmodified use at short distances and high energies. In this regime, the FM pair potential (see page 9) is used instead of the EAM interaction. In table IV, the distances used for the transition from the Cu electron density are given as well as those for the transition in the Cu-Cu pair-potential. Figure 12 shows the pair potentials and the applied spline between them. In addition, the figure shows the distances $r_{CuCu,1}^{eq}$, $r_{CuCu,sp}^{FM}$ and $r_{CuCu,sp}^{EAM}$ relative to the spline region. Note that $r_{CuCu,sp}^{EAM}$ is rather close to $r_{CuCu,1}^{eq}$. Figure 15 shows the energy of a pair of Cu atoms as a function of the distance.

Table III: Quantities used for constructing the EAM potential for Cu. These quantities are the lattice constant r_{latt} and the first, second and third neighbour distance, $r_\kappa^{eq}, \kappa = 1, 2, 3$, atomic volume Ω, the bulk modulus B, the Voigt average shear-modulus G_v, the cohesive energy E_c, and the unrelaxed mono-vacancy formation energy E_{1V}^{UF}. The two values given are the input value for the fit (left) and on the right the output from the fit. The second part of the table lists some quantities that are useful in the context of our Cu simulations. The elastic constants given here [78] are actually used for calculating the values of G_v and B using the formula's from §3.2.9. The mass of Cu is also given, in amu as well as in kg.

quantity	unit	in	out (fitted)
r_{latt}	Å	3.61496	
$r_1^{eq} = r_{\text{latt}}/\sqrt{2}$	Å	2.55616	
$r_2^{eq} = r_{\text{latt}}$	Å	3.61496	
$r_3^{eq} = r_{\text{latt}}\sqrt{3/2}$	Å	4.42740	
Ω	Å^3	11.8100	
ΩB	eV	10.104	10.173
ΩG_v	eV	4.0278	4.0514
E_c	eV	3.54	3.5444
E_{1V}^{UF}	eV	1.3	1.372
m	amu (kg)	63.546	$(105.51 \cdot 10^{-27})$
c_{11}	GPa	168	
c_{12}	GPa	121.4	
c_{44}	GPa	75.4	
A	-	3.19	
ν_{P}	-	0.419	

Table IV: The EAM potential parameters for Cu. We have used the values chosen by Oh and Johnson [58, Oh Johnson 2] for β, γ, δ and c. The values of ϕ^e, a, b and n are found by fitting equations (10, 12, 61, 64, 65) to the values in table III. The parameters r_{sp}^{FM} and r_{sp}^{EAM} determine the switch from FM to EAM in the pair potential, the parameters r_z and Δr_z determine the electron density fall-off. The table is split in two parts. The first contains the parameters for the element specific EAM functions, F_{Cu} and f_{Cu}. These are used in §3.1.3 as well for the Cu-Mo interaction. The second part of the table contains Cu-Cu pair interaction specific parameters. †: The value of k_{Cu} is discussed in §3.1.3.

specific for	parameter	unit	value
Cu	β	-	6.0
	δ	-	20.0
	k_{Cu}	†	0.45349
	a	eV	-4.09728
	b	eV	-1.70112
	n	-	0.441494
	r_z	Å	2.08
	Δr_z	Å	0.025
	r_1^{eq}	Å	2.55616
	r_c	Å	4.8567
Cu-Cu	γ	-	8.5
	δ	-	20.0
	ϕ^e	eV	0.36951
	r_{sp}^{FM}	Å	1.50
	r_{sp}^{EAM}	Å	2.50
	r_1^{eq}	Å	2.55616
	r_c	Å	4.8567

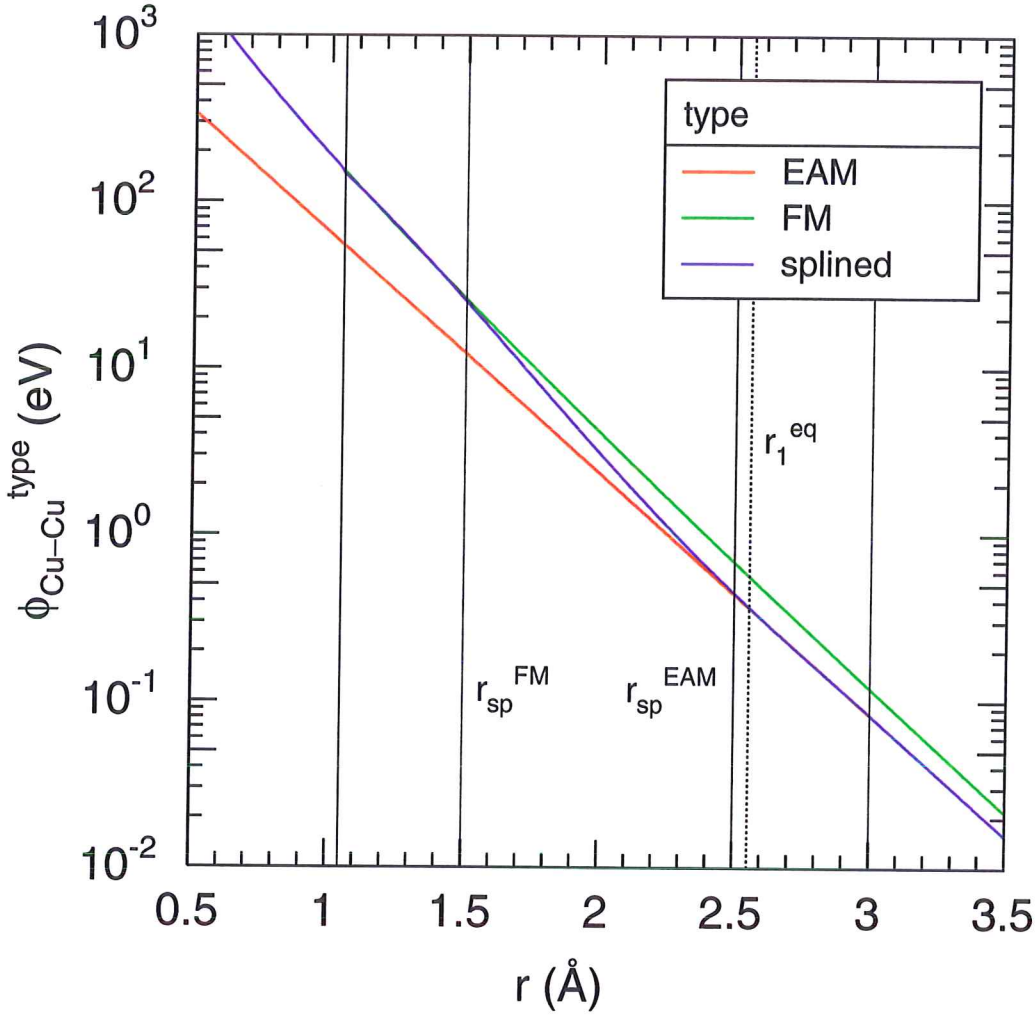

Figure 12: Transition between the Cu-Cu EAM and FM pair potentials constructed by a spline-fit. In the figure, the dotted vertical line is the Cu first neighbour distance, r_1^{eq}. The first and second vertical lines give the interval of the FM pair potential to which the spline is fitted, the third and fourth line give the fit interval of the EAM pair potential. Between r_{sp}^{FM} and r_{sp}^{EAM} the spline is used to represent the Cu-Cu pair potential. The electron density fall-off takes place around $r_z = 2.08$ Å, which lies within this interval.

3.1.2 Mo-Mo

The EAM interaction we use for the Mo-Mo interaction is the Johnson-Oh bcc EAM potential (JO-EAM) [42, Johnson Oh], which proposes, in addition to equations (10, 12), the following equations for: the embedding energy

$$F_I(\rho_i) = -(E_c - E_{1V}^{UF})\left(1 - \ln\left(\frac{\rho_i}{\rho_I^{eq}}\right)^{n_I}\right)\left(\frac{\rho_i}{\rho_I^{eq}}\right)^{n_I}, \tag{69}$$

the electron density function

$$f_I(r_{ij}) = k_I\left(\frac{r_{ij}}{r_{II,1}^{eq}}\right)^{-\beta_I}, \tag{70}$$

and the EAM pair potential

$$\phi_{II}^{EAM}(r_{ij}) = \sum_{\zeta=0}^{3} K_{II,\zeta}\left(\frac{r_{ij}}{r_{II,1}^{eq}} - 1\right)^{\zeta}. \tag{71}$$

In these equations we have the seven constants β_I, k_I, n_I, $K_{II,\zeta}$ (ζ =0–3) and the two quantities E_c, E_{1V}^{UF}. Constants β_I and k_I have the same meaning as for the OJ-EAM interaction (see §3.1.1). We use the values chosen by Johnson and Oh for β_{Mo} and k_{Mo}. The constants n_I, $K_{II,\zeta}$ (ζ =0–3) are calculated from equations relating them to E_c, atomic volume Ω, the ratio of the equilibrium next-nearest and nearest neighbour distance, $r_{II,2}^{eq}/r_{II,1}^{eq}$, the bulk modulus B, the Voigt average shear modulus G_v, the anisotropy ratio A (these three are combinations of the cubic elastic constants c_{11}, c_{12}, and c_{44}) and to E_{1V}^{UF} [42]. The experimental values for Mo are given in table V and the resulting Mo EAM parameters are listed in table VI. For large distances $r_{sc} < r < r_c$ the density function $f_{Mo}(r)$ is substituted by the polynomial $f_{Mo,c}(r)$ with the following properties [42]: $f_{Mo,c}(r_{sc}) = f(r_{sc})$, $f(r_{sc}) = f'_{Mo,c}(r_{sc})$ and $f_{Mo,c}(r_c) = f'_{Mo,c}(r_c) = 0$. It connects smoothly to the original function at r_{sc} and then gradually falls to zero at r_c. The distances r_{sc} and r_c are the ones chosen by Johnson and Oh. The pair potential has been treated in the same manner, using the same values for r_{sc} and r_c. Note that the JO-EAM interaction extends up to next-nearest neighbours.

For the lattice constant, r_{latt}^{MoMo} (and therefore also for Ω), a slightly different, more accurate value is used than the value of 4.150 Å used by Johnson and Oh. Several other notable differences exist between the original JO-EAM potential and the version described by Klaver [47, 49, 48] (which is the one used here), namely:

1. For distances smaller than $r_{MoMo,sp}^{FM} = 1.59$ Å the Fi-Mo potential is used. Between $r_{MoMo,sp}^{FM}$ and $r_{MoMo,sp}^{EAM} = 2.08$ Å, the range where their values are almost the same, the two functions are smoothly connected by a spline. The electron density is multiplied with function $h(r)$, see equation (16) above, with $r_z^{Mo} = 1.8$ Å and $\Delta r_z^{Mo} = 1.025$ Å. Note that this transition causes a small shoulder to appear in the potential of a pair of Mo atoms, figure 15. For distances smaller than $r_{stiff}^{MoMo} = 2.70$ Å the JO-EAM was already stiffened.

Table V: Quantities for constructing the EAM potential for bcc Mo. These quantities are the lattice constant r_{latt} and the first, second and third neighbour distance, r_κ^{eq}, $\kappa = 1, 2, 3$, atomic volume Ω, the bulk modulus B, the Voigt average shear-modulus G_v, the anisotropy ratio A, the cohesive energy E_c, and the unrelaxed mono-vacancy formation energy E_{1V}^{UF} [42]. The two values given are the input value and the value found from tests of the Mo-Mo interaction [47]. The second part of the table lists some quantities that are useful in the context of our simulations, such as the elastic constants and the mass of Mo (in amu as well as in kg).

quantity	unit	in	out
r_{latt}	Å	3.1472	3.1472
$r_1^{eq} = \sqrt{3} r_{\text{latt}}/2$	Å	2.7256	
$r_2^{eq} = r_{\text{latt}}$	Å	3.1472	
$r_3^{eq} = \sqrt{2} r_{\text{latt}}$	Å	4.4508	
Ω	Å^3	15.586	
A	-	0.78	0.78
ΩB	eV	25.68	25.88
ΩG_v	eV	12.28	-
E_c	eV	6.81	6.81
E_{1V}^{UF}	eV	3.10	3.19
m_{Mo}	amu (kg)	95.94	$(159.2 \cdot 10^{-27})$
c_{11}	GPa	450	
c_{12}	GPa	173	
c_{44}	GPa	125	
ν_{P}	-	0.278	

Table VI: The EAM potential parameters for Mo. The value for β is the value chosen by Johnson and Oh [42]. The values of $K_\zeta, \zeta = 0$–3 and n are found from the values in table V above. The quantities E_c and E_{1V}^{UF} are repeated here as they are directly used in equation (69). The parameters r_z and Δr_z determine the electron density function fall-off, the switch from FM to EAM in the pair potential is determined by r_{sp}^{FM}, r_{sp}^{EAM}, and r_{stiff} as well. The cutoff in ϕ_{Mo} and f_{Mo} is governed by distances r_{sc} and r_c, which are determined by ks and by kc. The table is split into two parts. The first part contains the parameters for the element specific EAM functions, F_{Mo} and f_{Mo}. The second part of the table contains the Mo-Mo pair interaction specific parameters. †: The value of k_{Mo} is discussed in §3.1.3.

specific for	parameter	unit	value
Mo	β	-	5.0
	k_{Mo}	†	1.0
	n	-	0.592708
	E_c	eV	6.81
	E_{1V}^{UF}	eV	3.10
	r_z	Å	1.8
	Δr_z	Å	0.025
Mo-Mo	K_0	eV	-0.45159
	K_1	eV	-1.65312
	K_2	eV	11.58783
	K_3	eV	-0.32467
	r_{sp}^{FM}	Å	1.59
	r_{sp}^{EAM}	Å	2.08
	r_{stiff}	Å	2.70
	r_1^{eq}	Å	2.7256
	r_2^{eq}	Å	3.1472
	$ks = (r_{sc} - r_2^{eq})/(r_3^{eq} - r_2^{eq})$	-	0.1
	r_{sc}	Å	3.28
	$kc = (r_c - r_2^{eq})/(r_3^{eq} - r_2^{eq})$	-	0.5
	r_c	Å	3.80
	r_3^{eq}	Å	4.4508

2. To avoid discretisation errors due to the very steep slope of the embedding function near $\rho = 0$ (the curvature tends to $-\infty$), F_{Mo} is multiplied with the function

$$G(\rho) = 1 - e^{-\frac{1}{2}\left(\frac{\rho}{\rho_G}\right)^2}, \tag{72}$$

where $\rho_G = 0.5$. This slightly modifies F_{Mo} for small values of the electron density, where the impact (on the embedding energy) of doing so is negligible.

3.1.3 Cu-Mo

The Cu-Mo interaction is special in the sense that it involves two different elements, instead of being a single-element interaction. The previously described EAM potentials for the Cu-Cu (§3.1.1) and the Mo-Mo interactions (§3.1.2) are based on the well known stable crystal structures of Cu (fcc) and Mo (bcc). For the Cu-Mo interaction, with two non mixing elements that have different equilibrium structures, not much data is available that can be used to construct an interaction for the thermal energy range. No such problems exist for the high energy (short distance) Cu-Mo interaction as we again used the FM pair potential which is valid for this interaction as much as it is for any of the other metal-metal interactions we used.

Pair potential part For the (thermal energies) EAM pair potential part of the Cu-Mo interaction we have not used the "mixing method" described by Johnson ([41] or [40]) for constructing a mixed interaction potential from those for the single-elements, as we were at the time not aware of the publication. There are however more important reasons for not using this method. Johnson's model is made strictly for fcc-fcc binary alloys, so that both use the same set of EAM functions. The article only describes the method for a first neighbour distance model, neglecting higher neighbour shells. These limitations enable an analytically solvable inversion from $\rho(r)$ to $r(\rho)$. Johnson sees his simple functions as an example, useful for explaining the method, which can be expanded for use in more realistic simulations. The model is a simplified EAM method, and while it could certainly be used as a starting point for more physically valid/correct EAM potentials, expanding the model would have cost to much effort to be done in the context of the current study. The limitation to first neighbours is not sufficient if a discrimination between the fcc and hcp structure is required, as at least third neighbours have to be taken into account for this. The limitation to only fcc materials is clearly not sufficient for the Cu-Mo system.

Instead of Johnson's method the equations for the Cu OJ-EAM interaction pair potential, equations (63, 65, 67, 68), are used to form a Cu-Mo EAM pair potential including the values of γ_{CuCu}, δ_{Cu} and c_{CuCu}, see the second part of table III. The reason for using the Cu-Cu EAM functions instead of the Mo-Mo functions (or any other form) is that, in this study, the main topic is the behaviour of Cu even in cases where it is in contact with a Mo substrate.

Table VII: The EAM pair potential parameters for Cu-Mo. We used the values chosen by Oh and Johnson [58, Oh Johnson 2] for use with the Cu JO-EAM interaction for γ, δ and c. The value of ϕ^e_{CuMo} is found using the procedure described in the text. The table also lists the first neighbour distance and the pair potential cutoff distance for Cu-Mo, as well as the distances that determine the switch from FM to EAM in the pair potential, r^{FM}_{sp} and r^{EAM}_{sp}. The embedding part is that for Cu and for Mo (parameters are in tables IV and VI).

specific for	parameter	unit	value
Cu-Mo	γ	-	8.5
	δ	-	20.0
	ϕ^e	eV	5.0
	r^{FM}_{sp}	Å	1.342
	r^{EAM}_{sp}	Å	2.4745
	$c = r_c/r^1_{eq}$	-	1.9
	r^{eq}_1	Å	2.6409
	r_c	Å	5.018

We want to preserve the sensitivity of Cu to third neighbours also when these include Mo atoms.

We are not aware of any literature value for the Cu-Mo neighbour distance $r^{eq}_{CuMo,1}$ in a crystal. Therefore, we used the average of the Cu and Mo equilibrium neighbour distances instead,

$$r^{eq}_{CuMo,1} = \frac{r^{eq}_{CuCu,1} + r^{eq}_{MoMo,1}}{2} = 2.6409 \text{ Å}, \tag{73}$$

with the other distances $(r^{eq}_2, r^{eq}_3, r_c)$ scaling accordingly. Note that this leads to a cutoff that is larger than for the Cu-Cu and Mo-Mo interactions.

The Φ^{EAM} "amplitude" factor ϕ^e_{CuMo}, see equation (63), is used to fit the EAM pair potential part to the Cu-Mo FM pair potential. Since not much is actually known about the EAM Cu-Mo interaction while the FM pair potential is just as valid here as it is for the other two metal-metal interactions, it is convenient to have the EAM Cu-Mo pair potential use the FM potential as a "template" for obtaining the correct values for $r^{FM}_{CuMo,sp}$ and $r^{EAM}_{CuMo,sp}$. In the r-range between those values, ϕ^{FM}_{CuMo} and ϕ^{EAM}_{CuMo} are replaced by a spline that is fitted to the two functions in the areas next to $r^{FM}_{CuMo,sp}$ and $r^{EAM}_{CuMo,sp}$ (see §2.1.5), exactly the same way as done for the FM-EAM transition of the Cu-Cu and Mo-Mo interaction pair potentials. Figure 13 shows the EAM pair potential curves ϕ^{EAM}_{CuMo} at five test-values of ϕ^e_{CuMo} as well as the FM pair potential, ϕ^{FM}_{CuMo}. The figure shows that the value $\phi^e_{CuMo} = 0.436$ eV gives a good match between the two pair potentials for the r-range between $r^{FM}_{CuMo,sp}$ and $r^{EAM}_{CuMo,sp}$. Also in the figure, the dotted vertical line is drawn at $r^{eq}_{CuMo,1}$, and two solid vertical lines are drawn at $r^{FM}_{CuMo,sp}$ and $r^{EAM}_{CuMo,sp}$. The values of the parameters used for the construction of the Cu-Mo pair potential are summarized in table VII.

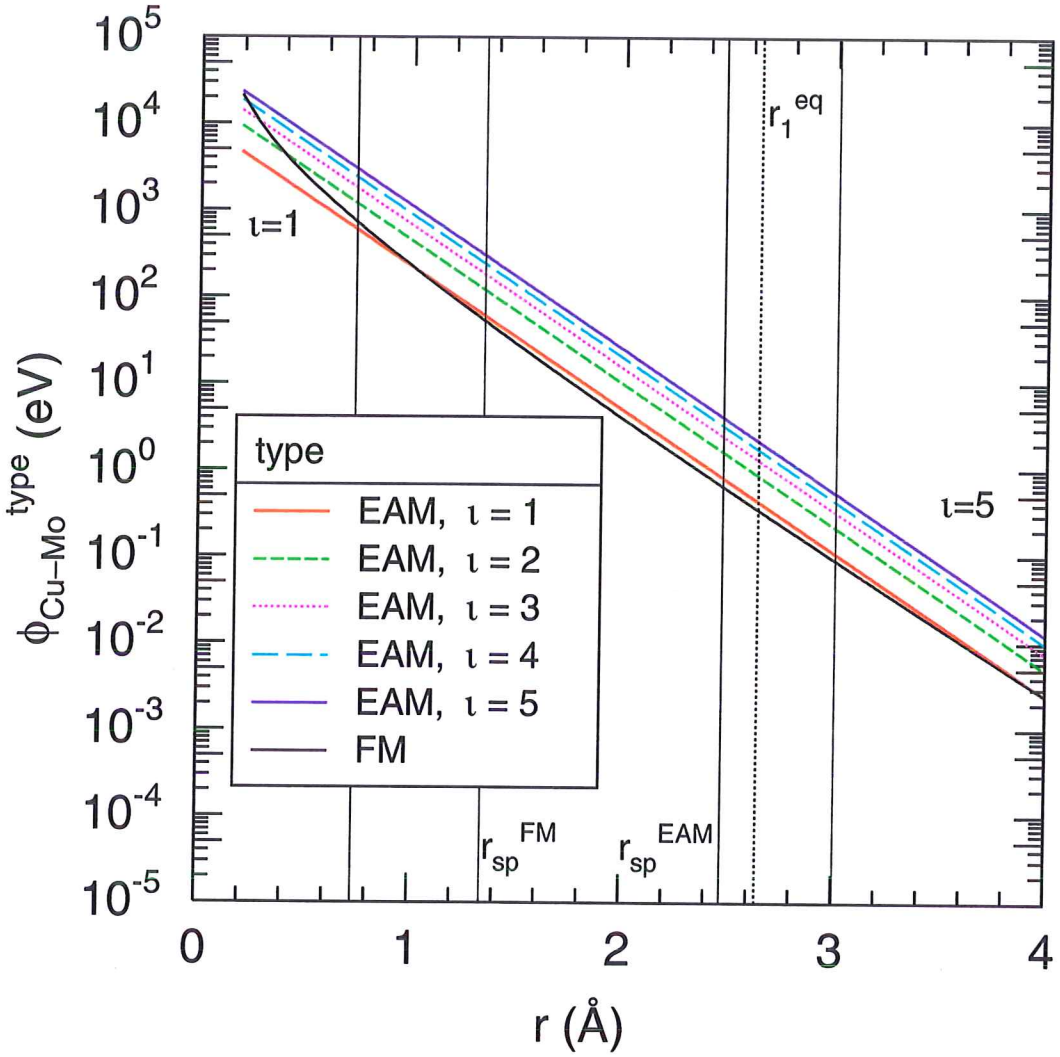

Figure 13: Fitting of the Cu-Mo interaction EAM and FM pair potentials. The EAM pair potential function ϕ_{CuMo}^{EAM} is fitted to the FM pair potential function ϕ_{CuMo}^{FM} by varying ϕ_{CuMo}^{e} by $\iota * 0.436$ eV, $\iota = 1$–5 (0.436–2.18 eV). The curves for ϕ_{CuMo}^{EAM} at those five values of ϕ^e are given in the figure, as well as the curve for ϕ_{CuMo}^{FM}. In the figure, the dotted vertical line is the Cu-Mo first neighbour distance, $r_{CuMo,1}^{eq}$. The first and second vertical lines give the interval of the FM pair potential to which the spline is fitted, the third and fourth line give the fit interval of the EAM pair potential. The transition from ϕ_{CuMo}^{FM} to ϕ_{CuMo}^{EAM} takes place in the r-range between the second and third line, $r_{CuMo,sp}^{FM}$ and $r_{CuMo,sp}^{EAM}$. In this interval the pair potential is represented by a spline. $r_{MoMo,sp}^{FM} = 1.59$ Å, $r_{MoMo,sp}^{EAM} = 2.08$ Å. For reference: the fall-off in the Cu and Mo electron densities takes place around $r_z^{Cu} = 2.08$ Å and $r_z^{Mo} = 1.8$ Å respectively.

Embedding part The embedding energy functions used are those for Cu, equation (61), and for Mo, equation (69), with the electron density following from equation (12) together with the element specific electron density functions f_{Cu}, equations (62, 64) and f_{Mo}, equation (70).

The most important property to fit is the cohesion energy of a (hypothetical) CuMo crystal. The only free parameter we have at our disposition is the electron density scaling ratio k_{Cu}/k_{Mo}. We have determined a value of k_{Cu}/k_{Mo} to obtain a value of +0.27 eV for the heat of formation of a bcc (or more accurately, a CsCl-structured) crystal of $Cu_{50}Mo_{50}$, as formed from an equal amount of atoms of (bulk) *bcc* Cu and (bulk) bcc Mo [8, Baskes MEAM]. This leads to a value of 0.435 for the ratio k_{Cu}/k_{Mo}. For historical reasons, ie. the Mo electron density was used in earlier published work [49, 48, 47] and [29], we kept the value k_{Mo} at 1.0 and used a value of 0.435 for the Cu scaling factor k_{Cu}.

3.1.4 Noble-gas and metal — noble-gas interactions

Only the purely repulsive Fi-Mo Screened Coulomb pair potentials (FM) are used for the interactions of Ar and He with each other and with Cu and Mo, see figure 14, and figure 16, which shows the potential energy for the noble-gas interactions. This use of only FM is motivated by the very low attractive energy (van der Waals type) of the interactions involving noble-gas atoms.

Recently, de Hoog has found indications that for her simulations of Thermal Desorption Spectroscopy (TDS) the FM Cu-He interaction might be incorrect [19, 15, de Hoog Mast.thesis]. In these simulations, de Hoog has implanted 75 eV and 1000 eV He^+ ions in some of the layers described in the current work ($EVAP_s$, see table XIV on page 74). She found that the He atoms produce an unexpectedly high number of vacancies in Cu. Neither de Hoog [19] nor Klaver [47, Klaver Mast.thesis] have observed any He-filled defects in which the number of He atoms was higher than the number of empty Cu sites representing the volume of the defect. Also, de Hoog has only found one He atom in an interstitial position in the Cu lattice. Looking at figure 14, we see that the He-He interaction shows a repulsion that is comparable to the Cu-He interaction for distances between $\sim$ 2.6 Å and $\sim$ 2.8 Å, above which it is more repulsive. This is the same range as the Cu-Cu (and Mo-Mo) equilibrium neighbour distance (Cu-Cu: 2.56 Å; Mo-Mo: 2.73 Å).

On the basis of these results and in view of a recent comparison between several He-He interaction potentials by van der Werf [80], which shows that our He-He pair potential has a larger positive value (more repulsive) than the other He-He interactions in the range of 1–3 Å, de Hoog recommends that *ab initio* calculations should be performed to cross-check the validity of the currently used He-He, He-Cu and He-Mo pair potentials.

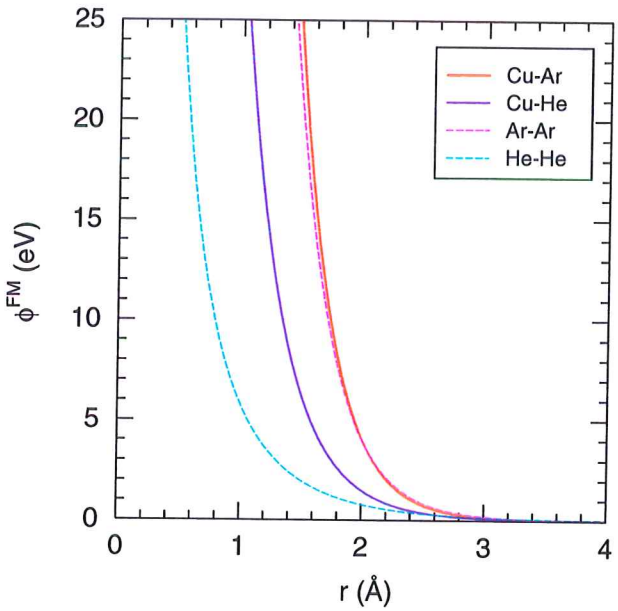

Figure 14: Potential energy (in eV) as a function of distance (in Å), for combinations of Cu, Ar and He. The figure is the same as figure 2 in [19]. The figure shows that the He-He interaction is more repulsive than the Ar-Ar and Cu-Ar interactions for distances larger than $\sim$ 3.2 Å. It is comparable to the Cu-He interaction for distances between $\sim$ 2.6 Å and $\sim$ 2.8 Å, above which it is more repulsive. For reference: the Cu-Cu equilibrium neighbour distance is 2.56 Å (Mo-Mo: 2.73 Å).

3.1.5 Graphs

To be able to understand how the interactions behave, we find it useful to show the potential energy curves in graphical form. To this end, figures 15 and 16 show the potential energy of *pairs* of atoms of all types as a function of the distance between the atoms. Figure 15 shows the potential energy of combinations of pairs of the metal atoms we use, Cu and Mo, using the EAM interactions described above. Note that, since the EAM interaction is not expressible as a sum over pairs, the interaction of a metal atom with *more than one* metallic interaction partner has a different form than that shown in figure 15. Therefore figure 15 does not represent the situation in the solid state. We can see that the Mo-Mo interaction has a small shoulder at the transition from FM to EAM. This same shoulder is also found in the Cu-Mo interaction, which may be originate from the Mo electron density. From both the Mo-Mo and the Cu-Mo interactions we see that for decreasing r values, the potential energy first rises relatively abruptly near r_z^{Mo}, and then "waits" for the completion of the transition in the pair potential. Figure 13 shows that the spline representing ϕ_{CuMo} lies above ϕ_{CuMo}^{FM}. It seems that a transition at smaller r, would have been better with the Cu-Mo pair potential. This would however have required modifing the transition in the Cu and Mo electron densities as well, which is undesirable as it alters the Cu-Cu and Mo-Mo interactions. The current findings may indicate that using a wider transition region in the Mo-Mo interaction would have been better than the current choice.

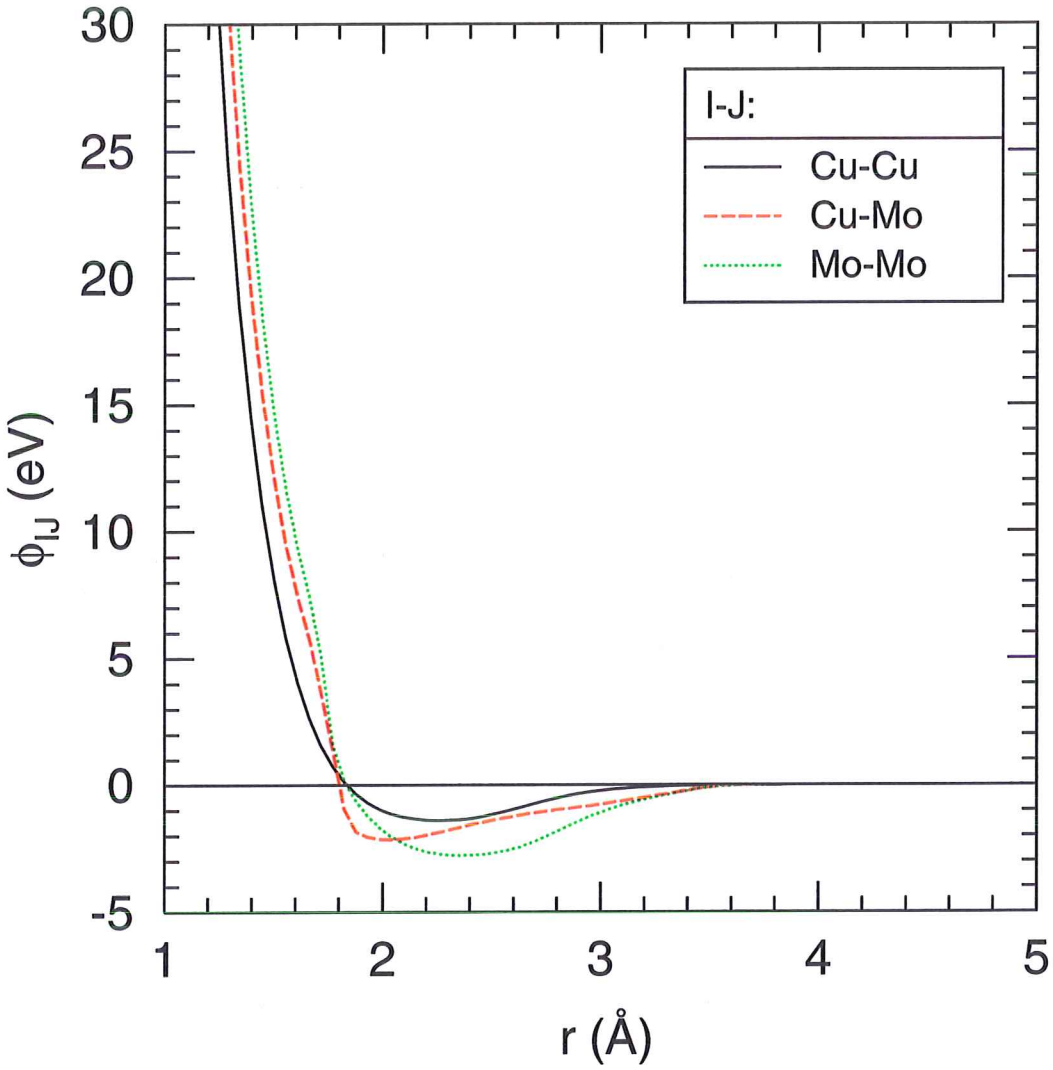

Figure 15: Potential energy of Cu-Cu (black solid curve) Cu-Mo (red broken curve) and Mo-Mo dimers (green dotted curve) as a function of the distance between the two atoms. Note that higher coordinated atoms do not follow these plots (see text). For reference: The Cu-Cu equilibrium distance is 2.56 Å, Mo-Mo: 2.73 Å; The transition in ϕ_{CuCu} takes place between $r^{FM}_{CuCu,sp} = 1.50$ Å and $r^{EAM}_{CuCu,sp} = 2.50$ Å (table IV), for Mo-Mo (table VI) between: $r^{FM}_{MoMo,sp} = 1.59$ Å and $r^{EAM}_{MoMo,sp} = 2.08$ Å, and for Cu-Mo (table VII) between: $r^{FM}_{MoMo,sp} = 1.34$ Å and $r^{EAM}_{MoMo,sp} = 2.47$ Å; The fall-off in the Cu and Mo electron densities takes place around $r^{Cu}_z = 2.08$ Å and $r^{Mo}_z = 1.8$ Å respectively, see the first part of tables IV and VI.

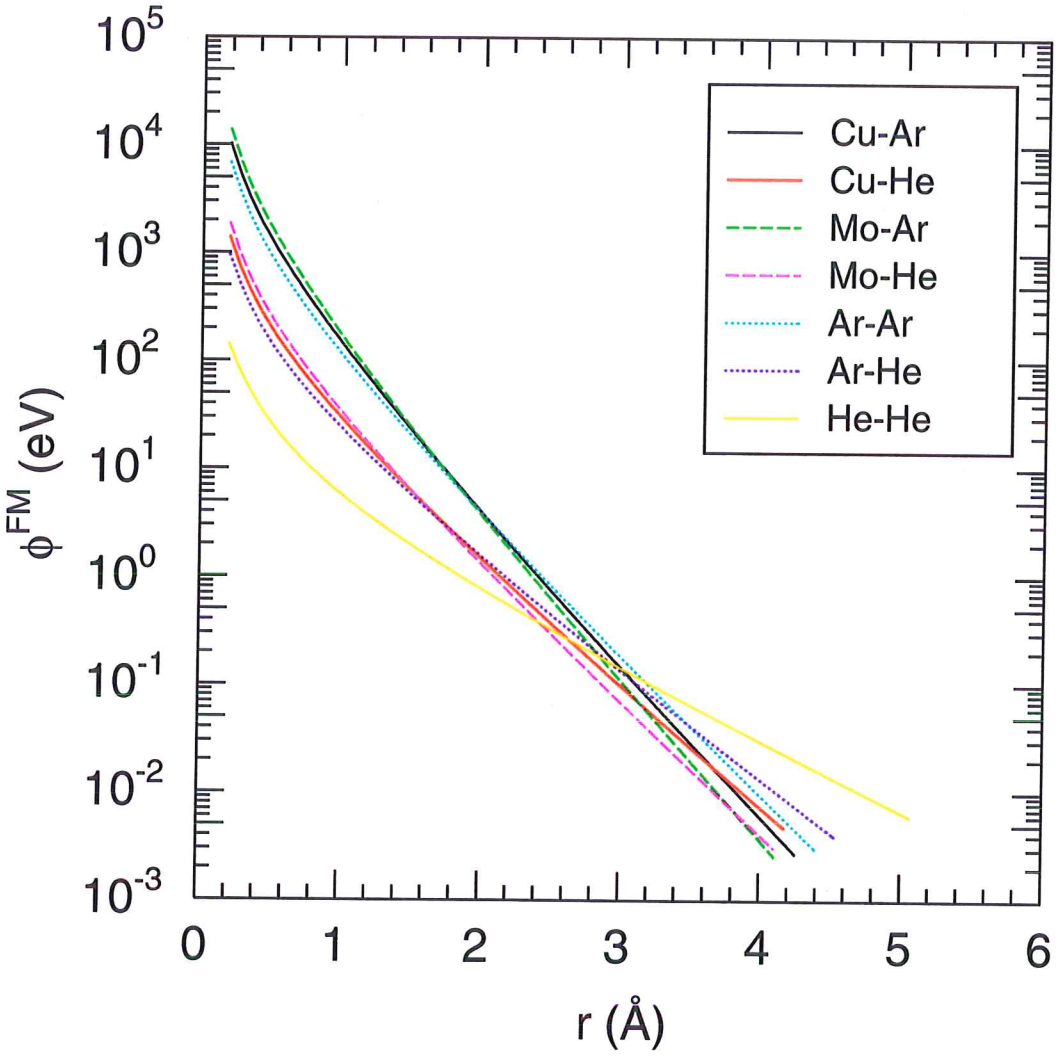

Figure 16: Potential energy for all metal — noble-gas and noble-gas — noble-gas interaction pairs as a function of the distance between the two atoms. For reference: the Cu-Cu equilibrium distance is 2.56 Å (Mo-Mo: 2.73 Å).

3.2 Analysis tools

To analyze our results, we use several techniques and principles. In this secion a survey of these techniques as well as an explanation of the conventions and assumptions we use will be given.

3.2.1 Special words and phrases

height and z-planes We often use the term plane, or height, denoting a division in k slices over the z-direction of the films. Atoms are considered to be within one plane if their z-coordinates are closer together than a distance z_{test}. From earlier simulations with Mo [47, 49, 48] and the first results with Cu on Cu (§4.2) we found that a value $z_{test} = 1.1$ Å gives good results. In more complicated systems (see [29, 15, 19], §4.3) and when looking along high index crystal directions, the planes have a ragged appearence, with atoms rows "missing" from one and appearing in another plane. Recently we modified the process to make it possible to look at planes rotated over polar angle θ and azimuthal angle ψ from the z-axis. We denote the planes by the index k For the top substrate plane we use $k = 0$, the next-to-highest is $k = -1$, etc..

Rapid quenching to 0 K Deposition at high temperatures introduces a random displacement of atoms around their positions, which makes the configurations harder to visualize for analysis. Therefore, in most cases we rapidly quench the configurations to low temperature ($< 50\ K$) (using static relaxation, page 20). When doing this, one has to realize that the density of the film is affected, and that strains and stresses are introduced as we use two materials with very different coefficients of linear thermal expansion.

Conventions when using hard-ball figures Unless excplicitly mentioned, the horizontal direction of the hard-ball figures is parallel to fcc[211] for Cu/Cu, and to bcc[110] in Cu/Mo simulations, with the vertical parallel to fcc[110] and bcc[001] repectively. This agrees with the orientation seen in figure 4 (page 27). Most of the colouring schemes use (a repetition of) seven colours, going from blue to green, yellow, red and magenta. In most of these figures, the Mo (and Ar) atoms are black. All hard-ball figures are for cooled configurations, unless explicitly mentioned otherwise.

3.2.2 Potential Energy

A plot of the potential energy per atom as a function of height provides an impression of the ranges over which the Cu-Mo interface and the surface have an influence, and also provides information on the relative interface energies of films deposited using EVAP and IBAD.

3.2.3 Counting-neighbours

Number of neighbours The number of neighbours n that an atom has within a predefined distance is a powerful help in identifying if the atom is a

regular bulk atom, a free atom, an atom near a vacancy, or an atom located near an interstitial, etc. For the Mo atoms, we use a distance that lies between the nearest and next-nearest neighbour distances in the equilibrium crystal (at r_c^{MoMo}, see §3.1.2). For Cu, we use a distance between the nearest and next-nearest neighbours as well. In table VIII the values for r_n are given. The third column of the table gives the number of neighbours when the atom is in its own perfect crystal lattice. For Ar and He this value is not very relevant.

Table VIII: Values for the radius r_n of the sphere surrounding an atom, in which atoms are counted as neighbours. The most important types of pairs in this study are denoted in bold font. The third column shows the number of neighbours for an element in its equilibrium lattice structure, n_{eq}. For our own reference, the third column lists the system type that should be used with our program "party" for counting the neighbours of a specific type of pairs. This program is used in a large number of the analysis methods described in this section.

type pair	r_n (Å)	n_{eq}	party "sys-type"
Ni-Ni	3.0	12	10
Cu-Cu	3.09	12	21
Cu-Mo	3.44	-	21
Mo-Mo	3.8	14	11–13, 21
Mo-Ar	3.8	14	11
Cu-Ar	2.79	12	22
Cu-He	3.15	-	23
Mo-He	3.15	-	23
Si-Si	3.094	4	41
Si-Ar	3.45	-	41
Ar-Ar	3.8	12	11, 41
He-He	2.5	-	22, 23

Surface atoms For each specific crystallographic surface, we can find the number of neighbours n_{surf} that an atom lying *in* a surface plane would have, and also the number of neighbours n_{adatom} that an atom has wich lies *on* a surface plane. For an fcc (111) surface, an atom *in* the surface (plane) has $n_{surf} = 9$ neighbours, while an atom *on* the surface has $n_{adatom} = 3$ neighbours. For a bcc (110) surface these numbers are $n_{surf} = 10$ and $n_{adatom} = 4$.

3.2.4 Deposited thickness and deposition rate

All depositions are performed with a fixed atom arrival rate α_{in} into the simulation box. However, because of (self-)sputtering of atoms, the deposition rate may be lower than calculated directly from the arrival rate. Also, the actual thickness is not necessarily equivalent with the thickness as calculated from the number of planes, as the number of atoms that makes up a layer may vary slightly. This happens, for instance, at the onset of growth of the currently deposited Cu films. In addition, the planes are found to still become denser when the film surface has already progressed further by several tens of planes.

Coverage Θ, nominal thickness D and deposition rate α_D In most cases, we have used the number of atoms in a substrate plane, M_0, and a (standard) plane separation d_k to obtain the coverage Θ and the nominal thickness D of the film from the number of atoms N_{film} ($= N_{bound} - N_{substrate}$) in the film:

$$D = d_k\Theta = d_k\frac{N_{film}}{M_0} \equiv \frac{N_{film}}{\sigma_D}, \tag{74}$$

with $1/\sigma_D$ the number of film atoms per Å deposited, which is dependent on the box size. From the increase of number of atoms with deposition time

$$\frac{\mathrm{d}N_{film}}{\mathrm{d}t} = \alpha_{t,in} - \alpha_{t,out} = \alpha_t^{eff}, \tag{75}$$

with $\alpha_{t,in}$ and $\alpha_{t,out}$ the number of atoms sent towards and removed from the film (e.g. by sputtering) per time unit, and α_t^{eff} the effective deposition rate we can find the evolution of the thickness with deposition time

$$\alpha_D^{eff} = d_k\alpha_\Theta^{eff} = \frac{\mathrm{d}D}{\mathrm{d}t} \overset{\text{eqn. 74}}{=} \frac{\mathrm{d}N_{film}}{\mathrm{d}t}\frac{1}{\sigma_D} = \frac{\alpha_t^{eff}}{\sigma_D}. \tag{76}$$

Choice of M_0 and d_k As mentioned, M_0 is dependent on the box size. It is also dependent on the crystal structure and orientation (either of the substrate, or the one expected for the deposited film). For the Cu/Mo systems M_0 is the number of atoms in a bcc (110) Mo plane, with d_k equal to $d_{Mo\ bcc}(110) = 2.2254$ Å as plane separation distance (or "plane thickness"). For the Cu on Cu simulations we use the number of atoms in a Cu fcc (111) plane for M_0 and a plane separation distance $d_k = d_{Cu\ fcc}(111) \simeq 2.087$ Å.

3.2.5 Roughness of the film

RMS roughness R In earlier work on Mo [62, 49, 48, 29], the RMS surface roughness of the deposited film was used to compare the effects of different deposition parameters. We can use the information gathered from these studies to know more about the Cu film growth. The relatively simple roughness parameter R is defined as the root mean square (RMS) variation of the z-coordinates of the surface atoms. Which of the atoms are surface atoms is determined from their number of neighbours n (see §3.2.3). Because of this way of determining the surface atoms, the "surface" is not limited to the macroscopic surface only; without a further selection, atoms within internal low-density regions will also be selected, leading to a very high roughness, which will only become higher as the deposition continues. This can be understood as the minimum z-coordinate does not increase, while the maximum increases with thickness.

We have made an additional selection in determining the roughness of the Cu/Mo films, mainly to avoid the interface being seen as a surface, but also other internal features of the film. We found that z-planes that contain surface atoms are the only ones that contain more than 15-30 atoms with 9 neighbours (2–4 in the small systems), the exact number differing between the simulations.

This selection causes a saw-tooth-like distortion of the R-curves, see 48, as succesive planes fall out of this limit as the deposition continues, so that atoms within them stop contributing to the roughness. For the earlier Mo simulations, this issuse was not encountered, as the difference in number of neighbours seen for surface atoms and for atoms close to observed point defects is larger in Mo. Also, these simulations mainly contained point-defects.

Usually we look at the evolution of R with time or thickness. When the layer grows in a purely plane-by-plane mode (see §2.5.2), the $R(D)$ plot will be a repetition of parabolic curves with a maximum height equal to half the plane separation distance d_k.

Height-map like views For visualization, we frequently display the atoms coloured by their z-plane number k (mostly viewed from above) so that the surface profile can be seen, as can other thickness- or height-profiles. In most of these cases, it is convenient to show the Mo atoms in **black**, to either see the substrate surface (interface) better, or be able to better observe the interdiffusion between Cu and the Mo substrate. With films that have low roughness one would typically expect to see only a few colours, while very rough films would display many colours. Growth according to the solid-on-solid model would typically show a range of colours with the span (ie. the number of colours visible) remaining constant during the deposition, so that a constantly changing colour-pallete would be seen.

3.2.6 Plane-filling

When analysing the filling of planes, we make comparisons with the simplest solid-on-solid model, in which the filling of a plane is determined solely by the probability that an atom arrives on the plane beneath it. In other words, the probability that an atom ends up in in plane k, $P(k)$, follows directly from the number of empty sites on top of the previous plane $k-1$, not taking into account the diffusion from or to other planes. This number of sites depends on the difference between the $N(k-1)$ occupied sites in plane $k-1$, and the $N(k)$ sites taken away because of the filling up of plane k. Using $M(k)$ to denote the maximum number of atoms in plane k one obtains

$$P(k) = \left(\frac{N(k-1)}{M(k-1)} - \frac{N(k)}{M(k)} \right). \tag{77}$$

Multiplication by α_t^{eff} (or by σ_D) leads to the filling-up rate

$$\frac{\mathrm{d}N(k)}{\mathrm{d}t} = \alpha_t^{eff} \left(\frac{N(k-1)}{M(k-1)} - \frac{N(k)}{M(k)} \right), \tag{78}$$

or, alternatively

$$\frac{\mathrm{d}N(k)}{\mathrm{d}D} = \sigma_D \left(\frac{N(k-1)}{M(k-1)} - \frac{N(k)}{M(k)} \right), \tag{79}$$

where $N(k)$ (or N_k) is the number of atoms in plane k and α_t^{eff}, σ_D and D are defined in §3.2.4. Via a Laplace transform it is possible to obtain the solution for

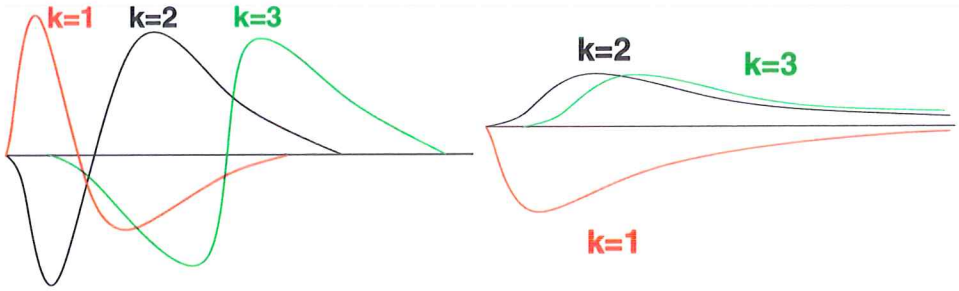

Figure 17: Sketches of the β_k shapes for the Frank—van der Merwe growth mode (left) and the Volmer—Weber growth mode (right). The first plane has a much different shape.

$N(k)$ as a function of thickness. However, here we simply look at the difference β_k between the plane-filling as observed and the plane-filling as calculated if the solid-on-solid model would be valid at that particular moment

$$\beta_k(D) = \frac{\mathrm{d}N(k)}{\mathrm{d}D} - \sigma_D \left(\frac{N(k-1)}{M(k-1)} - \frac{N(k)}{M(k)} \right), \tag{80}$$

which equation yields the value zero when the solid-on-solid model applies. This tests whether the probability $P(k)$ really is the only factor determining the plane-filling, or that other factors, like diffusion between planes, are also of influence. If the s-o-s model applies, we would expect a $\sqrt{(D)}$ (or $\sqrt{\Theta\, d_{\mathrm{plane}}/M_{\mathrm{substrate}}}$) R-dependency.

For the Frank—van der Merwe growth mode (plane-by-plane growth), see §2.5.2, β_k would have a sawtooth shape, as sketched in figure 17 (left). At first, the growth of plane k (except for the first plane) lags behind (ie. $\beta_k < 0$) the solid-on-solid model because plane $k-1$ is first completed. Once plane $k-1$ is completed, β_k becomes larger than zero, as plane k will grow much faster than in the solid-on-solid model, because all atoms arriving in the system contribute to plane k, and not to other planes, as they would in the solid-on-solid model.

The Volmer—Weber growth mode (island- or 3D-growth) will look more like the solid-on-solid model than plane-by-plane growth. We would expect β_k to start out with a positive value for low k planes (figure 17 (right)), as planes are resistant to wetting the underlying substrate, then slowly diminish while the while the islands develop, and continue with a value for β_k that is positive for the lower k planes and probably somewhat negative for the higher k ones, when three-dimensional crystals have formed and begin to grow more in the lateral directions.

The Stranski—Krastanov growth mode would have a β_k equal to that for Frank—van der Merwe growth when k is small, but for higher values of k a switch to the more solid-on-solid model-like behaviour of Volmer—Weber growth would be seen in β ($\beta \sim 0$). Figures (50–54)(b) show something like the sketched behaviour for the Frank—van der Merwe growth mode, and a bit of Volmer—Weber growth as well.

3.2.7 Atom history listing

For each atom we keep track of its first point of condensation and its final position in the system. This can be used to obtain information about the prevailing diffusion and recoil displacements during the deposition. For instance, the value $\Delta z = z_{initial} - z_{final}$, the difference between the height at first occurrence of an atom in the film, and its final heightgives information about the movement of atoms between planes. If an atom has a negative Δz then the atom arrives at a lower z (plane) than where it ends up, so it moves upward in the film. If Δz is positive, the atom moves down after arrival in the film. Plotting z_{final} versus Δz for a crystal shows a dotted pattern of atoms moving from one plane (containing a small range of z-values) to another, giving more or less discrete movement steps, see for instance [62] (which uses $z_{initial}$ versus $\Delta z = z_{final} - z_{initial}$). In such figures, downwards sloping diagonal lines connect atoms originating from a specific plane. Figures 50–54(c) of the current work show such dotted patterns for Cu on Mo deposition simulations.

It is also possible to calculate the mean square drift of atoms in the first (and, in principle, every other) plane, getting a measure of the effective diffusion that has taken place, and compare this to the available diffusion data to get an effective diffusion time. This is not done yet, but is planned as part of further research conducted on the current systems.

3.2.8 Spherical Harmonics Functions — symmetry and rotation

Steinhardt, Nelson and Ronchetti [67] (SNR) have developed a use of Spherical Harmonics functions to describe the symmetry of the coordination polyhedron of an atom from the vectors "connecting" the atom to its n neighbours. SNR use a function $f(\theta, \psi)$ defined on a unit sphere. The function $f(\theta, \psi)$ is zero, except in the n points $P(\theta_i, \psi_i)$ where "bond"-vectors between the central atom and atoms i penetrate the sphere. In these points the function is a δ-function of the angles θ and ψ:

$$f(\theta, \psi) = \sum_{i}^{n} \delta(\theta - \theta_i, \psi - \psi_i). \tag{81}$$

The function $f(\theta, \psi)$ can be expanded into a series of spherical harmonics functions $Y_{lm}^{*}(\theta, \psi)$ (see SNR [67]) much like a Fourier series of a function periodic in a two-dimensional plane. We write

$$f(\theta, \psi) = \sum_{l=0}^{\infty} \sum_{m=-l}^{l} Q_{lm} Y_{lm}^{*}(\theta_i, \psi_i), \tag{82}$$

from which the coefficients Q_{lm} can be obtained according to

$$\begin{aligned} Q_{l,m} &= \int_{\theta} \int_{\psi} Y_{lm}(\theta, \psi) \sum_{i=1}^{n} \delta(\theta - \theta_i, \psi - \psi_i) \sin\theta \, \mathrm{d}\theta \, \mathrm{d}\psi \\ &= \sum_{i=1}^{n} Y_{lm}(\theta_i, \psi_i), \end{aligned} \tag{83}$$

Every neighbour i of the central atom contributes $Y_{lm}(\theta_i, \psi_i)$ to coefficient Q_{lm}. SNR introduce the mean coefficient $\bar{Q}_{lm}$ (with $l = 0, 1, 2, \ldots, \infty$ and $m = -l, \ldots, l$, see above) which is equal to equation (83) except for a factor n:

$$\bar{Q}_{lm} = \frac{1}{n} \sum_{i=1}^{n} Y_{lm}(\theta_i, \psi_i) . \tag{84}$$

These numbers $\bar{Q}_{lm}$ give information about the *local* symmetry and the orientation of the surrounding "neighbour lattice" relative to the Cartesian axes.

Local crystal geometry—rotational invariant coefficients If we want to obtain information regarding the crystal structure in the system, we are only interested in the crystal symmetry around the individual atoms and not in the orientation of this "crystal" with respect to the Caresian axes. We therefore use, instead of $\bar{Q}_{lm}$, the rotationally-invariant set of numbers Q_l ($l = 0, 1, 2, \ldots, \infty$):

$$Q_l = \left(\frac{4\pi}{2l+1} \sum_{m=-l}^{l} \bar{Q}_{lm}^{*} \bar{Q}_{lm} \right)^{\frac{1}{2}} . \tag{85}$$

The numbers Q_l are the rotational-invariants formed from the expansion coefficients of the set of bonding-directions of an atom in spherical harmonics functions. We call them the "Spherical Harmonics" of an atom for short. As Q_0 and Q_l ($l = 1, 3, 5, \ldots, \infty$) are zero, these coefficients are not used in evaluating the local crystal symmetry.

For computational ease we only use Spherical Harmonics with $l \leq 12$ (6 numbers, see above). We look as far as r_n (§3.2.3, table VIII) of the atom-pairs involved, also to reduce computational and memory requirement, and, more fundamentally, because we really want to look at the *local* crystal symmetry S surrounding atom A. For all crystal structures, a specific set of Spherical Harmonics exists. Currently we have only determined the Spherical Harmonics for the bcc, fcc, hcp, diamond, and the icosahedral structure (which regularly occurs in liquids and in amorphous materials, ie. glasses). Table IX gives the first six spherical harmonics ($l = 2, 4, 6, 8, 10, 12$) for these five implemented symmetries.

We determine the RMS difference between the Q_l^i-values of an atom i in the system and the characteristic values Q_l^S of a crystal symmetry S listed in table IX, yielding for each atom the number a_S^i that expresses how closely its coordination polyhedron resembles S,

$$a_S^i = \sqrt{\frac{1}{K} \sum_{k=1}^{K} \left(Q_{2k}^i - Q_{2k}^S \right)} \ , K = 6. \tag{86}$$

Next, for each atom, the symmetry type S that gives the smallest a_S^i value is determined. When, in addition, this value is smaller than a certain preset value a_S^c, the atom is considered to "have the symmetry S". When the smallest a_S^i is larger than a_S^c, the atomic symmetry is considered "undefined". We call this the

Table IX: Values of $Q_l, l = 2, 4\text{–}12$ for the bcc, fcc, hcp, icosahedral and diamond symmetries. The names of the last two are used in a shortened form, "ico" and "dia", in the remainder of this work. Below the structure indication, the number of neighbours used (in the perfect bulk structure) for determining these Q_l^S-values (S: symmetry) is shown in parentheses. For the meaning of a_S^c, see equation (86). On the bottom line, the colour used for visualizing an atom with that local crystal symmetry is given.

l	bcc (14)	fcc (12)	hcp (12)	ico(sahedron) (12)	dia(mond) (4)
2	0.0	0.0	0.0	0.0	0.0
4	0.03637	0.1909	0.09722	0.0	0.5092
6	0.5107	0.5745	0.4848	0.6623	0.6285
8	0.4293	0.4039	0.3170	0.0	0.2128
10	0.1952	0.01286	0.01017	0.3630	0.6502
12	0.4048	0.6001	0.5650	0.5854	0.4153
a_S^c	0.11	0.11	0.11	0.11	0.11
colour	blue	green	red/orange	cyan	yellow

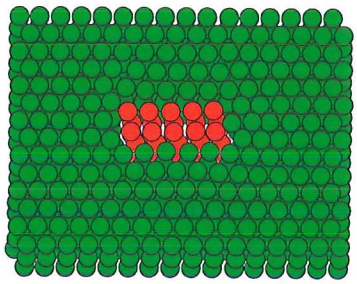

Figure 18: Sketch of three layers of fcc{111} planes containing an intrinsic stacking-fault, where two planes are locally in a hcp geometry.

"Symmetry index" (or symindex) S of atom i. When the number of neighbours of an atom is different from the number indicated in the table, the concluded symmetry might differ from the expected symmetry. The last line of the table the lists the colours with which we usually depict the different geometries. Examples of films visualised using the S-analysis are figures 34, 35, 36 (Cu/Cu) and figures 39–43, 63–65, (Cu/Mo). Figures 69–73, 55, 68, 86 and 66 all use S.

Stacking faults Stacking faults in fcc are clearly visible using the sym-index S as they all have one or more planes with hcp geometry. There are several stacking defects [7, 52]. In a twin or growth fault, the stacking order is reversed. For a microtwin, a second reversal takes place within a few planes. A reversal within two planes is an *intrinsic* or *extrinsic* fault (equivalent to a missing or an extra plane). An intrinsic stacking-fault (figure 18) forms between two Shockley partial dislocations, which have $\vec{b} = \frac{1}{6}d\{112\}_{\text{fcc}}$ *in* the fault plane [7] ($d\{112\}_{\text{fcc}}$: see figure 4). Using the S-analysis, these partials are often marked by bcc atoms. In the figures in the next section, most intrinsic faults are seen from the side of figure 18 (at 30° with the vertical "axis"). Figure 34 shows a clear example of an intrinsic stacking fault in a Cu/Cu film.

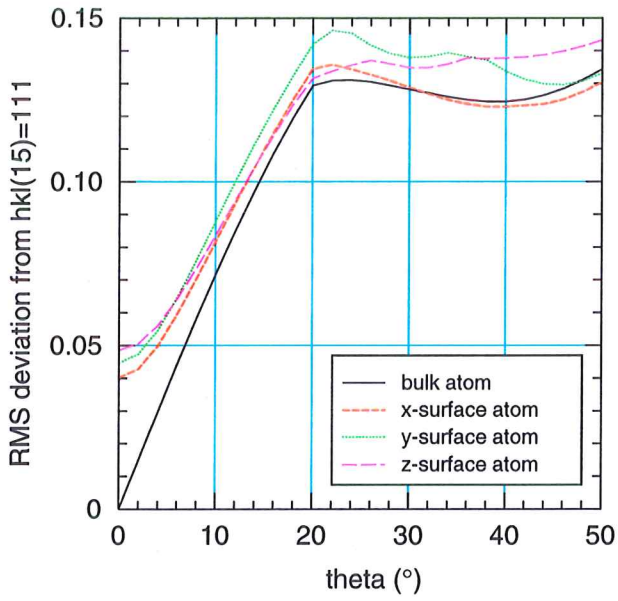

Figure 19: RMS deviation of the variant Spherical Harmonics as a function of the angle θ, both with respect to the fcc $\langle 111 \rangle$ orientation. The figure lists the value for a bulk atom, and for x-,y-,z-surface atoms.

Local crystal orientation—rotationally variant coefficients Another use of Spherical Harmonics is the determination of the approximate local Miller-indices at the position of an atom (called "hkl-analysis" in this work). This analysis uses the (sum of the) rotationally *variant* coefficients $\bar{Q}_{lm}$ (equation (84)), and makes it possible, given a certain symmetry S_i, to determine the approximate local orientation $\{hkl\}^i_S$, or, given a specific $\{hkl\}^i_S$ orientation as well, to determine the local deviation $\delta\{hkl\}^i_S$ from this specific crystal orientation.

The analysis is currently implemented for the fcc, the bcc, and the hcp structure. As expected, the hcp structure poses some problems in interpretation due to the non-cubic hcp unit cell. For translation of the analysis result into the polar angle θ, we use plots of the RMS deviation $\delta^{\theta}_{S\{hkl\}}$ from a $\{hkl\}$ orientation of crystal symmetry S as a function of the polar rotation angle θ of the test systems with respect to this orientation, see figures 19, 20, 21, 22 and 23 for these "calibration plots". An additional complication in using this analysis, which is also due to the coefficients being orientation-sensitive, is that atoms in the x-, y- and z-surfaces of a cubic crystal are seen as having different RMS deviations, especially at small angles $\delta\{hkl\}_S = \theta$. The calibration plots therefore list both the bulk value, and the value for the x-, y- and z-surface. Examples of this analysis are found in figures 63, 64, 74, 75, 84 (middle, right), and figures 65, 76 (right), all for Cu/Mo systems.

We have not yet determined the best manner of interpreting and visualising the results from this analysis method. In addition, we do not, currently, have a convenient manner of analysing both polar angle θ and azimuthal angle ϕ at the same time. Clearly, there still is much room for improvement of this analysis.

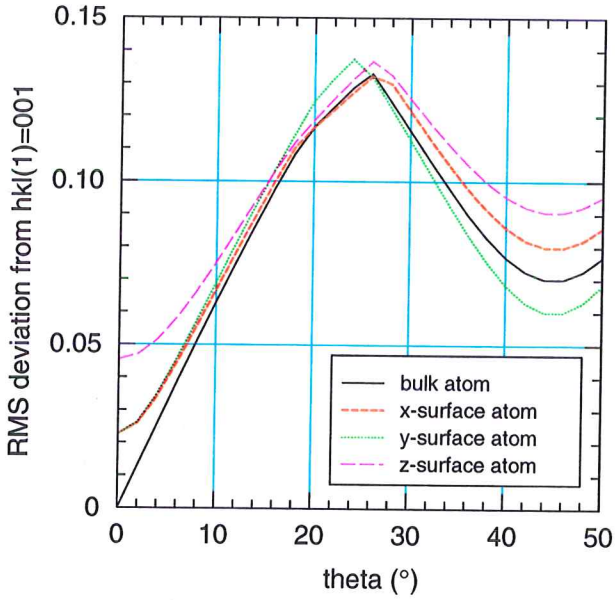

Figure 20: RMS deviation of the variant Spherical Harmonics as a function of the angle θ, both with respect to the bcc $\langle 001 \rangle$ orientation. The figure lists the value for a bulk atom, and for x-,y-,z-surface atoms.

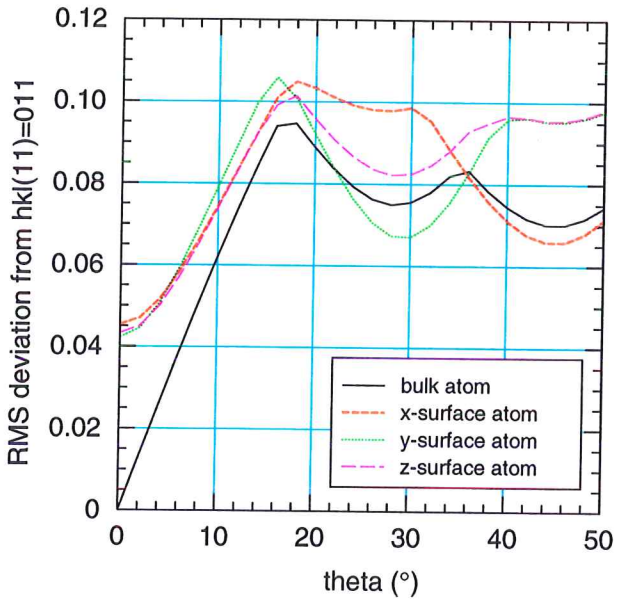

Figure 21: RMS deviation of the variant Spherical Harmonics as a function of the angle θ, both with respect to the bcc $\langle 110 \rangle$ orientation. The figure lists the value for a bulk atom, and for x-,y-,z-surface atoms.

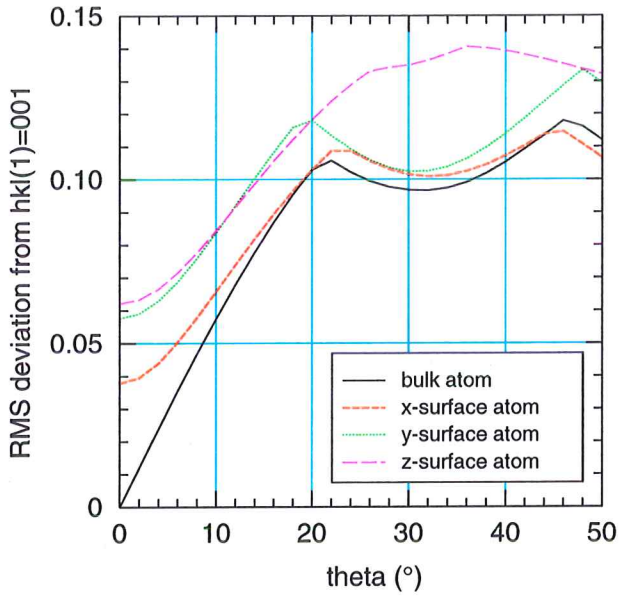

Figure 22: RMS deviation of the variant Spherical Harmonics as a function of the angle θ, both with respect to to the hcp $\langle 001 \rangle$ orientation. The figure lists the value for a bulk atom, and for x-,y-,z-surface atoms.

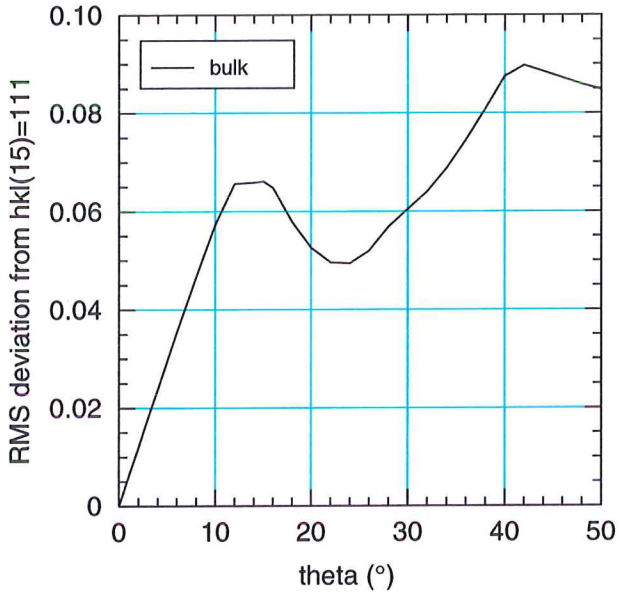

Figure 23: RMS deviation of the variant Spherical Harmonics as a function of the angle θ, both with respect to the hcp $\langle 111 \rangle$ orientation. This figure does not list the values for x-,y-,z-surface atoms, as there are several different values for each of the surfaces, further complicating the analysis. Therefore, we do not look at the deviation of these surface atoms.

3.2.9 Stresses in the layers

In each configuration, we can calculate the stress tensor at each atom, equation (38) on page 21. It is not always simple to translate this information to the macro-stress operating in the layer, due to a multitude of small local variations of the stresses. These variations do signify a locally different situation such as a defect in the lattice, but it is at present not very clear how to interpret the results in a more general way.

3.3 Reduced quantities

As is the usual practice in simulations, we use reduced quantities in the program code, chosen in such a way that the values for energy, distance, temperature etc. are not large or small but near unity, which would not be the case for SI units. By doing this, the effect of numerical errors is lowered, and incorrect values due to programming errors are more easily discerned. All quantities can be expressed in (a combination of) a characteristic interaction-energy ϵ, -distance σ and atom mass m_0, together with the Boltzmann constant k_b, thus forming an alternative system of (reduced quantities and corresponding) units. Table X gives an overview of the reduced quantities used during the currently reported work. The basis for the units is not the Cu/Mo system, but instead a Ni/B-system, as used by van Ee [81], which explains the values of ϵ, σ, and especially the used m_0. Note that $k_B^* = 1$ and $\hbar^* = 0.0106$.

As a consequence of using reduced quantities, results that are reported in SI units may have values that look strange, because of the translation from reduced quantities. In this work almost all results have been converted to SI.

Table X: Reduced quantities, based on ϵ, σ and m_0. Reduced quantities have an "*" to visually distinguish them from non-reduced quantities.

reduced quantity	unit
Boltzmann constant $k_B^* = k_B/k_B$	$k_B = 1.381 \times 10^{-23}$ J K^{-1}
energy $E^* = E/\epsilon$	$\epsilon = 0.0872$ eV $= 1.40 \times 10^{-20}$ J
length $r^* = r/\sigma$	$\sigma = 2.684$ Å $= 2.684 \times 10^{-10}$ m
mass $m^* = m/m_0$	$m_0 = 58.71$ amu $= 9.75 \times 10^{-26}$ kg
density $\varrho^* = \varrho/\sigma^{-3}$	$\sigma^{-3} = 0.0517$ Å^{-3} $= 5.17 \times 10^{-32}$ m^{-3}
volume $V^* = V/\sigma^3$	$\sigma^3 = 19.34$ Å^3 $= 1.934 \times 10^{-29}$ m^3
specific heat $C^* = C/k_B$	$k_B = 1.381 \times 10^{-23}$ J K^{-1}
temperature $T^* = T/(\epsilon/k_B)$	$\epsilon/k_B = 1012$ K
force $F^* = F/(\epsilon/\sigma)$	$\epsilon/\sigma = 5.21 \times 10^{-11}$ N
force constant $K^* = K/(\epsilon/\sigma^2)$	$\epsilon/\sigma^2 = 0.194$ N m^{-1}
pressure $P^* = P/(\epsilon/\sigma^3)$	$\epsilon/\sigma^3 = 7.226 \times 10^8$ Pa
Dirac constant $\hbar^* = \hbar/\sqrt{m_0\epsilon}$	$\sqrt{m_0\epsilon} = 0.0106 = 9.926 \times 10^{-33}$ J s
velocity $v^* = v/\sqrt{\epsilon/m_0}$	$\sqrt{\epsilon/m_0} = 297$ m s^{-1}
time $t^* = t/\sqrt{(m_0\sigma^2)/\epsilon}$	$\sqrt{(m_0\sigma^2)/\epsilon} = 0.709$ ps
frequency $\nu^* = \nu/\sqrt{\epsilon/(m_0\sigma^2)}$	$\sqrt{\epsilon/(m_0\sigma^2)} = 1.41 \times 10^{12}$ Hz
diffusion coefficient $D^* = D/\sqrt{\epsilon\sigma^2/m_0}$	$\sqrt{\epsilon\sigma^2/m_0} = 1.02 \times 10^{-7}$ m^{2}s^{-1}

3.4 Summary of methods and explanation of simulation parameters

This subsection sums up the types of simulations performed. The first part details the different simulations performed to obtain the system properties that are reported in §4.1, and explains how the simulations are analysed to obtain these results. The second part describes the parameters of the deposition (reported reported in 4.1.7). In view of the arguments in §2.4, the description of the Cu on Cu deposition simulations includes (on page 72) a brief discussion of the temperature-control used (see §2.1.8).

3.4.1 Diffusion and system properties

Atomic volume and thermal expansion From a single simulation at one temperature, the atomic volume can be determined. When combining multiple temperatures, we can obtain the coefficient of (linear) expansion.

The simulations are performed with both temperature and pressure control activated, and in a simulation box with periodic boundary conditions in three dimensions to simulate a bulk material.

Starting from an initial configuration, created with a kinetic energy corresponding to T_{inital}, the system is maintained at T_{set} and P_{set}. The system relaxes and reaches an equilibrium state after $t_{equilibration} = 3.5$–10.6 ps. After equilibrating, the system is kept in this situation for 7.1–14.2 ps, during which the value of the temperature, pressure and the other thermodynamic averages can be recorded. From this, the average values are determined, as well as the standard deviation.

Melting Temperature An interesting method for determining the melting temperature of a system is the so called two-phase method as described by Belonoshko *et al.* [10] (see also [3, 55]). This method uses the atomic volume change with temperature to determine the melting temperature.

The method starts from a simulation box in which one half has the atoms attached to anchor points, and the other half of the atoms is unrestricted. This system is heated to well above the experimental melting temperature of the studied material, with pressure control active. Now, the unrestricted half of the system is allowed to melt fully, while the anchored half remains solid, thus creating a two-phase (solid-liquid) system, with each phase occupying one half of the simulation box. In this way nucleation problems are circumvented.

Next, this system is used as the initial configuration for a series of simulations at different temperatures. The anchors are removed, so that the whole system is again unrestricted in its movement. The series of simulations is performed with pressure control at ambient pressure (1 bar) and temperature control at a specified temperature in the range around the expected melting temperature. The system is allowed to find a new equilibrium. Depending on the fractions of solid and liquid phase, the atomic volume will be different. At low temperatures, the system will become (almost) completely solid, while at temperatures well above the melting temperature, the system will become

(almost) completely liquid. For temperatures near the melting temperature, the system unpredictically ends up either as a solid or as a liquid. We can check that the atoms are liquid or solid by using the symindex described above, which is done for a few of the simulations. Alternatively, we determined the presense/absense of a lattice by visual inspection of the atom positions, but this is a more arbitrary measure.

The system size is an important factor in the accuracy of the result. Choosing a too small system will result in a too high melting temperature. However, Belonoshko *et al.* [3] found that above $N = 1000$, thus starting with $N_{solid} = N_{liquid} = 500$ atoms in each phase, the obtained melting point is independent of system size. Their results do show that the hysteresis zone that is seen around the melting temperature, where the solid/liquid ratio is unpredictable, is smaller for larger system sizes. We used $N = 1000 (= 2 * 500)$.

Ahuja, Belonoshko and Johansson [3] as well as Morris *et al.* [55] have shown that this method provides the true melting temperature of the system, while the "heat-until-it-melts" is much less reliable, as results are highly dependent on the heating rate. To verify this, two of such "heat-until-it-melts" simulations were performed for a thin Cu film, as deposited on a Mo substrate. For this, configurations are used from EVAP_s and EVAP_b1 (see below, starting from page 73). Table XI lists the simulations parameters. The melting temperature lies between the start of melting at $T_{melt,i}$ and $T_{melt,e}$, whereall Cu is liquid.

Table XI: Heating of Cu/Mo(110). The starting configurations are produced by the deposition simulations described in table XIII (at Θ, D of the used configurations are listed here). The starting temperature for these heating simulations is equal to the deposition temperature (1012 ± 30 K).

parameter	unit	heating 1	heating 2
heating rate	K ps^{-1}	47.579	2.3789
duration	ps	42.54	1064
T_{end}	K	3036	2534
from simulation	-	EVAP_b1	EVAP_s
Θ	monolayers	6.07	7.02
D	Å	13.5	15.6

Elastic constants As the simulation code can provide all components of the stress tensor for each atom (see equation 38) the elastic constants are derived from applying a small (elastic) strain to a system that is in equilibrium. The volume average stress components of the system are determined after a period of equilibration, both for a positive and for a negative strain of 0.1%. Averaging the two values for the elastic constants gives c_{11}, c_{12} and c_{44}. The other elastic constants can then be derived from the equations in §2.2.

Diffusion For the different diffusion studies, several types of systems are used. All of these simulations are performed with a fixed temperature and without pressure control after the initial relaxation.

Bulk vacancy diffusion Bulk vacancy diffusion is studied using a 3D periodic fcc Cu system containing 2047 atoms and a vacancy. The system is first annealed for 0.709 ps at the simulation temperature. The jump frequency is determined by counting the number of jumps that occurs between successive configurations recorded at intervals of 1.42 ps during several hundreds of ps. A jump event is counted when at least 5 neighbour-changes (see §3.2.3 above) have occurred in the atoms around a potential jump and one of these atoms is displaced by at least 1.1 Å, half the jump distance λ. This procedure is performed at temperatures of 819 ± 14, 1012 ± 23 and 1215 ± 34 K. The resulting jump frequencies are used to obtain an activation energy Q_{vacdiff} and D_0 using the appropriate equations in §4.1.7.

Adatom diffusion Cu adatom diffusion was studied on Cu(111) and on Mo(110). The simulations are performed in much the same manner as the vacancy diffusion simulations. The mean square drift is determined for a range of different time intervals between configurations, ranging from 14.2 to 350 ps, giving various values for $\langle \Delta r^2 \rangle / \Delta t$. By doing this, however, the larger Δt, the fewer values are available. To determine the jump frequency, the path of the adatom is stored as well, using the coordinates of the adatom at $\sim$ 14 fs intervals. Between all successive positions, the occurrence of a jump event is checked with the coordinates that are closest in time. Here, a jump event is counted when at least one neighbour-change has taken place since the last jump, together with a displacement by at least $\frac{1}{2}\lambda = 1.1$ Å. The procedure assumes a relatively static substrate and no exchange with the substrate.

The Cu adatom on Cu simulations use a six planes thick Cu surface, with the bottom two planes anchored. The dimensions are 30.992×29.8222 Å or 6×10 unit cells, with the orientation as shown in figure 4, ie, x an fcc $\langle 211 \rangle$ direction and y an fcc $\langle 110 \rangle$ direction. This results in 120 atoms per plane and a total number of 720 atoms in the system, plus one adatom on the surface. The simulations are performed at 202, 304, 406, 607, 810, 1012, 1214, and 1417 K. The last simulation led to melting and is not used. All of the simulations lasted 709 ps, including an initial equilibration period of 7–14 ps, depending on the temperature, as determined from the evolution of temperature, pressure and potential energy in the system.

For the Cu adatom on Mo simulations the same starting configuration is used as for the smaller Cu-Mo EVAP simulations, denoted as "s" in table XIII below. The simulations are performed at 607, 810, 1012, 1214 and 1417 K, and at some lower temperatures, which show no diffusion and are consequently discarded. All simulations lasted 709 ps, including an initial equilibration period of 7–14 ps, determined in the same manner as for the Cu surface diffusion.

A third set of surface diffusion simulations is performed using an as deposited Cu film on Mo(110). The starting configuration is taken from the Cu on Mo deposition EVAP_s, see below, at a coverage of 1.7, when the first monolayer is completely formed as a pseudomorphic bcc layer. All atoms above this first Cu monolayer are removed, except one, which becomes the adatom. For the rest the procedure is the same as for the other two surface diffusion series.

3.4.2 Deposition runs

The Cu atoms are in all cases introduced with a (kinetic) energy of 0.1744 eV, along a slightly off-normal direction, at a polar angle $\theta_{z,\text{intro}} = 15.0°$ and azimuthal angle $\psi_{z,\text{intro}} = 13.0°$, to be in agreement with the film growth eriments performed in our group (see for example [29, 15, 19]). For all deposition runs, the lowest two substrate planes are anchored to their equilibrium positions. The box x and y dimensions are kept constant (no pressure control), even when going to high temperatures, while the z-axis is increased occasionally to make room for the growing free surface. The empty space above the surface should be kept small for reasons of computational efficiency.

Cu-Cu EVAP Two different simulations of Cu EVAP deposition on Cu(111) are performed, see table XII. The main differences are the system size and the temperature during the simulation. The system size is based on the experimental value for the lattice constant at 300 K, not on the lattice constant appropriate for "our" Cu at 300 K.

Table XII: Deposition of Cu on Cu(111). The deposition parameters are chosen to match the experimental situation, see [29, 15, 19, 47, 48] and the text above. See the text for the deposition temperatures. The x-direction is the fcc[110] and the y-direction lies along the fcc[211] direction, rotated by 90° with respect to the orientation of figure 4 (page 27). The literature value for the Cu lattice constant is used for the box size (see table III). $N_{tot,subs}$ is the number of atoms in the substrate, K_{subs} is the number of substrate planes and $M_{k,subs}$ is the number of atoms per substrate plane. For our own reference, the bottom rows give the deposition time (in t^*) and the version of our simulation code used. †: new T-control.

parameter	unit	EVAP_{Cu1}	EVAP_{Cu2}
box size $x \times y$	unit cells	30×18	16×10
	Å^2	76.686×79.694	40.8991×44.275
$M_{k,subs}$		1080	320
K_{subs}		2	6
$N_{tot,subs}$		2160	1920
α_t	atoms ns^{-1}	2821	940
α_D	Åns^{-1}	5.451	6.132
$D_{\max}$	Å	25.30	34.11
camelion	version no.	7.11	7.21
		7.12	7.24†
		7.21	
deposition time	t^*	6550	6210

EVAP_{Cu1} For the larger EVAP_{Cu1}, initially, the temperature was set to $T_{required} = 303.6$ K. At the time, the arguments presented in §2.4 had not been fully realised. The required temperature is not reached in the majority of the system, due to a failing temperature control. For most of the simulation time, the temperature of the non-bottom atoms in the film, the "other-bound

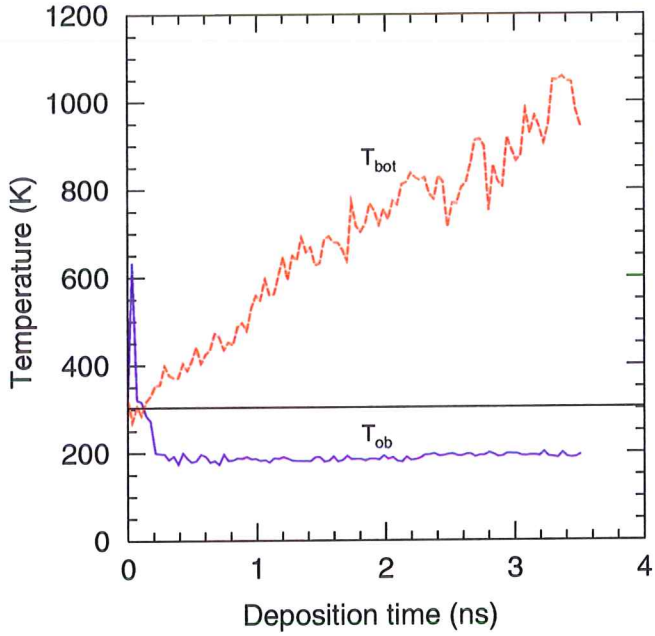

Figure 24: Temperature of the atoms during the EVAP$_{Cu1}$ simulation. The blue line marked T_{ob} gives the temperature of the other-bound atoms (see page 19). The red line marked T_{bot} shows the temperature of the anchored atoms (the substrate), which can be seen to rise sharply during deposition, to compensate for the growing number of low temperature atoms. The horizontal black line is $T_{required}$, see equation (34). The system temperature is close to $T_{required}$ during the entire simulation.

atoms" (page 19) is 200 K, see figure 24. The overall temperature is at $T_{required}$ (black line), but the bottom atoms (the original substrate) are at a much higher temperature, compensating for the increasing number of low temperature other-bound atoms.

The T-control problem is discovered only recently, as a result of looking at T_{bot} and T_{ob} seperately. Consequently, all earlier deposition simulations with our MD code ([61, 62, 58, 49]) suffer from this problem. For the Mo deposition runs from [61, 62], and the earlier ones from [58, 49], the fact that the temperature is other than the one expected may not have a large impact. Most of these simulations are performed at $T_{required} = 300$ K, $\sim 0.1 T_{melt,Mo}$. For Cu deposition, however, the argumentation in §2.4 has much more significance.

EVAP$_{Cu2}$ In the smaller EVAP$_{Cu2}$ simulation the temperature is initially set to 1214 K as we began to realise the time-temperature problem (§2.4), partly, from analysing the results of EVAP$_{Cu1}$. Figure 25 shows the actual temperature to be much lower, starting at $\sim$ 600 K and slowly increasing to 800 K at $\sim$ 2.8 ns. At this point, a new temperature control was introduced, with the characteristics as described earlier (in §2.1.8). This solves the temperature problem. The introduction of the new temperature control in this Cu simulation, with $T_{required}$ set to 1113 K, results in a rapid increase of the temperature to reach the required value, which is then maintained. $T_{required}$ is lower now to be certain that the Cu does not undergo melting.

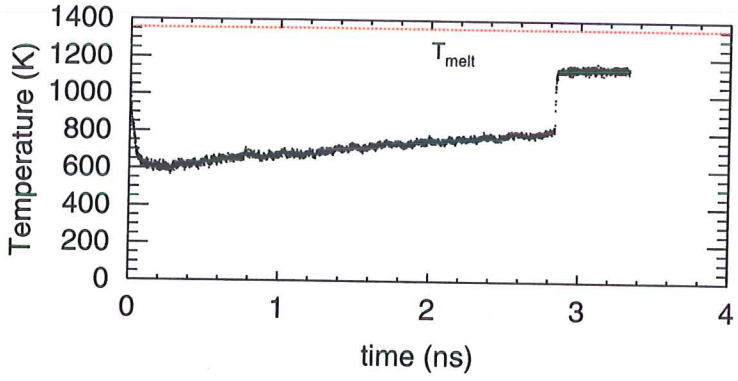

Figure 25: Temperature of the other-bound atoms during the EVAP_{Cu2} simulation. The red line is the experimental melting point of Cu, 1356 K [83].

Cu-Mo deposition For deposition of Cu on Mo, the choice of box dimensions is important. In a perfect (111) orientation, Cu would never perfectly fit within the box prescribed by a Mo (110) substrate. There are however some optimum dimensions, for which the Cu and Mo are almost coincident. In fact, as mentioned in §2.5.1, the mismatch is close to that for the perfect Nishiyama-Wasserman-x relationship, so that in the Mo bcc[110] direction, for each 6 Mo cells, 5 Cu cells would almost fit. It is however not possible to totally avoid restricting the epitaxial relationships that may occur. Due to the use of periodic boundary conditions, the Cu deposited on the Mo substrate is always restricted to certain discrete numbers of atoms (unit cells) per plane, depending on the atom size and on the orientation θ of the Cu unit cell relative to the Mo substrate. The relative dimensions of the Cu and Mo unit cells in a specific orientation can be found using figure 4 on page 27. The fitting into the rigid simulation box (with a surface that is kept constant during the simulation) enforces a certain coincidence lattice. In deciding on the box-size, it is assumed here that $\theta = 0°$ for the epitaxial orientation that occurs (the NW-x relation), which enables us to determine the box size that results in as good a fit of the Cu as possible. Using a larger box that is an integer times this good-fit box-size gives the Cu atom more "room" to accommodate the forced coincidence. For smaller boxes, the amount of strain will increase.

Table XIII lists the three different substrates used for the Cu on Mo depositions. The third, "very small" system is only used in one short simulation. Note that the literature value of the Cu lattice constant at 300 K (see table III) is used in determining the simulation-box size. In table XIV, the deposition conditions are given for these simulations. All of them are performed with the new temperature control and have a constant temperature of 1012 ± 20 K for the whole system.

Table XIII: Data for the three used Mo substrates. All have the (110) orientation, with [100] along x and [110] along y, and a plane separation $d_k = d_{k,Mo}\{110\} = 2.2254$ Å. The box sizes are determined in such a way as to minimize the effect of a forced coincidence. Using a larger box will in general decrease the effect as well. Note that in determining this, the literature value of the Cu lattice constant (see table III) is used and that the box xy-surface is held fixed during the simulation.

parameter	unit	system size		
		very small	small	big
box size $x \times y$	unit cells	11×6	18×10	36×40
	Å^2	34.619×26.705	56.650×44.508	113.30×178.03
$M_{k,subs}$		168	360	2880
K_{subs}		4	6	4
$N_{tot,subs}$		672	2160	11520
designation		"v"	"s"	"b"

Table XIV: Deposition of Cu on Mo(110). Table XIII lists the different substrates that are used. The deposition parameters are chosen to match the experimental situation, see [29, 15, 19, 47, 48] and page 71. The table also gives the effective deposition rate in Å ns^{-1} and in the coverage Θ ns^{-1}. The Cu atom flux is approximately equal in all simulations (312–373 atoms Å^{-2} ns^{-1}). For the IBAD simulations, 100 eV Ar is used, with 10% fast (250 eV) Ar atoms. For our own reference, the bottom of the table also lists the maximum time (in reduced time t*), the platform and the version of our simulation code used. Pmmx/L: 233MHz Pentium®MMX™with RedHat®Linux 5.2; PIII/L: Pentium® III 450/500 with RedHat®Linux 6; Cray: Cray®T3E AC128-128 UNICOS/mk 2.0.5 of Delft TU. †: except for the thickness range 6.7–23.45 Å, during which 1 CPU (PIII/Linux) was used. ‡: "p-" is for parallel, nothing or "SE" (just a change of naming) is the single CPU version. Version 7.27 is the first to use the neighbour table.

parameter	unit	$EVAP_v$	$EVAP_s$	$EVAP_{b1}$	$EVAP_{b2}$	$IBAD_s$	$IBAD_b$
substrate		very small	small	big	big	small	big
$\alpha_{t,in}$ (atoms)	ns^{-1}	433.6	940	7052	7052	940	7052
$\alpha_{\Theta,in}$	Θ ns^{-1}	2.581	2.611	2.449	2.449	2.611	2.449
flux	Å^{-2} ns^{-1}	0.4521	0.3728	0.3496	0.3496	0.3728	0.3496
α_D^{eff}	Å ns^{-1}	5.749	5.813	5.447	5.449	5.470	5.082
α_Θ^{eff}	Θ ns^{-1}	2.583	2.612	2.448	2.449	2.458	2.284
flux_{eff}	Å^{-2} ns^{-1}	0.4521	0.3728	0.3495	0.3496	0.3510	0.3261
IAR Ar/Cu	ratio	0	0	0	0	0.1	0.1
250/100 eV Ar	fraction	0	0	0	0	0.1	0.1
$D_{\max}$	Å	24.2	55.2	53.3	78.0	49.1	72.6
#CPU's		1	1	1	8	1	8 †
camelion	version ‡	7.27	7.24	7.27	p-7.27	7.24	p-7.27
			7.26	9.1	p-9.1	7.26	7.27
				SE9.13			9.1
							p-9.1
simulation time	t*	5940	14920	13860	21160	14100	20700
platform		Pmmx/L	Pmmx/L	PIII/L	Cray	Pmmx/L	Cray†

4 Results

In this section the results obtained from the simulations listed in §3.4 are presented and analyzed. The analysis methods have been described in §3.2. Some of the data is shown in the form of graphs, while much of the microstructure will be discussed using hard-ball pseudo-3D plots of configurations.

The setup of the current section is as follows. First, subsection 4.1 lists properties of the Cu-Cu and Cu-Mo systems. These can be seen as a validation of the used interactions (§3.1). The properties described in this section are also useful as a basis for the understanding of the results of the deposition simulations.

In subsection 4.1.7 the deposition simulations are investigated. We will first address the deposition of Cu on Cu, in §4.2, and then, in §4.3, continue with the more complex situation of Cu deposited on Mo. The first stage of the evolution of the film during deposition of Cu on Mo will first be described in general, followed by a more in-depth study of the differences in the later stage of the deposition.

Finally, in the last part of the section, the influences of the system size and of type and number of processors is investigated.

4.1 System properties

Determining the physical properties of the system is an important part of the validation of the EAM interaction model. The Cu-Cu interaction (see §3.1.1) has been constructed during this study and was not used previously in our research group, contrary to the Mo-Mo and the noble metal interactions (see §3.1.2 and §3.1.4). The Cu-Mo interaction (§3.1.3) has been developed especially for this work. Therefore, such a validation is of great importance for assessing the degree of reality and the possible limitations of the simulation results.

4.1.1 Atomic volume and coefficient of expansion

Atomic volume Determining the atomic volume Ω for our Cu interaction is interesting both as a test of the interaction itself, and because Ω influences the mismatch with the Mo lattice.

Table XV lists the density ϱ and atomic volume Ω at several temperatures, as well as the experimental values at 293 K (20°C) at ambient pressure. In figure 26, Ω is plotted versus the temperature (□). The resulting coefficients of expansion can be found in table XVII. From table XV it can be seen that our Cu-Cu interaction yields a Cu atom that is slightly too large, $\sim 3.7\%$ in volume and $\sim 1.2\%$ in atomic diameter at 300 K. The nearest neighbour distance at 300 K is 2.587 Å in the simulations (at 1000 K, this is 1.631 Å), as compared to 2.556 Å experimentally.

As a consequence of the Cu being too large, the misfit r_{m} with Mo will be reduced and Cu will not fit unstrained into a simulation box-size based on its 300 K experimental value as is done for the depositions, see tables XII–XIV in §3.4.2. Due to the large expansion coefficient of Cu, see below, using

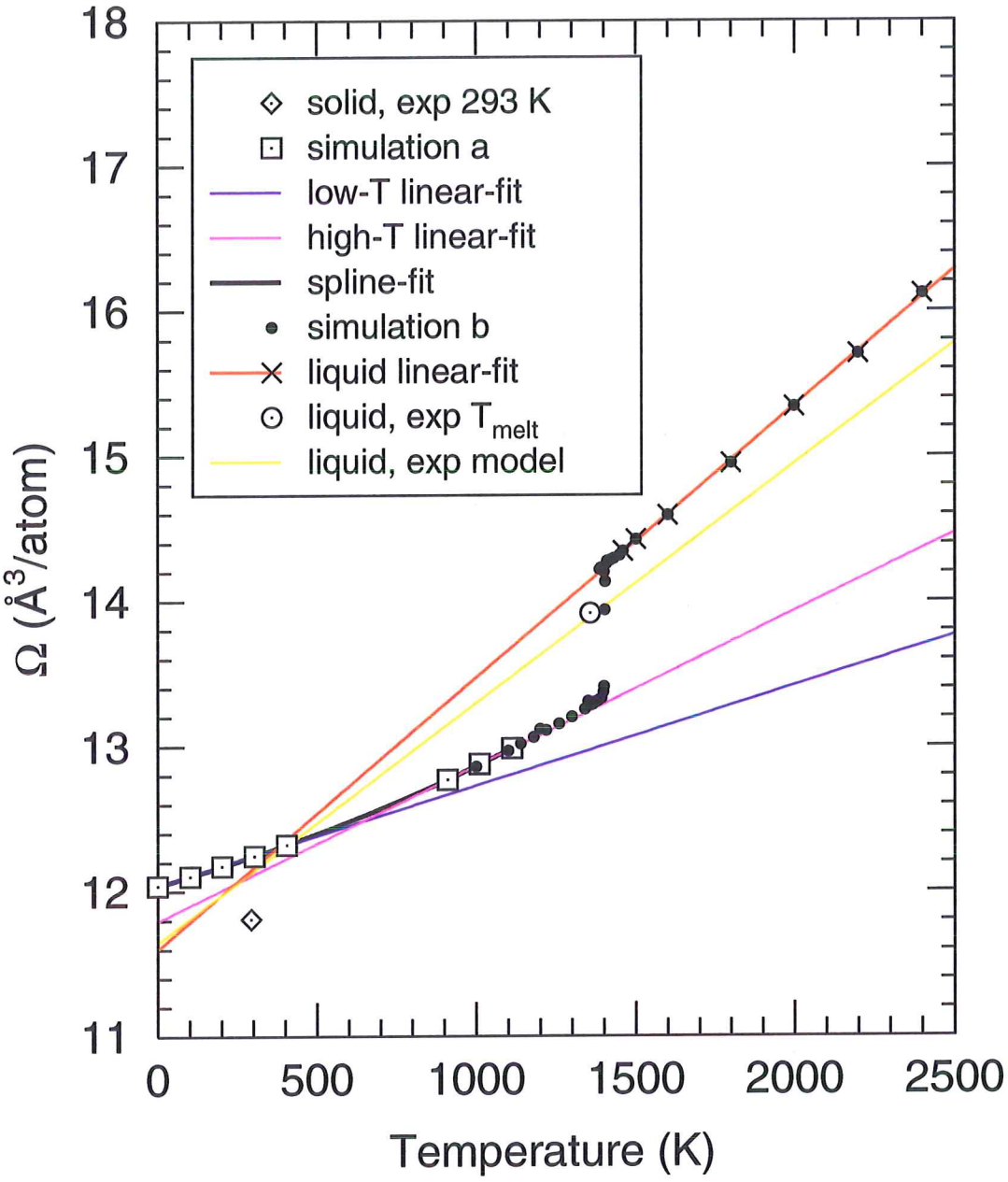

Figure 26: Atomic volume Ω versus temperature for Cu in the simulations. From the available data, three distinct regions are seen with a different direction coefficient. The first dataset, determined from equilibrating a 3D-periodic system at several temperatures (⊡), gives values for low temperature expansion (blue line) and for high temperature expansion (magenta). The second dataset (•), obtained from a two-phase coexistence method, see §4.1.2, makes it possible to determine the expansion of the liquid phase (red line, points ×) as a function of temperature. The value for Ω_{liquid} is given as well, together with a (linear) volume expansion line, based on density values from a simple linear model, see text.

Table XV: Number-density ϱ_n and atomic volume Ω for several temperatures. The experimental value for 293 K (20 C°) [13] is also given ($^{\dagger a}$). The table also lists the values for liquid Cu at the melting temperature as well (exp.: $^{\dagger b}$; sim.: ‡).

T (K)	ϱ_n (10^{-2} atoms Å^{-3})	Ω (Å^3)
$293^{\dagger a}$	8.493	11.81
$1356^{\dagger b}$	7.1863	13.915
0.002	8.3058	12.0398
304 ± 3	8.1660	12.246
1012 ± 3	7.7683	12.877
1392 ± 13	7.50	13.3
$1392 \pm 13^{\ddagger}$	7.03	14.2

these box sizes at high temperatures also poses problems when quenching a configuration. However, we only use high temperature to compensate for the temperature versus time problem signaled in §2.4 so looking at the high temperature structure may not be ideal either.

The size difference is made possible by the combination of the allowed fit-error, and the fact that Ω is implicitly fitted during the construction of the Cu-Cu interaction (in ΩG_v and ΩB), see table IV. This also makes that it is not immediately clear what value for Ω results from the fit. The effect is enhanced by the use of room temperature experimental quantities in what is essentially a fit for a 0 K situation. From this result, we can expect the elastic constants to deviate from the experimental ones as well.

The thermal expansion coefficient From the values of the atomic volume we have determined the thermal expansion of Cu in three temperature-ranges which make up distinct regimes: expansion at low temperatures ($T \leq 400$ K), at high temperatures (above $0.6\,T_{melt}$), and expansion of the liquid phase, see figure 26. The figure also shows the variation of the liquid as based on the experimental value of ρ_n and density-change C_{ρ_n} with a simple linear model for C_{ρ_n} [13]. Table XVI lists the obtained values for C_{ρ_n} and the volume-expansion C_V in these regimes.

Table XVI: Change of density (C_{ρ_n}) and of atomic volume (C_V) with temperature T. The experimental values for liquid Cu at $T_{melt}{}^{\dagger} = 1357$ K (1083 C°) [13] is also listed.

T-range	C_{ρ_n} (10^{-6} Å^{-3} K^{-1})	C_V (10^{-3} Å^3 K^{-1})
solid ($T \leq 400$ K)	(-4.66 ± 0.07)	(0.69 ± 0.02)
solid ($T \geq 900$ K)	(-6.4 ± 0.2)	(1.07 ± 0.03)
liquid ($T \geq 1400$ K)	(-8.1 ± 0.1)	(1.87 ± 0.04)
liquid at $T_{melt}{}^{\dagger}$	-7.59	1.65

In addition, we fitted a spline to the (T, Ω)-data points, from which we

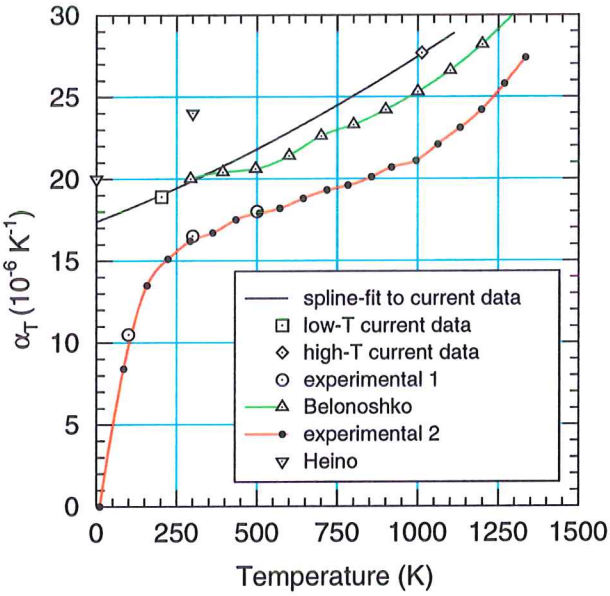

Figure 27: Coefficient of linear thermal expansion α_T for Cu. The black curve results from the spline fit in figure 26. Also shown are the values resulting from the red and blue lines in figure 26 (low T: ⊡, high T: ◇) and some experimental values (⊙ [13] and • [10]), as well as the values calculated by Belonoshko *et al.* [10] from MD simulations (△) and the values from EAM MD simulations reported by Heino [33] (▽).

obtain the coefficient of linear thermal expansion, see figure 27 and table XVII, where the current values are compared with experimental data and other simulations.

From the comparison, we find that our expansion coefficient is consistently higher than the experimental values by about 25% and also slightly higher than those calculated by Belonoshko *et al.* [10]. A recently published Cu-Ta EAM study by Heino [33] reports values for the linear thermal expansion coefficient that are considerably higher than the results of the current Cu EAM interaction (48% too high at 300 K). The quantum regime, below 250 K, is clearly not modeled in the current simulations. It seems that the same can be said for the EAM interactions used in [33]. Notably, the 0 K linear thermal expansion in [33] is approximately equal to our 300 K value.

4.1.2 Melting point

Using the two-phase method described by Belonoshko *et al.* (§3.4, see also [10] and [3, 55]) we found (see figure 28) that below 1380 K, Cu is solid and above 1405 K it is fully liquid. In between, the phase is undetermined. This effect is typically seen for small systems. The method results in a melting temperature $T_{melt} = (1392 \pm 13)$ K. Using a larger system will narrow down the transition region. Compared with the experimental value of $T_{melt,lit} = 1356$ K, our value is (36 ± 13) K too high. This is a very acceptable result for an EAM interaction.

Table XVII: Coefficient of linear thermal expansion α_T at several temperatures, as obtained from figure 27. Some values found from MD simulations by Belonoshko *et al.* [10] (†), and from another recent Cu MD EAM study [33] (‡) are given as well. The experimental values for several temperatures are also given ($^\clubsuit$ [51]; $^\diamondsuit$ [10]), as well as some values for the linear expansion for several temperature ranges ($^\spadesuit$ [13]). To compare with these values, we give a linear approximation of $\alpha_{T,\ell}$ for low and high temperatures from the two temperature ranges identified in figure 26.

T (K)	α_T (10^{-6} K^{-1})
102	18.19
200	19.06
303	19.91
503	21.84
1002	27.49
293†	20
496†	20.6
1000†	25.3
0‡	20
300‡	24
100$^\clubsuit$	10
200$^\clubsuit$	16.5
500$^\clubsuit$	18
293$^\diamondsuit$	16.2
994$^\diamondsuit$	21.1
0 – 400	18.9
900 – 1000	27.7
273 – 373$^\spadesuit$	17.1
293 – 473$^\spadesuit$	17.2
293 – 773$^\spadesuit$	18.3
293 – 1273$^\spadesuit$	20.3

Table XVIII: Heating of as-deposited films. Two system sizes were used. The heating rate is lower for the smaller system. At $T_{melt,i}$ the first Cu atoms melt, at $T_{melt,e}$ all Cu is liquid.

	$T_{melt,i} - T_{melt,e}$ (K)	heating rate (K ps^{-1})
1	1310 – 1570	47.579
2	1215 – 1310	2.3789

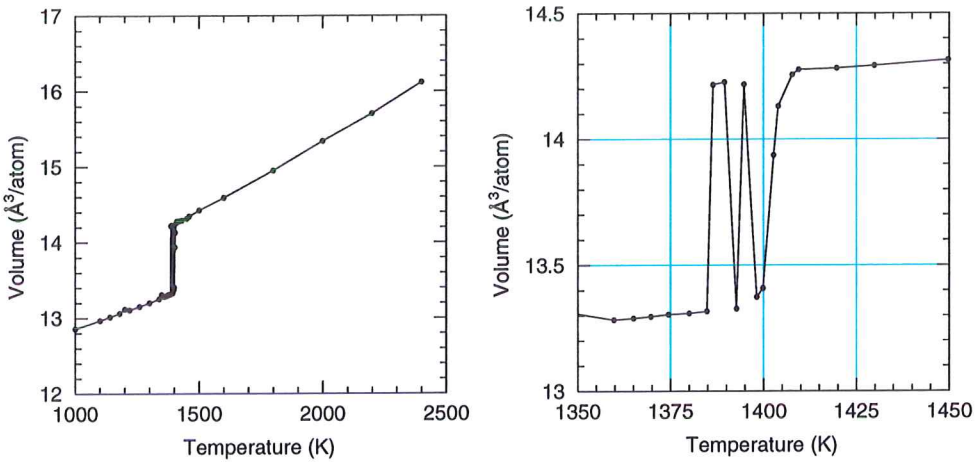

Figure 28: Atomic volume at ambient pressure as a function of temperature, found using a two-phase periodic system (see §3.4, and [10]). The graph on the left is an overview (the data is also shown in figure 26), the right provides a closer look at the region of T_{melt}. The solid-liquid transition is accompanied by a jump in the atomic volume. Near the transition temperature, the phase is undetermined.

For two "heat-until-it melts" simulations of as deposited thin Cu films on Mo, the resulting melting range is listed in table XVIII. The temperature $T_{melt,i}$ is lower than $T_{melt,lit}$ of Cu, as expected for as deposited thin films (see §3.4 and the Cu/Mo deposition results, §4.3). Temperature $T_{melt,e}$ depends on the heating rate. Clearly, the first heating simulation gives a much too high upper limit for T_{melt}, which is due to the high heating rate that is applied.

Annealing results with our deposited Cu/Mo films showed some surface melting of the Cu film when simulating above 1200 K [19]. As these are not bulk Cu crystals but instead non-perfect thin Cu films, this is not surprising.

4.1.3 Elastic constants and moduli

The values for the elastic constants c_{11}, c_{12} and c_{44} are determined for three temperatures. G_v and E, as well as ν_P and A are calculated using the equations from §3.2.9, see table XIX.

There is considerable difference between our results and most of the reference values, especially for the ratio of c_{44} and c_{11}, and for A, but also for B and G_v at $\sim$ 300 K. The results hardly change with pressure. There is a strong trend towards lower elastic constants with temperature. One would expect the 0 K values to be close to the literature values, as we essentially fitted 0 K situation using a combination of 300 K and minimum energy values. The poor result is related to the large Ω, but this would seem to lead too low B and G_v rather than high values. In view of these differences between literature values and our own, it is unfortunate that at the time of creation of the Cu-Cu interaction, no determination of stresses was implemented in our simulation-code yet. The Cu EAM potential used in [6] does do a better job of reproducing the (extrapolated) experimental elastic constants at 0 K, but this interaction also shows notable

Table XIX: Elastic constants and moduli for several temperatures at ambient pressure. The experimental values for the elastic constants at 293 K and ambient pressure are given as well (†: [38]). The elastic constants reported in a recent Cu-Ta EAM study ($^{\ddagger a}$: (exp., from [45]; the 0 K data is extrapolated) and $^{\ddagger b}$ (EAM [45]) are also given. The moduli are calculated from these results using the equations from §3.2.9.

T (K)	c_{11} (GPa)	c_{12} (GPa)	c_{44} (GPa)	c_{44}/c_{11} -	B (GPa)	G_v (GPa)	ν_P (GPa)	A -
$293^{\dagger}$	168	121.4	75.4	0.449	136.9	54.6	0.419	3.19
$0^{\ddagger a}$	176	125	82	0.466	142	59.4	0.415	3.22
$0^{\ddagger b}$	174	124	78	0.448	141	56.8	0.416	3.12
$300^{\ddagger b}$	145	104	57	0.393	118	42.4	0.418	2.78
0.000	203	142	97	0.477	162	70.4	0.412	3.18
304 ± 3	198	134	89	0.445	155	66	0.404	2.78
1012 ± 3	145	98	66	0.455	114	49	0.403	2.81

differences between the MD and experimental elastic constants at 300 K. This indicates that obtaining an EAM interaction for Cu which gives correct elastic constants at more than one temperature is not easily accomplished.

4.1.4 Surface energies

Table XX compares our value for the surface energy of the Cu(111) and the Cu(100) surface with literature values given by Baskes [8, MEAM], both experimental (polycrystalline) and from MEAM, by Mehl and Papaconstantopoulos [52] who give an experimental value and a result from Thight Binding (TB) simulations , the values given by Ackland *et al.* [1] using Finnis-Sinclair N-body potentials (ATVF), EAM values from [33], Effective Medium Theory (EMT) values [31], and some experimental values. None of those values are very well reproduced between experiment and simulation. Still, we can conclude that our value is rather low but comparable to other simulation data.

Table XX: Surface energies for the $Cu(111)_{fcc}$ and $Cu(100)_{fcc}$ surfaces compared with several simulation and experimental values. All values are in Jm^{-2}.

source	$U_{Cu\,fcc\{111\}}$	$U_{Cu\,fcc\{100\}}$
this study	1.183	1.296
exp.poly cryst.[8]	1.77	-
exp.1-cryst. [52]	2.6	-
ATVF [1]	0.947	1.233
EAM [52]	-	1.83
EAM [33]	1.205	1.304
MEAM [52]	-	2.49
MEAM [8]	1.41	1.65
EMT [31]	1.185	1.296
TB [52]	3.34	3.04

4.1.5 Stacking fault energy and crystal energy

For bulk Cu the energy difference between fcc and hcp is $\Delta U_{Cu,fcc\rightarrow hcp} = +0.004$ eV per atom, compared with an experimental value of +0.006 eV per atom [8], so our value is of the same order of magnitude, but somewhat smaller than the experimental value. As the stacking-fault energy is closely related to $\Delta U_{Cu,fcc\rightarrow hcp}$ we can expect the stacking-fault energy to be of the same order of magnitude as the experimental value. The energy difference between fcc and bcc is $\Delta U_{Cu,fcc\rightarrow bcc} = +0.04$ eV, equal to the experimental value reported by Baskes [8].

Table XXI: Comparison of the differences in crystal energies of fcc with hcp, $\Delta U_{\mathrm{Cu,\,fcc\rightarrow hcp}}$, fcc with bcc, $\Delta U_{Cu,\,fcc\rightarrow bcc}$ and the stacking-fault energy, $\Delta U_{\mathrm{Cu}\{111\}\ \mathrm{stacking-fault}}$ between this work and literature values reported by Baskes [8].

source	$\Delta U_{\mathrm{Cu,fcc\rightarrow bcc}}$ (eV)	$\Delta U_{\mathrm{Cu,fcc\rightarrow hcp}}$ (eV)	$\Delta U_{\mathrm{Cu}\{111\}\ \mathrm{stacking-fault}}$ (eV Å^{-2})
this study	+0.04	+0.004	?
[8]	+0.04	+0.006	0.0046
[35]	-	-	(0.0031 ± 0.0013)

4.1.6 Cu desorption energy from Mo{110}

The first and second monolayer desorption energies of our simulations are in excellent agreement with experiments of thermal Cu desorption from a Mo(110) substrate by Paunov and Bauer [59]. In their study, the desorption energies at a coverage of $\Theta = 1$ and $\Theta = 2$ monolayers are 3.53 and 3.17 eV, respectively. The values of the condensation energy determined at 1012 K for one of the deposited films of Cu on Mo(110), see EVAP_s in §4.3, are found to be 3.56 and 3.22 eV at $\Theta = 1$ and $\Theta = 2$ respectively. The values are only slightly different from the experimental values. Even more significant, the difference between the two energies is almost the same. In table XXII, the values are listed. As these desorption energies are influenced by many factors, it is encouraging to find such close agreement.

Table XXII: Desorption energies at a coverage of $\Theta = 1$ ($U_{\mathrm{desorp,\,L1}}$) and at $\Theta = 2$ ($U_{\mathrm{desorp,\,L2}}$), and their difference for the current study and a thermal Cu desorption experiment by Paunov and Bauer [59]. Al values are in eV.

Desorption energies	$U_{\mathrm{desorp,\,L1}}$	$U_{\mathrm{desorp,\,L2}}$	difference
this study	3.59	3.22	0.37
literature	3.53	3.17	0.36

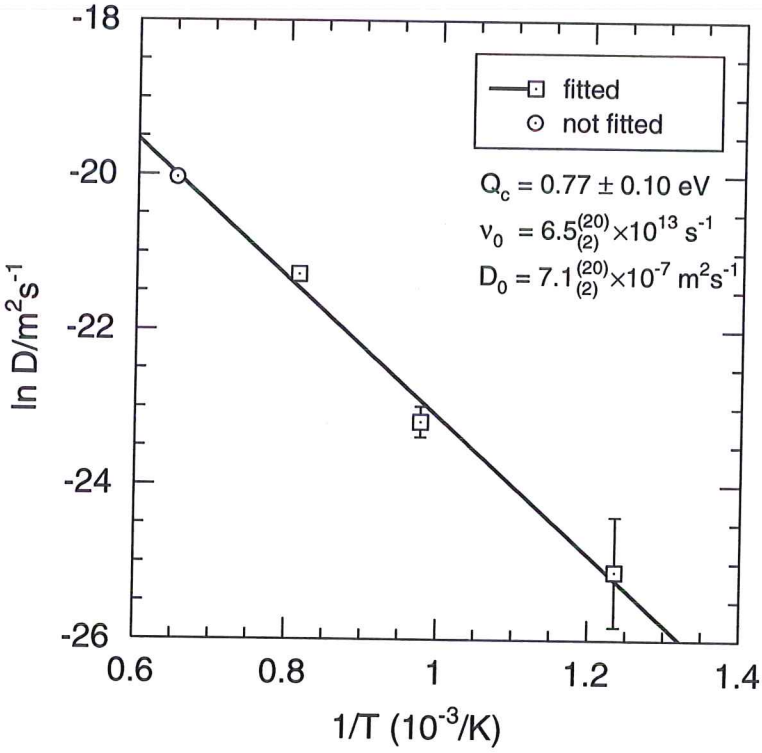

Figure 29: Vacancy diffusion in bulk Cu. We performed vacancy diffusion simulations at four different temperatures. For the simulation details, see §3.4. The fourth simulation is included in the fit because of the occurrence of surface melting of the crystal.

4.1.7 Diffusion

Bulk vacancy diffusion Four vacancy diffusion simulations were performed at different temperatures, three of which are used for fitting to equation 45 (page 22). The fourth run showed melting of the crystal, and is consequently not included in the fit. See figure 29 for the results. Note that the fourth data point does lie on the fitted line.

Using equation (45), we can fit the jump frequencies ν to find a vacancy migration energy of Q_{vac} =(0.77 ± 0.10) eV and a frequency factor of $\nu_0 = 6.5 \times 10^{13}$ s^{-1}, with $D_0 = 7.1 \times 10^{-7}$ m^{2}s^{-1}. This compares to the literature values of $Q = 0.88$ eV [51]. Landolt-Börnstein [53] report $D_0 = 0.1 \times 10^{-4}$ m^{2}s^{-1} (which translates into $\nu_0 = 9.2 \times 10^{14}$ s^{-1}) and a vacancy migration activation energy of $Q = 2.04$ eV. With the vacancy formation energy of 1.3 eV, this translates into $Q_{vac} = 0.75$ eV.

Diffusion of a Cu adatom on a Cu(111)surface For the growth mode of a film and the resulting structure, surface diffusion is an important aspect. In this respect, surface diffusion of Cu on both a Cu(111) surface and on Mo(110) substrates are of interest. The current paragraph mainly deals with diffusion of a Cu adatom on a Cu(111) surface, at a range of temperatures, giving the relevant diffusion parameters. These are determined from the mean square drift

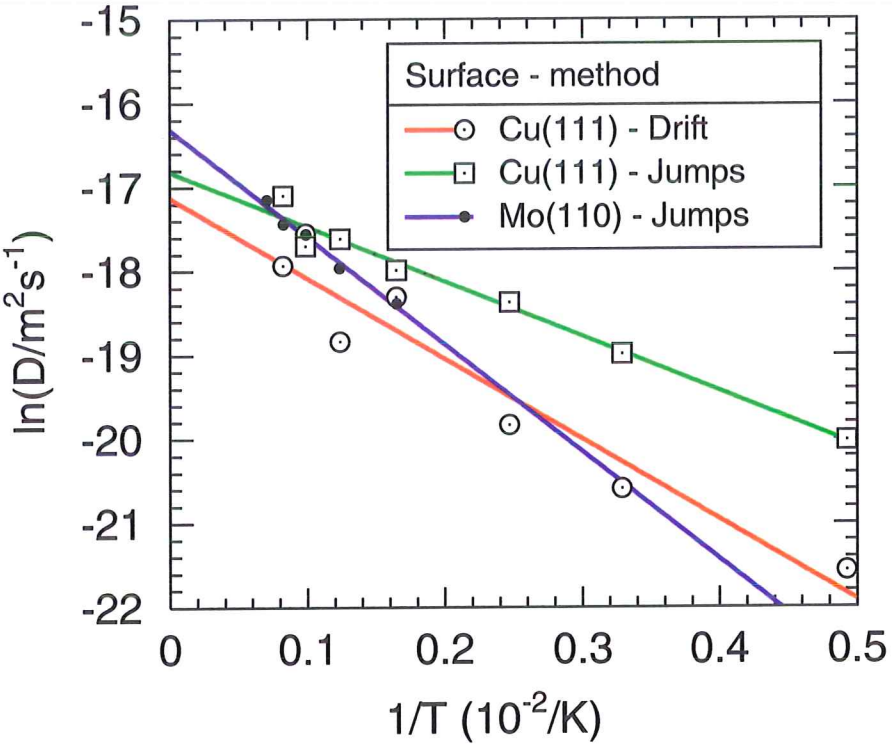

Figure 30: Arrhenius plot of Cu adatom diffusion on a Cu(111) surface (blue, red and magenta lines) and on a Mo(110) surface (green line). The lines for the Cu(111) surface show two methods used for determining the diffusion, with the red line determined from the mean square drift of the atoms and the green line determined from the jump frequency. For Mo, only the jump frequency method is used (blue line).

as well as from the jump frequency. Figure 30 shows the surface diffusion as an Arrhenius-plot. The results for Cu adatom diffusion on Mo are shown here as well.

From the data shown in the figure, we find $Q = 0.057$ eV for the activation energy and $\nu = 3.1 \times 10^{12}$ s^{-1} for the jump frequency in the temperature range of 300–1200 K for the Cu adatom diffusion on a Cu(111) surface. A simulation at 1417 K showed melting, and was not used. These values were determined by counting the number of atomic jumps. When instead the mean square displacement rate of the adatom was used, we found the values $Q = 0.082$ eV and $\nu = 2.1 \times 10^{12}$ s^{-1}, in accordance with reference [2]. In figure 31 two characteristic examples of the diffusion path of a Cu adatom (red line) on the Cu(111) surface are given. The positions of the crystal atoms are the positions at the time of the first configuration. The picture would not be much different with any of the other configurations, as the surface is stable and almost static as compared to the adatom.

Figure 31 shows that at lower temperatures the adatom often has the tendency to move in a, sometimes incomplete, hexagonal orbit around a surface atom, rather than carry out random-jumps, which are only occasionally seen. Less than one percent back-jumps, where the atom moves into the previous

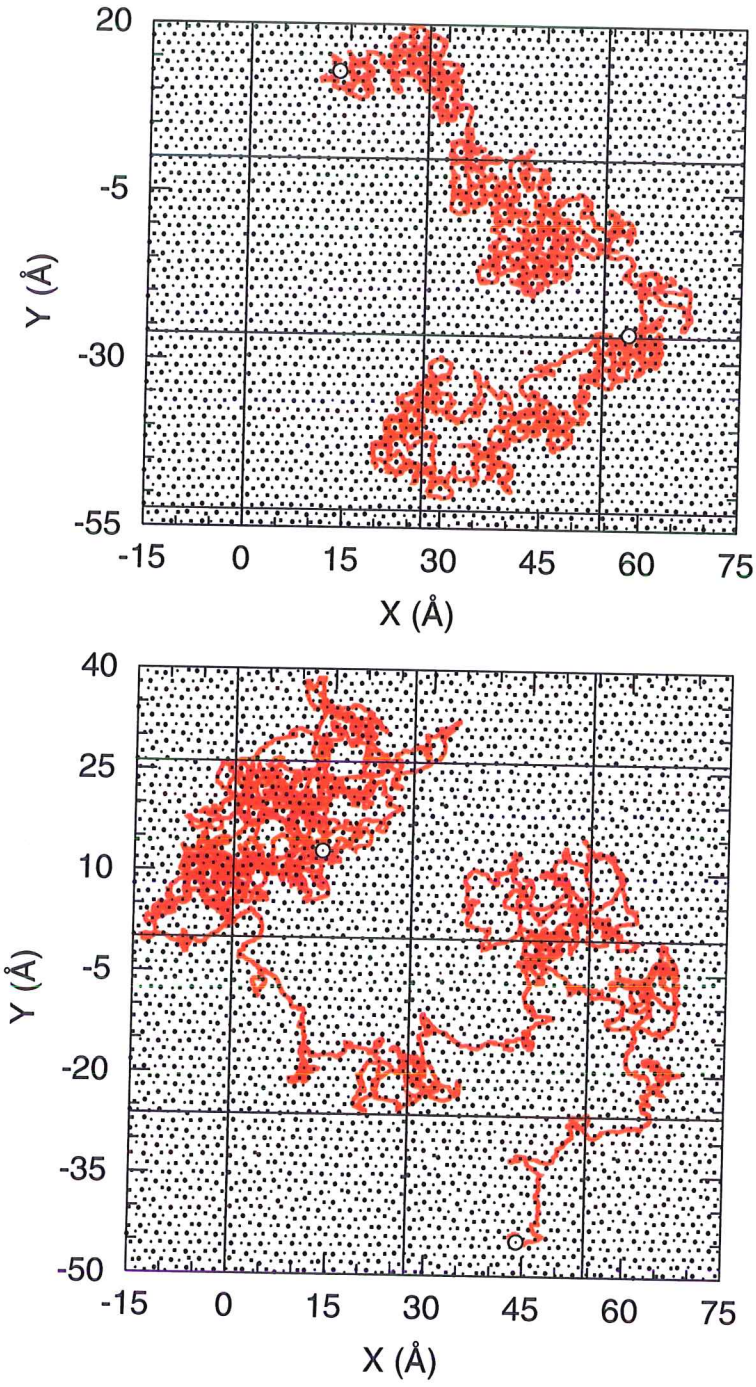

Figure 31: Diffusion path of a Cu atom (red) on a Cu(111) surface at (607±18) K (top) and at (1215±34) K (bottom), recorded during 709 and 497 ps respectively. Only the three top planes of the Cu crystal are shown (from topmost to lowest plane: •, ·, ·). The crystal positions are those of the first configuration, but the picture would not be much different when the positions from any of the other configurations would have been used. At the lower temperature, the atom tends to persist in hexagonal "orbits" around a surface atom. At the higher temperature, the path is much more like that of a random-walk.

position, take place. The hexagonal path is coincident with the surface geometry, see figure 4 on page 27, where a hexagon results from combining six triangles PQR. In between these atoms, a hexagonal path exists that has a lower energy. At the higher temperature, the behaviour tends to that of a random-walk situation, but some multiple jumps seem to take place as well. At lower temperatures, below 600 K, the behaviour is similar as at 600 K. For temperatures that lie between the temperatures in the two shown examples, a transition from correlated motion to random-walk occurs between 800 and $\sim$ 1000 K, or 0.57–0.72 T_{melt} (not shown).

In their EAM MD study of Ag on a Ag (111) surface, Boisvert and Lewis [12] see a low temperature (200 K, ie. 0.16 $T_{melt,Ag}$ [83]) diffusion path for Ag that follows the hexagonal geometry of the surface, but here, the atoms do show a waiting time between jump events, characteristic of random-walk, while we see no such thing between successive steps in the hexagon path. At 700 K, the path superficially may resemble the high temperature behaviour currently observed for Cu, although the shown section of the path is too short to base a definite conclusion on. At 900 K (0.73 $T_{melt,\ Ag}$), Ag moves by a Brownian motion, indicating that at this temperature diffusion is not dependent on the surface geometry. Boisvert and Lewis find a transition in this behaviour between 400 and 800 K (0.32–0.65 $T_{melt,Ag}$). They also conclude that the jump frequency is a better measure for diffusion with an Arrhenius temperature dependency than the drift is.

Kallinteris, Evangelakis and Papanicolaou [43] find from their EAM MD study on Cu at low temperature ($\leq$ 900 K) an activation energy of 0.041 $\pm$ 0.002 eV and a diffusion constant $D_0 = 2 \pm 0.1 \times 10^{-4}\,\mathrm{cm^2 s^{-1}}$. For high T, they report values of $0.087 \pm 0.008\,\mathrm{eV}$ and $7 \pm 1 \times 10^{-4}\,\mathrm{cm^2 s^{-1}}$. Their data shows that at higher temperature exchange begins to play a role, and that an additional jump becomes possible, along $\langle 110 \rangle$, with an energy of 0.1 eV. Above 1100 K, spontaneous creation of adatoms took place. For the 1200 K simulation, *we* observed an exchange event as well. Therefore, at higher temperature, the additional jump mode may play a role in our simulations as well, especially considering the events that appeared to be multiple-jump events. The diffusion path of figure 31, bottom, has several places where this jump might be identifiable.

The foregoing helps us understand why the value for the diffusion constant is remarkably different when determined from the drift or from the jump frequency. The reasons for the memory effect, and the underlying mechanisms, are less clear. We must conclude that at the lower temperatures correlated vibrational motion has significant influence, and that it is too simple to interpret diffusion as a single-atom process, so that the random-walk based model does not apply. Further study is required to obtain a better understanding of the principles involved in this diffusion behaviour, and also to find out if indeed Brownian motion takes place at high temperatures, or if a second jump process becomes activated at high temperature, leading to a differing diffusion behaviour.

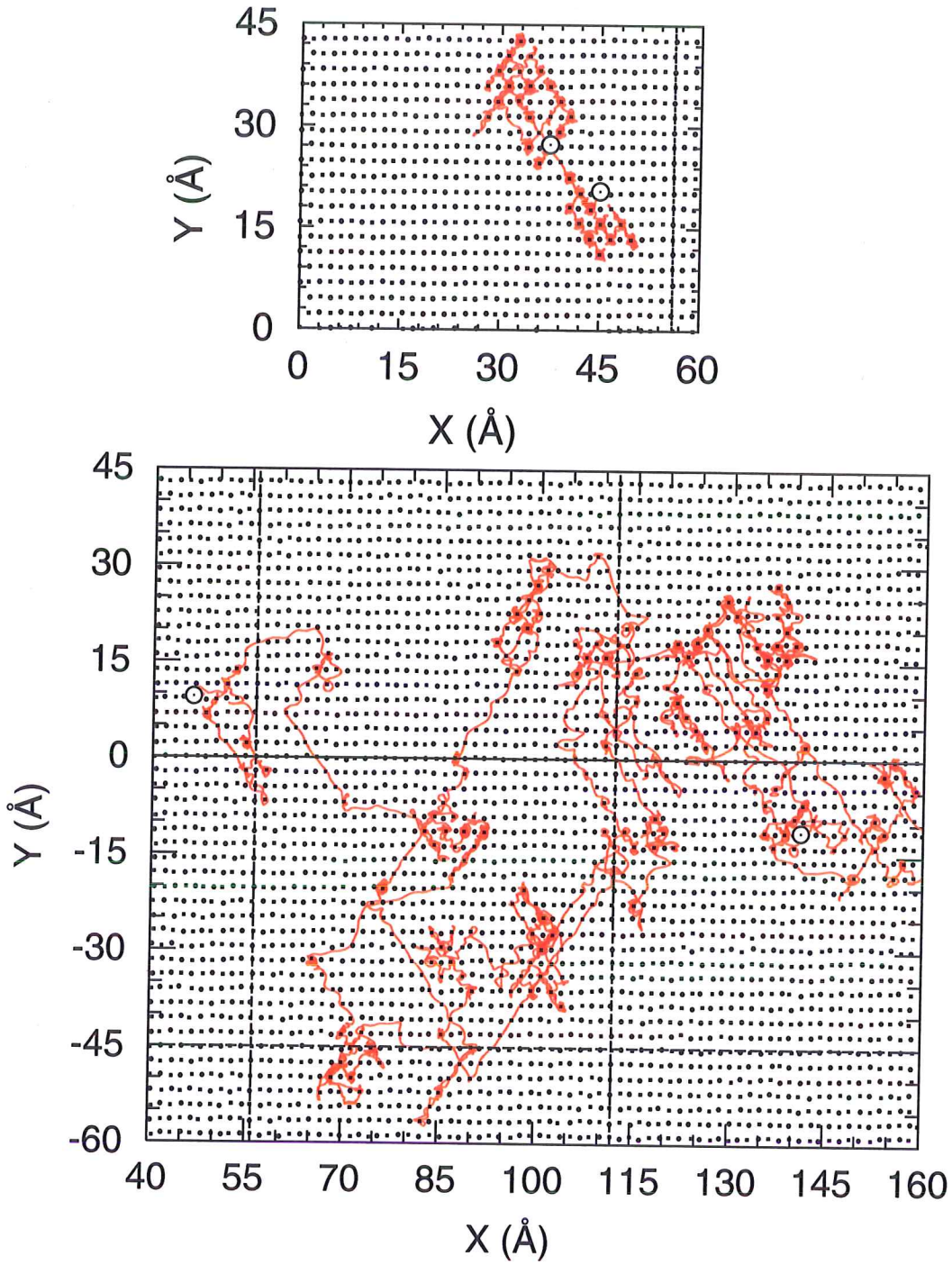

Figure 32: Same as figure 31, but showing the diffusion path of a Cu adatom on a Mo(110) surface at (606 ± 9) K (top) and at (1415 ± 21) K (bottom) recorded during 702 ps. Only the topmost Mo plane (•) and the one below that (·) are shown. At the lower temperature clear jumps can be seen with waiting times in between, indicative of random-walks. For the high temperature case it is more difficult to identify individual jumps.

Diffusion of a Cu adatom on a Mo(110) surface We have also studied surface diffusion of a Cu adatom on a Mo(110) surface, at a range of temperatures. The diffusion parameters are calculated only from the jump frequency, as the drift is less accurate (a positive linear relation between Δt and $\langle \Delta r^2 \rangle$ is not always clearly seen). In figure 30, the data is shown by the green line. The activation energy for Cu adatom diffusion on a Mo(110) substrate is found to be 0.110 eV, with $\nu_0 = 6.6 \times 10^{12}$ s^{-1} ($D_0 = 8.2 \times 10^{-8}$ m^{2}s^{-1}).

For diffusion on this surface we see a more random-walk behaviour than for the surface diffusion of a Cu adatom on a Cu(111) substrate, as clear waiting times can be seen, ie. the "spots" between the jumps, see figure 32. This indicates random-walk behaviour. On this surface, the adatom follows a diamond-shape path, in agreement with the surface geometry as shown in figure 4 by $ABCP$. For the higher temperature case, the individual jumps are more difficult to identify. Double and triple jumps occur frequently. It could be that T is too high here, so that Brownian motion takes place in addition to random-walk behaviour.

Figure 16 (page 55) shows that the binding energy to Mo is higher than to Cu, and that the potential energy well has steeper walls. If indeed Brownian motion takes place at high temperature, the diffusion behaviour should be closer together for the two surfaces, as their geometries no longer have a strong influence on diffusion. In figure 30 this can indeed be seen. Apart from this, on a Mo surface, an exchange mechanism is very unlikely, which simplifies the study of high temperature diffusion of Cu, up to melting of the Cu.

Diffusion of a Cu adatom on a Cu monolayer on a Mo(110) substrate As a next step, we studied the diffusion of a single Cu atom on a Cu monolayer that was deposited on a Mo (110) substrate (see EVAP$_s$ in §4.3), or in short, a Cu adatom on a Cu//Mo(110) surface.

At first thought, it may seem as if this behaviour should be fairly equal to that on a Cu(111) substrate, but on closer examination of the arguments this is not true, due to the influence of the underlying Mo substrate and the fact that the adatom is actually looking at a Cu monolayer that is deposited on this substrate. As a result, the Cu monolayer is not a Cu(111) plane, but instead the layer has a nearly perfect Mo(110) geometry. It is still made up of Cu atoms, so that the mobility should be considerably higher than on the uncovered Mo(110). Furthermore, due to an exchange of the adatom with the monolayer , a phenomenon not observed on a Cu (111) surface, obtaining the adatom diffusivity on this surface is difficult. Figure 33 shows the system in the initial and the final configurations. One can see that several atoms have moved considerably. In addition, the adatom has changed identity eight times. The atoms seem to show two or three clear exchange "chains". This phenomenon requires further study in order to establish the details of the diffusion mechanism at hand. In the deposition simulations, events like these can be expected to take place as well.

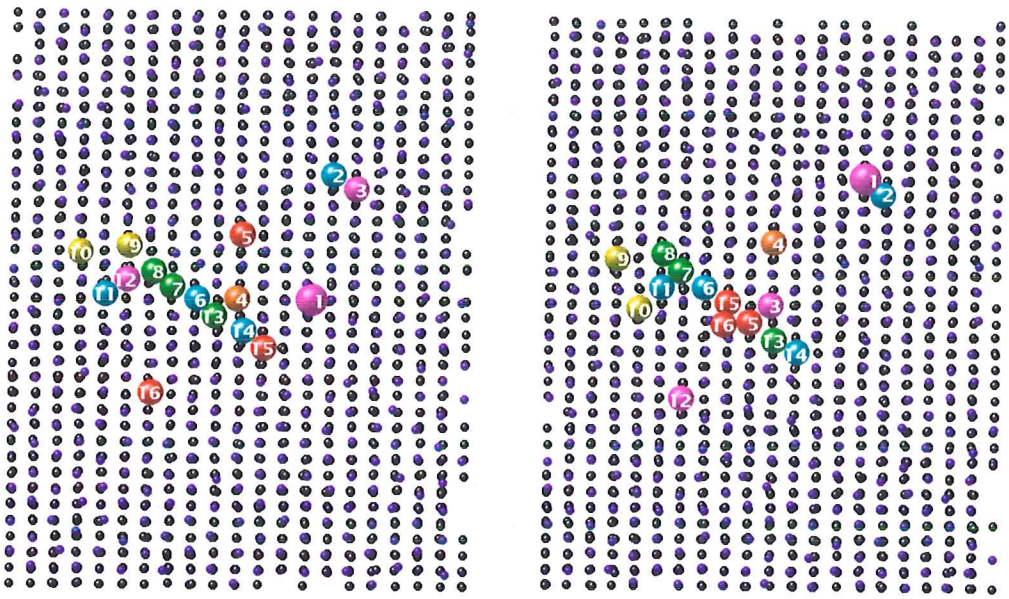

Figure 33: Hard ball view of the simulation of diffusion of one Cu adatom on an as deposited Cu//Mo(110) surface at $T = 1000$ K. The left shows the initial, the right the final configuration after 681 ps. The Mo atoms are black, while the Cu atoms are coloured according to their *net* displacement during the simulation (blue: < 1.5 Å; cyan: 1.5–3.1 Å; green: 3.1–4.6 Å; yellow: 4.6–6.1 Å; orange: 6.1–7.7 Å; red: 7.7–9.2 Å; magenta: > 9.2 Å). The blue Cu atoms and the (black) Mo atoms are made small. Most of them have not moved at all. The original adatom (1) is shown larger than the others. On the right, the (red) atom 16 is now the adatom. Atom 1 replaces atom 2, which replaces 3, etc. Atom 9 becomes an adatom but then replaces 10, etc. Atom 12 again replaces 6, 5 and then 13-15, and 15 again replaces atom 6. This leads to atom 12 again becoming an adatom, eventually replacing atom 16. The system size is $x \times y = 18 \times 10$ unit cells or 56.65×44.51 Å^2 (see substrate "s" in table XIII on page 74).

4.2 Deposition of Cu on a Cu(111) substrate

The first Cu deposition run, EVAP_{Cu1}, see §3.4, page 71, started at a temperature of 200 K. Note that this temperature is very low considering the arguments concerning time versus temperature, §2.4.

The deposited film at first shows a very rough surface. Figure 34, which shows a side view of the film with the atoms coloured according to their symindex S (see §3.2.8, §3.2.8), and figure 37 (left), which shows a view from the top of the simulation box, with the atoms coloured by their z-plane clearly illustrate this. Calling into attention again §2.4, the observed surface profile can be explained, as the applied deposition rate, in combination with this low temperature only leave room for low activation energy processes. With $t_{mono} = M/\alpha_t = 383$ ps (see table XII, page 71), bulk vacancy diffusion will not occur ($N_{vac.jump} = 10^{-15}$, equation (47)), and surface diffusion is only limited ($N_{surf.jump} = 44.5$ assuming Cu{111} surface facets).

In addition to the roughness profile a very interesting stacking-fault system can be seen in figure 34, where the atoms are locally hcp (red) instead of fcc (green), see 3.2.8. These regions are "terminated" by atoms that are marked as bcc (blue). One can see that already the first deposited plane has a stacking-fault region.

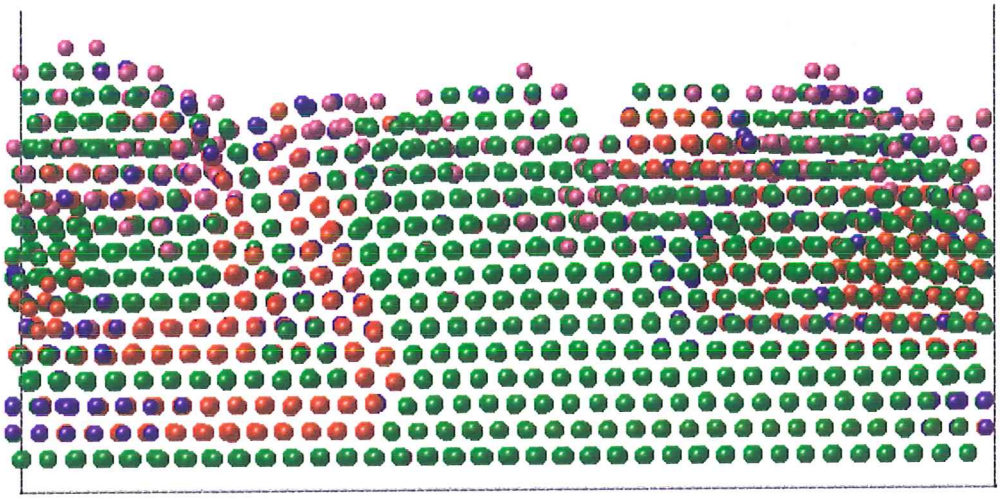

Figure 34: Side view of the copper deposition box after ~ 20.0 Å of Cu deposited. The two lowest planes are the substrate. The y-direction points to the left, the x-direction points out of the paper. The atoms are coloured by the symindex S. Note the complex stacking-fault, where the structure locally resembles the hcp structure, instead of fcc. As T is already very low, this figure is from a non-quenched configuration.

The deposited planes contain 1050 atoms, as opposed to the 1080 atoms in the substrate planes (a 97.2% relative atom-density). The difference is caused by the complex stacking-fault, with one atom row parallel to the stacking-fault missing. Figure 35 shows top views of this defect. Because of the creation of a stacking-fault parallel to the x-axis, the density along the y-axis is decreased by an atom (row), or a factor of $36/35 = 1.02857$. The density along the x-direction

remains the same. The lower plane-density is a result of the fact that our Cu is slightly bigger than real Cu ($\Omega_{300\mathrm{K}} = 12.246$ Å^3, so $r_1^{eq,300\ K} = 2.578$ Å, or 1062 atoms per plane versus the assumed $\Omega_{\mathrm{lit}} = 11.81$ Å^3, $r_1^{eq} = 2.556$ Å). At the start of the simulation, the impact of this was not fully realized, so that the substrate was created using the experimental Cu lattice constant (and the significance of the high pressure was not given enough consideration). The box is therefore smaller than the size would be if it had been equilibrated using pressure control in the lateral directions. The lateral dimensions are held fixed so that a simple expansion is impossible. The growing system tries to minimize its energy by finding alternatives to an overall lateral compressive stress. The stacking-fault is energetically favoured.

When the temperature is increased to 1100 K the atomic size increases to $\Omega_{1100\mathrm{K}} = 12.97$ Å^3 or $r_1^{1100\ \mathrm{K}} = 2.637$ Å (see figure 26) equating to 1015 atoms per plane. Two events are seen to take place. Firstly, we see a shear of the planes. The rows of Cu atoms that are not bound to anchor points, ie. all deposited atom rows rotate over an angle of arctan $\left(r_e^1/\left(2L_y\right)\right) \simeq 0.92°$, so that in the y-direction the atoms fit to the next atom row in the adjacent image-box (half a unit cell), such that the periodic boundary conditions remain fulfilled. In the y-direction, one atom row still misses. In the planes above the third, the x-direction also misses two rows (one cell). As a result, the distances along the x-direction of planes $k > 3$ are increased by a factor $30/29 = 1.0345$, while the distances in the y-direction are a factor $36/\left(35\cos\theta\right) = 1.0287$ larger than in the substrate for all deposited planes. The shear distortion adjusts the y-direction Cu-Cu separation of all cells so that the large stacking-fault that existed parallel to x is no longer needed for $k > 1$. Along the box y-axis, a stacking fault is created in planes $k = 2, 3$, in combination with two "head-to-head" (partial) dislocations to make sure that the sheared plane also fits in this direction. The higher planes have the above described number of atoms, with the rotated atomic rows. The complex stacking-fault is reduced in size from the initial defect seen in figure 34 (and figure 35), especially in the out of plane direction, and is now concentrated in the lower three deposited planes. Figure 36 show the dislocations and the stacking-fault, as well as the the clear θ rotation. As expected, the in-plane shear stresses σ_{44} are lowered due to the change in structure, while σ_{xx} and σ_{yy} do not undergo a clear net decrease.

A second effect of increasing the temperature is that the surface becomes much smoother, see figure 37, right, as compared to the left hand side. This is not surprising. At this temperature, the (bulk) vacancy diffusion is activated, with $N_{vac.jump} = 7.4$ and vacancies present, and surface diffusion, including all its irregularities, is greatly enhanced ($N_{surf.jump} = 651$). The defect in the first three planes may also enable diffusion along fault lines.

Another Cu deposition run, EVAP$_{Cu2}$, was performed using a smaller simulation box of 44.275×40.899 Å^2, see table XII on page 71. Because of the smaller system size, we have deposited a film of up to ~39 Å. The temperature was set to 1214 K. As can be seen in figure 25, or 38, the actual temperature was much lower, starting at $\sim$ 600 K and slowly increasing to about 800 K at 2.8 ns, after which the new temperature control that was introduced resulted in a rapid increase of the temperature to about 1110 K, accompanied by the

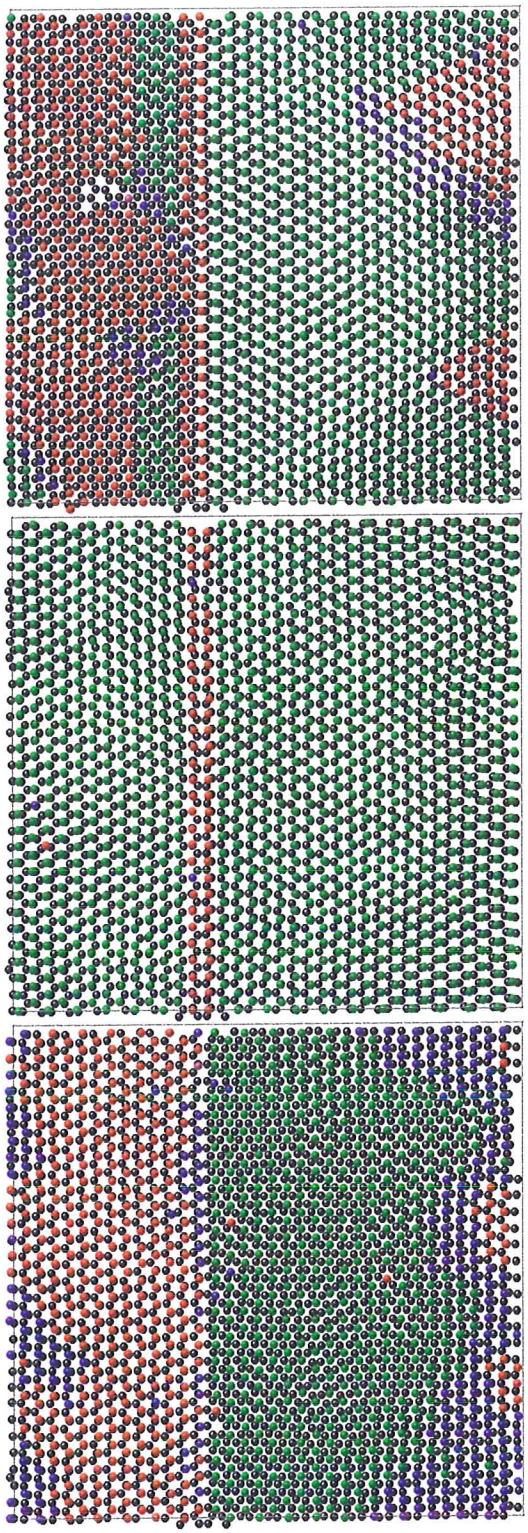

Figure 35: Top views of the the first three deposited planes (bottom to top: first, second and third deposited plane) from the EVAP$_{Cu1}$ simulation. The atoms are coloured by S (fcc: green; hcp: red and bcc: blue, see §3.2.8). The two substrate planes are shown in black underneath each of the three planes. The first two deposited planes have 1047 atoms, and three vacancies, the third plane only contains 1044 atoms, but is not completed yet. The side viewed in figure 34 is the bottom side in each of the views above. As T is already very low here, this figure is from a non-quenched configuration.

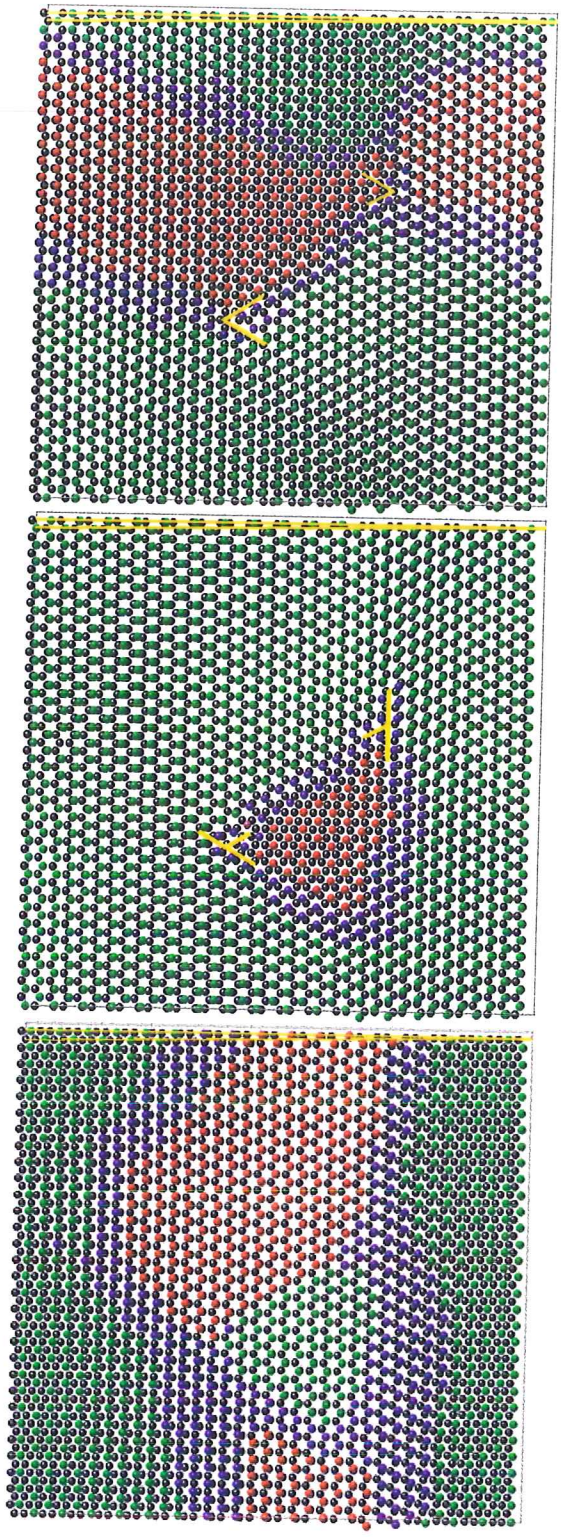

Figure 36: Top views of the first three deposited planes (bottom to top: first, second and third deposited plane) from the EVAP$_{Cu1}$ simulation. The atoms are coloured by S (fcc: green; hcp: red and bcc: blue, see §3.2.8). The two substrate planes are shown in black underneath each of the three planes. This figure shows the same as figure 35 but then after increasing the temperature. For all three planes, the y-atom rows make an angle of 0.92° with the simulation box. In the second and third plane, the positions of the two partial dislocations are indicated. The three planes contain 1050, 1038+1 vacancy and 1039 atoms. The completed $k > 3$ planes now contain 1015 atoms.

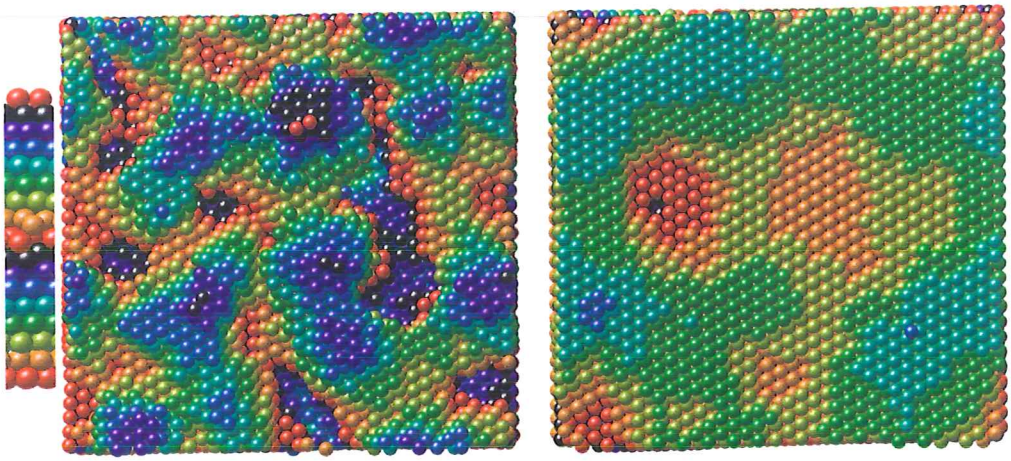

Figure 37: Top views of the simulation box of EVAP$_{Cu1}$ before (left, $T \simeq 200$ K) and after increasing the temperature (right, $T \simeq 1150$ K). The x-direction is shown vertically, y is horizontally (see table XII). On the far left, the height colouring-scale is shown in a vertical cross-sectional view. The right figure is made using a quenched configuration, the left system was already at low enough temperature.

development of a smoother surface like for the larger system. After increasing the temperature, the film remains very flat, with an RMS surface roughness of approximately 1 Å up to a coverage of at least 34 monolayers ($D \sim 80$ Å, not shown).

Just like in the first simulation, the box was too small to allow an unstrained Cu film. With the increase of the temperature, here too, the atom rows are rotated around the z-axis over such an angle that the periodic boundary conditions are still fulfilled, but leaving out several atom rows. As this is a smaller box, the angle has to be larger ($\sim 3.5°$) than for the first Cu deposition simulation. The planes have $\sim$ 295 per plane instead of the 320 atoms of the original planes. The planes above $k = 2$ consist of 10 rows of 16 atoms and 9 rows of 15 atoms instead of 20 rows of 16 atoms each, missing one row in the x-direction. Here too, a complex stacking-fault develops to relief the strain due to the rotation. We can see a combination of a "flat" plane stacking-fault, and a small stacking-fault defect at an angle of 60° to the planes, resembling what is seen in the larger system. Somewhat higher another in plane stacking-fault is created, giving the film a microtwin-like texture over the thickness. The higher planes are rotated over the same angle as the lower planes and contain no stacking-fault defects.

Summarizing, the copper simulations have shown that at a flat Cu(111) film grows on a Cu(111) substrate, provided that the temperature is sufficiently high to allow both surface and bulk diffusion. Various unfortunate simulation conditions make it difficult to conclude on the degree of defects in such a film. Point defects seem to be absent, but it is unclear if twinning and stacking-faults will be found under better circumstances. In the possibly strained Cu on Mo films, it is likely that stacking-faults are used to relieve strain.

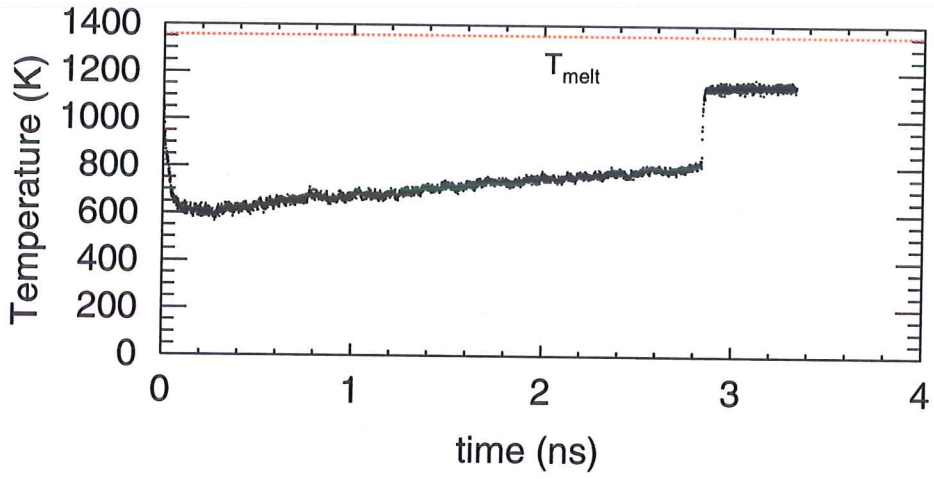

Figure 38: Temperature in Kelvin during the EVAP$_{Cu2}$ deposition run. The red line is the melting point of Cu as found from literature (for instance, [83]), at 1356 K. For these thin films, using our our interaction potentials, it appears that the melting temperature may lie closer to 1300 K (see §4.1) shown). This figure is the same as figure 25.

4.3 Deposition of Cu on a Mo(110) substrate

Knowing the Mo and Cu atom size (table V on page 47, and table XV in §4.1.1), the elastic constants (§4.1.3) and the Cu on Mo (110) surface diffusion energy (§4.1.7 on page 86), the value for the relative interaction between the substrate and film, ℓ, can be calculated from equation (57) on page 34. With the values from §4.1, this results at 1000 K in a value of:

$$\begin{aligned} \ell_{1000\text{ K}} &= \frac{1.2\,\Omega_{\text{Cu}}(c_{11}^2 - c_{12}^2)/(2c_{11})}{Q_{surf.diff} r_{\text{m}}^2} \\ &= \frac{1.2 \cdot 12.877\ \text{Å}^3\,(145^2 - 98^2)/(2 \cdot 145) \cdot 10^9\,\text{Pa}}{0.110\ \text{eV} \cdot 0.96526^2} = 5.94. \end{aligned}$$

Looking at figure 10 on page 35, this seems to be a rather large value, but it is close to the literature value of $\ell_{lit} = 5.88$ (see the end of §2.5.1). This small difference is attributable to a decrease in elastic constants c_{11} and c_{12} at this temperature, in combination with ℓ being proportional to Ω/r_{m}, which is higher at this temperature. Anyhow, from this ℓ and figure 10 it is still predicted that our films will initially be growing pseudomorphic, but only up to very low coverages ($\Theta < 0.57$), and then switches to an NW-x orientation relation, which is stable up to very large thickness at this mismatch value.

Although the results of the Cu/Mo(110) simulations differ in many details, they have several features and general trends in common. Not surprisingly, the initial phases of all simulations show many similarities. One of these is the growth mode and its change with coverage (thickness). This evolution is described first. Then, the discussion focuses on the development of the crystal structure and defects. For this, the focus will be shifted more towards differences between the simulations.

staircase figs.

The figures 39–43 are useful in the discussion of the growth mode and structure evolution. These figures show bird-eye views of successive configurations from the simulations, with the coverage/thickness increasing from bottom to top. The lowest coverage shown ($\Theta = 0.1$, $D = 0.2$ Å) is taken just after the start of the deposition, showing individual Cu clusters on the Mo(110) substrate. The Cu atoms are coloured according to the height above the substrate (see §3.2.5), the Mo atoms are black. For the large systems, the first Cu plane is greenish, the second is blueish, the third blue, the fourth red, and so on. The small systems use the same set of colours, but start with a different colour: blue for the first plane, red for the second, etc.. The next two coverages ($\Theta \simeq 1$ and $\Theta \simeq 3$) have the same colouring scheme. For the higher coverages, the Cu atoms are coloured according to their symindex S, indicating the local crystal geometry around the atoms (see §3.2.8). The Mo atoms remain black. In this later stage, the differences between the simulations increase and become clearer. In the following, these figures will be referred to as "staircase" figures. In addition to these, other figures are used to illustrate different features of the films, like the roughness.

Near the end of the section the simulations are compared by means of several features of the films, like amount of sputtering, intermixing, the mean volume and (potential) energy, etc..

4.3.1 The first deposited monolayer of Cu

In figure 44 one can see that locally, the substrate atoms are in a less favourable energetic state (higher potential energy) when one or more Cu atoms are close by although the energy of the system is still lowered by the adsorption of the atoms.

Initially, at the start of growth, the Cu atoms on the Mo surface can move around quite freely after impact. With a time t_{mono} of about 400 ps ($1/\alpha_{\Theta}^{eff}$ from table XIV) and the values for Cu on Mo adatom diffusion from §4.1.7, we find the number of jump events to be $N \sim 75$ per 0.1 monolayer of coverage. However, from lateral displacements of the atoms (at the end of the simulation), we find an effective diffusion time of only 7 ps.

adatoms

The adatoms often encounter other Cu atoms. When this takes place, they will form a dimer (or multimer). The dimers are quite mobile and a large number either breaks up or forms larger groups of atoms. In the staircase figures, adatom clusters can be seen at the lowest coverage ($\Theta \sim 0.1$). One observes that the adatoms conform to the substrate geometry. In addition to diamond shaped clusters ($ABCP$ in figure 4 on page 27), linear chains are seen along the bcc $\langle 111 \rangle$ directions (AB, BC etc. in figure 4). When tri- or other multimers are formed, these will grow and cluster to eventually form small compact groups of atoms. Later, as more atoms group together and form clusters in excess of four atoms, these clusters become immobile, with only edge-atoms attaching and detaching. At this coverage, the clusters start to coalesce and begin to form the first monolayer. Figure 45, comparing the positions of atoms at $\Theta = 0.2$ and at $\Theta = 0.3$ illustrates the described behaviour. We see clusters of atoms with a static "core", surrounded by atoms that attach or

immobile clusters

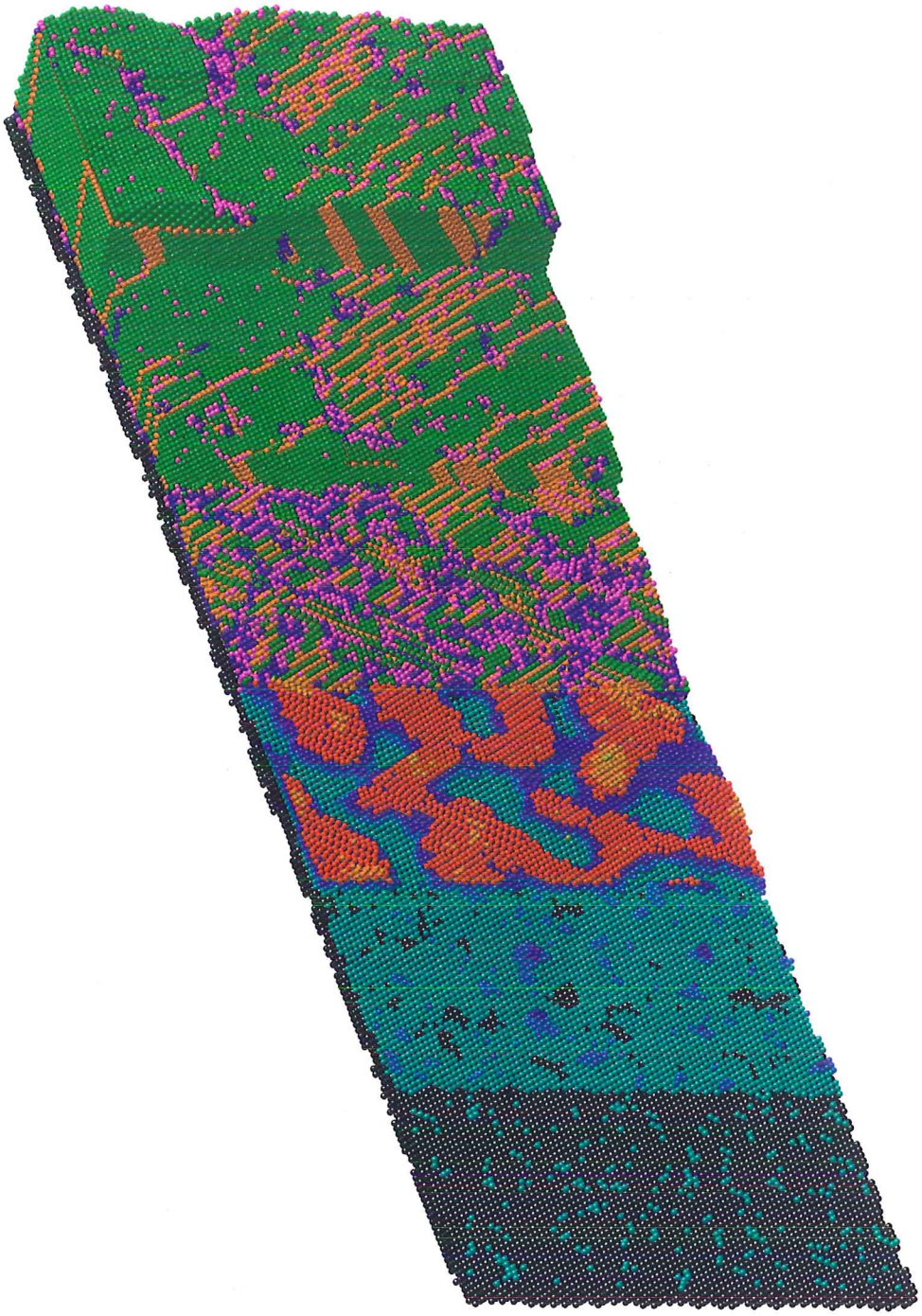

Figure 39: Six stages in the thermal deposition (EVAP) of a Cu film on Mo(110). Shown is the EVAP_{b1} run of table XIV. From bottom to top, the thickness increases: $\Theta = 0.10$, $D = 0.21$ Å; $\Theta = 1.10$, $D = 2.25$ Å; $\Theta = 3.36$, $D = 7.48$ Å; $\Theta = 4.89$, $D = 10.88$ Å; $\Theta = 9.44$, $D = 21.00$ Å; $\Theta = 23.94$, $D = 53.27$ Å. At the three highest coverages, the atoms are coloured by their symindex S (see §3.2.8), the three lower coverages are coloured by plane-height above the substrate (see §3.2.5).

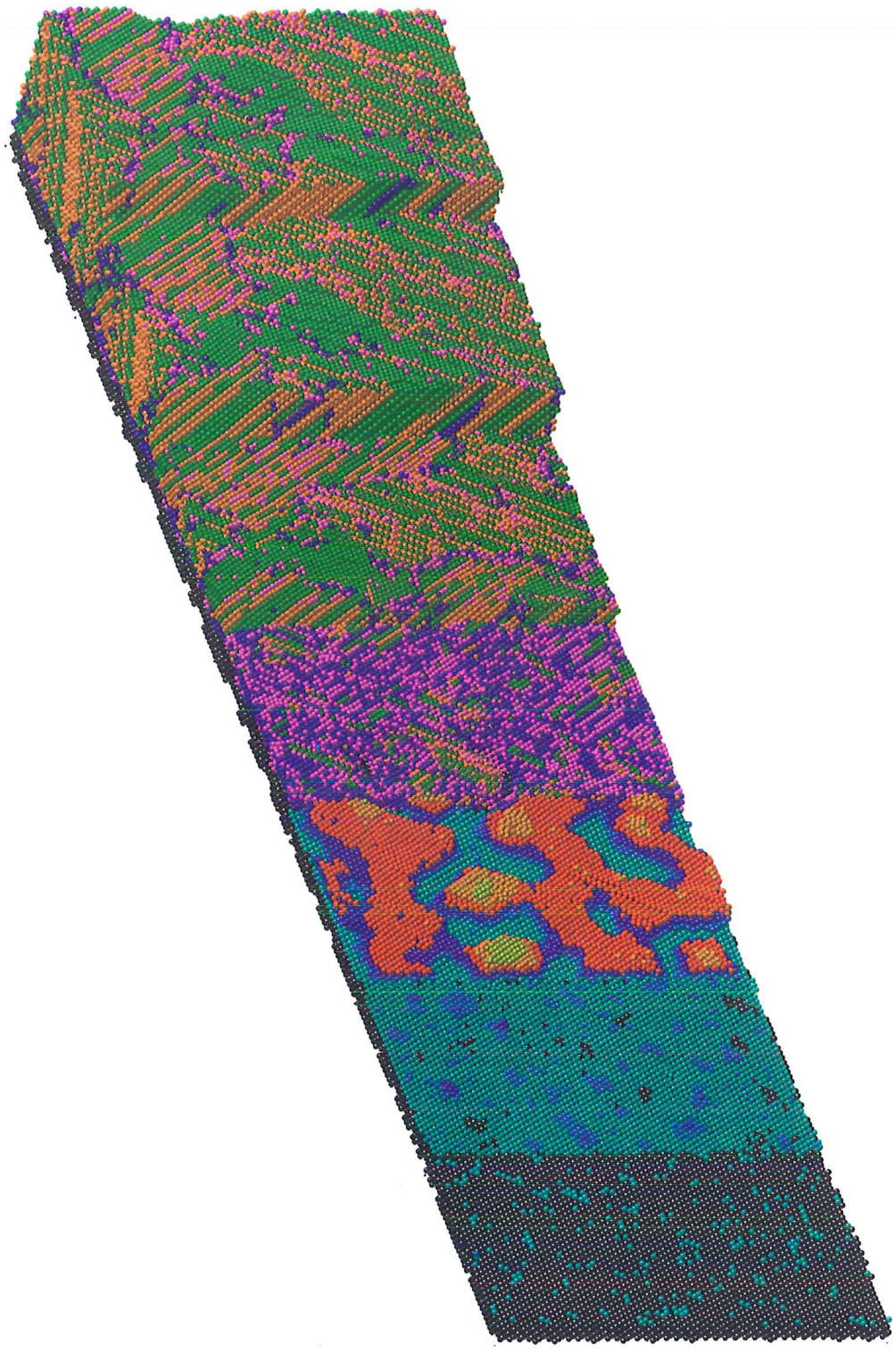

Figure 40: Seven stages in the thermal deposition (EVAP) of a Cu film on Mo(110). Shown is the EVAP_{b2} run of table XIV. From bottom to top, the thickness increases: $\Theta = 0.10$, $D = 0.21$ Å; $\Theta = 1.20$, $D = 2.65$ Å; $\Theta = 3.36$, $D = 7.48$ Å; $\Theta = 4.89$, $D = 10.88$ Å; $\Theta = 9.43$, $D = 21.98$ Å; $\Theta = 24.42$, $D = 54.34$ Å; and $\Theta = 34.31$, $D = 76.35$ Å. At the four highest coverages, the atoms are coloured by their symindex S (see §3.2.8), the three lower coverages are coloured by plane-height above the substrate (see §3.2.5).

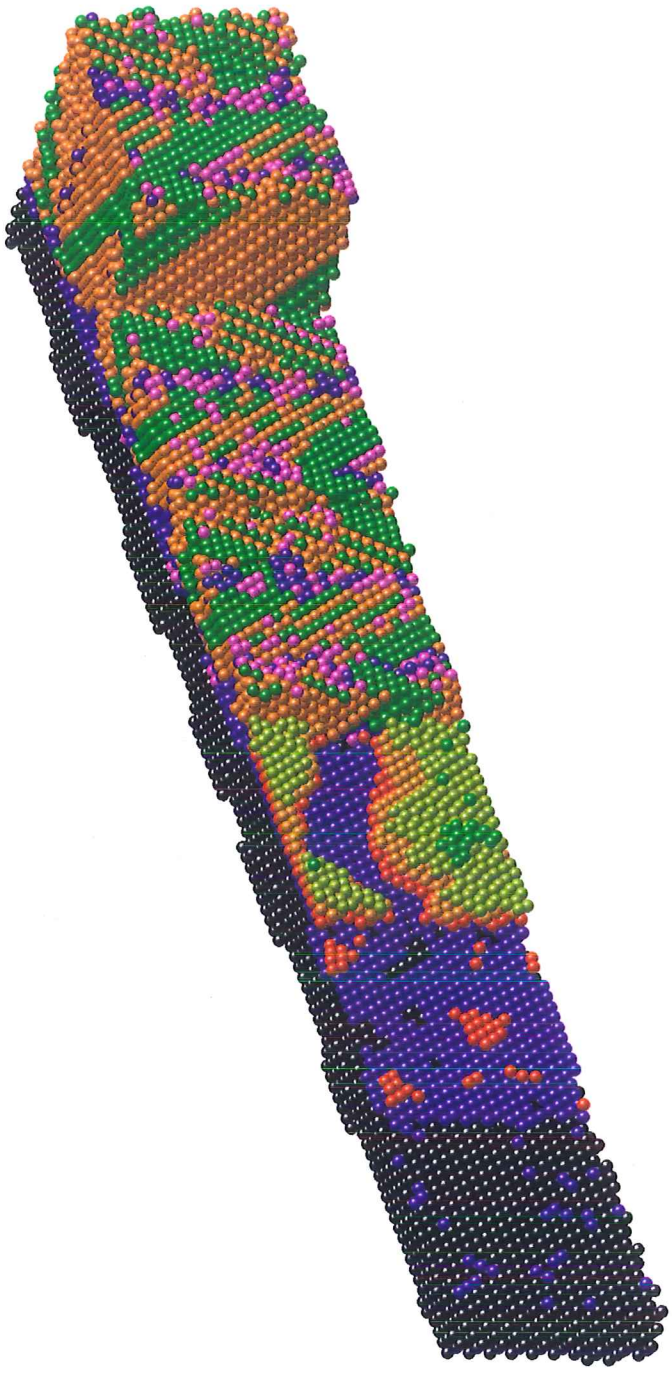

Figure 41: Six stages in the thermal deposition (EVAP) of a Cu film on Mo(110). Shown is the EVAP_s run of table XIV. From bottom to top, the thickness increases: $\Theta = 0.09$, $D = 0.21$ Å; $\Theta = 1.06$, $D = 2.36$ Å; $\Theta = 3.21$, $D = 7.13$ Å; $\Theta = 4.98$, $D = 11.09$ Å; $\Theta = 9.99$, $D = 22.22$ Å; $\Theta = 24.06$, $D = 53.54$ Å. At the three highest coverages, the atoms are coloured by their symindex S (see §3.2.8), the three lower coverages are coloured by plane-height above the substrate (see §3.2.5). The colouration scheme is the same as for figures 39, 40 but with the height-colours starting with red and blue for the first and second Cu plane.

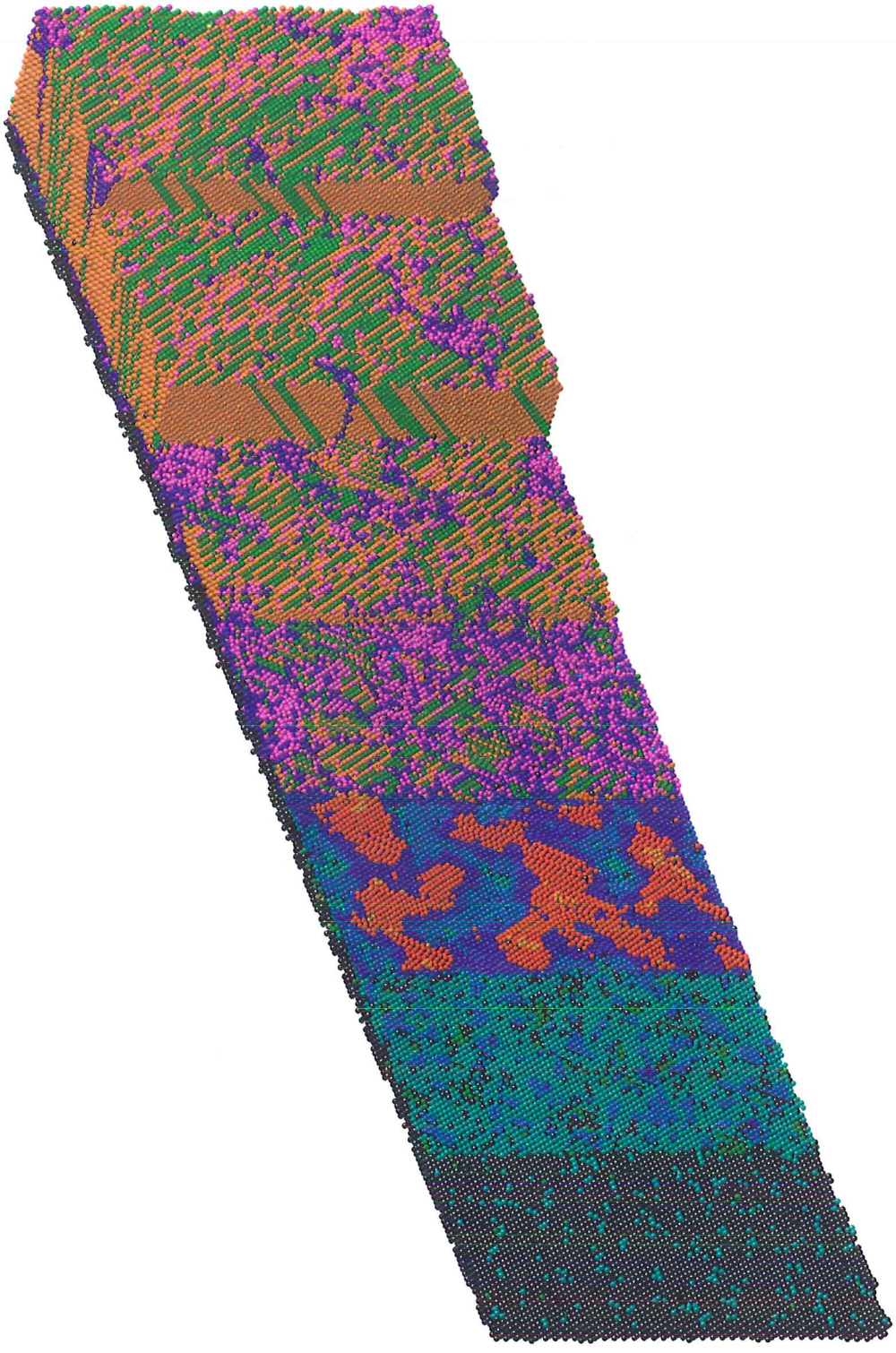

Figure 42: Seven stages in ion assisted deposition (IBAD) of a Cu film on Mo(110). Shown is the $\mathrm{IBAD_b}$ run of table XIV. From bottom to top, the thickness increases: $\Theta = 0.09$, $D = 0.20$ Å; $\Theta = 1.09$, $D = 2.42$ Å; $\Theta = 3.23$, $D = 7.18$ Å; $\Theta = 5.02$, $D = 11.17$ Å; $\Theta = 9.365$, $D = 20.84$ Å; $\Theta = 23.92$, $D = 53.23$ Å; and $\Theta = 33.77$, $D = 75.16$ Å. At the four highest coverages, the atoms are coloured by their symindex S (see §3.2.8), the three lower coverages are coloured by plane-height above the substrate (see §3.2.5). The colouration scheme is the same as for figures 39, 40, but the figure also shows Cu atoms within the substrate (green).

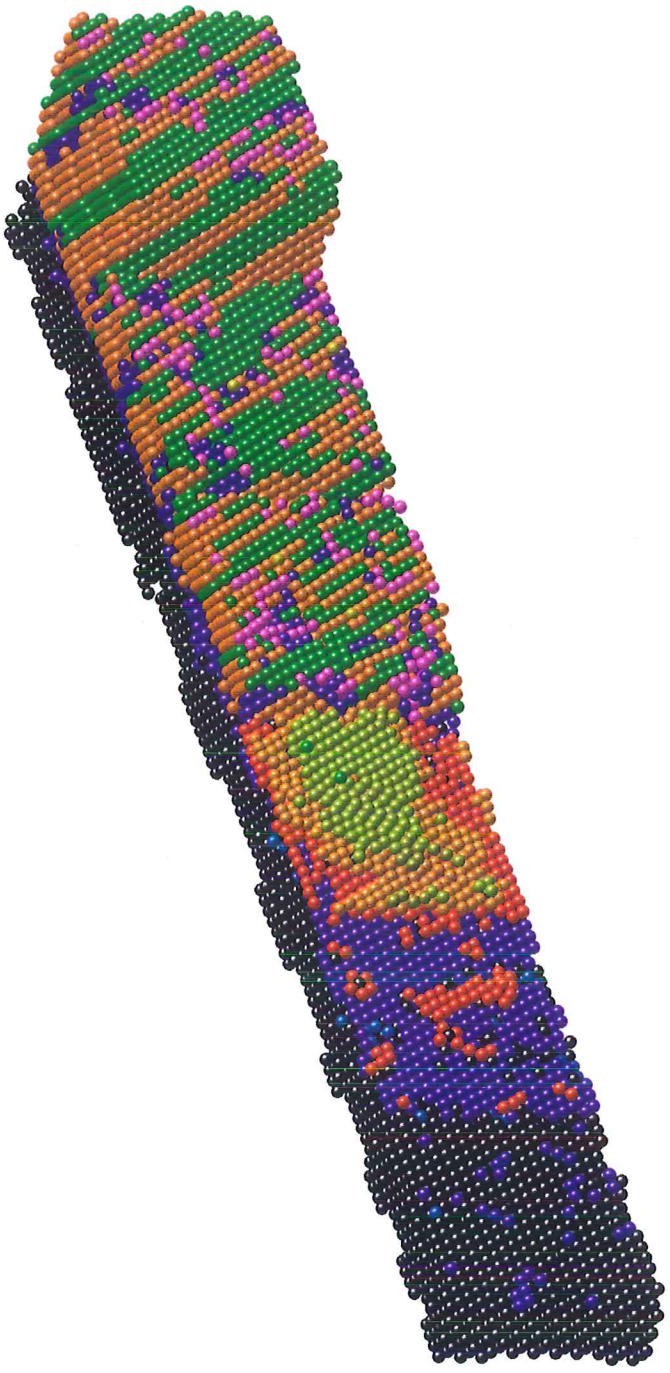

Figure 43: Six stages in ion assisted deposition (IBAD) of a Cu film on Mo(110). Shown is the small IBAD_s run of table XIV. From bottom to top, the thickness increases: $\Theta = 0.11$, $D = 0.24$ Å; $\Theta = 1.13$, $D = 2.51$ Å; $\Theta = 3.24$, $D = 7.22$ Å; $\Theta = 5.02$, $D = 11.17$ Å; $\Theta = 9.42$, $D = 21.98$ Å; $\Theta = 24.55$, $D = 54.63$ Å. At the three highest coverages, the atoms are coloured by their symindex S (see §3.2.8), the three lower coverages are coloured by plane-height above the substrate (see §3.2.5). The colouration scheme is the same as for figure 41 but the figure also shows Cu atoms within the substrate (blueish).

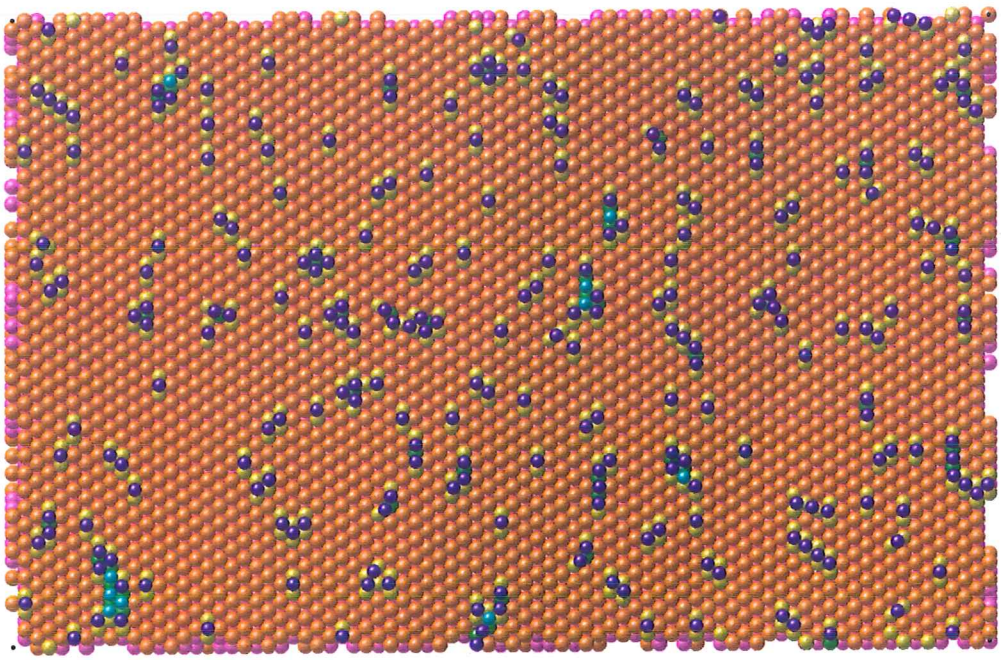

Figure 44: Early stages of the deposition (top view), showing Cu adatoms forming clusters on the Mo surface. The atoms are coloured by potential energy (magenta: -6.85 – -6.45 eV; orange: -6.04 – -5.63 eV; yellow: -5.63 – -5.22 eV; green: -5.22 – -4.80. eV; cyan: -4.80 – -4.41 eV; and blue: -4.41 – 4.00 eV). The bulk of the substrate is magenta, with the surface being orange. Cu adatoms are mostly blue, but some are cyan, depending on the proximity of other adatoms. Characteristic patterns of yellow and green Mo atoms are visible underneath the adatoms. The figure shows a (quenched) configuration of $\mathrm{EVAP}_{\mathrm{b1}}$, at a coverage of ~ 0.1 (272 atoms). This configuration is the same as the first step in the $\mathrm{EVAP}_{\mathrm{b1}}$ staircase, figure 39.

detach from it, or move along the edges of the cluster. The single adatoms have moved the largest distances, but dimers have also moved. Most tri- and dimers are incorporated in clusters of atoms, or have grown in size to groups of four or more atoms. From the figures we can conclude that the critical nucleus for growth of immobile clusters on Mo{110} is 4–6 atoms.

critical nucleus for clusters

The rapid formation of the adatom clusters explains how the diffusion of single adatoms is limited. The clusters are not as mobile as single adatoms, so overall diffusion is lowered. We do find however, that after the clusters grow together, the atoms are mobile within these larger clusters or two-dimensional island, see figure 45. Eventually, atoms initially forming di- or multimers may have moved some 15 Å apart when the monolayer is finished, and at the end of our simulations, at least one former pair of atoms was found 25 Å apart, with only one of the atoms remaining in the first plane, and the other in the third plane. Other data confirms this high mobility in the bulk part of the film. The reader is referred to figures 50–54(c), where the low-z part of the horizontal axis shows the mobility within the first few planes (during the entire simulation). These atom-history plots are discussed at a later stage.

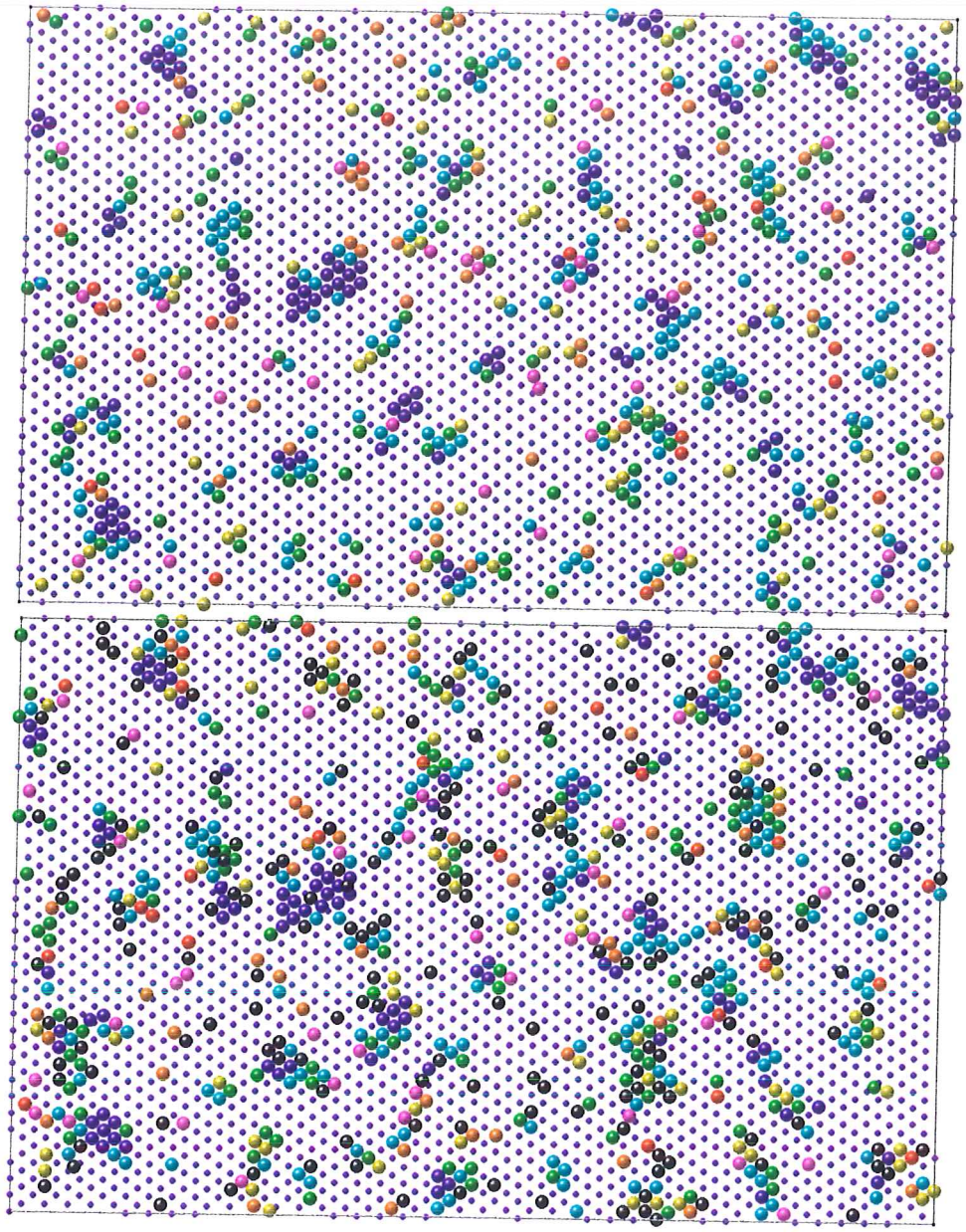

Figure 45: Overlay of the first Cu plane ($k = 1$) and the next-to-last (Mo) substrate plane ($k = -1$, smaller dots) from the EVAP_{b1} simulation. The top shows the positions of the atoms at $\Theta = 0.2$, the bottom the positions at $\Theta = 0.3$. Cu atoms at positions directly above a $k = -1$ atom are in pseudomorphic (bcc) positions. The atoms are coloured according to their *net* displacement between the two configurations. Colour-scale: blue: < 2.15 Å, includes all Mo; cyan: 2.15–4.3 Å; green: 4.3–6.4 Å; yellow: 6.4–8.6 Å; orange: 8.6–10.7 Å; red: 12.9–15.0 Å; magenta: > 15.0 Å; black (bottom): not a film-atom in the top configuration. The minimum jump-distance $\lambda = r^{eq}_{MoMo,1} = 2.726$ Å) so blue atoms have moved less than λ and each successive colour represents (about) one extra jump (however, keep in mind that we only see the atoms net movement). Groups of atoms in the first cofiguration (top) in which the atoms have a different colour may have broken up in the one at the bottom. If the atoms have colours that are adjacent (in scale), the groups may have rotated.

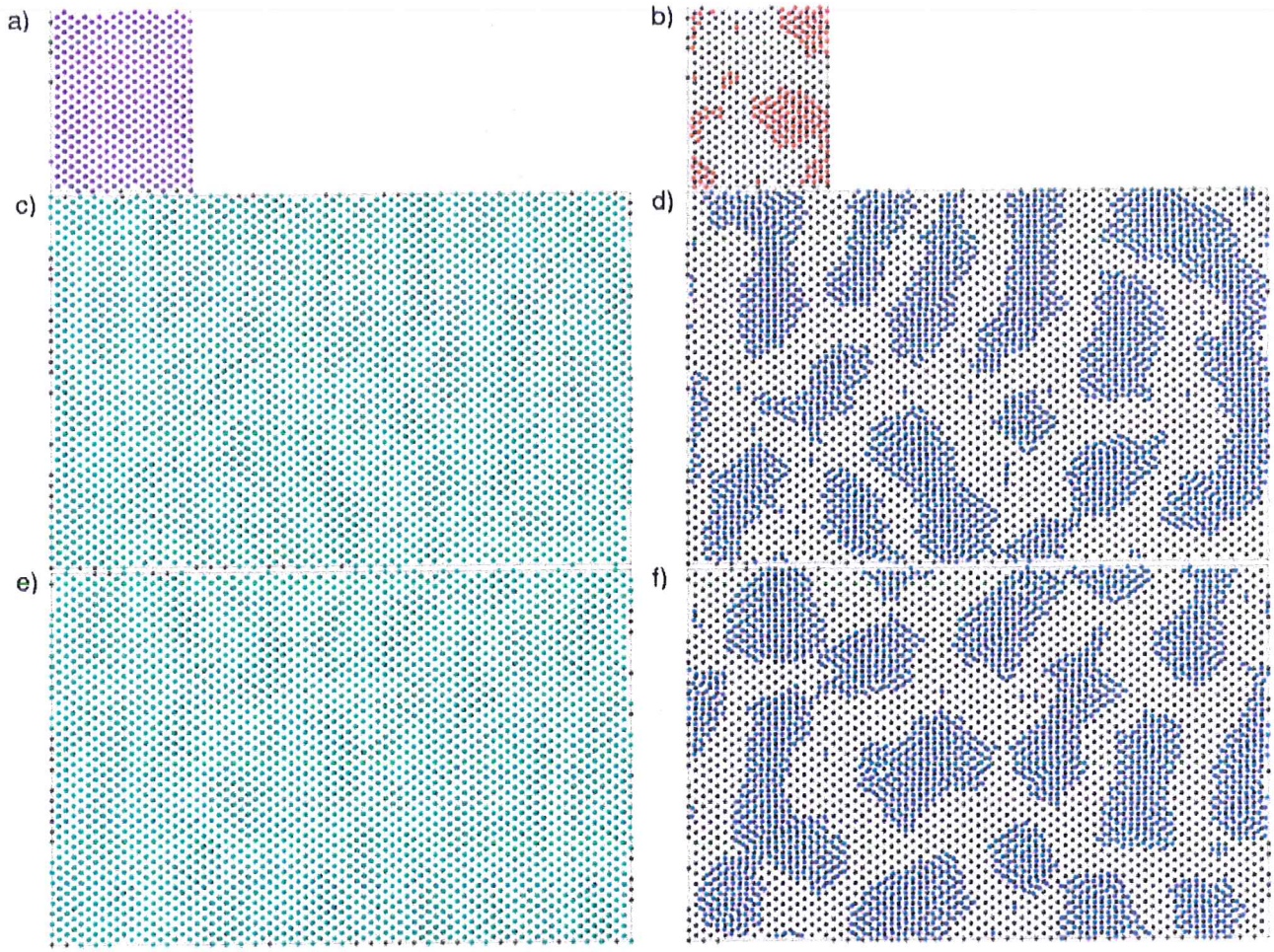

Figure 46: Overlay of the first Cu plane (blue/greenish) and the next-to-last (Mo) substrate plane (black) on the left. On the right the same substrate plane is shown, but with the second Cu plane (red/blueish). From top to bottom, the three different EVAP simulations are depicted (**a**,**b**: $\mathrm{EVAP_s}$; **c**, **d**: $\mathrm{EVAP_{b1}}$; and **e**, **f**: $\mathrm{EVAP_{b2}}$). The coverage is such that the first Cu plane is fully completed, at $\Theta = 1.59$ for the small system and $\Theta = 2.01$ for the two large. The figures use cooled configurations. Note that on the left, the Mo atoms are mostly invisible. See the text for a further explanation.

a Cu monolayer

The first Cu monolayer forms a pseudomorphic bcc(110) layer, almost perfectly following the geometry of the substrate, see figures 46 and 47.

These figures show the next-to-last substrate plane in black, together with the first Cu plane (left) or the second Cu plane (right). At this time instance the first monolayer is completely filled for the first time, at a coverage of $\Theta = 1.6$ (small systems) or $\Theta = 2$ (large systems). On the left, the first Cu monolayer almost overlaps with the substrate plane shown, indicating the pseudomorphy in this plane. For the second plane, pseudomorphy has the atoms in the middle between the substrate atoms. Note that this plane has almost no single Cu atoms, indicating a high diffusion rate, in agreement with the diffusion data from §4.1.7.

pseudomorphy

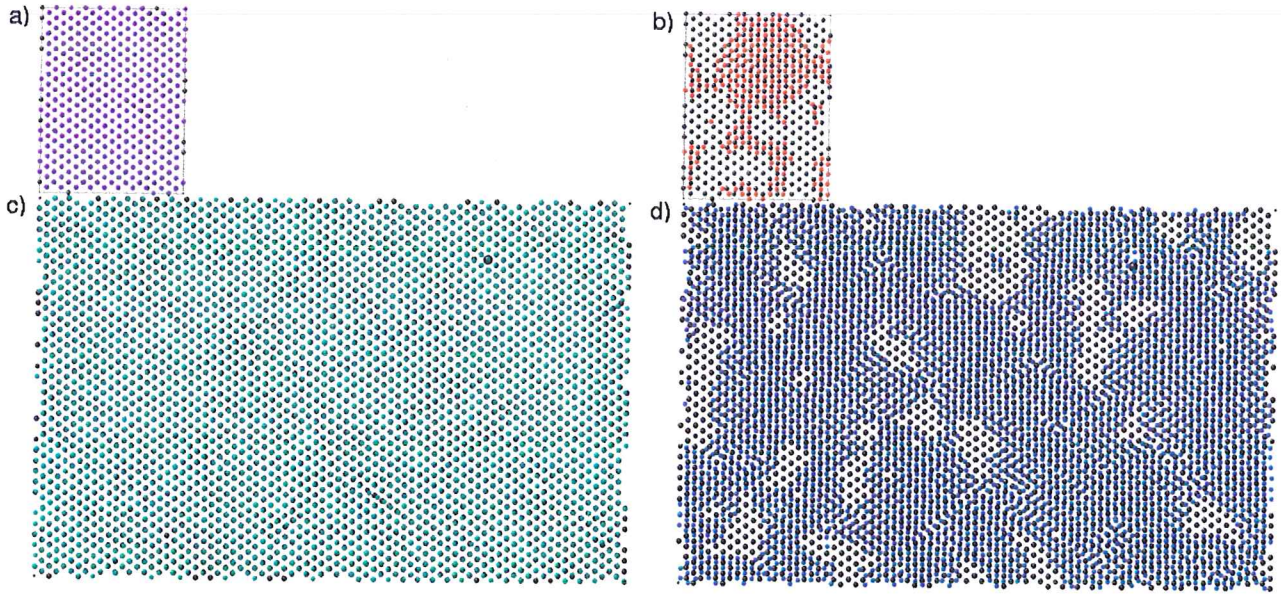

Figure 47: Overlay of the first Cu plane (blue/greenish) and the next-to-last substrate plane (black) on the left. On the right the same substrate plane is shown, but with the second Cu plane (red/blueish). Same as figure 46 but for the two IBAD simulations (**a**, **b**: IBAD_s;**c**, **d**: IBAD_b), at coverages of $\Theta = 1.60$ and $\Theta = 2.21$ respectively. The figures use cooled configurations. Note that on the left, the Mo atoms are mostly invisible. The large black atom is an argon atom in the substrate. See the text for a further explanation.

elastic strains

On the left, there are, dimly, patterns visible where the atoms show less overlap. Comparing these patterns with the views on the right shows that these regions are positioned underneath the edges of the islands in the second plane. This means that elastic strains are responsible for these deviations. At this stage , the "bulk" of these islands is pseudomorphic bcc, the edges are not.

The explanation for the difference in coverages needed to completely fill the first Cu plane can be found from statistics, as the larger systems contain more atom sites per plane which have to be filled up. In these systems, filling up the last few atoms takes place during the deposition of an extra $\Theta = 0.4$ monolayer of coverage. For IBAD, the first plane takes slightly longer to complete (for the small $\Theta = 0.01$ extra, for the large system an extra $\Theta = 0.2$. Note that in the EVAP systems, the second plane is far from completed, even while $\Theta = 2$ for the large systems. The remaining atoms are all in the higher planes.

4.3.2 Three-dimensional growth

Figure 48 shows that up to a coverage of $\Theta \simeq 0.75$ (1.7 Å) the Cu film evolves according to the plane-by-plane growth mode (or Frank—van der Merwe growth mode). This can be seen from R (see §3.2.5) as the roughness curves initially correspond closely to the parabolas expected for this growth mode.

However, before the first plane is completely filled, the next plane has already begun growing. This can be seen clearly from the second step of the staircases. As a result, after a coverage of $\Theta \simeq 1.4$ ($\sim$ 3.1 Å), the R curves

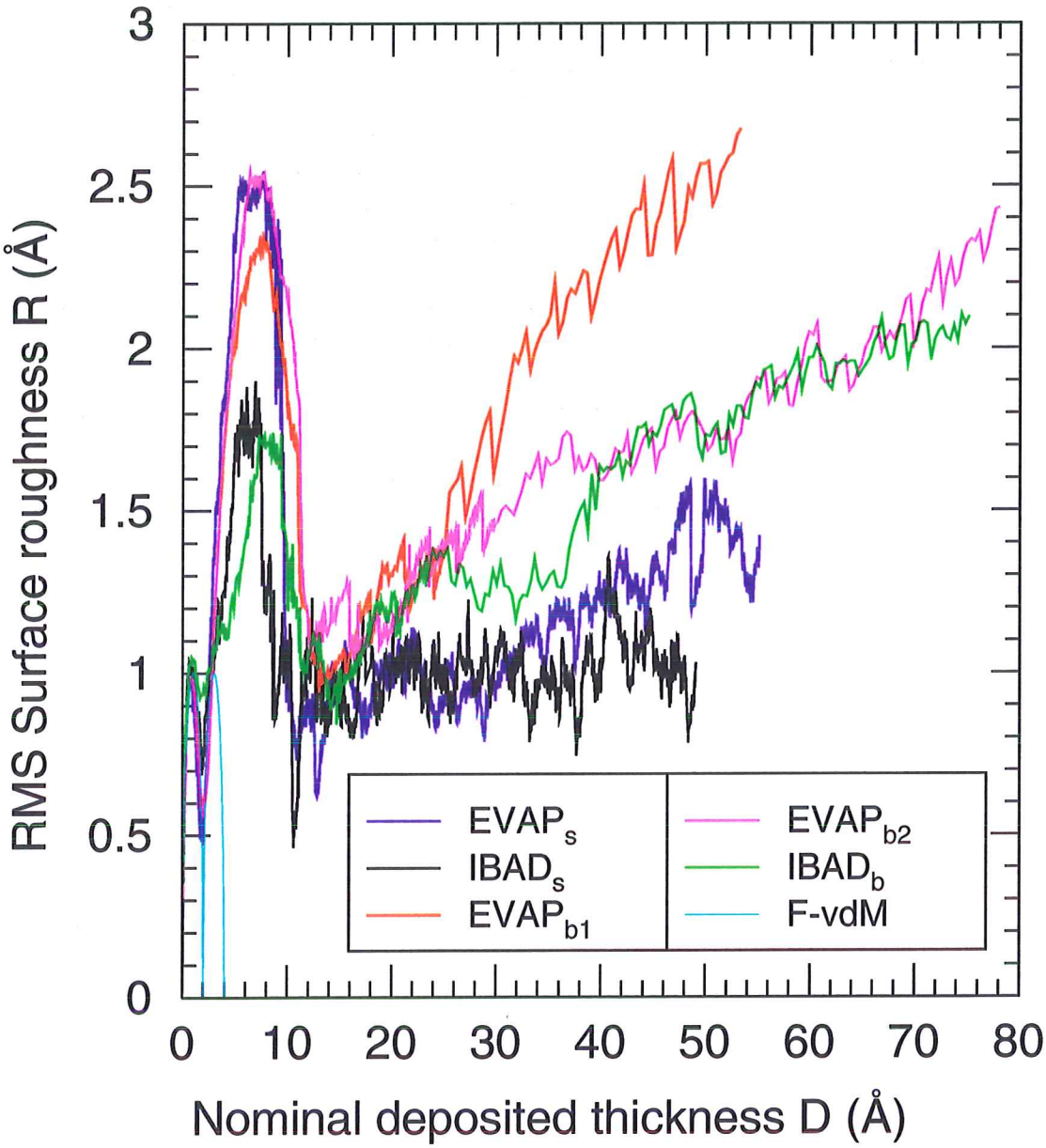

Figure 48: Development of the Root Mean Square surface roughness R of the simulations with thickness D. The cyan parabolas show the roughness evolution that would be seen for Frank—van der Merwe growth .

clearly deviate from the Frank—van der Merwe growth mode parabolas, see again figure 48. The IBAD simulations have a "background" roughness deviation of about 0.07 Å in the thickness range $\Theta \simeq 0$–2 (0–4.5 Å). In this coverage range, the IBAD R-curves lie above the EVAP and Frank—van der Merwe growth curves. The background is likely caused by mixing at the interface. Due to this background roughness, the start of the R curve lies higher for IBAD than for EVAP. The peak that follows the initial plane-by-plane behaviour is considerably lower for IBAD though. The evolution of the R curves at higher thicknesses is addressed later in this text.

What happens when the growth modes begins to deviate from the plane-by-plane mode is, that after a coverage of about $\Theta = 0.75$ monolayer ($\simeq 1.7$ Å, not shown) atoms start to sporadically cluster on top of the first Cu plane, building the second Cu plane. From step two of the staircase figures ($\Theta = 1.0$, $D = 2.2$ Å) it appears that the critical nucleus for island formation on the first Cu monolayer is about 12–15 atoms. Only a few, large, clusters form, which are immobile and grow in the lateral direction on top of the first plane. At a coverage of $\Theta \simeq 1.0$ already, the clusters begin to show growth in the surface normal direction, with the atoms in the next (third) Cu plane quickly filling-in the available sites. The roughness does not show this early deviation clearly. In the staircases though, the described effect is visible. The first monolayer is almost completed, and has several Cu atom clusters on top of it. We also see that the growth of the islands is three-dimensional (3-D) growth, as the second layer has already started to grow, even with the first plane not yet completely filled. In the larger systems, the third layer has already started to grow at this stage. The small systems also have growth of the third plane before completion of the first plane at $\Theta = 1.4$ ($\simeq 3.1$ Å, not shown). In the larger systems, before completion of the first plane ($\Theta = 2.0 \simeq 4.5$ Å, see above), the fourth plane already contains a few atoms. At that coverage the smaller systems have some fourth plane atoms as well (not shown).

3-D islands, critical nucleus

The described behaviour indicates that the growth is actually of the Stranski—Krastanov type, where, after an initial period of plane-by-plane growth, at a certain critical thickness the conditions for Frank—van der Merwe growth (see §2.5.2) are no longer fulfilled (in this case, the condition of strong cohesion), and the layer shows three-dimensional islands developing on the previously grown flat layer. In this case, the requirement of strong cohesion to the substrate is no longer fulfilled as the film thickness increases.

Three-dimensional growth is seen to develop further, accompanied by a rise in roughness to (1.71 ± 0.05) Å (IBAD) or (2.4 ± 0.1) Å (EVAP) at a coverage of $\Theta \simeq 2.3$–3.5 (5.1–7.8 Å), as the roughness curves in figure 48 show.

As an illustration of how this peak "forms", we can see the surface roughness clearly increase from the first to the third step of the staircases as increasingly more planes have started growing (but are incomplete at this point). At ~ 7 Å, the third step of the staircase figures, the films clearly show the resulting three-dimensional surface with valleys and hills forming on top of the first Cu plane. For all simulations, four different heights are visible in the islands. In the larger EVAP_{b2} system, a fifth plane (colour) is also visible, in agreement with its R-curve which show a higher roughness for this simulation than for the other

R-peak

EVAP simulations. For the IBAD simulations, the second Cu plane is more complete and the islands are less pronounced. As we will see in figure 66 and figure 67, the symindex S of the atoms in the islands is predominantly bcc.

The staircase figures for the IBAD simulations clearly show a significant amount of Cu atoms that are in a lower plane than the, normally, first Cu plane. The atoms are in the substrate. Although the Mo atoms that are located in the Cu planes are more difficult to make out in these figures, they are present. This intermixing is discussed in more detail in §4.3.7.

After three-dimensional growth is fully developed at $\Theta \simeq 3.5$, this high level of roughness is maintained up to a coverage of $\Theta \simeq 4.1$, where the effect of islands growing together abruptly reduces the roughness so that R is only about 1 Å at $\Theta \simeq 6$, see figure 48 again. This growing together of the island structures happens in a quite interesting manner. From the fourth step of the staircase figures and from figures 46 and 47 (right), it is clear that the islands-structures are elongated along the y-direction, which is the substrate [100] direction. Another important set of directions for the islands are the diagonal substrate [111] directions. The third staircase steps show that the islands at that coverage have a zigzag shape along this direction. In this step one can see also that the islands structures form "bridges" along this direction. As the coverage increases, the number of these bridges grows, forming small patches of uncovered area in between, "dips". The smaller dips, that show less than 10 plane-1 atoms, are filled up within $\Theta \simeq 0.1$ of coverage. Larger dips remain open for 0.3–1.5 monolayer coverage but are eventually filled up as well, so that the lower planes become more and more complete, see figure 49 (EVAP_{b1}). It appears that broad dips with smooth, straight edges (facets) are the last to be filled up. As the islands of the IBAD simulations are less well defined, these simulation do not show the described behaviour as clearly as the EVAP simulations do. Height-height correlation data shows that in the large systems, the "period" of island growth is ~ 55 Å in the bcc(110) direction. The smaller systems only measure 44.5 Å in this direction.

Valley's fill up

Figure 49 (top) illustrates the smoother surface that is obtained at $\Theta = 6$ (13.3 Å, EVAP_{b1}) as compared to the third step in the staircases ($\Theta \sim 3.4$, $D \sim 7.5$ Å), and the bottom and middle configurations of figure 49 ($\Theta = 4$, $D = 9$ Åand $\Theta = 5$, $D = 11$ Å). In figure 49 (top), a little of the lower planes can still be seen, but most of the surface atoms are situated in the fourth and fifth Cu plane. The fourth step of the staircase figures and figure 49 (middle) shows that at $\Theta = 5$ coverage the roughness is already much decreased as compared to the previous step, although this is not in all cases clearly visible (in the staircases) due to the colouring-scheme used (with atoms coloured by their local crystal geometry S). With a bit of imagination, the position of the former islands can still be made out here from the pattern of plane-5 atoms and the position of the plane three "dip" (in the middle) as compared to the third staircase step for this simulation (figure 39).

Low R-values

The right hand side of figure 49 clearly show that the crystal structure does not change during the diminishing in roughness (which occurs largely) between the bottom and middle configurations. The observed fcc and hcp is located in the $k > 2$ planes, not in the lower two planes. The (evolution in) crystal

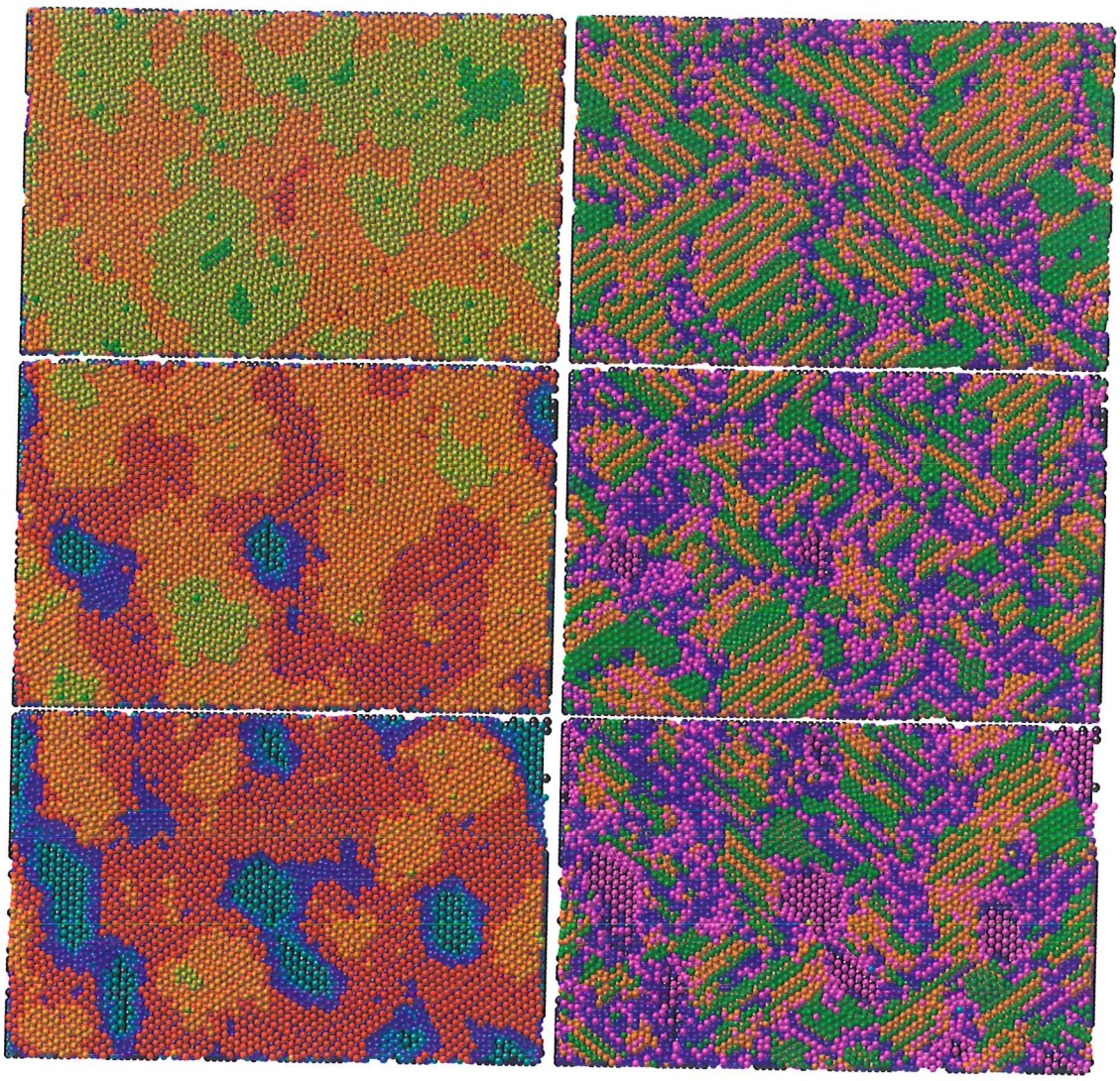

Figure 49: Top view of the EVAP_{b1} simulation (quenched) at $\Theta = 3.99$, $D = 8.87$ Å (bottom); at $\Theta = 4.89$, $D = 10.88$ Å (middle); and at $\Theta = 6.00$, $D = 13.35$ Å (top). On the left, the Cu atoms are coloured by height, on the right by local crystal geometry S, Mo is black in all figures. The middle configuration is the same as used for the fourth step in figure 39. The pictures on the right illustrate that the structure does not change much during the fall down in roughness, which largely occurs between the bottom and the middle configuration.

structure is discussed further in §4.3.3.

figures of:

R
β_k

atom-history

At this point, a new set of figures is introduced, figures 50, 51, 52 (EVAP) and 53, 54 (IBAD). These figures show three different quantities describing what happens during growth. The top, 50–54(a), gives the roughness again, this time for each simulation separately. Below that, the β_k-data shows the deviation of growth with respect to the solid-on-solid growth model (see §3.2.6). The third dataset, 50–54(c), shows the interplanar motion of atoms after arrival in the film. A positive value means that the initial condensation took place above the final position, indicating a downward motion of the atom (see §3.2.7). Diagonal downwards sloping lines connect the planes where the atoms have initially condensated. This will be designated as the atom-history.

The β_k-data from the figures show an initial high peak for the plane $k = 1$ and a negative peak for plane $k = 2$. This is in agreement with what we know about the growth mode, as plane 1 is largely completed before plane 2 starts growing on it so that filling up of available atom sites for the atoms in the plane strongly lags behind the creation of such sites. At the development of 3-D growth, there is a drop in positive peaks, with the plane $k = 3, 4$ curves assuming more elongated shapes that have a second small peak at the falling edge of the roughness curve, when the islands are filled up. The fifth plane then quickly fills up. Notably, the second plane as has a second, smaller, negative peak for the EVAP simulations, and only a very small positive peak, while the IBAD simulations have a clear positive peak here. Conversely, for EVAP the third Cu plane has no negative initial peak and even the fourth plane only has a small one while both have a negative peak for IBAD.

Figures 50–54(c) do not enable more than rough estimates of the amounts of inter-plane and in-plane diffusion. Later in this section (§4.3.7) atom history contour plots, figures 91–95, are presented in an attempt to obtain more quantitative results. The current figures show more detail however. Notable in the IBAD atom-history figures is, that some atoms are first detected in the top substrate plane ($k = 0$), and for the large system even in plane -1. Some of these atoms end up as high as plane 8. The atom-history plots shows that of the atoms in the first five or six planes, a considerable amount initially condenses in plane 1 (indicated by the diagonal line connecting the left-lower points), and a large amount also condenses on plane 2. A much smaller amount impinges at higher planes, up to $k = 5$. The atoms that condense in these first planes show a strong upward motion. The behaviour is different for planes higher than the fifth plane. For $k = 5$–8, there is also a strong upward motion, presumably at the filling up of the lower planes. The β_k-data show that plane 5 is the last plane to feature heavily in 3-D growth, in agreement with the coverage at which the reduction of the roughness takes place following this 3-D growth. From the sixth/seventh plane and onward, there is a clear change to steady state. At planes "above" this transition, a steady state is seen to develop in the atom-history plots, toward a situation where the bulk of the motion is within the plane, or between the plane and its two neighbour planes below and above, and some motion from higher planes downwards. This behaviour is maintained during the remainder of the deposition. The figures do not show the contributions of bulk and of surface diffusion, but from what we know of the two

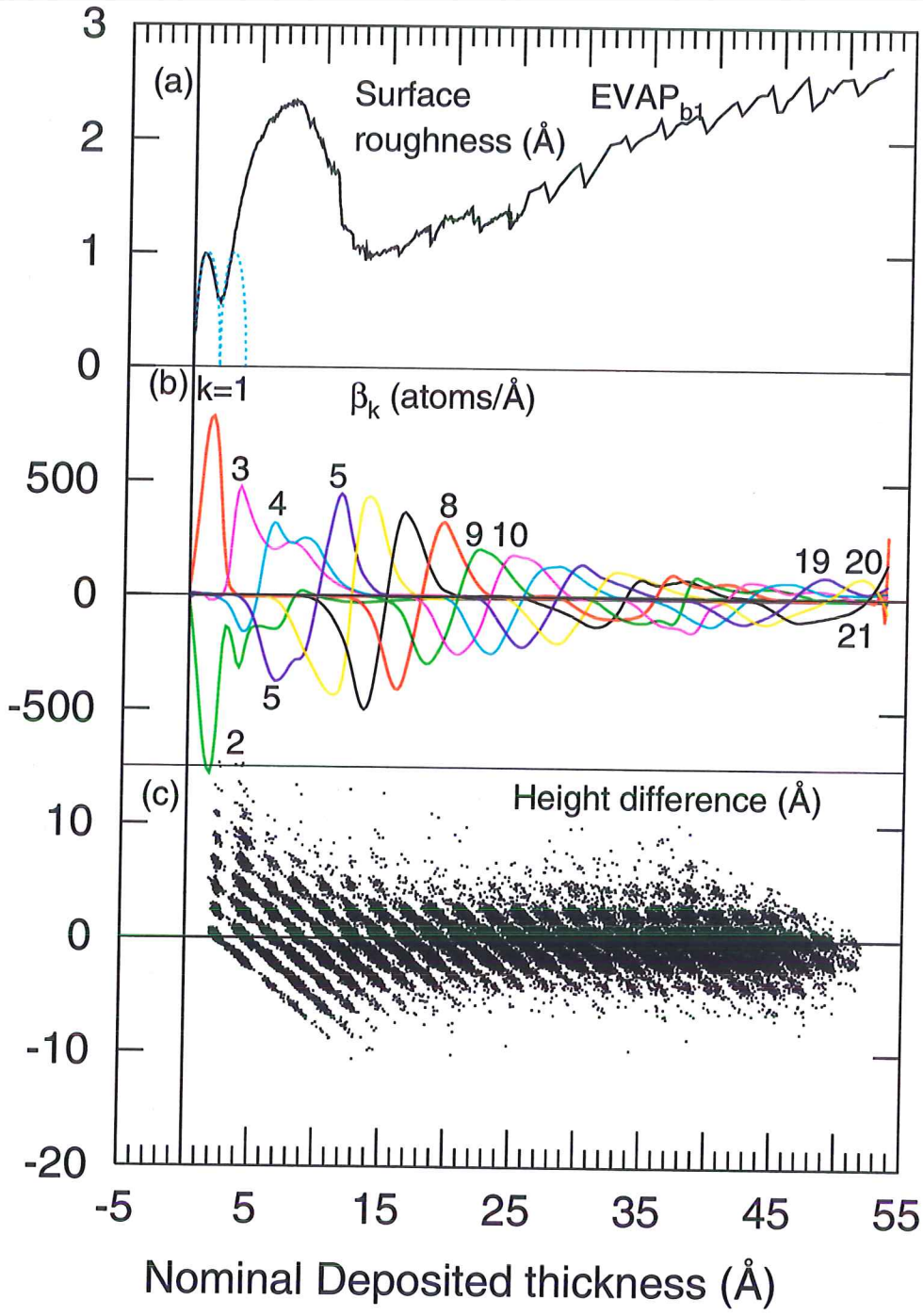

Figure 50: Data illustrating the evolution of a Cu film grown on Mo(110) by thermal evaporation ($EVAP_{b1}$): (a) Surface roughness (see §3.2.5). (b) Excess growth rates (compared to static solid-on-solid model) (k of Cu planes with index $k = 1, 2, 3, \ldots, 22$ (see §3.2.6). (c) Interplanar motion plot. Each point represents a Cu atom. The horizontal coordinate is its final height in the film, the vertical coordinate indicates how much higher (or lower) the atom has initially condensated on the film (see §3.2.7). Note that panel(c) is different from panels (a) and (b) in that it represents only a single time-instance (ie. the final situation).

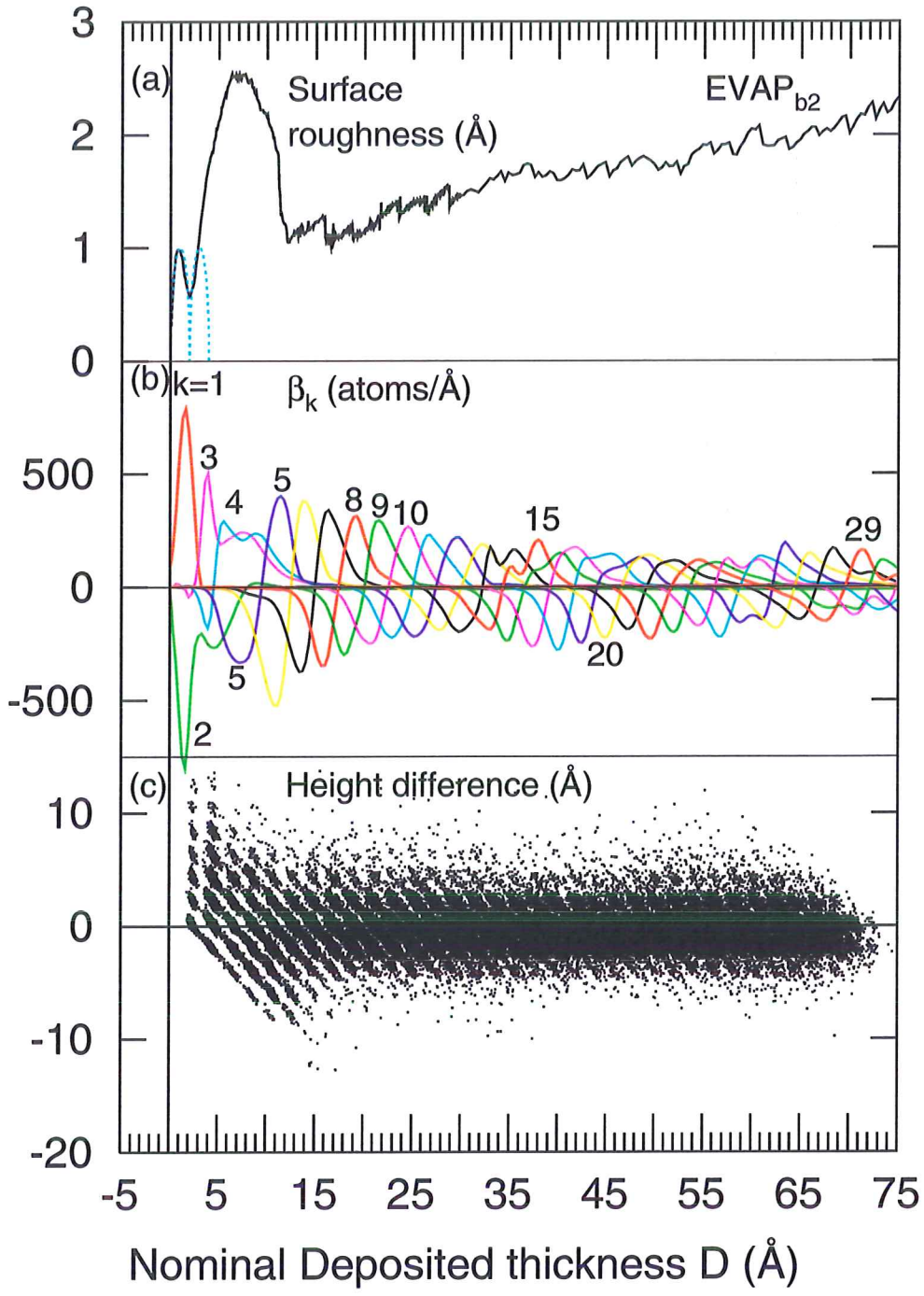

Figure 51: Data illustrating the evolution of a Cu film grown on Mo(110) by thermal evaporation (EVAP$_{b2}$): (a) Surface roughness R (see §3.2.5). (b) Excess growth rates (compared to static solid-on-solid model) (k of Cu planes with index $k = 1, 2, 3, \ldots, 32$ (see §3.2.6). (c) Interplanar motion plot. Each point represents a Cu atom. The horizontal coordinate is its final height in the film, the vertical coordinate indicates how much higher (or lower) the atom has initially condensated on the film (see §3.2.7). Note that panel(c) is different from panels (a) and (b) in that it represents only a single time-instance (ie. the final situation).

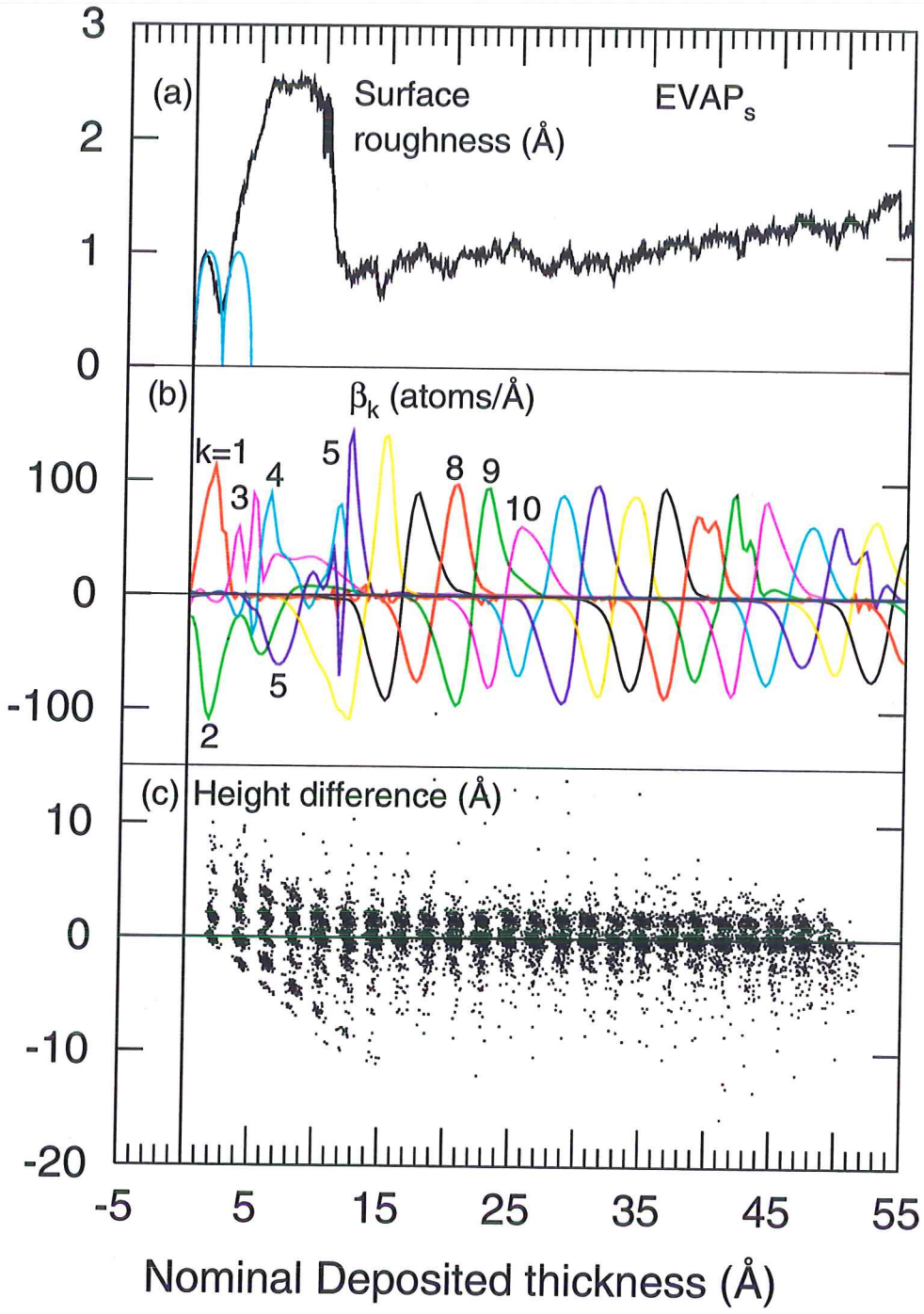

Figure 52: Data illustrating the evolution of a Cu film grown on Mo(110) by thermal evaporation (EVAP$_s$): (a) Surface roughness R (see §3.2.5). (b) Excess growth rates (compared to static solid-on-solid model) of Cu planes with index $k = 1, 2, 3, \ldots, 22$ (see §3.2.6). (c) Interplanar motion plot. Each point represents a Cu atom. The horizontal coordinate is its final height in the film, the vertical coordinate indicates how much higher (or lower) the atom has initially condensated on the film (see §3.2.7). Note that panel(c) is different from panels (a) and (b) in that it represents only a single time-instance (ie. the final situation).

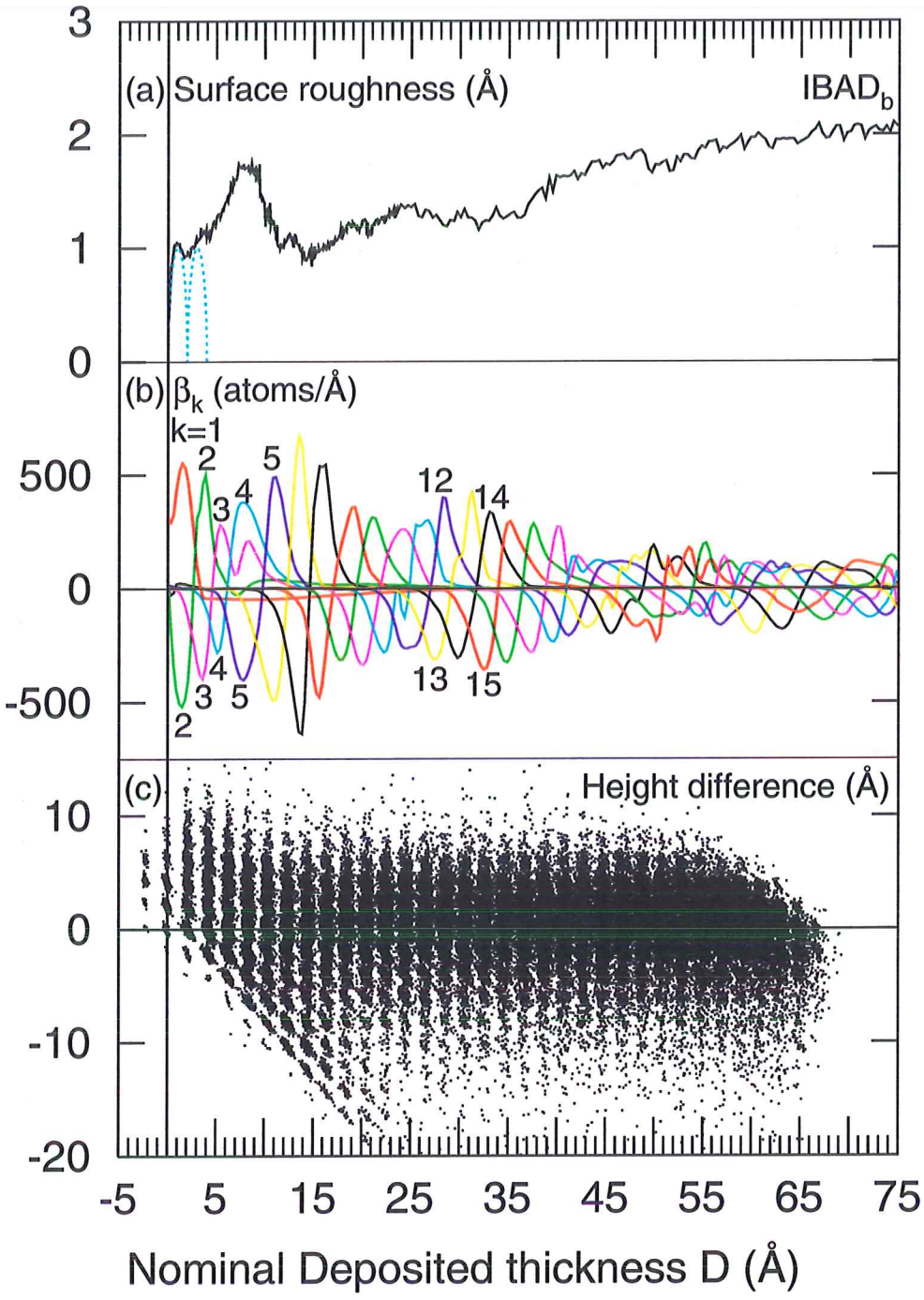

Figure 53: Data illustrating the evolution of a Cu film grown on Mo(110) by ion assisted deposition ($IBAD_b$): (a) Surface roughness R (see §3.2.5). (b) Excess growth rates (compared to static solid-on-solid model) of Cu planes with index $k = 1, 2, 3, \ldots, 32$ (see §3.2.6). The dotted line (barely visible) is the top substrate plane, which was initially completely filled. (c) Interplanar motion plot. Each point represents a Cu atom. The horizontal coordinate is its final height in the film, the vertical coordinate indicates how much higher (or lower) the atom has initially condensated on the film (see §3.2.7). Note that panel(c) is different from panels (a) and (b) in that it represents only a single time-instance (ie. the final situation).

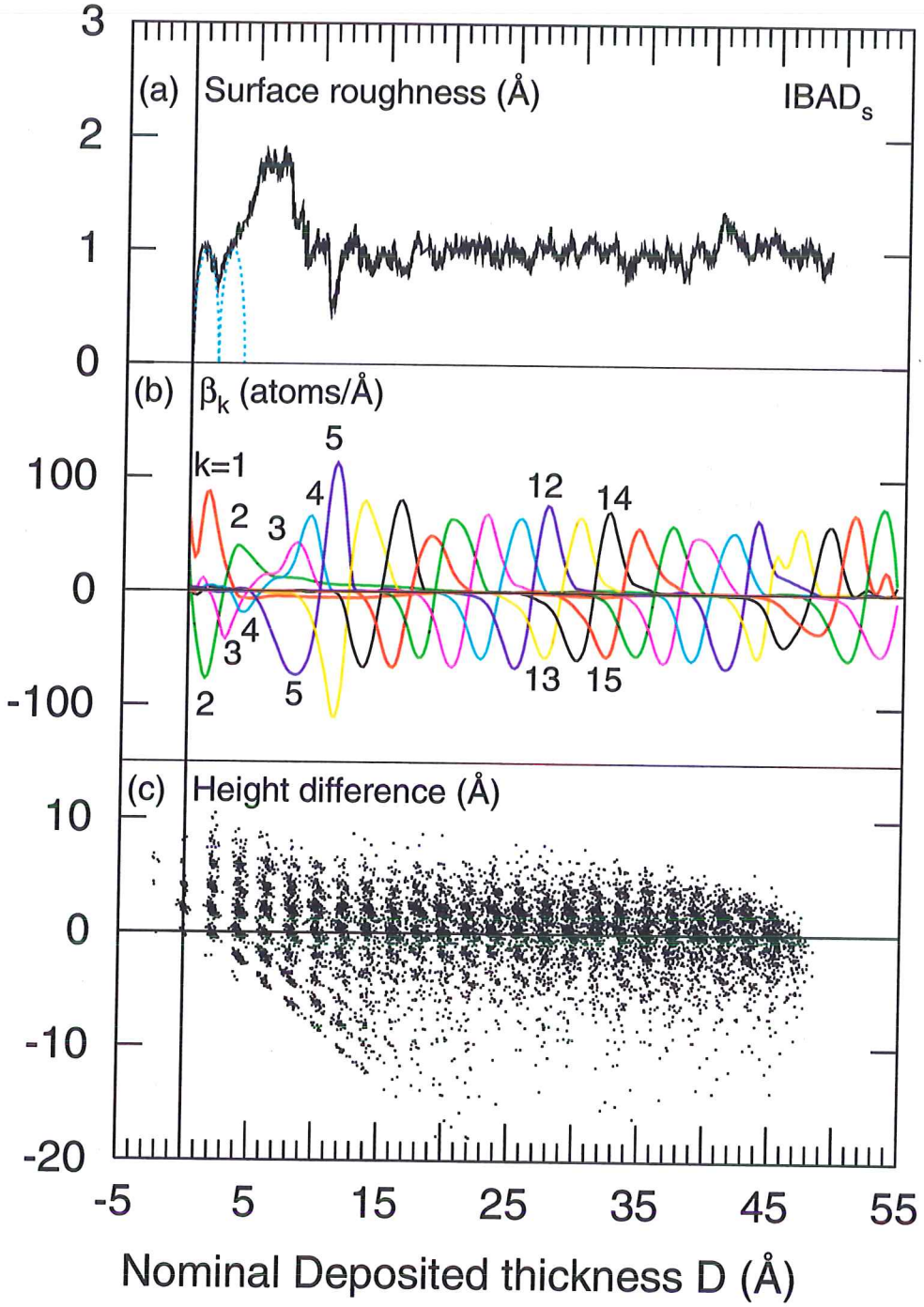

Figure 54: Data illustrating the evolution of a Cu film grown on Mo(110) by ion assisted deposition (IBAD$_s$): (a) Surface roughness R (see §3.2.5). (b) Excess growth rates (compared to static solid-on-solid model) of Cu planes with index $k = 1, 2, 3, \ldots, 24$ (see §3.2.6). The dotted line (barely visible) is the top substrate plane, which was initially completely filled. (c) Interplanar motion plot. Each point represents a Cu atom. The horizontal coordinate is its final height in the film, the vertical coordinate indicates how much higher (or lower) the atom has initially condensated on the film (see §3.2.7). Note that panel(c) is different from panels (a) and (b) in that it represents only a single time-instance (ie. the final situation).

processes (see §4.1.7) and the large amount of surface that is present during the 3-D growth stage, a mainly surface diffusion driven motion is the most likely in the initial phase, while during the steady state bulk diffusion will be the most important.

4.3.3 A structure emerges

In the initial stage of deposition, almost the only structure that is seen is the bcc structure. This is certainly the case for the first and second plane as shown above but remains true for the (incomplete) higher lying planes as well. From the staircase figures we see that the situation is different at higher coverages. The fourth step of the staircase figures shows what the simulations look like at a coverage of about $\Theta = 5$. There are clear structures visible in the figures. A comparison of this fourth step with the higher coverage steps shows that at this point, the first glimpses of what the final crystal structure will be are becoming visible. For the smaller systems, the final structure seems to have been developed in full at $\Theta = 5$. Other data shows that this is not true. Especially the lower planes still undergo a change, but the higher planes are not static either. In the remainder of this section, this is frequently illustrated. Part of the observed change, especially at higher coverages, is due to the passing of time but most of the change for lower coverages is attributed to the the increase in coverage. For the larger systems, the observed structure is still further away from the final structure, which is attributable to the increased freedom of movement of the structural features due to the larger system size.

All k

In the fourth step of the staircases, the Cu atoms in the large systems form regions of atoms which have $S =$ fcc and $S =$ hcp regions with stacking-faults, within a "matrix" of atoms that have $S =$ bcc (on the surface, part of the atoms has S undefined). The stacking-faults are shown by the alternating fcc and hcp diagonal lines of atoms (as seen earlier with Cu on Cu deposition), see §3.2.8. This is easily understandable from the stacking sequence. For instance, a stacking of planes like "ABCABCBCABC", containing a single stacking-fault has two hcp stacked planes (BCB and CBC). This *intrinsic* fault can be understood as consisting of a missing "A"plane between the two hcp stacked planes.

Looking at the fractions of the different crystal symmetries at this coverage, shown in figure 55, we see a pattern emerge. Clearly, the amount of bcc matrix atoms reduces strongly with increasing plane number k and the amount of fcc atoms increases with k. The amount of hcp atoms increases with k as well, but is reduced in the surface plane ($k = 5$) again. This plane has a low fraction of hcp atoms and a fraction of fcc atoms that is somewhat higher than for $k = 4$. The lowering of the fraction of hcp near the surface is seen throughout the remainder of the simulations. What happens is illustrated best by the highest three steps in the IBAD_b staircase (figure 42). These steps clearly have much more fcc atoms in the topmost plane than in underlying planes. The fcc lies on top of hcp regions as well as on fcc regions. The same thing happens at $\Theta = 5$, but on a smaller scale, as the close-packed regions are smaller here than at higher coverage. Notably, the EVAP_b2 configurations contain much less fcc and hcp than the other simulations. EVAP_b2 is also the only simulation for which

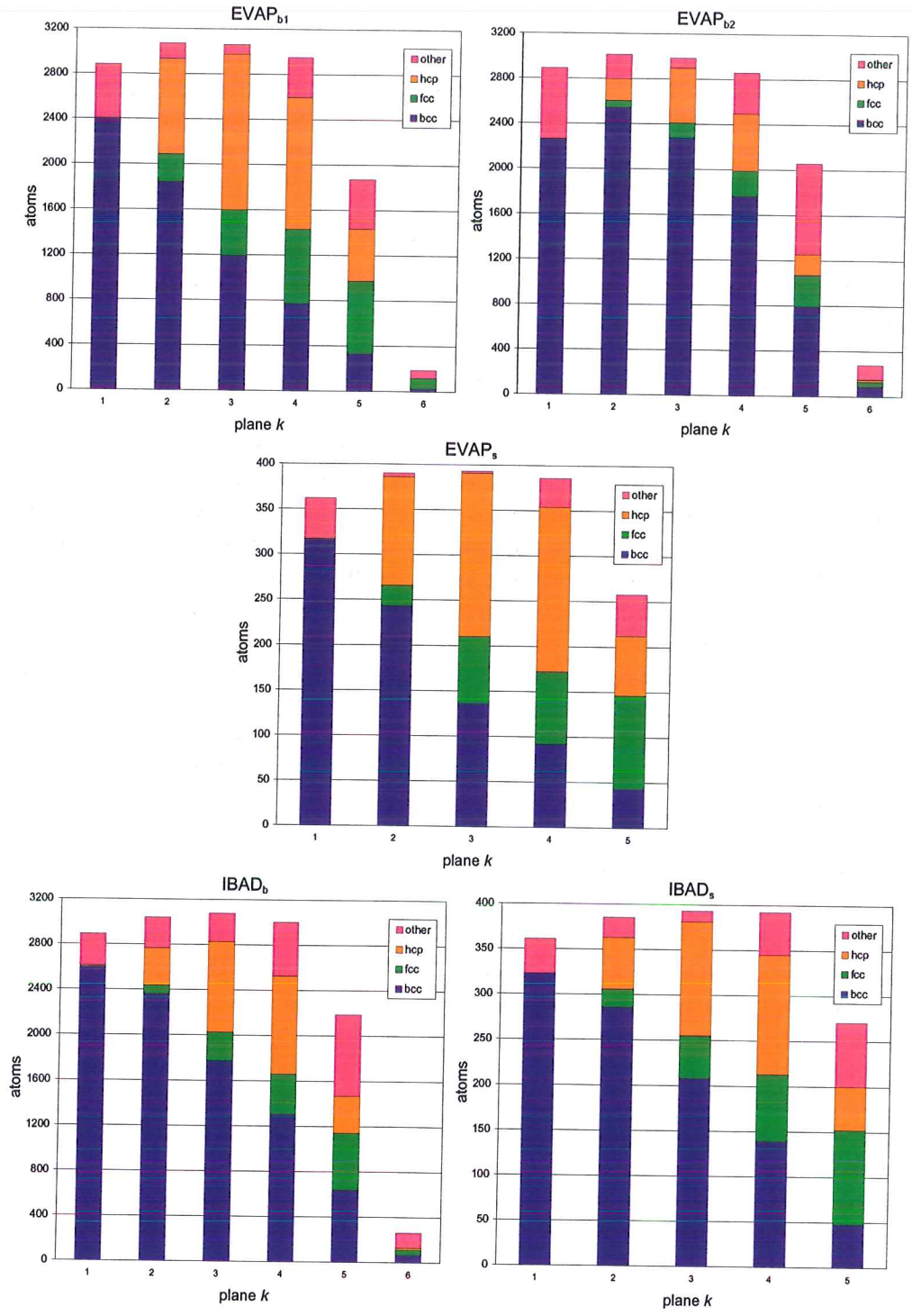

Figure 55: Crystal structures in the Cu on Mo deposition simulations at $\Theta \simeq 5$ ($\mathrm{EVAP_{b1,\,b2}}$: $\Theta = 4.89$; $\mathrm{EVAP_s}$: $\Theta = 4.98$; $\mathrm{IBAD_{s,\,b}}$: $\Theta = 5.02$, $\simeq 11$ Å). The number of atoms of each $S =$ bcc, fcc, hcp or other ($S =$ undefined, ico or dia, see §3.2.8) is given for the individual planes $k = 1, 2, 3, 4, 5$ and for the larger systems for $k = 6$ as well. The configurations are the same as those used for the fourth staircase step. It is clearly visible that the amount of $S =$ other atoms is higher at the interface, and increases towards the surface again.

the second plane contains more bcc than the first (at later stages of deposition, more differences in S-fractions are seen between the simulations). Globally, EVAP and IBAD, show the same behaviour at this stage, but EVAP has more "other" symmetries in the first plane and less in the second and third plane. EVAP also has more hcp and less bcc in the second plane than IBAD.

From the fractions of atoms with different S and from the earlier structure, there is a clear structural difference between the first Cu plane, the second plane and the higher planes up to the surface. For clarity, the structures will be described separately, starting with the first plane and continuing towards higher k planes.

$k = 1$ The first Cu plane is made up of bcc atoms and some with S unidentified. For lower coverage, figures 46 and 47 show that the first plane is pseudomorphic bcc at that earlier stage of the deposition. The high fraction of bcc atoms seen at $\Theta = 5$ for this plane indicates that this remains true during this stage of the deposition (see figure 55). Figures 56 and 57, left, illustrate this as well. In these figures, the first plane does not show clear deviations in the atom positions. There is still a very dim pattern visible in the figures but there are no spots were a clear deviation from the bcc geometry can be concluded apart from the few interstitials that are seen. Still, figure 55 shows that there is a significant amount of atoms with S undefined present in the first plane. A further difference with figures 46, 47 is that here, for both the EVAP and the IBAD simulations, plane 1 contains several interstitials. Also, the second plane is (almost) complete and shows a band-like structure. This is further discussed below, in §4.3.3. The mentioned interstitials are not, on their own, sufficient explanation for these undefined atoms, as there are only a few interstitials, and these do not heavily influence the positions of (many of) the surrounding atoms. Otherwise, the figures 56 and 57 would show a more clear deviation from bcc than is observed. Note that almost none of these interstitials form dumbbells, which would happen in bulk bcc [39]. Instead, most interstitials are in the form of crowdions with a length of 5 Cu atoms. The interstitials are also not necessarily in an undefined geometry themselves. However, they are close to the edges of larger areas that are concluded to have S undefined (not shown). Indeed, figures 56 and 57 show that the interstitials are close to the faintly visible patterns in the plane. The conclusion has to be that the cause of the atoms with $S =$ unidentified is not found (solely) within the first Cu plane. This means that the planes on top of it cause the local crystal geometry around some of the atoms to be undefined, as the underlying substrate remains bcc.

$k = 2$ At this coverage the second plane (figure 56 and figure 57, right) shows an alternating pattern of four bcc regions (with black atoms in between the blue ones) and four other regions where a chevron pattern is visible, with bands of high misfit along the bcc$\langle 111 \rangle$ direction (diagonal). In the small systems, only two different regions are seen, which is in agreement with the smaller size of the systems. The regions are also smaller, or rather, the alternating pattern is less disperse, with clearer boundaries. This is actually necessary, because at least one "period" of the alternation has to fit into the smaller simulation box. Comparing the left and right hand sides of the figures we conclude that the first plane interstitials are positioned underneath a misfit diagonal and close to an

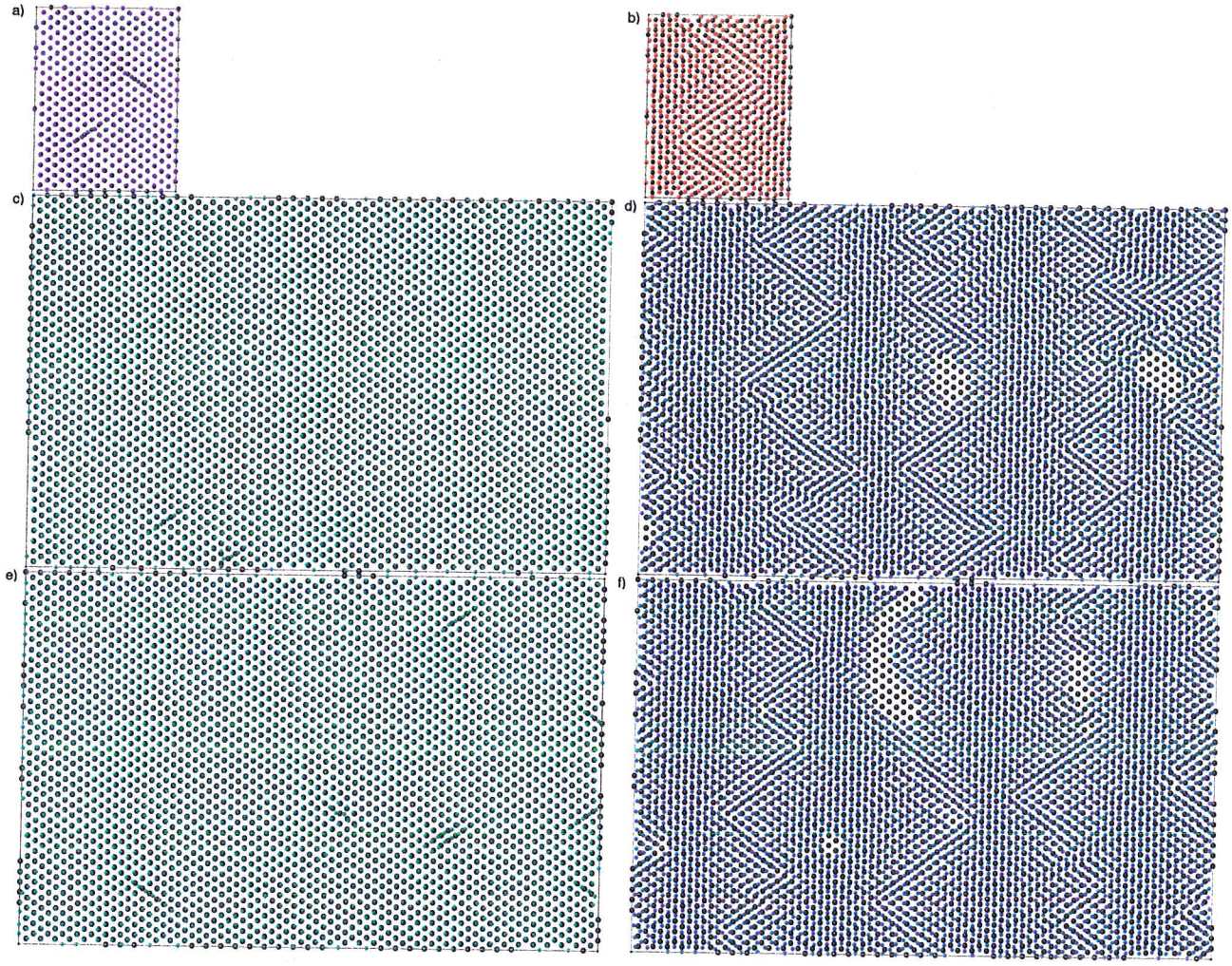

Figure 56: Overlay of the first Cu plane (blue/green) and the next-to-last (Mo) substrate plane (black) on the left. On the right the same substrate plane is shown with the second Cu plane (red/blue). From top to bottom, the three different EVAP simulations are depicted (**a**, **b**: $\mathrm{EVAP_s}$; **c**, **d**: $\mathrm{EVAP_{b1}}$; and **e**, **f**: $\mathrm{EVAP_{b2}}$). The coverage is $\Theta = 4.98$ for the small system and $\Theta = 4.89$ for the two large ones ($\simeq 11$ Å). See the text for further explanation. The figures use cooled configurations. Note that on the left, the Mo atoms are mostly invisible.

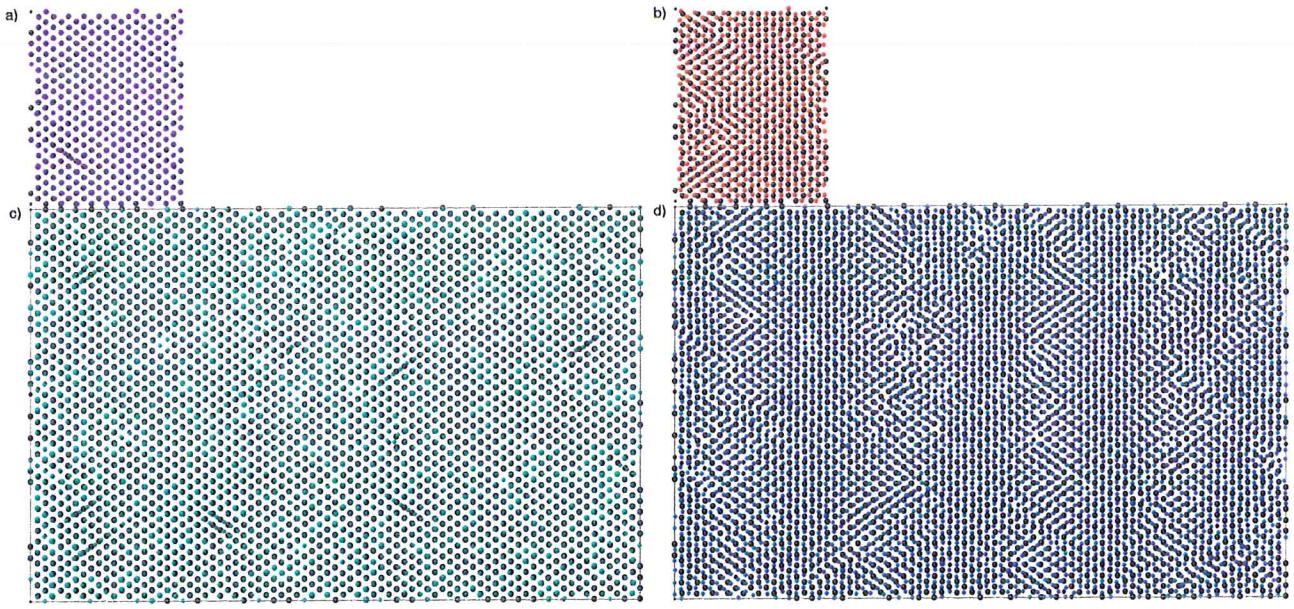

Figure 57: Overlay of the first Cu plane (blue/green) and the next-to-last substrate plane (black) on the left. On the right the same substrate plane is shown with the second Cu plane (red/blue). Same as figure 56 but for the two IBAD simulations (**a**, **b**: IBAD_s; **c**, **d**: IBAD_b). The coverage is $\Theta = 5.02$ for both systems ($\simeq 11$ Å). See the text for further explanation. The figures use cooled configurations. Note that on the left, the Mo atoms are mostly invisible. The "holes" are due to the presence of smaller Cu atoms in the substrate, that are completely eclipsed by higher Cu atoms. The Ar atom is show with a smaller radius than in figure 47.

intersection between two such lines. The undefined areas (on the left in figures 56 and 57, the areas where more black is visible) are positioned underneath the non-bcc areas of the second plane. The staircase figures show that in higher lying planes, fcc and hcp regions are located on top of these areas.

In order to understand what we see here it is useful to consider figure 58. This figure shows the first and second deposited monolayer of Cu for EVAP_v (at a coverage of $\Theta = 10.9$, $D = 24.2$ Å) in three slightly different top-down views that together show the relation between the positions of atoms in the two planes and their S. In this small system, the resulting structure is restricted to be much less complex than in the other simulations, so that it is more easily interpreted. Due to the in-plane periodic boundary conditions the Cu is forced into a coincidence with the substrate within the dimensions of the simulation box. The two top views of the figure give a good picture of the structure of the first plane, which is pseudomorphic to the bcc (110) substrate. From the two lowest views, a pattern of alternating fcc and hcp bands is seen to emerge in the second Cu plane. Although the first Cu plane has a mainly bcc geometry, still, at the boundaries of the fcc/hcp bands in the second Cu plane, the atoms of the first plane are locally in an undefined geometry, shown by the magenta strips. Note the buckling in the y-direction of the atomic rows parallel to the x-direction. Looking at figure 11 in section two (§2.5.1, page 37) and comparing this to the pattern seen in figure 58, top, we see that the second Cu plane is

$EVAP_\text{v}$

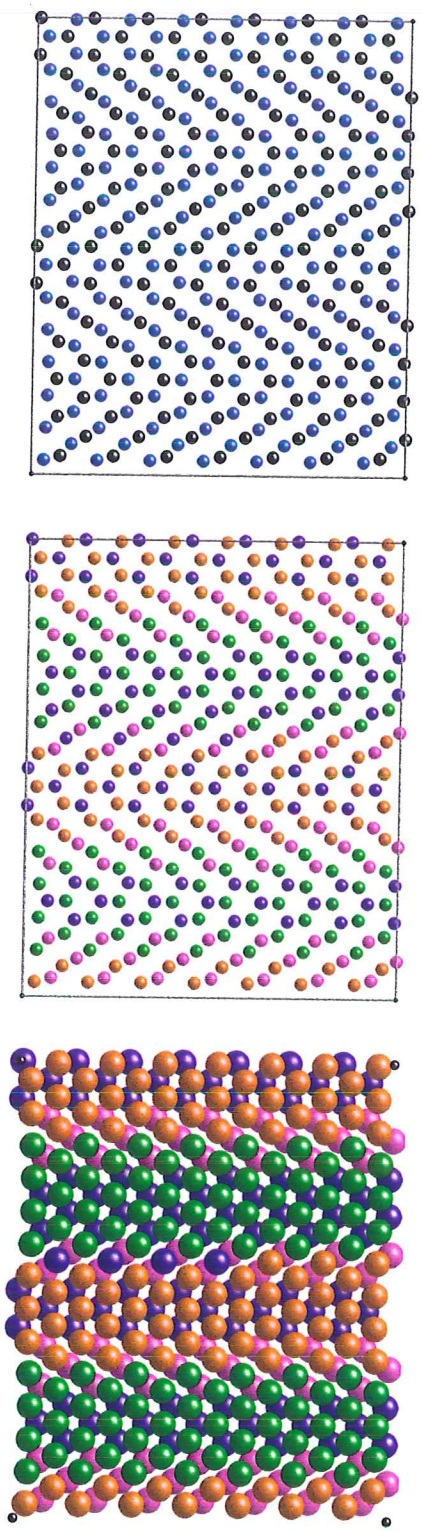

Figure 58: Three views of the first and second Cu plane from a configuration of $EVAP_V$. The top shows the first, pseudomorphic, Cu plane in black, with the second plane coloured blue. The middle view is the same, but with the atoms coloured by S. The bottom view has the same colouring scheme but shows the atoms as larger balls.

in the NW-x orientation, with a forced 14:11 y-direction coincidence with the bcc substrate and first Cu plane. The second plane has four bcc atoms at one of the boundaries between the fcc and hcp strips. It is not clear how these positions are special. It may well be that adjusting the values for a_S changes the number of atoms that are concluded to be in the bcc local geometry. This would however make them "undefined", which does not contribute to a better understanding of the (semi-)epitaxial relation seen.

Such patterns as seen here, consisting of fcc/hcp bands in the second plane, with some bcc atoms between them, accompanied by strips with $S =$ undefined in the first plane, are also present in the larger systems that are the main topic of this subsection, although in more complex form. Earlier, when looking at the Cu on Cu deposition results a similar effect was seen. There, the highest substrate plane is partly in the hcp crystal structure. This is due to the presence of a stacking-fault above it which is created in the first deposited Cu plane (see figure 34).

$k = 1, 2$

In conclusion, we see for the first two planes that at this coverage, $\Theta = 4.5$–6 ($\simeq$10–13 Å), the first plane is still pseudomorphic bcc. The second plane is at this stage still partly pseudomorphic bcc and partly in a close-packed crystal structure (fcc or hcp). Comparing the pattern in these regions with the patterns seen in figure 11, figure 8 (the pattern seen for perfect NW-x) and figure 58, it

$k > 2$

seems that a distorted NW-x pattern can be identified. Higher k planes have larger non-bcc areas than the second plane, which together add up to less bcc than in the second plane. The areas are otherwise similar in structure to the one described for the $k = 2$ plane, at least initially, up to $\Theta \sim 5.5$ (12.4 Å). At higher coverages, the structure of the planes undergoes a change, as described below. In figure 49, this is clearly visible, especially when comparing the middle and top configurations. The surface plane ($k = 5$) contains a relatively large fraction of fcc. This excess fcc is located in single atom rows at the surface.

4.3.4 Crystal structure change with thickness

All k

In the coverage range of $\Theta \simeq 6$–11 ($\simeq$ 13–24.5 Å), the R-curves show no large deviations between the simulations, with R values that are roughly stable at about 0.8–1.35 Å. The most notable difference between the simulations is that the larger systems actually have a slowly increasing roughness, while the smaller systems have a roughness that more or less corresponds to their R-values before 3-D growth and is maintained at that level. This is reflected in the β_k curves, where planes $k = 6$–11 all have the characteristic plane-by-plane down-up wiggle (see §3.2.6), although the wiggles shown by planes 9–11 strongly differ in magnitude between the simulations, and also in shape. The atom-history shows not much change either, except for a larger spread in z- and Δz-values in the planes that grow near the end of this coverage (thickness) range ($k = 9$–12). Note that this does leave room for considerable in-plane motion though.

A closer look at the development of the crystal structure of the deposited films reveals that the above described picture of the emerged structure at $\Theta \simeq 5$ does not remain static during the continued deposition, as is clearly visible in the staircase figures. Although not independent, the structural change can be

separately described for the first plane, for the second plane, and for planes with $k > 2$. This last group of planes can be considered to be (the) "bulk"-film planes. The change in crystal structure taking place within the first Cu plane is described first, followed by that of the second plane and thereafter, the change in structure for the higher k planes is described.

$k = 1$

After the first plane is fully complete as a pseudomorphic bcc plane it still densifies. In comparing the figures 46, 47 to 56, 57 this densification can be attributed to the creation of Cu interstitials. The number of interstitial Cu atoms that the plane contains increases. At $\Theta \sim 7.5$ ($D = 17$), figures 59 and 60, left, the number of interstitials is again higher and this increase continues, eventually resulting in the pattern seen in figures 61, 62 (left) at $\Theta \sim 24.5$ ($D = 54.5$ Å). Note that this "pattern" should not be interpreted as a static situation, instead, the overall picture is not altered much, but the position of the interstitials varies during the simulation. Most of the interstitials seen for these last figures are present already at a coverage of $\Theta \simeq 10$ monolayers. In principle, the β_k-data reflects this increase in atoms, as the plane grows despite the fact that there are really no (regular) atom positions available. As this effect is relatively small, with less than 0.6 % of a monolayer interstitials for the EVAP simulations, it is not seen clearly in the EVAP simulations. For IBAD though, the number of interstitials is considerably higher, of the order of 5 % of a monolayer , so that the effect can be seen in the β_k figures. Currently, the completion of a layer is determined with M_1 equal to the final value $N_{1,\text{final}}$ at the end of the simulation. Therefore, the first plane is deemed incomplete when not yet all interstitials are present (see §3.2.6 for the exact effect of N_k, M_k). Thus growth of the plane still lags the growth expected according to the s-o-s model, resulting in a elongated negative tail in the β_1-data for IBAD.

$k = 2$

Figures 59 and 60, right, show that at a coverage of $\Theta = 7.5$ the structure of the second plane has evolved into one with much less bcc than at $\Theta = 5$. Also, and most clearly visible in the large Cu/Mo systems, there is a structural difference between the EVAP and IBAD simulations at this coverage. For EVAP, the second Cu plane is made up of a combination of alternating Moiré-"streaks" roughly oriented along the x-axis (the bcc[110] direction) and larger versions of the diagonal bands that were also present earlier, together with some strips oriented along the y-axis. For IBAD however, the structure of the second plane is at this point still relatively unaltered. Also notably is that at this coverage the structure of EVAP_s is considerably more simple, and more like the low coverage situation, than that of the larger EVAP systems.

views of selected planes

Again introducing a new set of three figures, one each for all of the large systems, which show three related sets of information for a selection of planes at $\Theta \simeq 7.5$ ($D = 16.7$ Å), we can further identify the patterns of plane $k = 2$ seen in figures 59, 60. It is tempting to linger while looking at the figures 63–65, and study all information contained in them at once. For now however, lets start by restricting ourselves to just the lower left pictures, showing the crystal structure of plane 2. In comparing these pictures with the other data we have on the second plane, the Moiré-streaks in figure 59 and in figure 61 are concluded to consist of alternating fcc and hcp streaks in a matrix of bcc surrounded

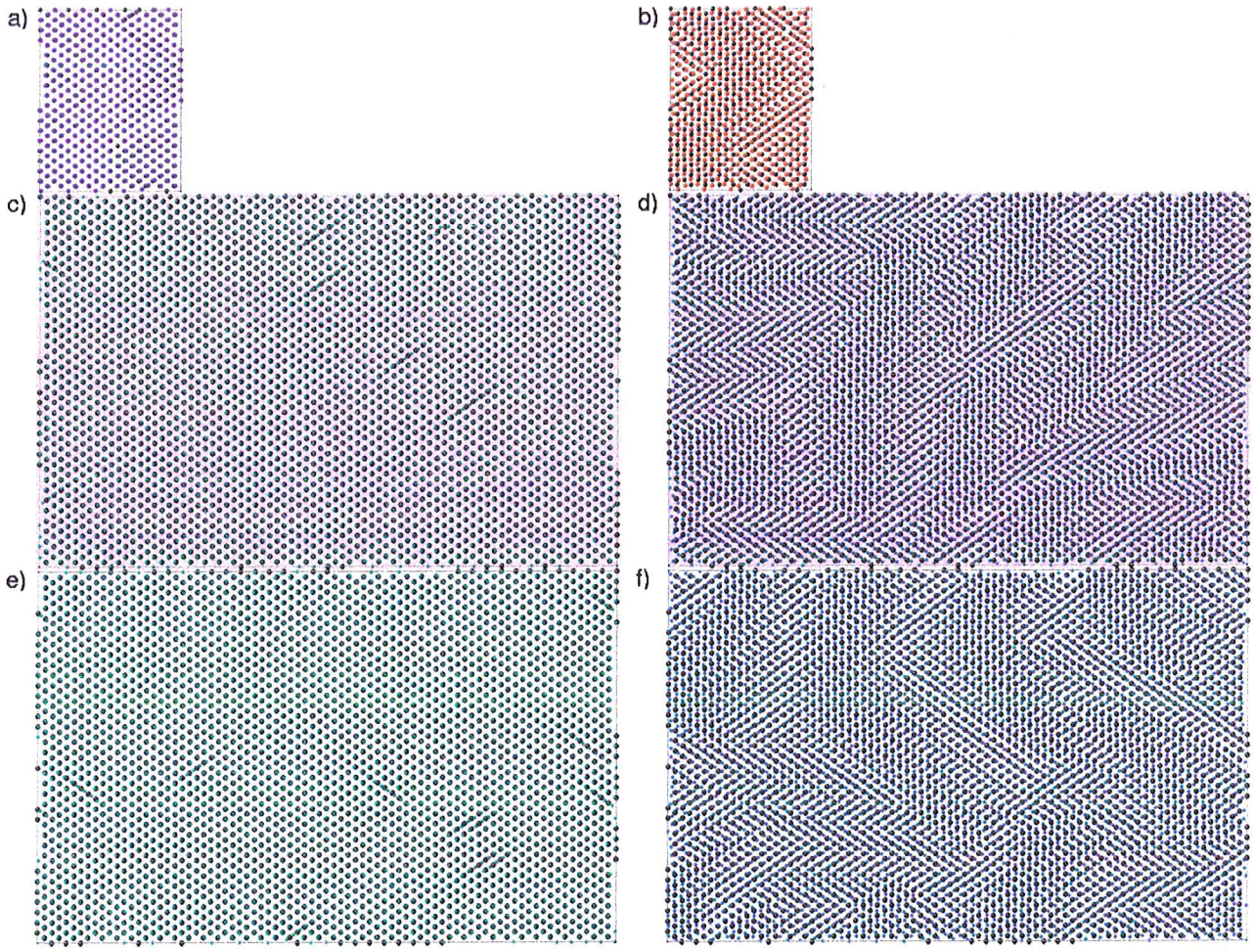

Figure 59: Overlay of the first Cu plane (blue/green) and the second highest substrate plane (black) on the left, and on the right the same but for the second Cu plane (red/blue). Shown are the three different EVAP simulations (**a**, **b**: $\mathrm{EVAP_s}$, $\Theta = 7.5$; **c**, **d**: $\mathrm{EVAP_{b1}}$, $\Theta = 7.53$; and **e**, **f**: $\mathrm{EVAP_{b2}}$, $\Theta = 7.52$.

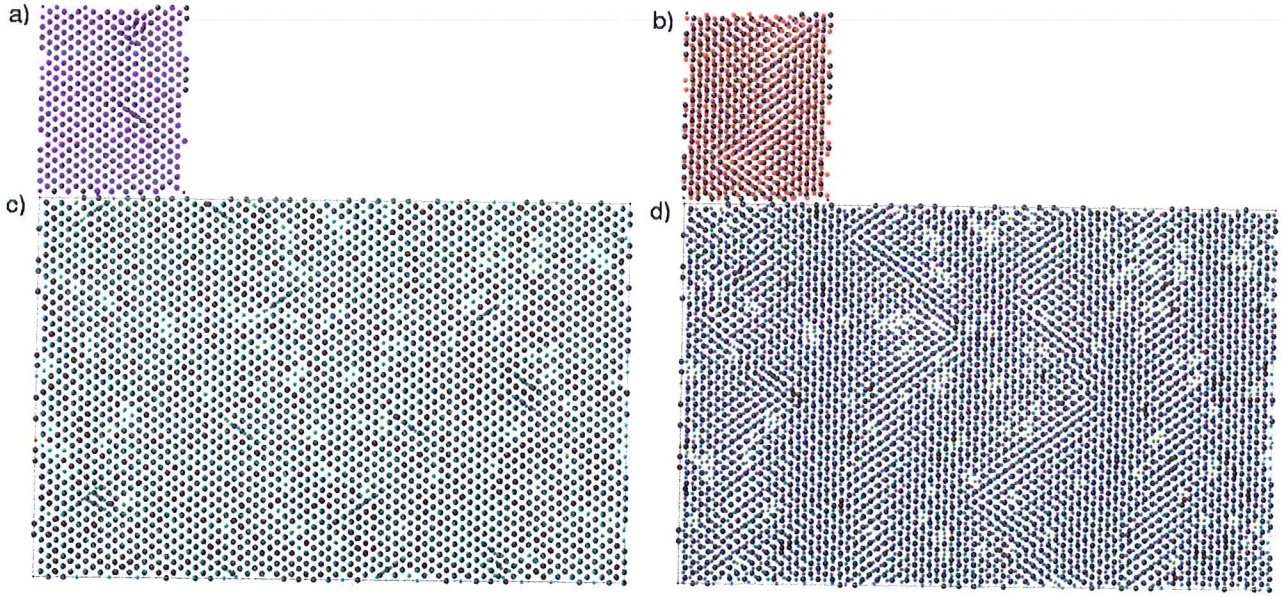

Figure 60: Overlay of the first Cu plane (blue/green) and the second from top substrate plane (Mo black, Cu red/yellow) on the left, and on the right the same substrate plane with the second Cu plane (red/blue). Shown are the two IBAD simulations (**a**, **b**: $\mathrm{IBAD_s}$, **c**, **d**: $\mathrm{IBAD_b}$), both at a coverage of $\Theta \simeq 7.5$.

atoms. The fcc/hcp alternation seen for these streaks is reminiscent of that seen in figure 58 for the very small $\mathrm{EVAP_v}$ simulation. This, together with the pattern from figure 59, leads to the conclusion that these streaks are in a NW-x like orientation relation with the first (bcc) Cu plane, a hetero-epitaxial relation for a single-element interface. A comparison of the pattern seen in figure 59 for the y-oriented strips to the pattern seen for a Cu/Mo imperfect KS-orientation in figure 11, bottom (§2.5.1, page 37) seems to indicate that these strips, and part of the bcc matrix atoms, exhibit a KS orientation relation with the first Cu plane. When comparing the first and fourth row of table XV (page 77), the atomic volume of Cu at several temperatures, it is clear that the mismatch applicable here is different from the mismatch used to construct figure 11. As explained in §2.5.1, it is therefore to be expected that the orientation of the rotational fringes visible in the y-oriented strips is altered from that seen in figure 11 (bottom).

It is remarkable that for $\mathrm{EVAP_{b1}}$, all patterns are oriented along only one of the diagonals, while the patterns in $\mathrm{EVAP_{b2}}$ are along both of the diagonals. Even in the first plane, this behaviour can be identified by the positioning of the interstitials. Looking back, it may be visible as early as in figure 46, left ($\Theta = 5$). The small system, $\mathrm{EVAP_s}$ seems to have more in common with $\mathrm{EVAP_{b2}}$ than with $\mathrm{EVAP_{b1}}$, but with a "twinning" line parallel to the horizontal instead of to the vertical, see figure 59. Both are the smallest system dimension, but it is unclear if this is a coincidence or not.

With IBAD (figure 65) we see that there are patches of hcp atoms and only some fcc atoms in plane 2, but in general there is little change between figures 57 and 60. It is notable that the hcp patches are elongated along the

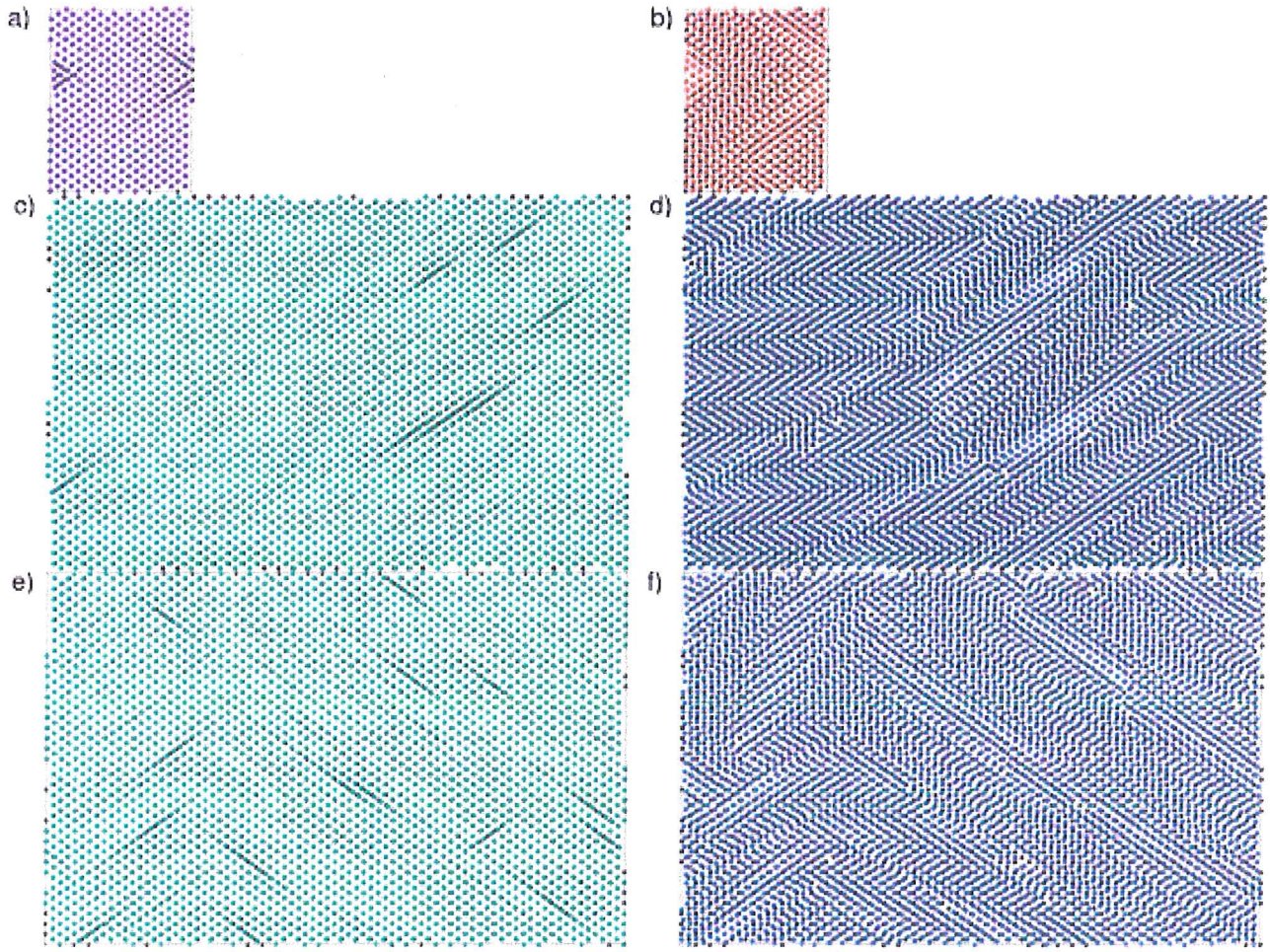

Figure 61: Overlay of the first Cu plane (blue/green) and the second highest substrate plane (black) on the left, and on the right the same but for the second Cu plane (red/blue). Shown are the three different EVAP simulations (**a**, **b**: $\mathrm{EVAP_s}$, $\Theta = 24.06$; **c**, **d**: $\mathrm{EVAP_{b1}}$, $\Theta = 23.94$; and **e**, **f**: $\mathrm{EVAP_{b2}}$, $\Theta = 24.42$.

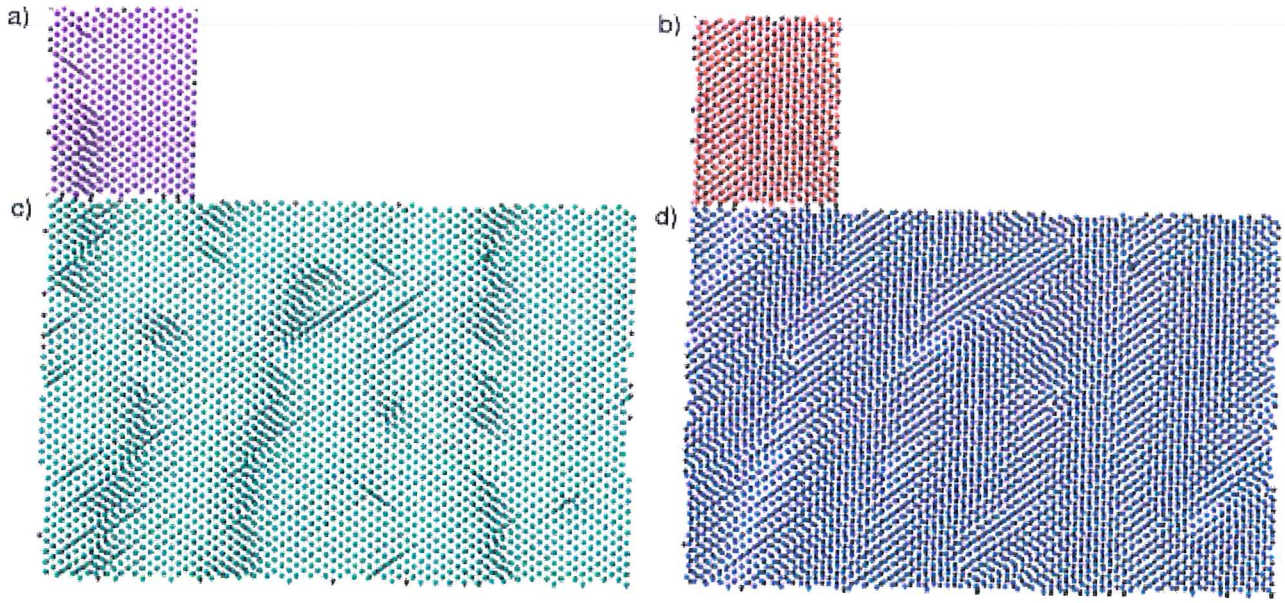

Figure 62: Overlay of the first Cu plane (blue/green) and the second from top substrate plane (Mo black, Cu red/yellow) on the left, and on the right the same substrate plane with the second Cu plane (red/blue). Shown are the two IBAD simulations (**a**, **b**: $\mathrm{IBAD_s}$, $\Theta = 24.55$; **c**, **d**: $\mathrm{IBAD_b}$, $\Theta = 23.92$).

y-direction, while such a pattern is absent for EVAP, where the predominant direction is a diagonal through the simulation boxes. This difference may be due to intermixing. It is also possibly connected to the visibly wider "boundaries" between strips of pseudomorphic structure in plane $k = 1$. Plane $k = 2$ also contains more bcc atoms in IBAD.

For both IBAD and EVAP we see that as a result of the alternating fcc/hcp (and bcc) regions in plane 2, part of the atoms in the first plane is not any more seen as bcc but instead has S undefined (figures 63–65, bottom left). These atoms lie underneath the boundaries of the alternating regions in plane 2, similarly to what was seen for the small $\mathrm{EVAP_v}$ system earlier. This effect is combined with the introduction of the interstitials which itself results in the change of S for a one or two atoms close to the interstitial from $S =$ bcc to fcc or hcp local symmetry, in the same way as seen previously for lower Θ. With the increase in number of interstitials seen through the series of figures 46–56–59–61 (EVAP) and figures 47–57–60–62 (IBAD) there is a tendency for the interstitials to group together. This effect is accompanied by a local change of the structure to an undefined situation. In the EVAP simulations, the increase of the number of interstitials is much slower and ends at about 0.56 $\%_{monolayer}$ interstitials, while IBAD has much more interstitials (3.9 $\%_{monolayer}$ extra atoms for $\mathrm{IBAD_b}$ and 3.1 $\%_{monolayer}$ for $\mathrm{IBAD_s}$) and thus has a considerably modified structure for the first plane. $k = 1$

The structure of the higher planes, $k > 2$, can be concluded to have a clear relation with the structure of the second plane. From figures 63–65, top, we see a partly fcc and partly hcp structure, with both containing stacking-faults (mainly intrinsic, showing two hcp planes in an fcc matrix, see §3.2.8) $k > 2$

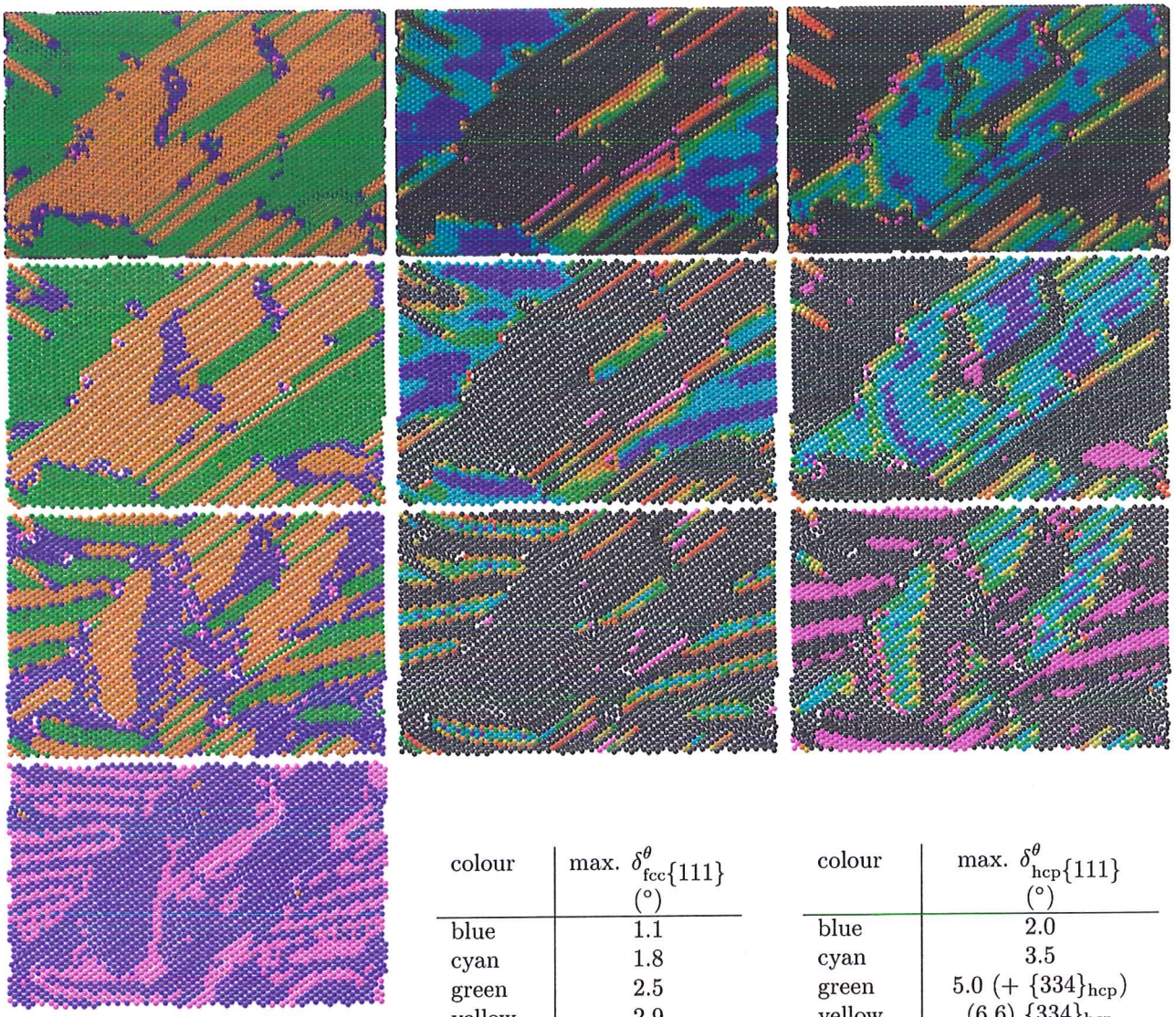

colour	max. $\delta^{\theta}_{\mathrm{fcc}}\{111\}$ (°)
blue	1.1
cyan	1.8
green	2.5
yellow	2.9
orange	3.2
red	4.5
magenta	5.2 + $\{334\}_{\mathrm{fcc}}$
black	$S \neq$ fcc

colour	max. $\delta^{\theta}_{\mathrm{hcp}}\{111\}$ (°)
blue	2.0
cyan	3.5
green	5.0 (+ $\{334\}_{\mathrm{hcp}}$)
yellow	(6.6) $\{334\}_{\mathrm{hcp}}$
orange	(8.1) $\{334\}_{\mathrm{hcp}}$
red	(9.9) $\{334\}_{\mathrm{hcp}}$
magenta	(11.8) $\{001, 012\}_{\mathrm{hcp}}$
black	$S \neq$ hcp

Figure 63: A selection of planes of $\mathrm{EVAP}_{\mathrm{b1}}$ at $\Theta = 7.52$. From left to right, the same plane is shown with atoms coloured by S, and by the deviation δ^{θ} from two specific crystal orientations (see §3.2.8): $\delta^{\theta}_{\mathrm{fcc}}\{111\}$ and $\delta^{\theta}_{\mathrm{hcp}}\{111\}$, with the non-fcc (non-hcp) atoms shown in black. At the higher deviations, a different set of orientations may be more closely matched. In these cases, this (these) are indicated. From bottom to top, the first, second, and third plane are shown. The top pictures are a view of the configuration from above, with a "cap" cut away from the top of the film.

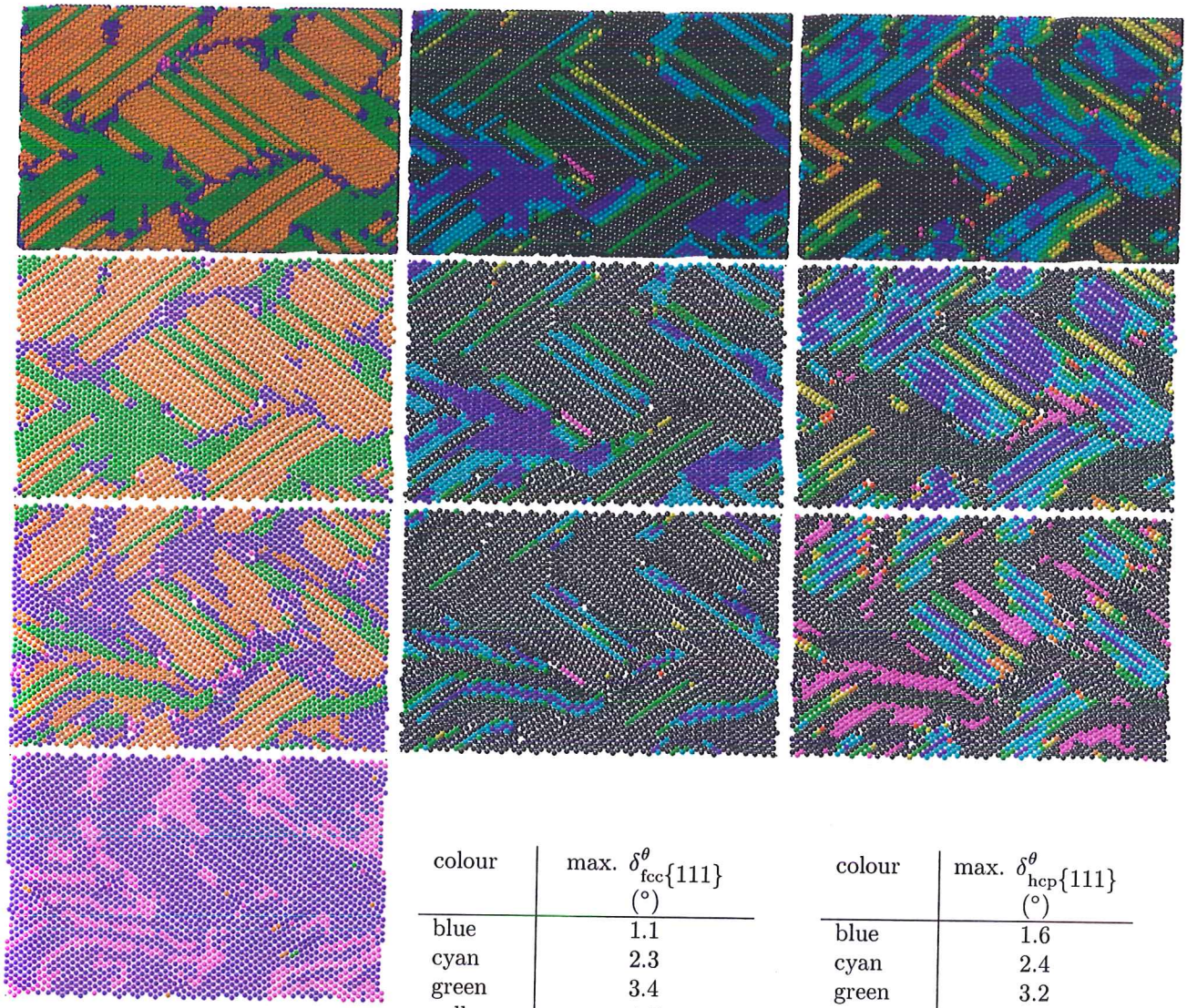

colour	max. $\delta^{\theta}_{\mathrm{fcc}}\{111\}$ (°)
blue	1.1
cyan	2.3
green	3.4
yellow	4.7
orange	5.6 + $\{344\}_{\mathrm{fcc}}$
red	(6.9) $\{344, 334\}_{\mathrm{fcc}}$
magenta	(8.2) $\{334\}_{\mathrm{fcc}}$
black	$S \neq$ fcc

colour	max. $\delta^{\theta}_{\mathrm{hcp}}\{111\}$ (°)
blue	1.6
cyan	2.4
green	3.2
yellow	4.0
orange	5.0
red	6.0 + $\{344\}$
magenta	6.9 + $\{001\}_{\mathrm{hcp}}$
black	$S \neq$ hcp

Figure 64: A selection of planes of $\mathrm{EVAP}_{\mathrm{b2}}$ at $\Theta = 7.52$. From left to right, the same plane is shown with atoms coloured by S, and by the deviation δ^{θ} from two specific crystal orientations (see §3.2.8): $\delta^{\theta}_{\mathrm{fcc}}\{111\}$ and $\delta^{\theta}_{\mathrm{hcp}}\{111\}$, with the non-fcc (non-hcp) atoms shown in black. At the higher deviations, a different set of orientations may be more closely matched. In these cases, this (these) are indicated. From bottom to top, the first, second, and third plane are shown. The top pictures are a view of the configuration from above, with a "cap" cut away from the top of the film.

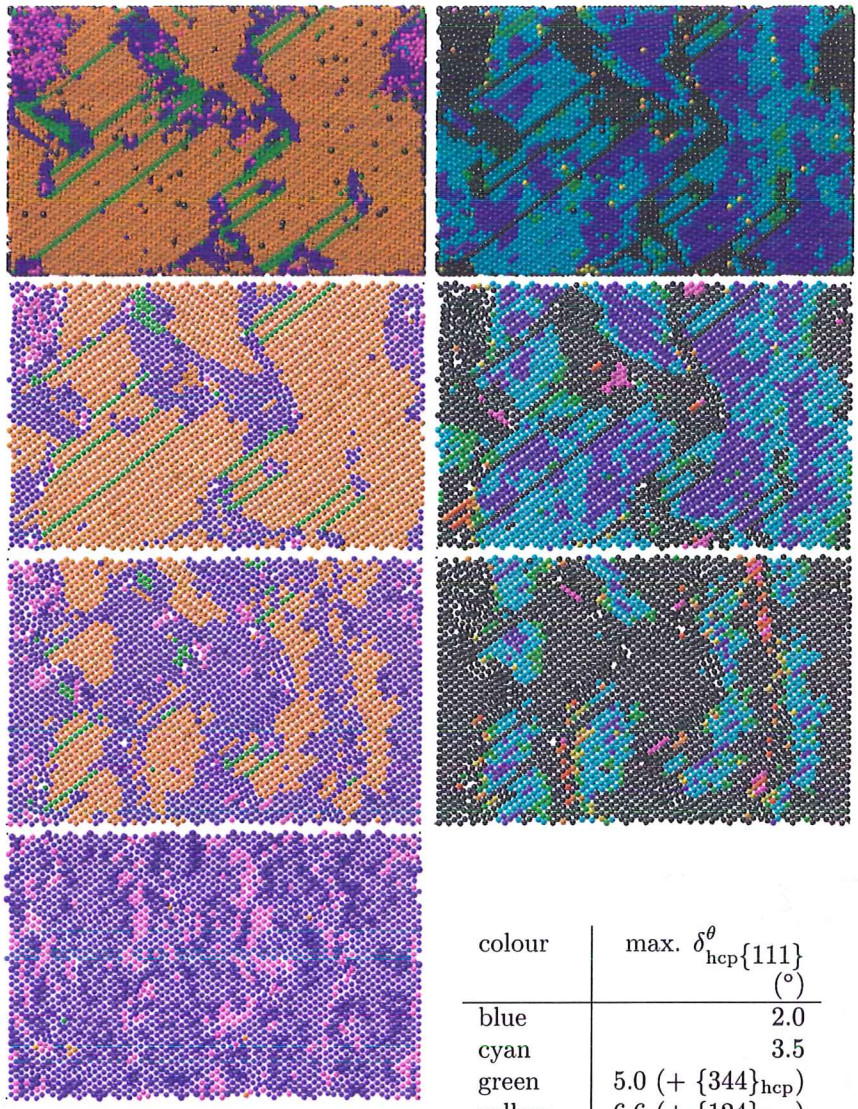

colour	max. $\delta^{\theta}_{\mathrm{hcp}}\{111\}$ (°)
blue	2.0
cyan	3.5
green	5.0 (+ $\{344\}_{\mathrm{hcp}}$)
yellow	6.6 (+ $\{124\}_{\mathrm{hcp}}$)
orange	8.1 + $\{344\}_{\mathrm{hcp}}$
red	$\{344\}_{\mathrm{hcp}}$
magenta	$\{001\}_{\mathrm{hcp}}$ + other
black	$S \neq$ hcp

Figure 65: A selection of planes of $\mathrm{IBAD_b}$ at $\Theta = 7.52$. From left to right, the same plane is shown with atoms coloured by S, and by the deviation δ^{θ} from a specific crystal orientation (see §3.2.8):$\delta^{\theta}_{\mathrm{hcp}}\{111\}$, with the non-hcpatoms shown in black. At the higher deviations, a different set of orientations may be more closely matched. In these cases, this (these) are indicated. From bottom to top, the first, second, and third plane are shown. The top pictures are a view of the configuration from above, with a "cap" cut away from the top of the film. The few fcc planes between the hcp ones are mostly in a $\{344\}_{\mathrm{fcc}}$ orientation, with some in $\{014\}_{\mathrm{fcc}}$ and a few edges are seen to have a $\{122\}_{\mathrm{fcc}}$ orientation.

terminated by one to three bcc atoms in each plane. The regions are surrounded by "walls" of bcc atoms, that could be grain boundaries. In any case, the visible atomic rows longer than about a halve box-x seem to have two small kinks in them, at roughly the same "latitude" at which two stacking-faults end in groups of bcc atoms. IBAD still has almost no fcc in these planes too, apart from the few stacking faults ribbons of close-packed planes.

Bcc collapse — a phase transition Figure 66 shows the development of the fractions of atoms with a specific S for all of the simulations. Clearly, they all have a peak in the fraction of bcc during the 3-D growth stage. At higher coverages, as the structure starts to evolve, the fractions of hcp and fcc increase. In all simulations, there is a sudden downfall in the fraction of bcc atoms, and a simultaneous rise in the fraction of hcp between $\Theta \sim 6$–7.5 ($D = 13$–17 Å). The pseudomorphy can no longer be sustained (for $k > 1$), and a phase transition takes place. Figure 67 shows the slope of the bcc-curves from figure 66, illustrating the sharp transition in the fraction of bcc atoms. Note that the phase transition takes place at a higher coverage/thickness than fall in roughness, and that the roughness and growth mode (β_k) do not show significant changes during the collapse in bcc atoms. From the figure we can also conclude that during island growth, of the deposited atoms, 50–70 % takes on a bcc geometry. For the large systems this is also accompanied by a rise in the fraction of fcc atoms. The small systems have an increase in fcc fraction as well but this occurs only near the end of this coverage range, from $\Theta \sim 8$–9 ($D = 18$–20 Å).

All k, $\Theta \rightsquigarrow 24$

During the remainder of the deposition the fraction of fcc and the fraction of hcp atoms varies widely between the simulations. For EVAP_{b1}, the initial rise in hcp is halted as the fraction of fcc sharply increases. However, we have so far not found any indication that something special takes place here in this simulation. Both the fractions of bcc and that of undefined atoms continually decreases after this coverage (thickness) mark, lets say from $\Theta \sim 6$ or 13.4 Å, at a point where 3-D growth has already ceased. After the sudden decrease in bcc following the 3-D growth, there is an intermediate coverage range ($\Theta = 9$–18, $D = 20$–40 Å) where these fractions roughly diminish linearly with the coverage/thickness. In figure 67, we see that the number of bcc atoms slightly decreases for these coverages. Above this, the decrease is probably inverse with the coverage/thickness, as the absolute number of bcc atoms increases, but only very slightly (small positive value in figure 67), while the number of atoms in the system increases. The very small increase in number of bcc atoms is associated with defect production (figures 77–81 later in the section clearly illustrate this effect). At this advanced stage near the end of most of the performed simulations, the bcc atoms are mainly concentrated in the first two planes, while the undefined atoms are found in the first Cu plane and in the surface planes. The higher k (bulk) planes are divided in fcc and hcp, with a evenly distribution over the planes, see figure 68, which shows the amount of atoms of S for $\Theta \sim 24$ ($D = 54$ Å). The composition of the lower planes remains relatively unaltered from figure 55, except for the higher amount of

simulations vary in fcc/hcp ratio

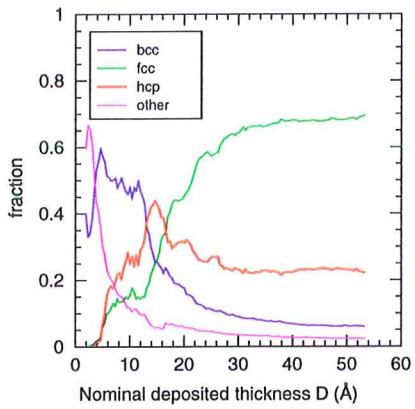

(a) $\mathrm{EVAP_{b1}}$

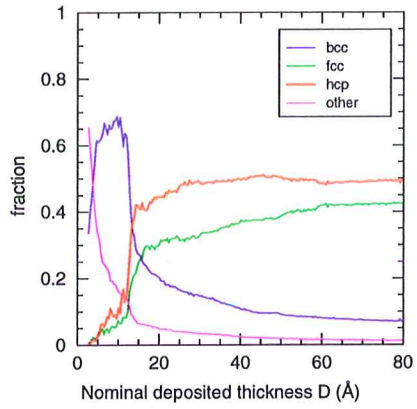

(b) $\mathrm{EVAP_{b2}}$

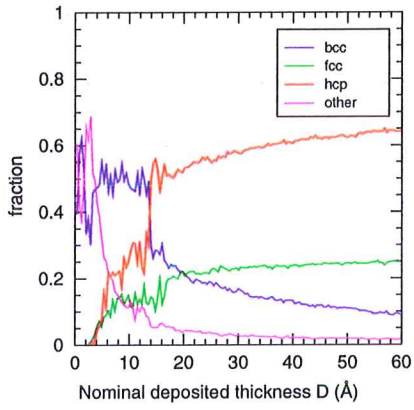

(c) $\mathrm{EVAP_s}$

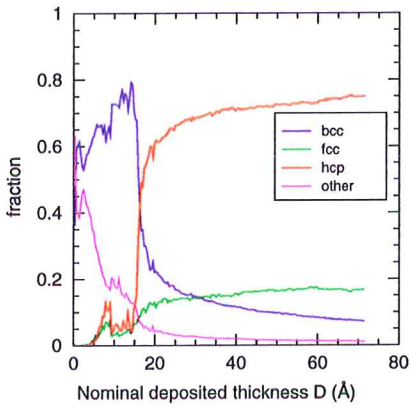

(d) $\mathrm{IBAD_b}$

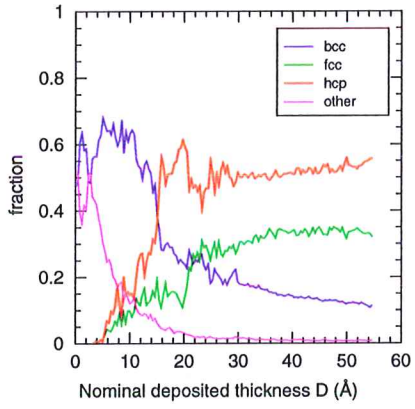

(e) $\mathrm{IBAD_s}$

Figure 66: Fraction of each $S =$ bcc, fcc, hcp or undefined (ico and dia are only negligible fractions). Bottom left is $\mathrm{IBAD_b}$, right is $\mathrm{IBAD_s}$. In the middle, $\mathrm{EVAP_s}$ is given, top left is $\mathrm{EVAP_{b1}}$ and top right is $\mathrm{EVAP_{b2}}$. Data is from quenched configurations.

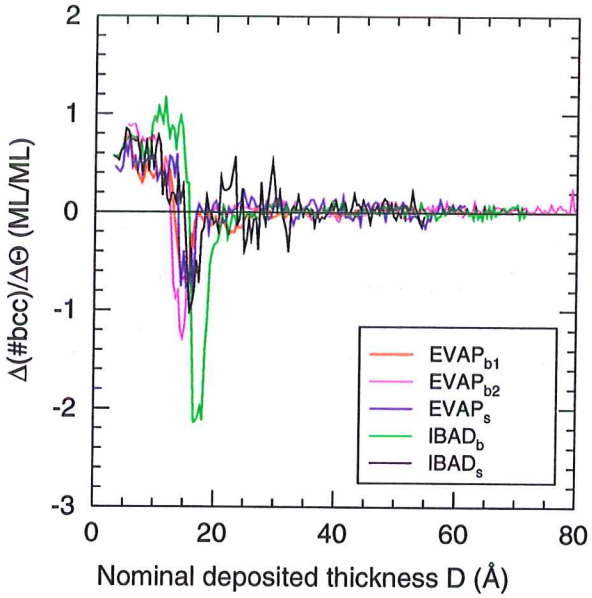

Figure 67: Increase in amount of bcc atoms with increasing coverage versus the thickness (the slope of the curves from figure 66). Note that the peak in the roughness due to island growth is found at a coverage of $\Theta \sim 2.5$–5.4 ($D = 5$–12 Å).

atoms in an undefined local symmetry.

The average (and the distribution of the) number of neighbours shows if the planes can be seen as bulk-like (see §3.2.3). From this, as well as from the change in structure as shown in figure 68, we can see that the interface region is two layers thick, with perhaps a small influence up to the fourth Cu plane. The (influence of the) surface spans five atomic planes for the large systems. In the small systems this is only three planes.

Development of a nanostructure From the previously described structure consisting of alternating bcc strips and hcp/fcc regions ($\Theta \sim 5$) mainly oriented along the y-direction, the amount of bcc decreases and grain-like regions form in the $k > 2$ planes for coverages above $\Theta \sim 5$–5.5 ($D \sim 11$–12 Å). The structure that emerges for the $k > 2$ planes starting from about $\Theta = 4.5$, ($D \simeq 10$ Å) continues its development though. For $\Theta \simeq 4.5$–7 ($D \sim 10$–16 Å) the amount of bcc atoms strongly reduces. This is accompanied by a change from the former y-axis orientation to a more diagonal orientation of the visible structures. As seen in figures 63–65, at a coverage of $\Theta \simeq 7.5$ bcc atoms are seen near boundaries of regions of uniform structure/orientation for planes $k > 2$. In fact, it turns out that these bcc "fences" between the regions form a network-structure through the entire film thickness. Projecting the $(x, y$-)positions of these bcc atoms onto a single (xy-)plane shows this, as visible in figures 69–73. In these figures ("bccdot-plots") each dot represents a bcc atom in any of the $k > 2$ planes. Following the development of the pattern formed by these dots during the deposition, a clear change is seen in the film. The figures show a

$k > 2$

bccdot-plots

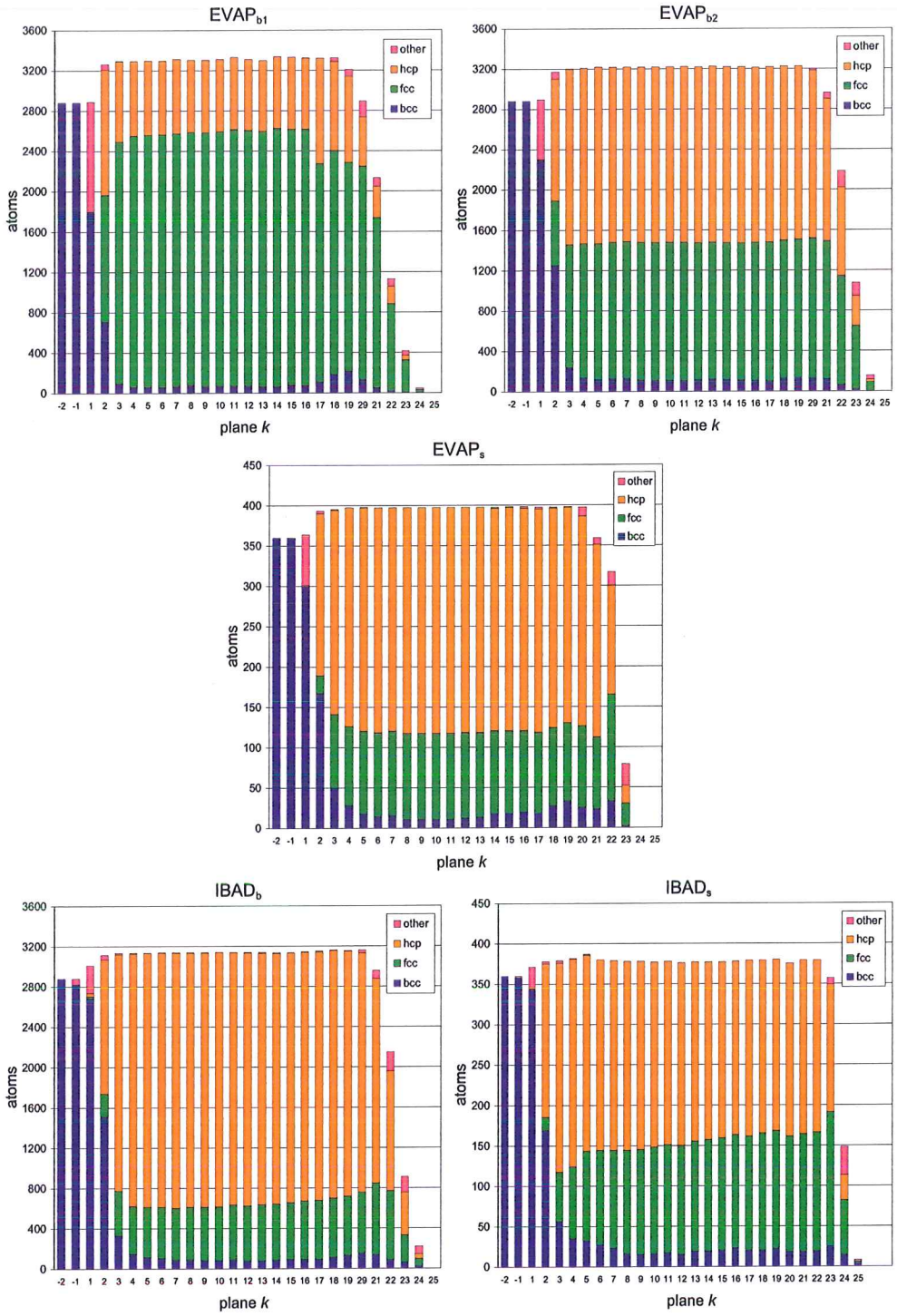

Figure 68: Crystal structure in the Cu on Mo deposition simulations at $\Theta \sim 24$ ($\mathrm{EVAP_{b1}}$: $\Theta = 23.94$; $\mathrm{EVAP_{b2}}$: $\Theta = 24.42$; $\mathrm{EVAP_s}$: $\Theta = 24.06$; $\mathrm{IBAD_s}$: $\Theta = 24.55$; $\mathrm{IBAD_b}$: $\Theta = 24.42$; $D \sim 54$ Å). The number of atoms of each S = bcc, fcc, hcp or other (S = undefined, ico or dia, see §3.2.8) is given for the individual planes $k = 1, 2, 3, \ldots, 25$ and for the two top substrate planes, $k = -1, -2$ as well. The configurations are the same as those used for the fifth staircase step (all are quenched). We can see that in all simulations, the fraction of fcc is higher in the surface planes than in the bulk. For IBAD, the fraction fcc actually slightly increases with k.

selection of configurations at characteristic thicknesses so that this development becomes visible.

In all simulations the previously concluded change away from a y-axis oriented is seen. Notably, for EVAP the change takes only until a thickness $D \simeq 13.5$ Å, equivalent to $\Theta = 6.1$, while for IBAD_s, the change does not occur before $D \sim 15.5$ Å$/\Theta = 7.0$. For IBAD_b there exists, briefly and not visible in the shown pictures, a predominantly diagonally oriented structure, which is followed by a reappearance of y-axis oriented structures which are retained at higher coverages. In the EVAP simulations, a network is seen consisting mainly of x- or somewhat diagonally oriented bcc "fences", with only some interconnecting y-oriented strips. With IBAD the y-oriented strips or patches (IBAD_s) are the main feature. In this network, ring-like structures are seen. Not visible from the limited selection of pictures shown, these rings pulsate, with the bcc-atom fences of bcc atoms expanding and retracting. Above $\Theta \sim 9$ ($D = 20$ Å), the rings collapse and the amount of bcc in the $k > 2$ planes diminishes. This development is visible in figure 66. The small EVAP simulation, EVAP_s also has this diminishing amount of bcc atoms, but here there are no rings visible, only a development of two thin strips of bcc atoms along the x-direction, which then remain unchanged during the rest of the simulation. In the other simulations, above $\Theta = 9$, $D = 20$ Å, there is an increasing concentration of bcc atom "curls" forming a wall along the y-axis. Later the individual bcc curls evolve into two wall-like features in the larger systems. This structural feature is clearly demonstrated in the staircases fifth step. It seems as if the IBAD_s simulation only has room for one of these walls. Perpendicular to the walls, the curls change into loops along which the walls move back and forth, again pulsating (not really visible from the shown pictures). In the large systems, the walls seem to move closer together, creating one smaller and a larger area between them (remember, the systems have periodic boundaries). There are also one or two more individual ring-like features visible. In all simulations, the curls and ring-like features undergo an oscillating lateral motion with a frequency of about 15 MHz and an amplitude of 2–5 Å (not shown).

All k

Now returning to the crystal structure at $\Theta \sim 24$, $D = 54.5$ Å, shown in numbers by figure 68 for all individual planes, and figures 74–76 (left) that show the way these numbers are placed within the planes, we can recognize the pattern of bcc atoms from the bccdot-plots. It is clear that the small amount of bcc atoms still present in the bulk is located in the structures from the bccdot-plots. The increased amount of hcp in plane 18 and plane 19 of EVAP_b1, seen in figure 74 is explained by the existence of a hcp patch which is visible at the top of figure 74. From the staircase figure 39 and the amount of hcp in higher planes we see that this is only a single (tilted) hcp plane segment between two stacking fault lines. Looking at the structure, the first plane now has a imperfect pseudomorphic structure, containing patches with unidentified structure, especially for IBAD. In the higher planes, the Moiré-streaks disappear and the band-regions grow in size, "eating" away the bcc matrix until only their boundaries are decorated/marked by bcc atoms. This results in a nano-grained structure.

$k > 2$

To combine the information that the bccdots-plots offer with that from

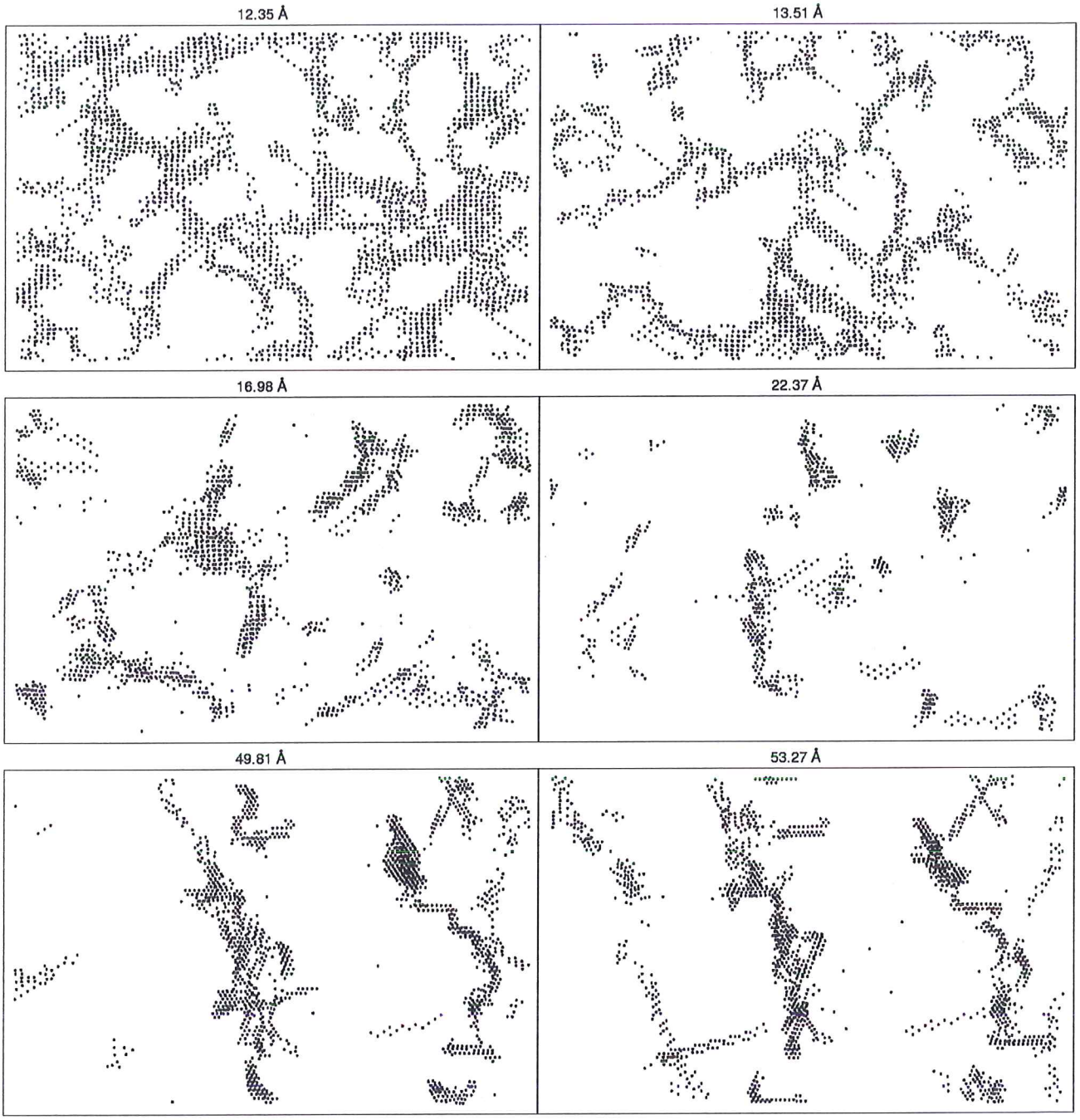

Figure 69: Development of film nanostructure during continued deposition for $\mathrm{EVAP_{b1}}$. Shown is a top-down projection of the positions of the bcc atoms in the planes with $k > 2$ for several thicknesses (coverages). Clearly, there is an initial strong reduction in the amount of bcc atoms, followed by the development of a network of bcc atoms, which breaks up and then forms two grain boundaries. All data is from quenched configurations. In the text, the figure is referred to as a bccdot-plot.

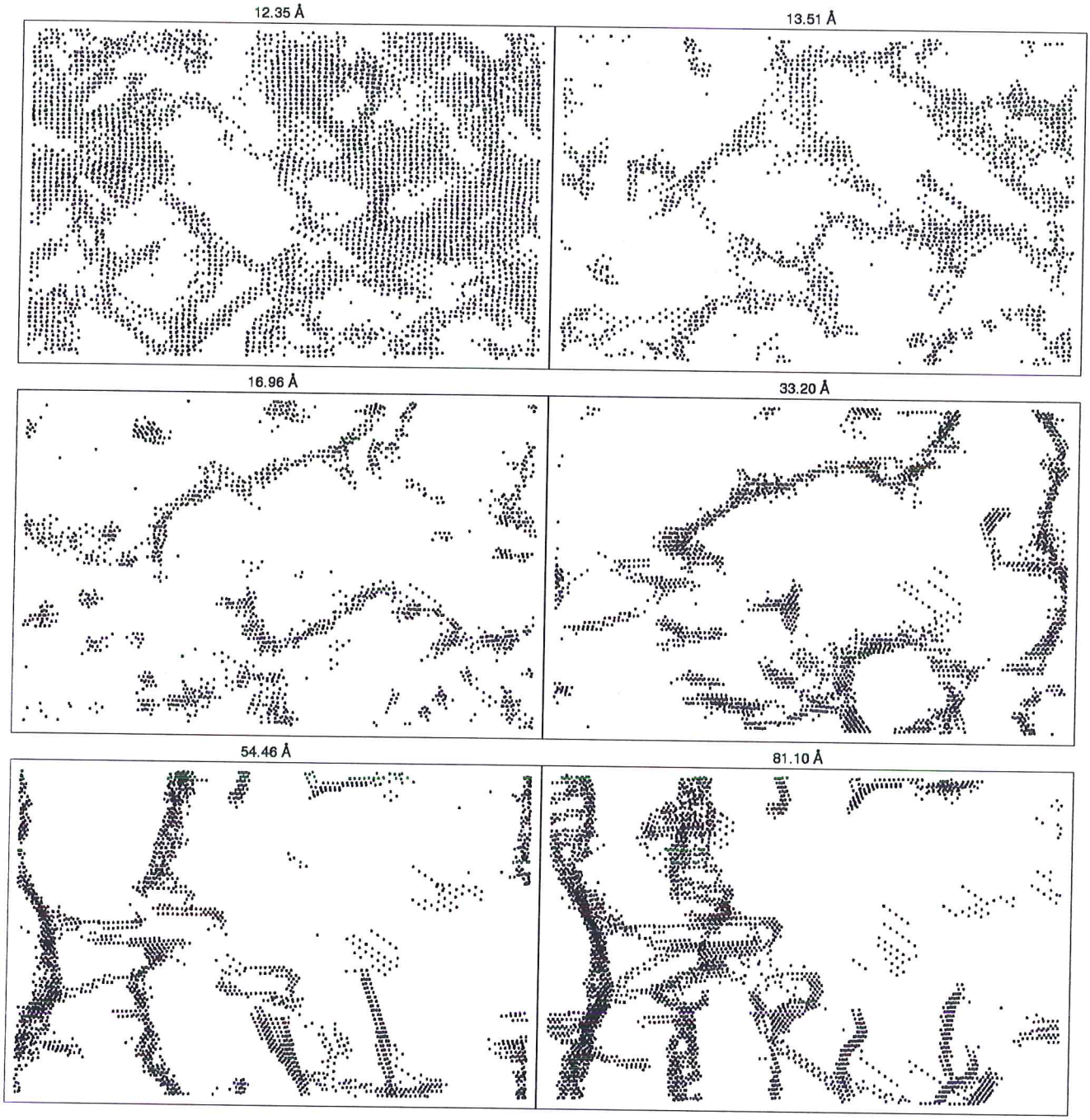

Figure 70: Development of film nanostructure during continued deposition for $\mathrm{EVAP}_{\mathrm{b2}}$. Shown is a top-down projection of the positions of the bcc atoms in the planes with $k > 2$ for several thicknesses (coverages). Clearly, there is an initial strong reduction in the amount of bcc atoms, followed by the development of a network of bcc atoms, which breaks up and then forms two grain boundaries. All data is from quenched configurations. In the text, the figure is referred to as a bccdot-plot.

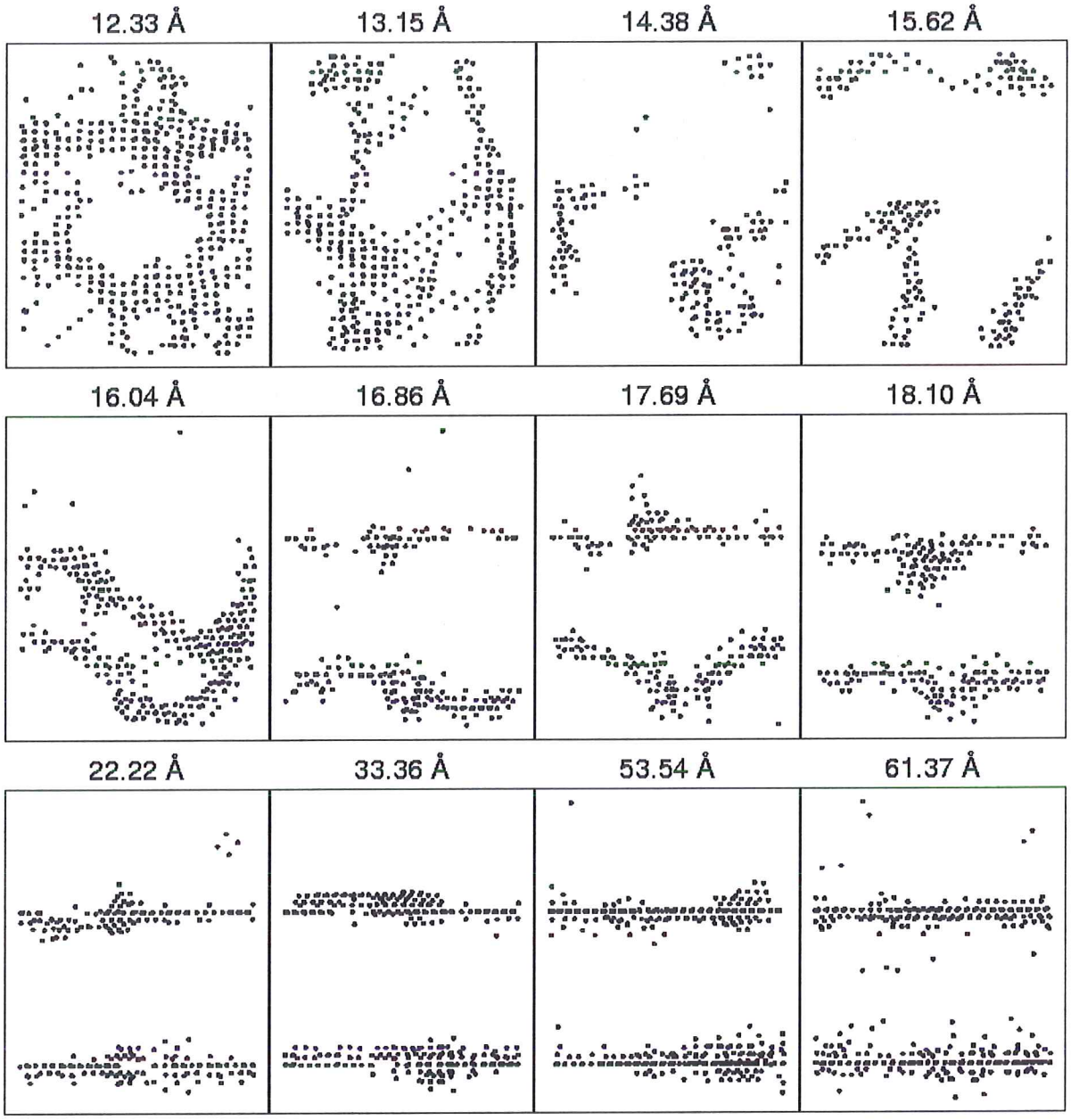

Figure 71: Development of film nanostructure during continued deposition for $EVAP_s$. Shown is a top-down projection of the positions of the bcc atoms in the planes with $k > 2$ for several thicknesses (coverages). Clearly, there is an initial strong reduction in the amount of bcc atoms, followed by the development of a network of bcc atoms, which breaks up and then forms two grain boundaries. All data is from quenched configurations. In the text, the figure is referred to as a bccdot-plot.

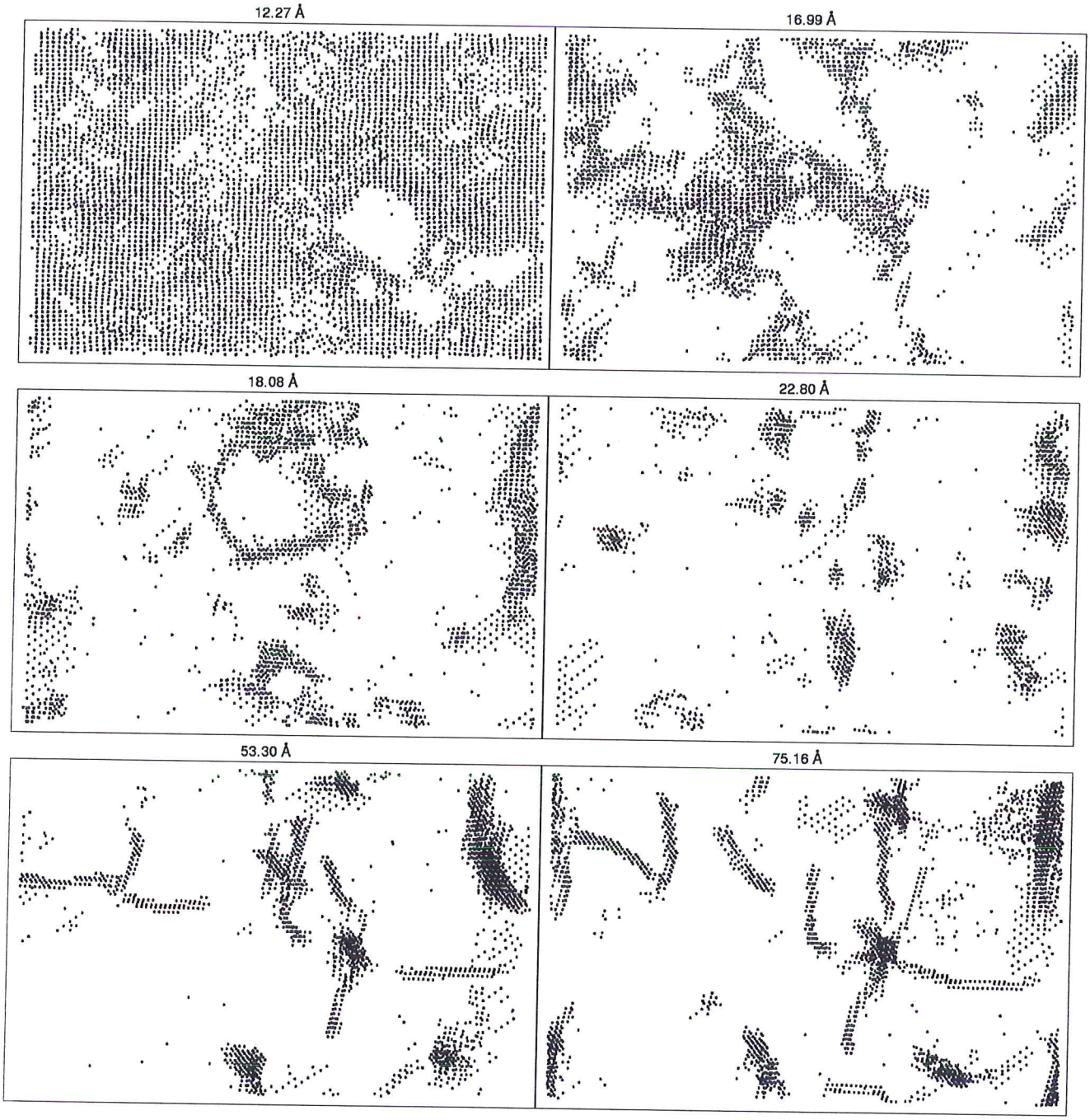

Figure 72: Development of film nanostructure during continued deposition for $\mathrm{IBAD_b}$. Shown is a top-down projection of the positions of the bcc atoms in the planes with $k > 2$ for several thicknesses (coverages). Clearly, there is an initial strong reduction in the amount of bcc atoms, followed by the development of a network of bcc atoms, which breaks up and then forms two grain boundaries. All data is from quenched configurations. In the text, the figure is referred to as a bccdot-plot.

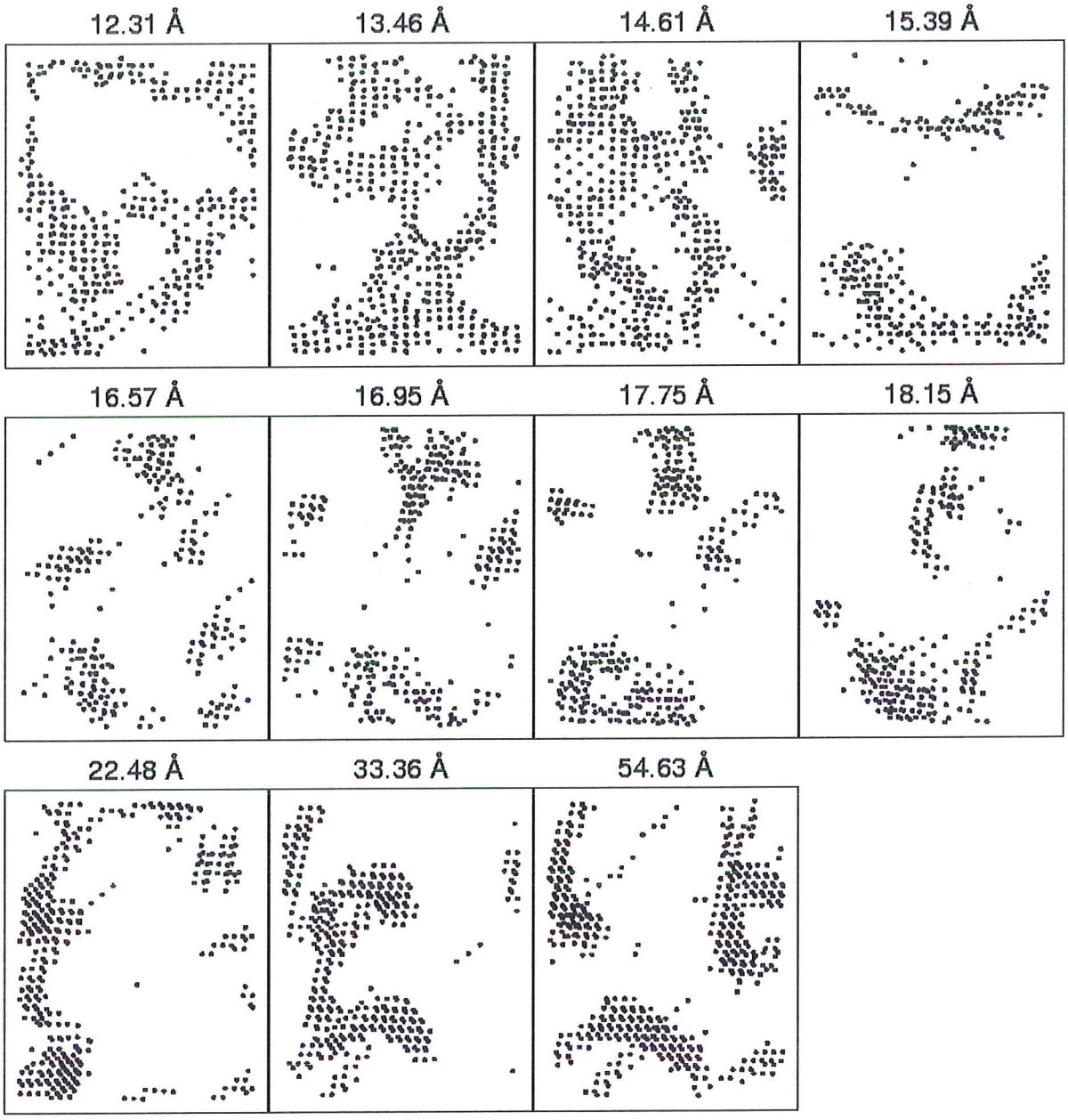

Figure 73: Development of film nanostructure during continued deposition for $IBAD_s$. Shown is a top-down projection of the positions of the bcc atoms in the planes with $k > 2$ for several thicknesses (coverages). Clearly, there is an initial strong reduction in the amount of bcc atoms, followed by the development of a network of bcc atoms, which breaks up and then forms two grain boundaries. All data is from quenched configurations. In the text, the figure is referred to as a bccdot-plot.

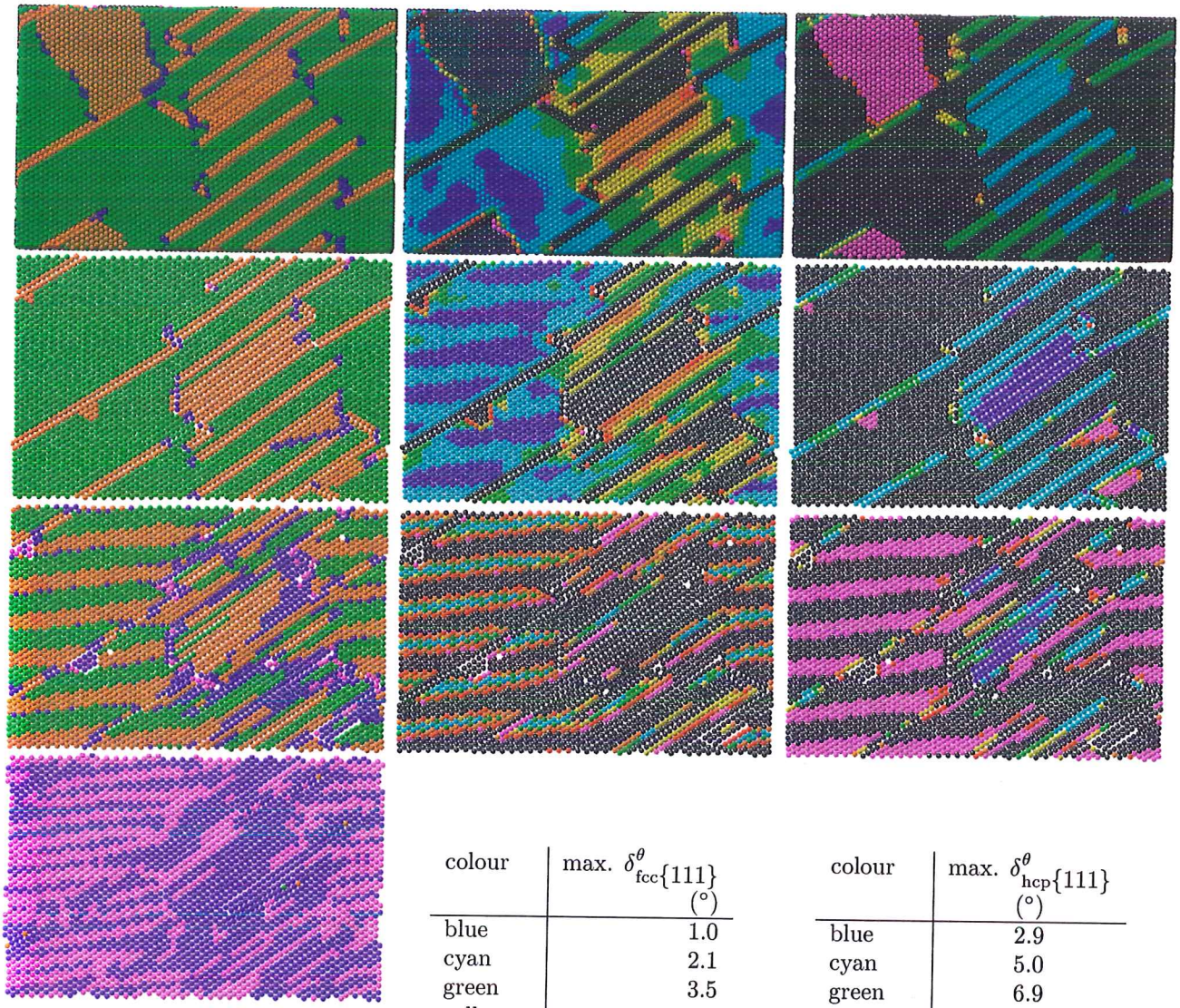

colour	max. $\delta^{\theta}_{\text{fcc}\{111\}}$ (°)
blue	1.0
cyan	2.1
green	3.5
yellow	4.6
orange	5.8
red	6.9
magenta	$8.2 + \{334\}_{\text{fcc}}$
black	$S \neq \text{fcc}$

colour	max. $\delta^{\theta}_{\text{hcp}\{111\}}$ (°)
blue	2.9
cyan	5.0
green	6.9
yellow	$9.1 + \{124\}_{\text{hcp}}$
orange	$(11.7)\ \{012\}_{\text{hcp}}$
red	$\{124, 012\}_{\text{hcp}}$
magenta	$\{001\}_{\text{hcp}}$
black	$S \neq \text{hcp}$

Figure 74: A selection of planes of EVAP_{b1} at $\Theta = 23.94$. From left to right, the same plane is shown with atoms coloured by S, and by the deviation δ^{θ} from two specific crystal orientations (see §3.2.8): $\delta^{\theta}_{\text{fcc}\{111\}}$ and $\delta^{\theta}_{\text{hcp}\{111\}}$, with the non-fcc (non-hcp) atoms shown in black. At the higher deviations, a different set of orientations may be more closely matched. In these cases, this (these) are indicated. From bottom to top, the first, second, and third plane are shown. The top pictures are a view of the configuration from above, with a "cap" cut away from the top of the film.

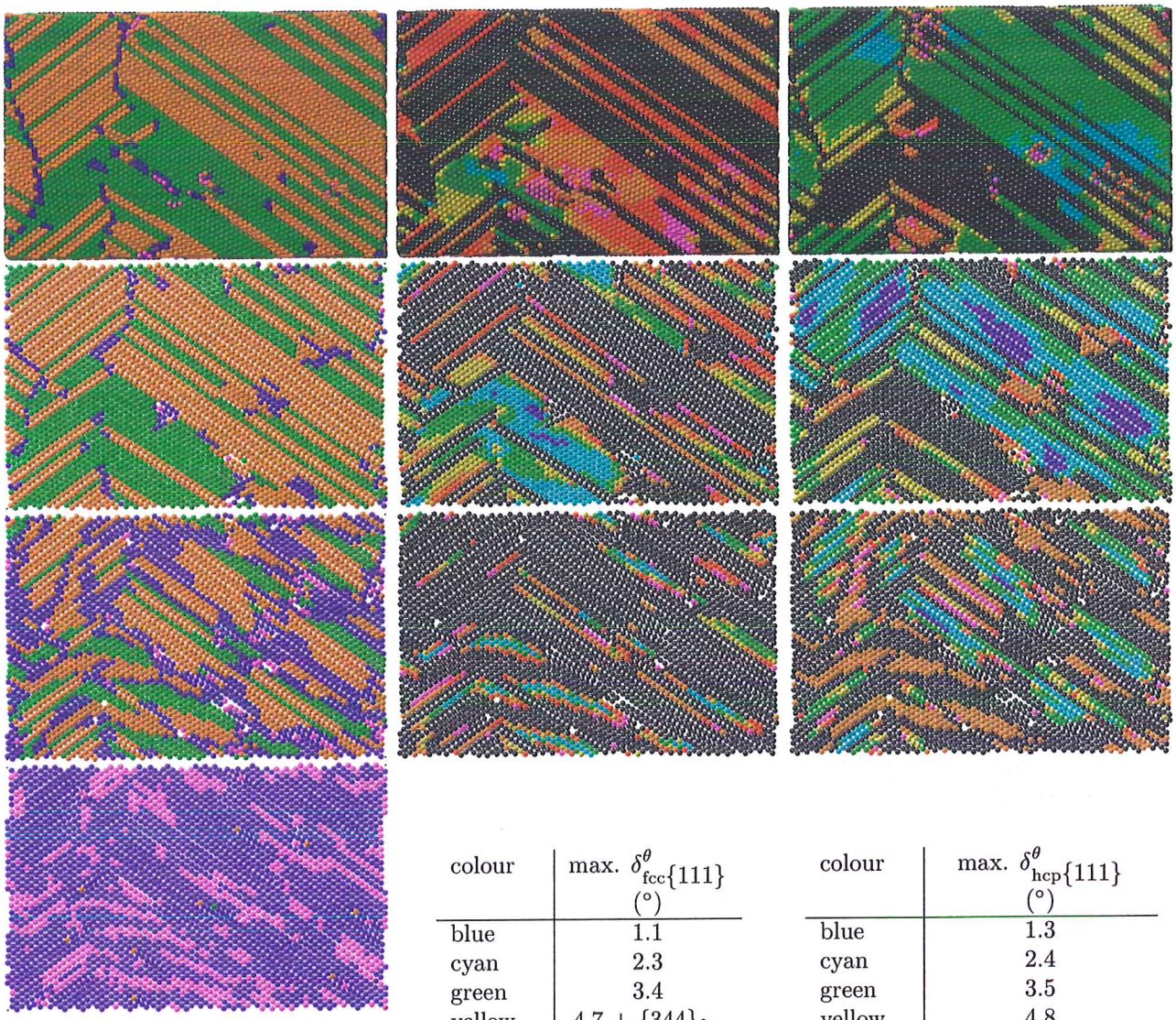

colour	max. $\delta^{\theta}_{\mathrm{fcc}}\{111\}$ (°)
blue	1.1
cyan	2.3
green	3.4
yellow	4.7 + $\{344\}_{\mathrm{fcc}}$
orange	(5.6) $\{344\}_{\mathrm{fcc}}$
red	(6.9) $\{344\}_{\mathrm{fcc}}$
magenta	(8.1) $\{334\}_{\mathrm{fcc}}$
black	$S \neq$ fcc

colour	max. $\delta^{\theta}_{\mathrm{hcp}}\{111\}$ (°)
blue	1.3
cyan	2.4
green	3.5
yellow	4.8
orange	6.1
red	7.3 + $\{344, 124\}_{\mathrm{hcp}}$
magenta	(8.7) $\{001, 124\}_{\mathrm{hcp}}$
black	$S \neq$ hcp

Figure 75: A selection of planes of $\mathrm{EVAP}_{\mathrm{b2}}$ at $\Theta = 24.42$. From left to right, the same plane is shown with atoms coloured by S, and by the deviation δ^{θ} from two specific crystal orientations (see §3.2.8): $\delta^{\theta}_{\mathrm{fcc}}\{111\}$ and $\delta^{\theta}_{\mathrm{hcp}}\{111\}$, with the non-fcc (non-hcp) atoms shown in black. At the higher deviations, a different set of orientations may be more closely matched. In these cases, this (these) are indicated. From bottom to top, the first, second, and third plane are shown. The top pictures are a view of the configuration from above, with a "cap" cut away from the top of the film.

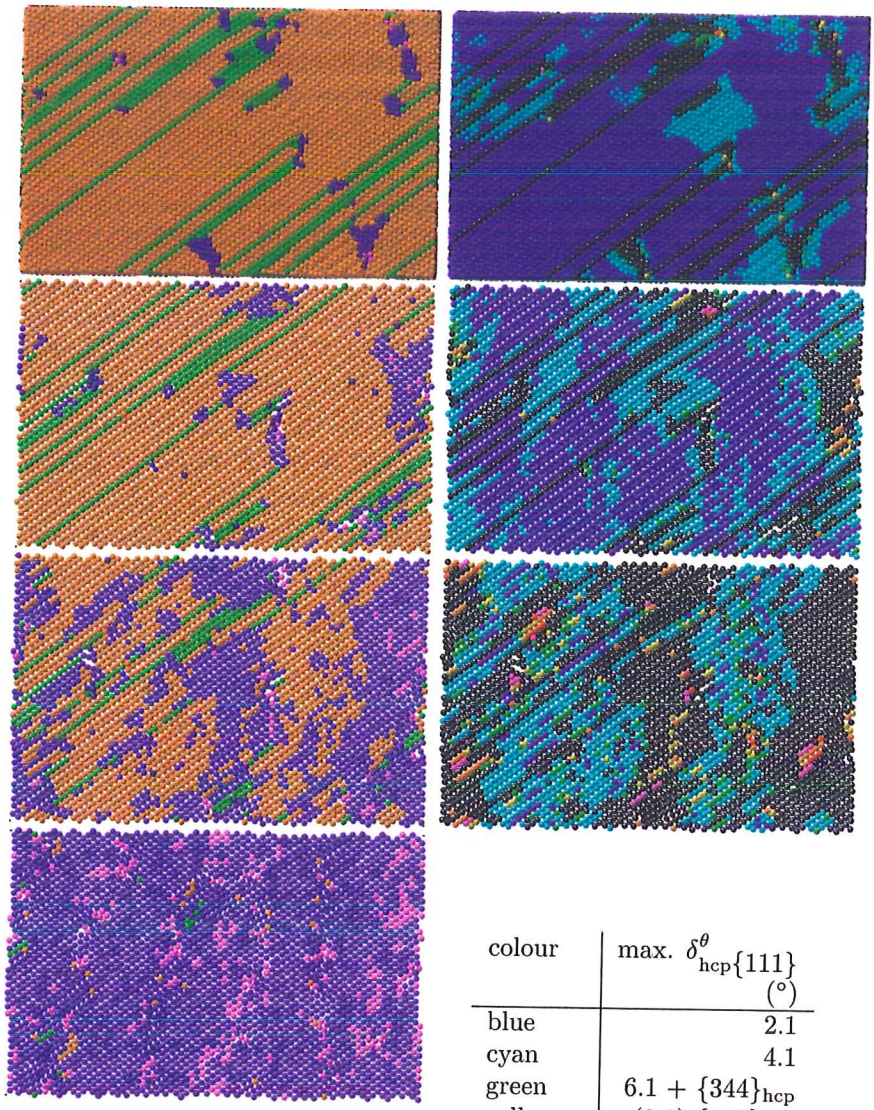

colour	max. $\delta^{\theta}_{\mathrm{hcp}\{111\}}$ (°)
blue	2.1
cyan	4.1
green	6.1 + $\{344\}_{\mathrm{hcp}}$
yellow	(8.1) $\{344\}_{\mathrm{hcp}}$
orange	(10.3) $\{344\}_{\mathrm{hcp}}$
red	$\{344\}_{\mathrm{hcp}}$
magenta	$\{001\}_{\mathrm{hcp}}$
black	$S \neq \mathrm{hcp}$

Figure 76: A selection of planes of $\mathrm{IBAD_b}$ at $\Theta = 24.42$. From left to right, the same plane is shown with atoms coloured by S, and by the deviation δ^{θ} from a specific crystal orientation (see §3.2.8): $\delta^{\theta}_{\mathrm{hcp}\{111\}}$, with the non-hcp atoms shown in black. From bottom to top, the first, second, and third plane are shown. The top pictures are a view of the configuration from above, with a "cap" cut away from the top.The few fcc planes between the hcp ones are mostly in a $\{344\}_{\mathrm{fcc}}$ orientation, with some in $\{014\}_{\mathrm{fcc}}$ and a few edges are seen to have a $\{122\}_{\mathrm{fcc}}$ orientation.

figures 74–76 in order to obtain a better impression of the crystal structure, 3-D views of the systems ("3D-bccdot" figures, showing the same atoms as the bccdot-plots but adding an extra dimension) near the end of the simulations are shown in figures 77–81. In the figures, the non-bcc atom made tiny (and $k > 2$). The bcc atoms clearly form chimney-like structures extending from the Cu/Mo interface upward to the surface. These are threading dislocations. At places, notably in the middle of the EVAP_{b1} figure, the dislocations enclose a stacking-fault area. Only a few isolated bcc atoms are visible, and most of these are at the surface. The seemingly isolated small patches of (or individual) bcc atoms, which are especially clear for IBAD_{b}, are actually connected to plane 2 bcc strips (see figures 74–76, 84–85 left, third from top). From the aforementioned figures, we can construct an image of what the film crystal- and nanostructure are. This reconstruction tells us that on top of the first Cu plane, located along atom rows containing interstitials double (and sometimes more) close-packed planes of hcp or fcc develop at an angle of 60° with the substrate plane. These planes extend up to the surface. They divide the remaining (hcp or fcc) atoms in the z-planes into domains. Looking at the stacking sequence within the z-planes, we find that the different geometry close-packed planes indeed are located at stacking faults.

3D-bccdot figs

fcc/hcp crystal with stacking-faults

From now on, the analysis of the symindex-texture really shows that a fcc/hcp crystal evolves, with stacking-fault like regions in between, probably to relieve stress. These stacking-faults are "decorated" or "terminated" by atoms seen as bcc. Earlier, we mentioned that Shockley partial dislocations produce such an effect of two close-packed planes of hcp within a fcc crystal between them. It is easily imaginable that this happens for the hcp structure as well. However, closely looking at the pictures of the $k > 2$ planes, there are no clear dislocations visible. We do note, that in all cases, the end of one of the stacking fault regions is accompanied by an other stacking-fault ending, which is "approaching" from a reverse side. This results in the annihilation of the two partial dislocations, producing buckled close-packed planes (visible as atom row in the plane- and top views). The (partial-)dislocation lines seen through means of the bcc atoms extend from the second plane up to the surface in most cases. It turns out some of the dislocation lines form a ring which encloses a stacking fault area. At the higher coverages, the walls are formed by the aligning dislocation-lines, creating two grains. In both the EVAP_{s} and EVAP_{b2} simulations the stacking sequence reverses when crossing such a wall, indicating that micro-twins form. Note however, that in the small system, the stacking-fault is oriented along the x-axis, while in the large system the walls are oriented along the y-axis.

Crystal orientation Looking back at figures 63–65 ($\Theta = 7.5$) and figures 74–76 ($\Theta = 24$), clearly, we have only yet looked at their left hand side, showing the crystal structure within the planes. Now that the crystal structure is known, the other information in the figures can be studied. On the right, the pictures show the deviation from the predominant hcp-orientation in the films, which is the hcp{111} orientation. For EVAP simulations, there is also a middle column,

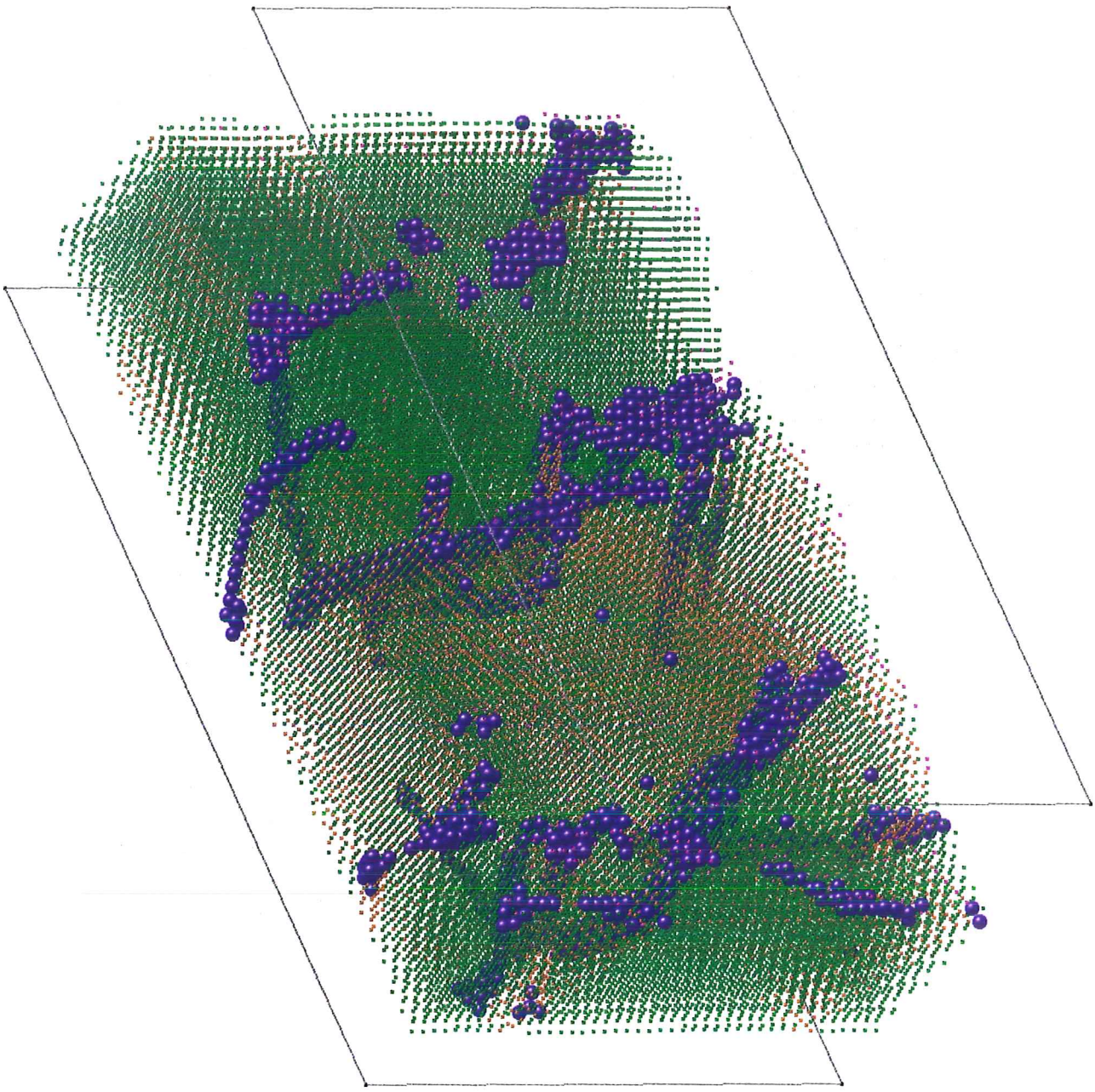

Figure 77: Three dimensional view of $EVAP_{b1}$ near the end of the simulation giving an impression of how the bccdot-plot pictures from figure 69 translate into the third dimension. Shown is a rotated 3-D view of the atoms of the planes with $k > 2$, coloured by S. This is the same configuration as used for the top staircase step and figures 68, 74 at $\Theta = 23.94$, $D = 53.27$ Å. The non-bcc atoms are the very small squares while the bcc atoms are shown at their normal size, creating a see-through effect. The gray lines indicate the box edges, connecting the black dots of the corners. The left edge (top) is at the left-lower corner of the bccdot-plots, while the right-most edge is at the top-right corner of these plots. This figure is referred to as a 3D-bccdot figure.

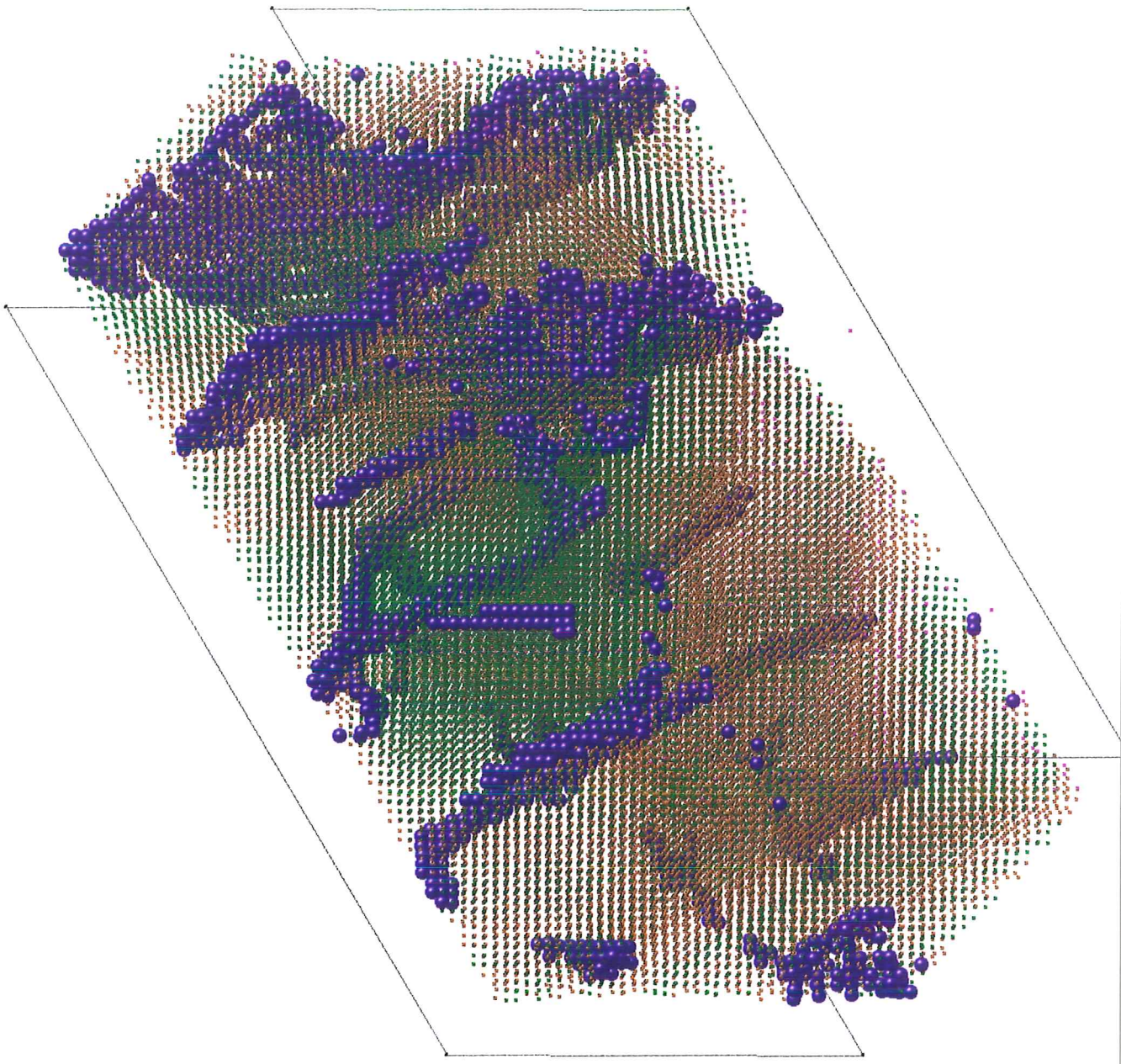

Figure 78: Three dimensional view of $\mathrm{EVAP}_{\mathrm{b2}}$ near the end of the simulation giving an impression of how the bccdot-plot pictures from figure 70 translate into the third dimension. Shown is a rotated 3-D view of the atoms of the planes with $k > 2$, coloured by S. This is the same configuration as used for figure 84 and for the top staircase step, $\Theta = 34.31$, $D = 76.35$ Å. The non-bcc atoms are the very small squares while the bcc atoms are shown at their normal size, creating a see-through effect. The gray lines indicate the box edges, connecting the black dots of the corners. The left edge (top) is at the left-lower corner of the bccdot-plots, while the right-most edge is at the top-right corner of these plots. This figure is referred to as a 3D-bccdot figure.

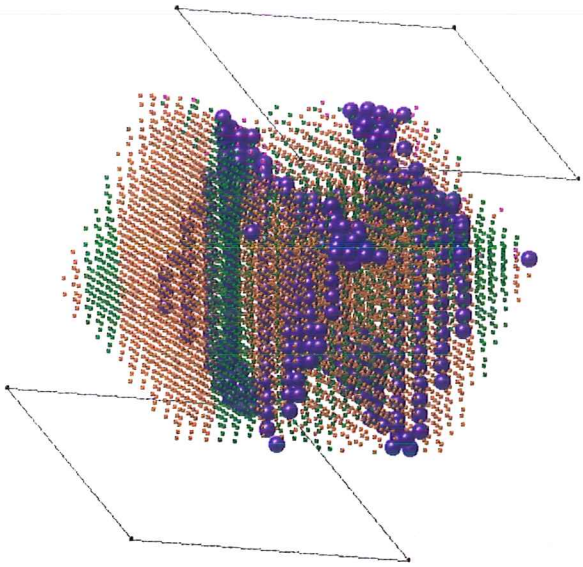

Figure 79: Three dimensional view of $EVAP_s$ near the end of the simulation giving an impression of how the bccdot-plot pictures from figure 71 translate into the third dimension. Shown is a rotated 3-D view of the atoms of the planes with $k > 2$, coloured by S. This is the same configuration as used for figure 68 and for the top staircase step, $\Theta = 24.06$, $D = 54.23$ Å. The non-bcc atoms are the very small squares while the bcc atoms are shown at their normal size, creating a see-through effect. The gray lines indicate the box edges, connecting the black dots of the corners. The left edge (top) is at the top-right corner of the bccdot-plots, while the right-most edge is at the bottom-left corner of these plots. This figure is referred to as a 3D-bccdot figure.

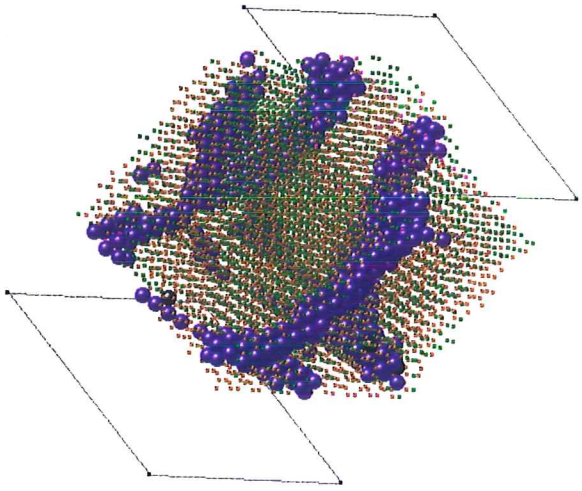

Figure 80: Three dimensional view of $IBAD_s$ near the end of the simulation giving an impression of how the bccdot-plot pictures from figure 73 translate into the third dimension ("3D-bccdot" figure). Shown is a rotated 3-D view of the atoms of the planes with $k > 2$, coloured by S, with the Mo atoms in black. This is the same configuration as used for figure 68 and for the top staircase step, $\Theta = 24.55$, $D = 54.63$ Å. The non-bcc atoms are the very small squares while the bcc atoms are shown at their normal size, creating a see-through effect. The gray lines indicate the box edges, connecting the black dots of the corners. The left edge (top) is at the top-left corner of the bccdot-plots, while the right-most edge is at the right-lower corner of these plots.

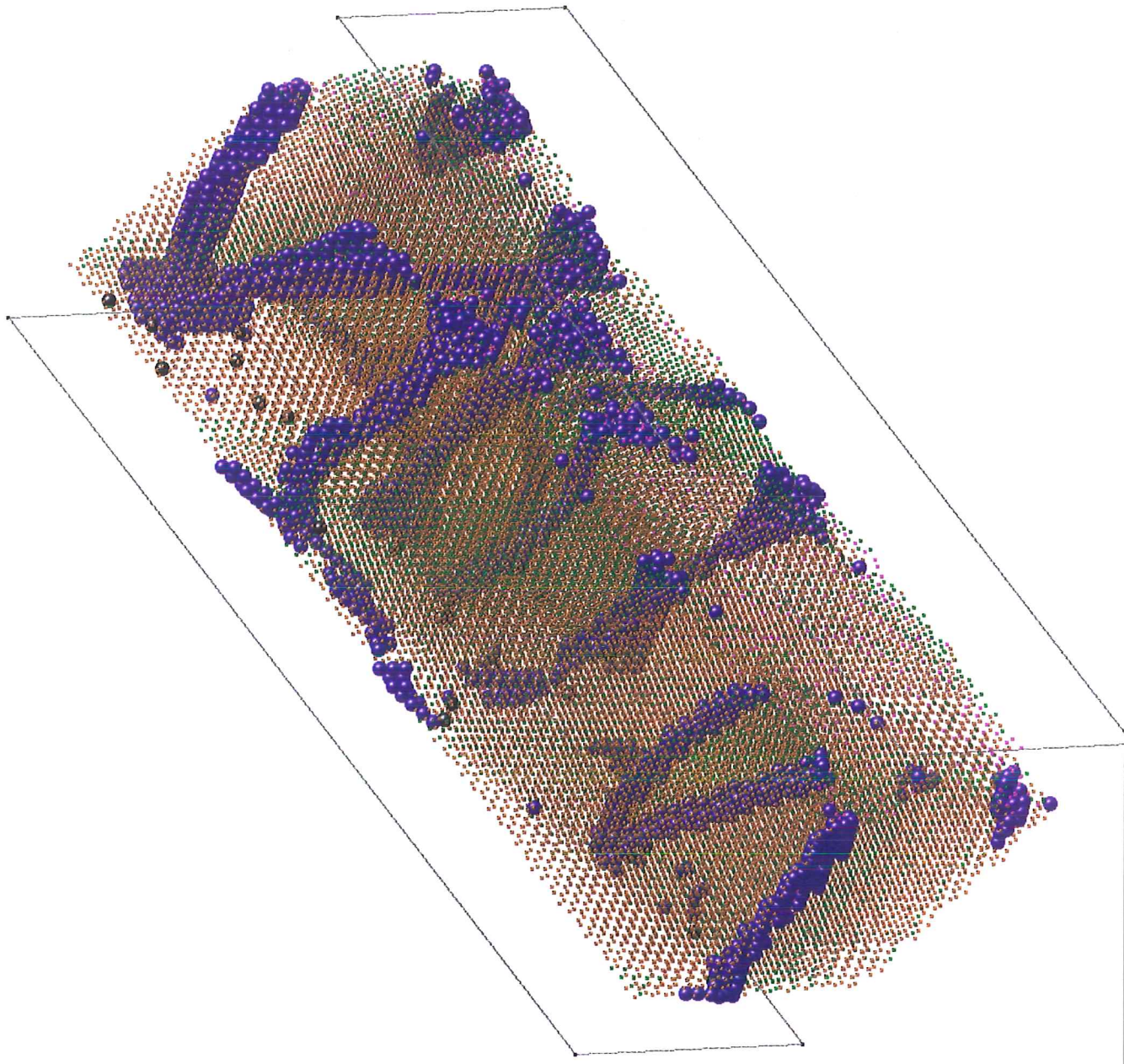

Figure 81: Three dimensional view of $IBAD_b$ near the end of the simulation giving an impression of how the bccdot-plot pictures from figure 72 translate into the third dimension ("3D-bccdot" figure). Shown is a rotated 3-D view of the atoms of the planes with $k > 2$, coloured by S, with the Mo atoms in black. $\Theta = 32.625$, $D = 72.60$ Å. The non-bcc atoms are the very small squares while the bcc atoms are shown at their normal size, creating a see-through effect. The gray lines indicate the box edges, connecting the black dots of the corners. The left edge (top) is at the top-right corner of the bccdot-plots, while the right-most edge is at the bottom-left corner of these plots.

showing the deviation from the predominant fcc orientation, fcc{111}. As the IBAD film has hardly any fcc, these pictures are absent there.

Note that the observed deviations δ^θ are only those that occur as a result of a rotation of a particular crystallographic plane-normal by an angle θ from the z-axis. A rotation ψ *around* this axis does not show up in the figures (see §3.2.8). The analysis can be applied to obtain both θ and ψ by also using another "looking" direction (by default the z-axis) and combine the results. This more cumbersome analysis is not yet completely developed. Further research has to be conducted in order to obtain the full, more easily interpretable, picture of how the crystallites are oriented within the Cu film. Nevertheless, we do get interesting information from the combination of the crystal structure and the θ-deviation from the main orientation.

In all the larger simulations, the fcc regions are mainly $\{111\}_{\text{fcc}}$ oriented, as understood above, with a deviation of up to some 5–10 degrees depending on the regions size. In the large, uninterrupted areas, the deviation is smaller, while in the more narrow regions or single planes wedged between two hcp strips or regions, the deviation is larger. Here too, some other orientations than $\{111\}_{\text{fcc}}$ show up, notably $\{344\}_{\text{fcc}}$. At the edges of the fcc areas, the orientation of a strip of two atoms is $\{334\}_{\text{fcc}}$ at some points (red vertical two atom edges near a dislocation, seen most clearly in the higher k EVAP_{b1} figures at $\Theta = 7.5$). A few of the single fcc planes also have this orientation. These two orientations are the ones closest to the $\{111\}_{\text{fcc}}$ orientation (of the 15 checked, see §3.2.8). The IBAD film has most of the fcc in the $\{344\}_{\text{fcc}}$ orientation. This is in agreement with these fcc atoms being located mostly in single or double planes between hcp regions and in all cases located only in small regions. In the figures we look at the close-packed fcc planes, apparently at a small angle to the paper. All k

The hcp areas mostly have a $\{111\}_{\text{hcp}}$ or $\{344\}_{\text{hcp}}$ orientation as well. Note however, that for hcp the closest packed planes are the $\{001\}_{\text{hcp}}$ oriented planes, so that these figures do not show close-packed hcp planes in the plane of the paper. An exception is the second Cu plane in which the hcp Moiré streaks in-between the fcc{111} oriented Moiré streaks are mostly in the $\{001\}_{\text{hcp}}$ orientation, with some of their edges seen as $\{012\}_{\text{hcp}}$, most clearly at higher coverage in the EVAP simulations. In the figures of 63–65 and 74–76, these regions are shown in magenta. They do not match the scale of the pictures. $k = 2$

In general, we see that the deviations of both hcp and fcc are larger in the diagonal band(s) than in the Moiré-streaks. At the boundaries of these streaks, the deviations also seem larger than in the middle (only visible for fcc). Both of these effects may be due to the closeness of a different crystal symmetry, which by itself results in a different spherical harmonic coefficient S (see figure 58). The small systems have a systematic deviation from $\{111\}_{\text{fcc}}$ (not shown), with a predominant fcc{344} orientation for EVAP, and fcc{122} for IBAD.

Identifying the dislocations Above, dislocations enclosing stacking fault areas were mentioned (see also §3.2.8), but looking at the planes presented in the figures 63–65 ($\Theta = 7.5$) and figures 74–76, these dislocations are not actually all that obvious. At several places there is clearly an edge dislocation visible

for the $\Theta = 7.5$ figures, but at the higher coverage, only a few of these can be identified by the short two atoms wide hcp "ridges" seen at an angle of $\sim 60°$ with the ends of the extra planes. We see a lot of bcc-terminated double hcp strips in the fcc and single or double fcc strips in the hcp regions but counting the atoms in these strips and comparing with the neighbouring regions reveals that they are equal. These features do not indicate dislocations within the z-planes. The staircase figures confirm that the hcp/fcc strips are close-packed planes, but at angles of $\sim 30°$ with the $z - planes$ normal. It is in these planes, both along the strips but also at $\sim 60°$ with them, that (partial) dislocations exist which enclose the strips. The deviation from the fcc/hcp {111} orientations exists to fit the atoms(rows) in the space between the fcc/hcp strips, creating a zigzag stacking fault pattern with a "zig"-deviation away from the direction for a {111} orientation leading from strip to strip and a "zag" step in the other direction over the strip. Figure 82 which shows a close-up of a close-packed plane from IBAD_b is an example of this. In the figures 63–65 and 74–76, this pattern can be seen to exist within the z-planes too. The stacking fault and thus the zigzag pattern can occur along any of the close-packed directions within the close-packed planes ($\langle 110 \rangle_{\text{fcc}}$ and the equivalent hcp directions, such as $[100]_{\text{hcp}}$, $[130]_{\text{hcp}}$ and $[233]_{\text{hcp}}$). With a set of Shockley partials a burgers vector $\vec{b}$ parallel to one of these directions is split into two partials $\vec{b}_\text{S}$ along the direction (equivalent to) $\langle 121 \rangle_{\text{fcc}}$, with a smaller magnitude [7]. At a more wide separation of the strips, the zig-slope can be flatter as the zag-step back remains of the same magnitude (the length of the partial burgers vector).

4.3.5 Growth-mode and R change above $\Theta \sim 10$

The R-curves of most simulations remain relatively unchanged right up to the end of the simulations. An exception in this is EVAP_b1, which shows a strong increase in roughness after $\Theta \sim 11$, $D = 25$ Å. From this coverage onward, the simulation has a high fraction of fcc (> 0.6) which only increases at higher coverage ($\simeq 0.68$ at $\Theta = 54$), see figure 66(a). The other simulations also show an increase in roughness, but much smaller. For the small systems, the increase is only by about 1 Å. EVAP_v only has a narrow peak in R and a very low roughness at other coverages, see figure 83. The hill-like features seen in the the large systems at higher coverages are one sixth to one half of the box surface (the staircase figures sort of show this), ie. $3350 - 10^4$ Å^2. The smaller systems have a surface of only 2521 Å^2 (calculated from table XIII, EVAP_v: 925 Å^2), so that these features can not fully develop, explaining the difference in roughness.

For EVAP_b2 and IBAD_b, the roughness curves seem to be similar, with a roughness that increases by about 0.05 Å for every 1 Å increase in D or 0.02 Å per monolayer coverage "starting" from $\Theta \sim 6.5$, where the 3-D growth subdues. These systems all have a lower fraction of fcc atoms than EVAP_b1. As such, it appears that the roughness on fcc{111} surfaces (close-packed surface planes) is higher than on hcp{111} surfaces (close-packed planes at an angle of 60° with the surface. The β_k-data from figures 50(b)–54(b) show that all simulations have a diminishing amplitude of the plane-by-plane growth wiggle above $k > 8$. This effect is especially strong for EVAP_b1 and somewhat less

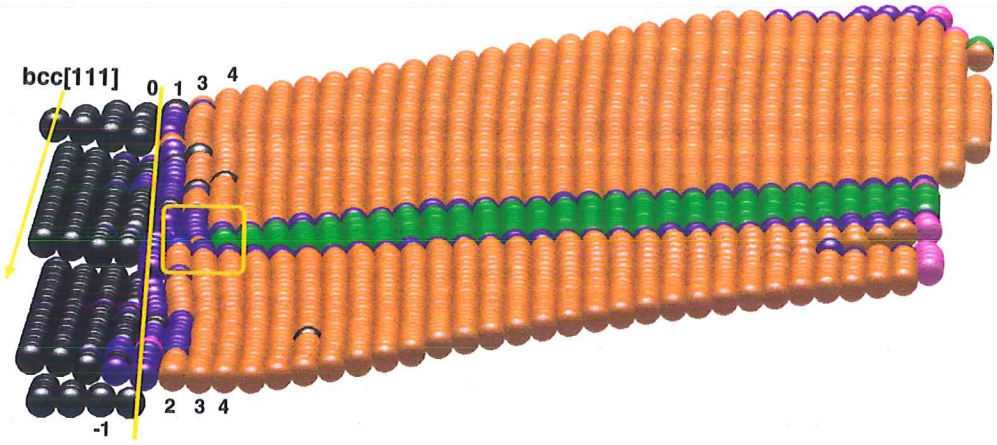

Figure 82: View of a close-packed plane (along a box diagonal, surface is on the right) of $\mathrm{IBAD_b}$ with Cu coloured by S and Mo black, showing the "zigzag" pattern created between two partial dislocations. The yellow line marks the interface, planes $k = -1$ to 4 are indicated. Inside the yellow box one can see an edge dislocation where the two partials meet. The shorter the distance between the partials, the stronger the kink in the atom rows. This configuration is also used for the highest coverage staircase step.

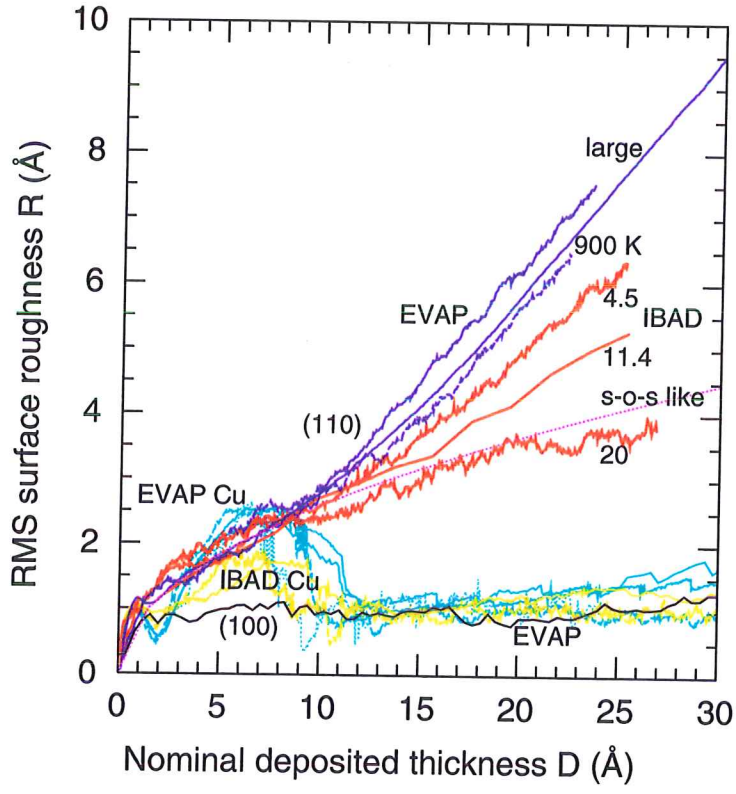

Figure 83: Comparison of the roughness of the current Cu on Mo(110) depositions and of several Mo depositions (see [48]). In the figure, the EVAP Cu simulations (4 sets, dotted line: $\mathrm{EVAP_v}$) are shown in cyan and the IBAD (2 sets) in yellow. The EVAP Mo(110) simulations are blue, with the IBAD Mo(110) in red. For the meaning of the specifiers for the Mo curves, the reader is referred to [48]. The magenta line with the label "s-o-s like" is the relation $R = \sqrt{0.667D}$.

so for the other two large simulations. In the small systems there is a much smaller decrease in peak height. The β_k-curves show the deviation from the s-o-s model, so clearly, the diminishing amplitude means that the plane-by-plane growth is "overshadowed" by a diffusion that is more even between the planes. A more symmetrical distribution of up/down movement would have this effect. Despite this less plane-by-plane growth like behaviour the resulting R-curves for all current simulations are considerably lower than the $\sqrt{(D)}$ (or $\sqrt{\Theta\, d_{\text{plane}}/M_{\text{substrate}}}$) R-dependency expected for the s-o-s model (see §3.2.6).

Comparing the roughness curves from figure 48 with those for several Mo depositions [48], see figure 83, we note several points. Firstly we see that during the 3-D growth stage, the roughness of the Cu films is comparable with that of Mo grown on a similar substrate. Secondly, it is clear that beyond the 3-D growth stage, the roughness of the Cu films is much lower than the roughness of Mo. Moreover, this remains true even when ignoring the column-growth associated steep increase at higher thickness that occurs for the various $R_{\text{Mo(110),EVAP}}$ curves (for $D > 25$ Å). The high-energy IBAD $R_{\text{Mo(110)}}$ curves display an s-o-s like behaviour, see the magenta curve in figure 83, which follows the relation $R = \sqrt{0.667D}$. Only the R-curve for Mo(001) has a roughness that is comparable to or lower than what is seen for Cu growth on Mo{110}. The Mo on Mo{110} EVAP simulations experience columnar growth, hence their high roughness.

4.3.6 At higher coverages

The EVAP_{b2} and IBAD_{b} simulations have been continued until they reach a coverage of $\Theta \sim 34$, ($D = 80$ Å) to find out if there are still changes in structure during the continued deposition above $\Theta = 24$ ($D = 54$ Å). As the defects and the boundaries between the regions (grains?) are marked by bcc atoms, the number of bcc atoms in the planes is a sort of measure of how many defects are present and how many regions form. From this we can conclude that the regions grow somewhat as the deposition continues, as figure 67 shows that only a very small amount of the atoms that are deposited become bcc in this stage of the deposition. The structure does keep changing during deposition, as already indicated by the growth of the regions. We can see that there is, unsurprisingly, a tendency to form a more uniform structure, with either the Moiré-streaks and fcc grains dominating, or the diagonal bands. At first, the valleys in the film surface are positioned around boundaries between regions, but at higher thicknesses this is not strictly true anymore.

The bccdot-plots show the structure in the entire film at several intermediate coverages. From comparing the "last" two pictures from figures 70,72 and the planes in figures 84 and 85 ($\Theta = 34$) with those same planes at $\Theta = 24$, figures 75 and 76, and also from comparing the two highest steps of the EVAP_{b2} and IBAD_{b} staircases (figures 40 and 42), it is clear that the structure remains much the same when going from 24 to 34 monolayers of coverage. The stable fractions of each S (figure 66) and the absence of large changes in bcc content of each plane between $\Theta = 24$ and $\Theta = 34$ (figures 68 and 86) indicate the same. A clear difference is the presence of a second grain boundary at $\Theta = 34$.

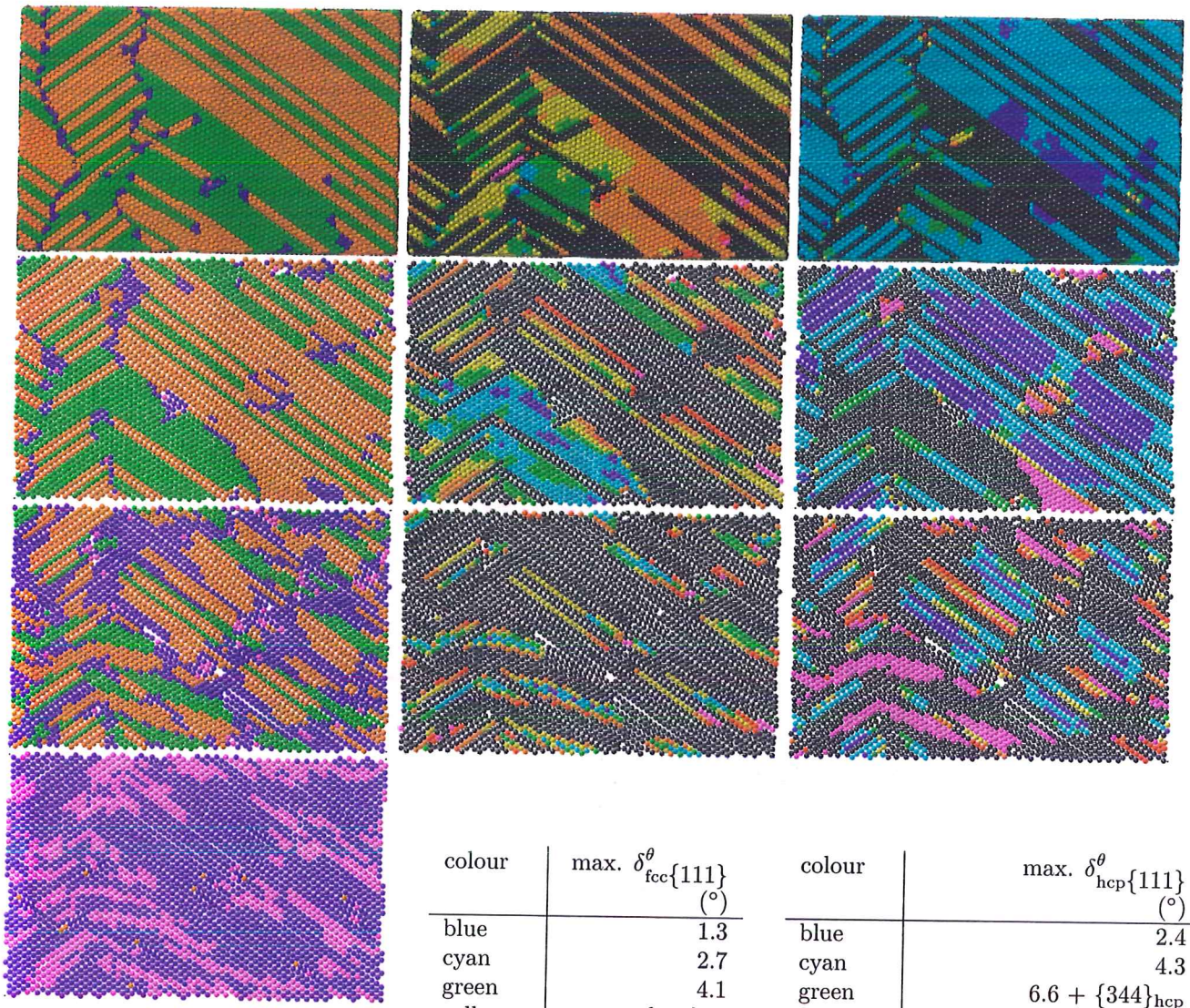

colour	max. $\delta^{\theta}_{\mathrm{fcc}\{111\}}$ (°)
blue	1.3
cyan	2.7
green	4.1
yellow	$5.4 + \{344\}_{\mathrm{fcc}}$
orange	$6.8\ (\{344\}_{\mathrm{fcc}})$
red	$8.3\ (\{334\}_{\mathrm{fcc}})$
magenta	$> 8.3\ (\{014\}_{\mathrm{fcc}})$
black	$S \neq \mathrm{fcc}$

colour	max. $\delta^{\theta}_{\mathrm{hcp}\{111\}}$ (°)
blue	2.4
cyan	4.3
green	$6.6 + \{344\}_{\mathrm{hcp}}$
yellow	$8.7 + \{344, 124, (012)\}_{\mathrm{hcp}}$
orange	$\{122, 012\}_{\mathrm{hcp}}$
red	$\{012, 001\}_{\mathrm{hcp}}$
magenta	$\{001\}_{\mathrm{hcp}}$
black	$S \neq \mathrm{hcp}$

Figure 84: A selection of planes of $\mathrm{EVAP}_{\mathrm{b2}}$ at $\Theta = 34.31$ ($D = 76.35$ Å). From left to right, the same plane is shown with atoms coloured by S, and by the deviation δ^{θ} from two specific crystal orientations (see §3.2.8): $\delta^{\theta}_{\mathrm{fcc}\{111\}}$ and $\delta^{\theta}_{\mathrm{hcp}\{111\}}$, with the non-fcc (non-hcp) atoms shown in black. At the higher deviations, a different set of orientations may be more closely matched. In these cases, this (these) are indicated. From bottom to top, the first, second, and third plane are shown. The top pictures are a view of the configuration from above, with a "cap" cut away from the top of the film.

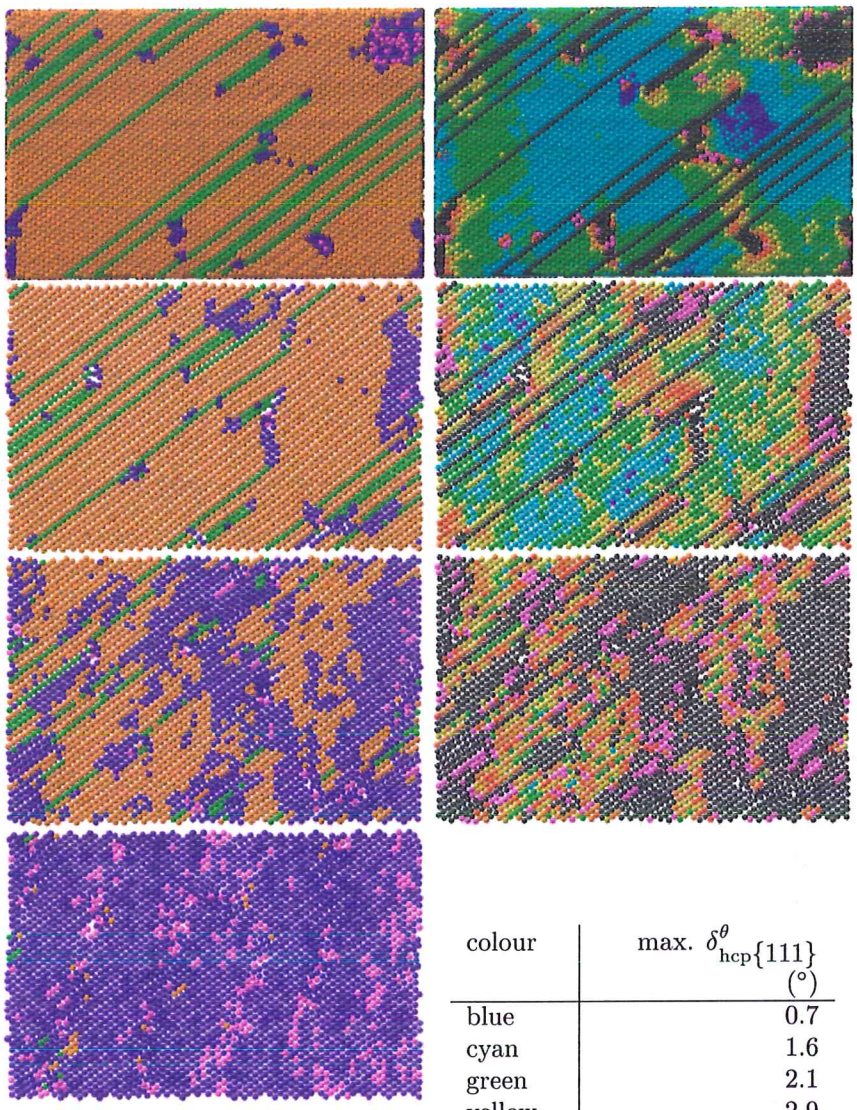

colour	max. $\delta^{\theta}_{\mathrm{hcp}\{111\}}$ (°)
blue	0.7
cyan	1.6
green	2.1
yellow	2.9
orange	3.5
red	4.3
magenta	$5.0 + \{124, 001\}_{\mathrm{hcp}}$
black	$S \neq \mathrm{hcp}$

Figure 85: A selection of planes of $\mathrm{IBAD_b}$ at $\Theta = 33.77$ ($D = 75.16$ Å). From left to right, the same plane is shown with atoms coloured by S, and by the deviation δ^{θ} from a specific crystal orientation (see §3.2.8): $\delta^{\theta}_{\mathrm{hcp}\{111\}}$, with the non-hcp atoms shown in black. At the higher deviations, a different set of orientations may be more closely matched. In these cases, this (these) are indicated. From bottom to top, the first, second, and third plane are shown. The top pictures are a view of the configuration from above, with a "cap" cut away from the top of the film. The few fcc planes between the hcp ones are mostly in a $\{344\}_{\mathrm{fcc}}$ orientation, with some in $\{014\}_{\mathrm{fcc}}$ and a few edges are seen to have a $\{122\}_{\mathrm{fcc}}$ orientation.

From plane-filling and β_k-data, we see that the growth becomes more and more like the solid-on-solid model, with smaller plane-by-plane growth peaks. For IBAD, this is much less noticeable. It does seem though as if the dampening of the peaks slows down near the $\theta \sim 23$ (50 Å) thickness mark even for the EVAP cases. However, EVAP_{b2} also has a next dampening from about 60 Å ($\Theta = 28$) onwards. There is not much change in the S-distribution as well when going from 55 Å to $\sim$ 80 Å. The same is true for the structure of the simulations and for the crystal orientations. The change seen is more of a consolidation. Still, the resulting structure is quite interesting.

Figure 86 is included partly for the sake of completeness, but the figure does show that the gradual increase of the fraction fcc with k in IBAD_{b} at 55 Å is not any more visible in the bulk at this higher thickness. The bcc fraction instead has a somewhat lower but stable value. In EVAP, the fraction of fcc is slightly higher here than at 55 Å. In figure 84 and 85 the crystal structure and the deviation from the main crystal orientation are shown at the end-point of these two simulations. We can see that the deviations from $\{111\}_{\text{hcp}}$ seem to have become smaller for the IBAD simulation. For the EVAP simulation additional different fcc orientations appear in addition to a small decrease in the amount of deviation for the rest of the regions. The larger hcp areas also have a clearly lower deviation at this coverage. The two y-oriented bcc rich walls, grain-boundaries, have moved closer together. The smaller grain between them will presumably disappear completely during continued deposition of this film.

4.3.7 A selection of data from the deposition simulations

For EVAP the Cu/Mo interface is atomically flat. For IBAD however, we have seen that the initially flat substrate surface is disrupted and inter-mixing takes place. Table XXIII lists the total amount of intermixing of Cu and Mo for all of the Cu on Mo deposition simulations, and sums up how many atoms of each type are introduced and removed (ie. sputtered out of the film). For reference, Gades and Urbassek find from a MD (Lennard-Jones) simulation of rare-gas bombardment of Cu by that the Ar refraction is a factor 0.9 (so 10% of the Ar remains in the film) with a Cu sputter coefficient of about 0.6 for 100 eV Ar [26]. Comparing the amount of removed Cu atoms for EVAP and IBAD, we find that almost all Cu removed in IBAD is due to the Ar atoms. With an IAR of 0.1 we then find a sputter coefficient of 0.59, equal to the result from [26]. The fraction of Ar refracted is 0.89 for the small system, and 0.96 for the larger system.

Figure 87 shows the Mo distribution within the simulation. How many Cu has found its way into the substrate can be guessed from the diminished amounts of Mo in the substrate planes (negative z-values in the figure), as these planes (almost) retain their original number of atoms (see figures 55, 68 for instance). From the earlier hard-ball figures and from slicing through the films using the rotated planes described in §3.2.1 (not shown), we found that the Mo atoms are all at substitutional sites in the Cu. The are Ar atom in the substrate is also substititional. The lower and highest (newest) Ar atoms in the Cu (IBAD_{b}) create a larger cavity of three and of four Cu atom positions

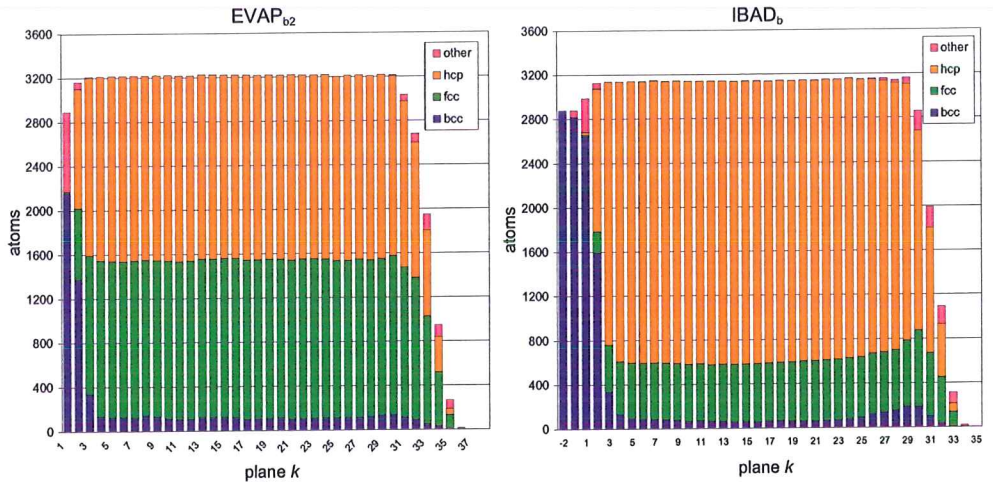

Figure 86: Crystal structures in the Cu on Mo deposition simulations at $\Theta \simeq 34$ (EVAP$_{b2}$: $\Theta = 34.89$ IBAD$_b$: $\Theta = 35.02$, $\simeq$ 75–80 Å). The number of atoms of each $S =$ bcc, fcc, hcp or other ($S =$ undefined, ico or dia, see §3.2.8) is given for the individual planes $k = 1, 2, 3, \ldots, 36$ and for IBAD$_b$, for the two top substrate planes, $k = -1, -2$ as well. The configurations are the last configurations for these simulations. For IBAD$_b$ this is the sixth staircase step. It is still clearly visible that the amount of $S =$ bcc, other atoms is higher at the interface, and increases towards the surface again. We can see also that in all simulations, the fraction of fcc is higher in the surface planes than in the bulk. For IBAD, the fraction of fcc has does not increase with k anymore in the bulk.

Table XXIII: Simulated deposition of Cu on Mo(110). The Cu atom flux Å^{-2} is approximately equal in all simulations ($\sim$ 373–312 atoms ns^{-1}Å^{-2}). The table also gives the effective deposition rate in Åns^{-1} and in Θ ns^{-1} (see §2.4), the fcc/hcp ratio in the film, and the mean atomic volume and potential energy of the bulk of the films. For the IBAD simulations, 100eVAr is used, with 10% fast (250eV) Ar atoms. The bottom part of the table show some data on Cu/Mo intermixing (see also figure 87).

quantity	unit	EVAP$_v$	EVAP$_s$	EVAP$_{b1}$	EVAP$_{b2}$	IBAD$_s$	IBAD$_b$
flux$_{eff}$	atoms Å^{-2} ns^{-1}	0.45	0.37	0.35	0.35	0.33	0.35
α_D^{eff}	Å ns^{-1}	5.75	5.81	5.45	5.45	5.47	5.12
α_Θ^{eff}	Θ ns^{-1}	2.58	2.61	2.45	2.45	2.46	2.30
Cu introduced		1826	9932	69246	105756	9399	99964
Cu removed	$\%_{\text{Cu intro}}$	0	0.01	0.003	0.003	5.93	5.89
Vacancies		1	0	0	0	2	4
Ar introduced		–	–	–	–	938	9992
Ar in film	$\%_{\text{Ar intro}}$	–	–	–	–	0.11	0.04
ratio fcc/hcp		-	0.385	3.147	0.865	0.575	0.222
$\langle\Omega\rangle_k$	Å^3	-	13.06	12.95	12.97	13.05	13.01
$\langle U\rangle_k$	eV/atom	-	-3.379	-3.390	-3.391	-3.386	-3.391
Mo in substrate	Θ	4	6	4	4	5.75	3.69
Mo in Cu film	$\%_\Theta$	0	0	0	0	23.1	27.7
Mo removed	$\%_\Theta$	0	0	0	0	1.2	3.7
Cu in substrate	$\%_\Theta$	0	0	0	0	24.4	31.4

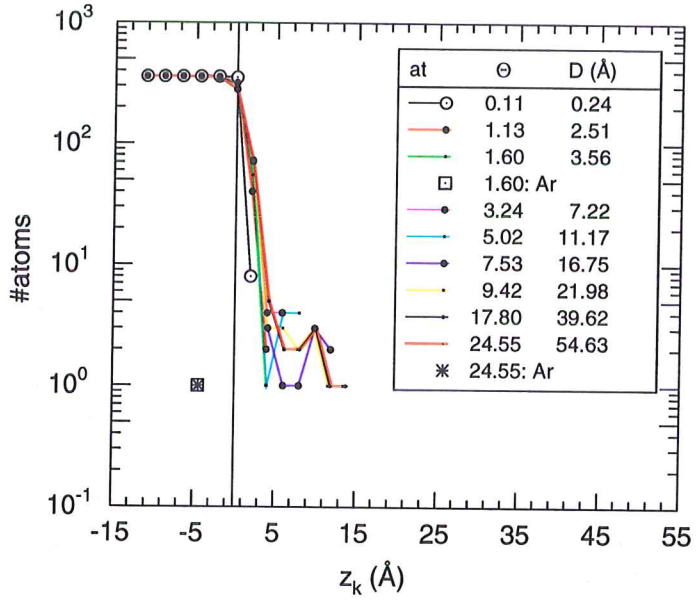

(a) Mo distribution in the $IBAD_s$ simulation. The amount of Ar is shown just "after" the first (only) Ar has arrived and at the end of the simulation. It seems as if the Mo atoms are stirred upwards.

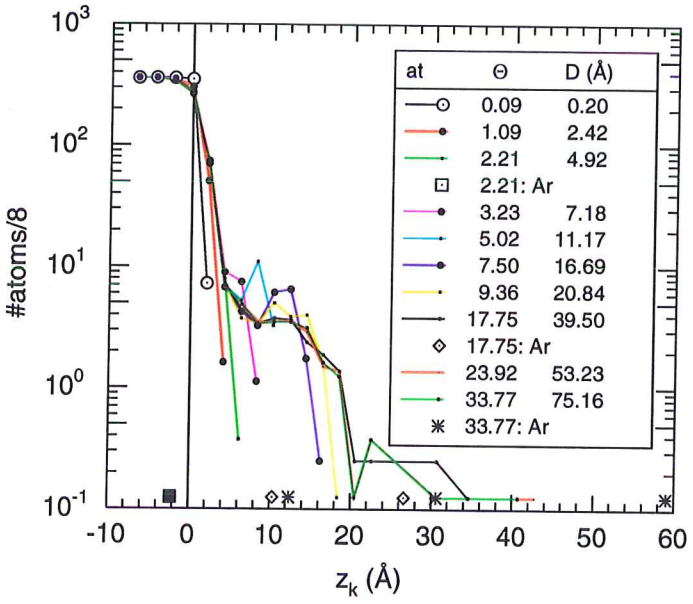

(b) Same as 87(a) but for $IBAD_b$. For comparison with that figure, the number of atoms is divided by 8 here. The Ar incorporation is shown at three coverages. Comparing the last two of these, it is clear that the Ar atoms in the Cu move upwards.

Figure 87: Distribution of Mo in the film at several coverages Θ, D. At some coverages, the Ar incorporation is shown as well. Horizontally, the "height" in the film is shown (in Å) counting from the top of the substrate. The vertical axis gives the number of Mo atoms at this height.

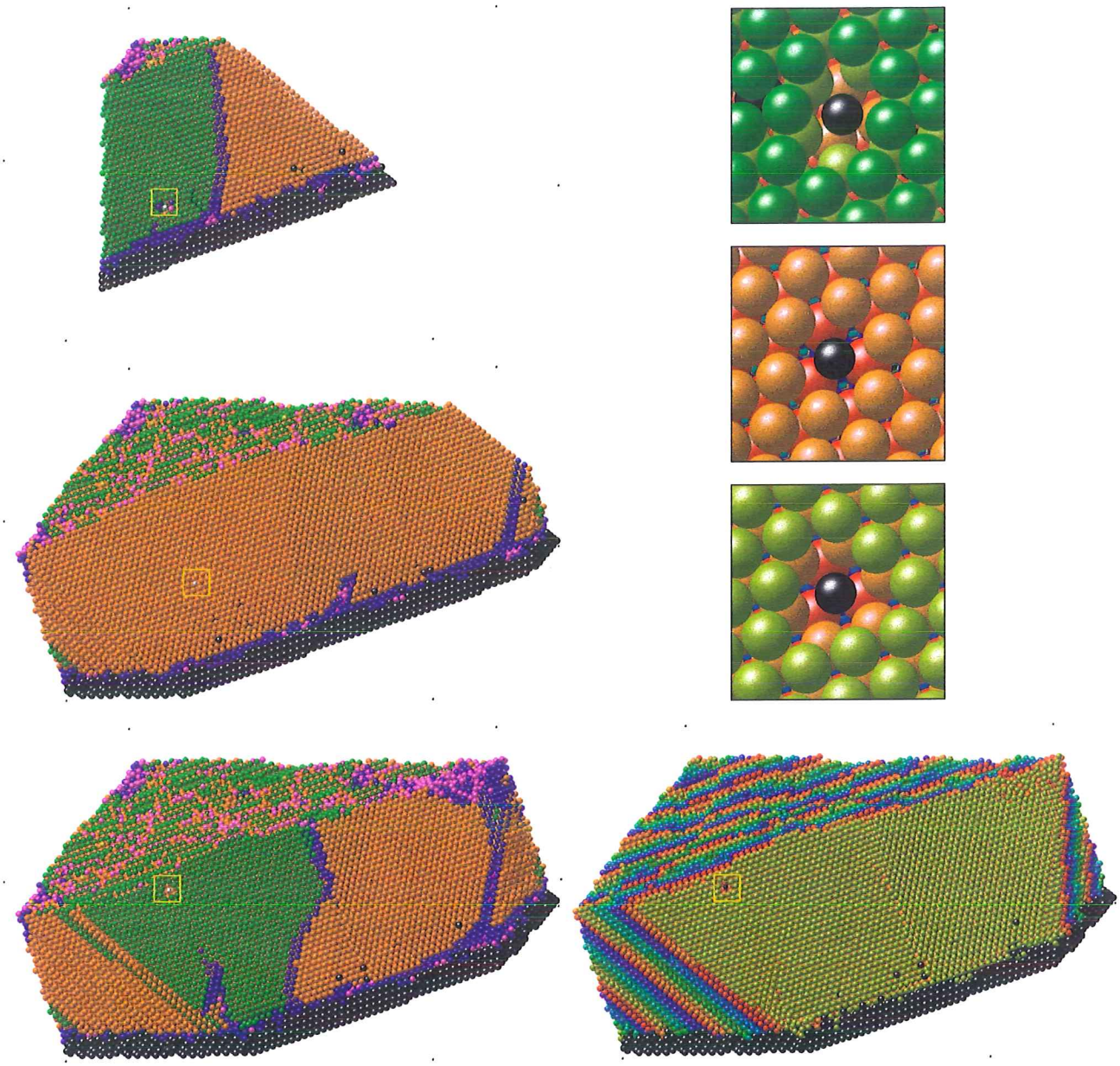

Figure 88: Three different cross-sections along close-packed planes in $\mathrm{IBAD_b}$ at $\Theta = 33.77$ ($D = 75.16$ Å), each containing an Ar atom. On the left, the Cu atoms are coloured by S, with Mo black and the Ar atom white. On the right, the Cu is coloured by the close-packed plane it is in, Mo and Ar are black. The bottom picture contains the same atoms as the left lower one. Above this picture, a detail is given of the left cross-sections, as indicated by the yellow rectangle. The Ar atoms shown in the bottom and top cross-sections are in cavities of three and four Cu positions, one in the "previous" plane, two and three in the visible plane. The Ar atom in the middle pictures is substitutional. The hcp part of the bottom cross-section contains a "step" in the lower part of the film above it, the bcc strip is a straight line, near the step, the bcc strip deflects).

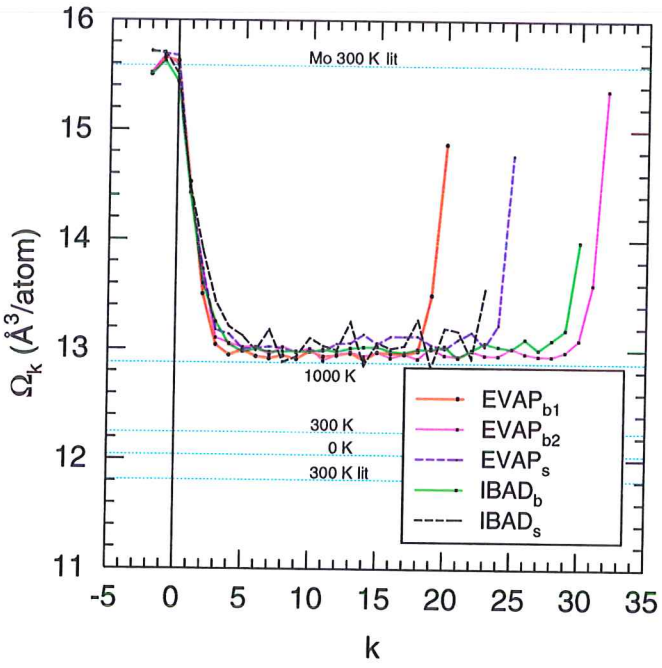

Figure 89: Mean volume per atoms per plane. The dotted cyan lines are values for bulk crystals at $P = 0$ and the specified temperature. The data is from unquenched configurations.

respectively, see figure 88, bottom and top. At lower coverage, the "bottom" one is at a point where a dislocation extends upwards, and seems to be at its core. At the end of the simulation, this dislocation has moved away, leaving the Ar behind. The "middle" Ar atom (figure 87(b); figure 88, middle) is substitutional at the end of the simulation. At the lower coverage, the atom is situated in a four-atom cavity. At the end of the simulation, IBAD_b contains 4 individual vacancies, wich are not seen at lower coverage. All are located in a hcp area, in the top half of the film. At lower coverage, a Cu self-interstitial is found (not related to the vacancies). All of the Ar atoms that are incorporated arrived with an energy of 250 eV. Figure 87 shows that most Mo atoms are removed from the substrate at coverages below $\Theta \sim 3.2$ ($D = 7.2$ Å) for both systems, with a small increase in intermixing until $\Theta \sim 5$ ($D = 11$ Å), which is more clear for the large IBAD system. This coverage corresponds to the end of the island growth stage. At higher coverage the Mo atoms are stirred up to higher planes, presumably due to the energy provided by the Ar atoms. Figure 87(b) indicates that the Ar atoms that are occasionally incorporated in the (large) IBAD Cu film move upward as well. The single Ar atom in the substrate arrived there during 3-D growth. Table XXIII shows that the amount of intermixing for the large system is larger than for the small system and also that more Mo is removed from the system. We have seen that the island growth stage last up to a higher coverage for the large system so that the arriving Ar atoms "see" the substrate for a prolonged period, which may explain the difference.

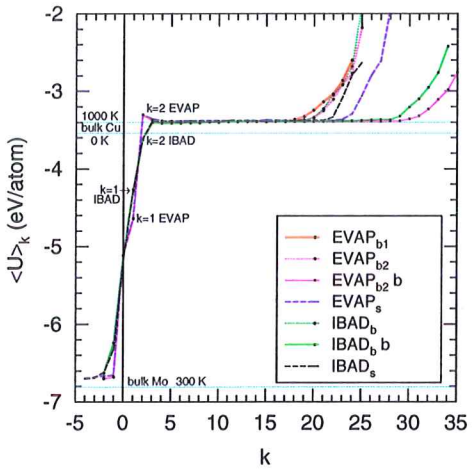

(a) All planes k. For the IBAD simulations, the top two substrate planes ($k = 0, -1$) have a higher energy while the two first film planes ($k = 1, 2$) have a lower energy than the "bulk" ($k > 2$). For EVAP only the top substrate plane, $k = 0$, has an increased energy and plane $k = 1$ has a lower energy. Plane $k = 2$ is more weakly bound than other planes.

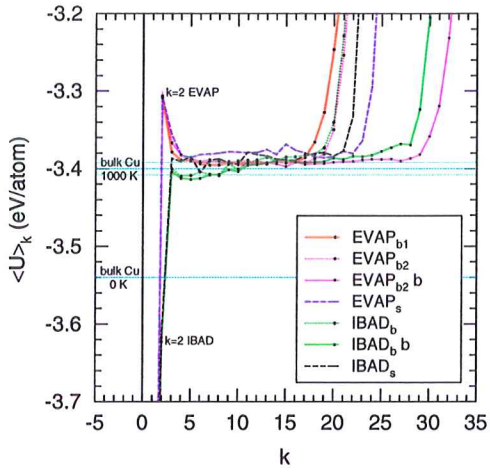

(b) Detail of figure 90(a) for the $k > 1$ planes. The small films have a higher energy than the equivalent bigger films. Both IBAD simulations show an increase in energy up to $k = 10$. At lower k, their energy is lower than for the EVAP simulations, at higher k, their energy is equal to or somewhat higher than EVAP.

Figure 90: Mean potential energy per atom. The dotted cyan lines are the bulk values for the element at a specific temperature (at 1000 K the outer two lines indicate the uncertainty in the data). The data is from unquenched configurations. The data for $\mathrm{EVAP_{b2}}$ and $\mathrm{IBAD_b}$ is shown at a coverage of $\Theta \sim 24$ ($D = 54$) and near the end of the simulations.

In figure 89, the mean volume per atom per plane at the end of each simulation is shown. The smaller systems have a higher atomic volume than the large (for $k > 5$). For $k \leq 4$ we see a sharp decrease in volume. For $k > 4$, the volume stabilizes at a value just above $\Omega_{Cu}^{1000\ \mathrm{K}}$ (bulk fcc Cu at $P = 0$, table XV). Note that for IBAD, the top substrate plane has a lower average volume. Figure 90 gives the mean potential energy per plane for each Cu on Mo deposition simulation. In the IBAD simulations, the top two substrate planes ($k = 0, -1$) have a higher energy while the two first film planes ($k = 1, 2$) have a lower energy than the "bulk" ($k > 2$), see figure 90(a). For EVAP only the top substrate plane, $k = 0$, has an increased energy and plane $k = 1$ has a lower energy than for IBAD. Plane $k = 2$ has a higher energy and is consequently more weakly bound than other film planes. From figure 90(b) we can conlude that the smaller systems have a higher energy than the equivalent larger systems for $k > 2$. Also, the IBAD simulations show an increase in energy with k, especially for $k \leq 10$, and another clear increase for planes close to the surface. The $\mathrm{IBAD_s}$ simulation has an oscillation in film volume between different planes. Only part of the variation can result from the plane separation algorithm.

Revision and recap of the atom history data Figures 91–95 give a more quantative picture of the atom-history shown in figures 51–54(c). From these figures we see that not much interdiffusion between different planes takes place in this later phase of deposition except between adjacent planes. This two-way process results in a dynamic equilibrium with atoms going up and atoms going down in approximately equal amounts. $k > 2$

When studying the atom history figures, one has to realize that as we look at higher z_{final} values, there comes a point where the picture will clearly deviate from the fully developed behaviour as we reach the surface and also that the value where this takes place increases with Θ (or D) at the end of the simulation. Also, keep in mind that in general atoms lower in the film have had more time to diffuse. Despite this, the seen behaviour does not change very much after the 3-D growth region is passed. This can be made out from the maximum $|\Delta z|$ seen, which is less than 10 planes (22.5 Å), except for IBAD_b where it is about 12 planes (27 Å). Figures 50(c)–54(c) actually contain more details on the extremes of the displacement. What is clearly noticeable in comparing these figures is that for IBAD the height (or width) of the "body" of the atom-history data "fish" is much higher than for EVAP, showing four (or three for the small system) different maxima for each z_{final} instead of just three (two for EVAP_s) for the bulk of the planes. Another difference is that the left-lower diagonal line signifying diffusion upward from the first Cu plane extends to much higher z_{final} values for IBAD than for EVAP. A third difference is the diffusion from atoms out of the substrate seen for IBAD. In all of the systems, the first Cu plane has a large maximum for $\Delta z = 0$. The second plane has a much smaller peak ($\sim 1/2$ of the $k = 1$ peak) and the next two or three planes have even smaller peaks here ($\sim 0.15 - 0.2$ of the $k = 1$ peak). For higher planes, the peak is comparable in size to the peak of plane 2. The EVAP_b1 simulations has larger $\Delta z = 0$ peaks for most of the "bulk" planes (magenta peaks), which is presumably related to the higher roughness in the simulation. $k \leq 1$ $k = 2$ $k > 2$

Looking at the shape of the maxima, we see that for the large EVAP systems these peaks have a skewed, elliptic shape while the small systems have much more rounded peaks. All peaks are however slightly elliptic. The elliptic shape becomes less elongated with increasing z_{final}. This shape means that atom that are eventually located "low" in a z-plane, initially arrived at a somewhat higher position. For the relatively "high" atoms, the reverse holds true. It seems that the planes are initially more parallel to the simulation box xy-plane and later rotate or buckle. This is in agreement with the observed crystal orientations. The higher k planes are already less parallel as they start growing. All of the larger systems show a smoother distribution of the atom history (they have an almost analog scale, as compared to the more discrete scale of the small systems.

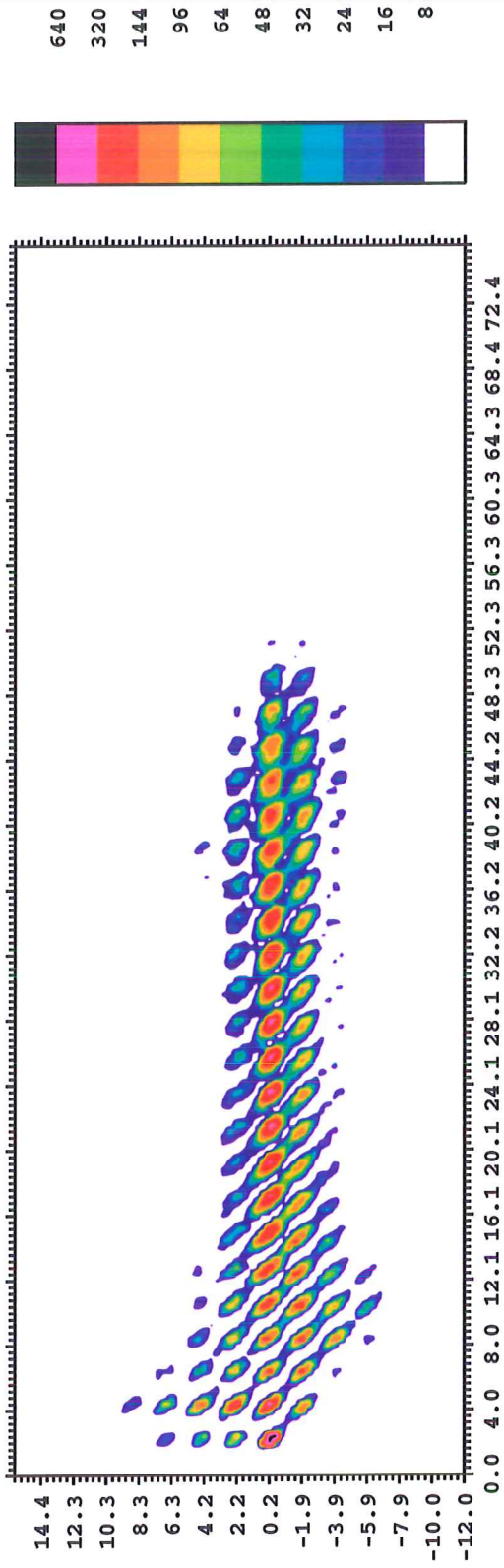

Figure 91: Atom history contour-plot for $\mathrm{EVAP_{b1}}$. The colour scale as shown on the right of the figure indicates the number of atoms in a certain z, Δz area (here: 0.4×0.4 Å). The data is the same as in figure 50(c).

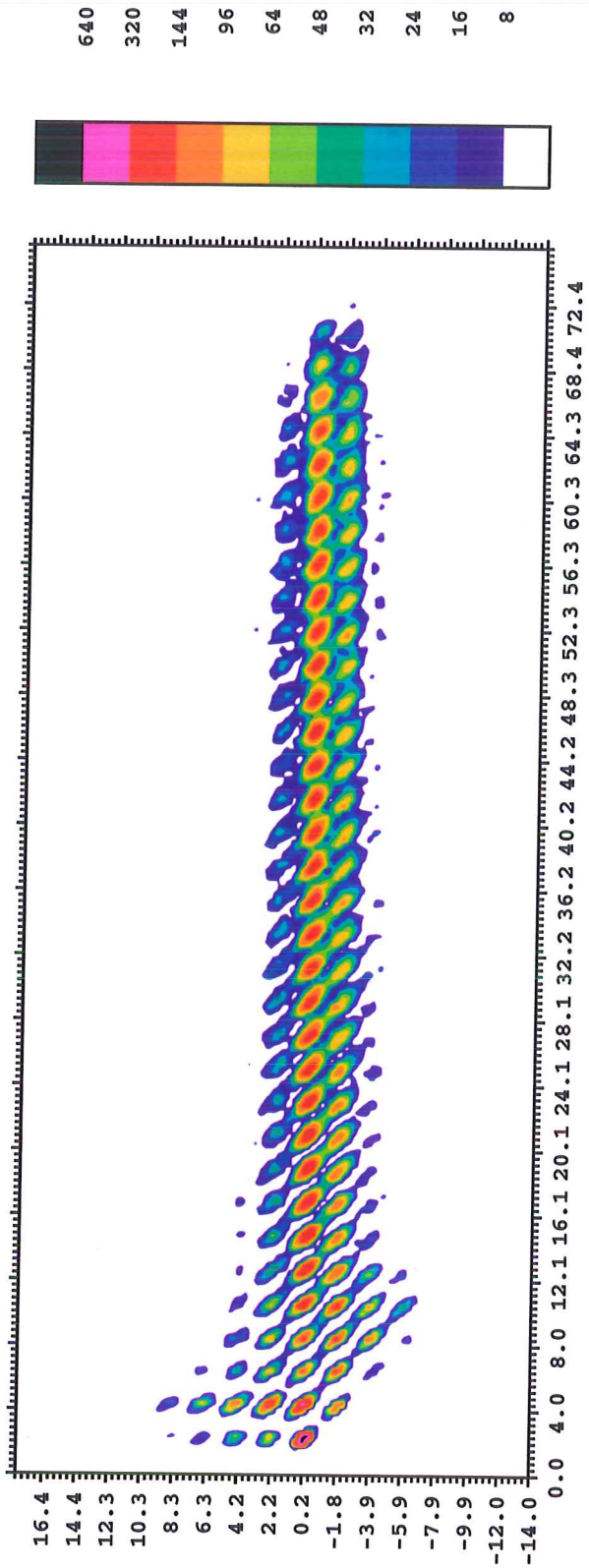

Figure 92: Atom history contour-plot for $\mathrm{EVAP_{b2}}$. The colour scale as shown on the right of the figure indicates the number of atoms in a certain z, Δz area (here: 0.4×0.4 Å). The data is the same as in figure 51(c).

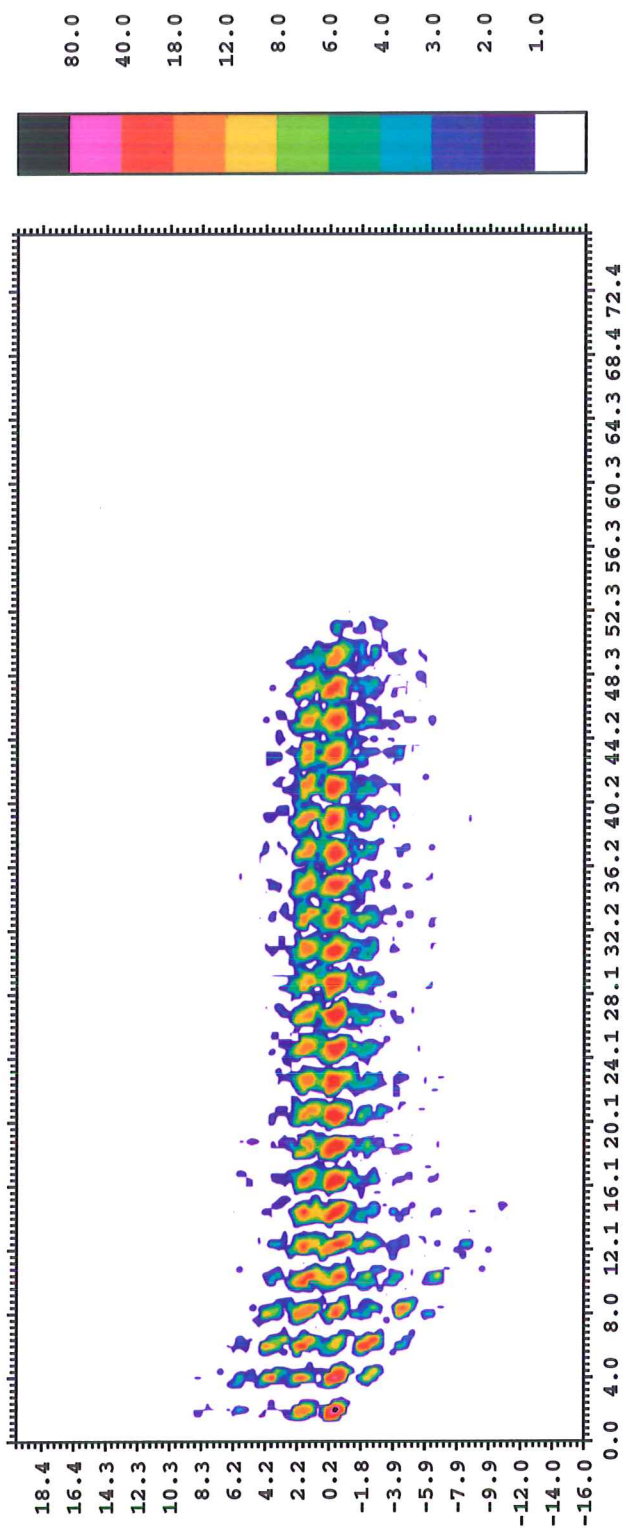

Figure 93: Atom history contour-plot for $EVAP_s$. The colour scale as shown on the right of the figure indicates the number of atoms in a certain z, Δz area (here: 0.4×0.4 Å). The data is the same as in figure 52(c).

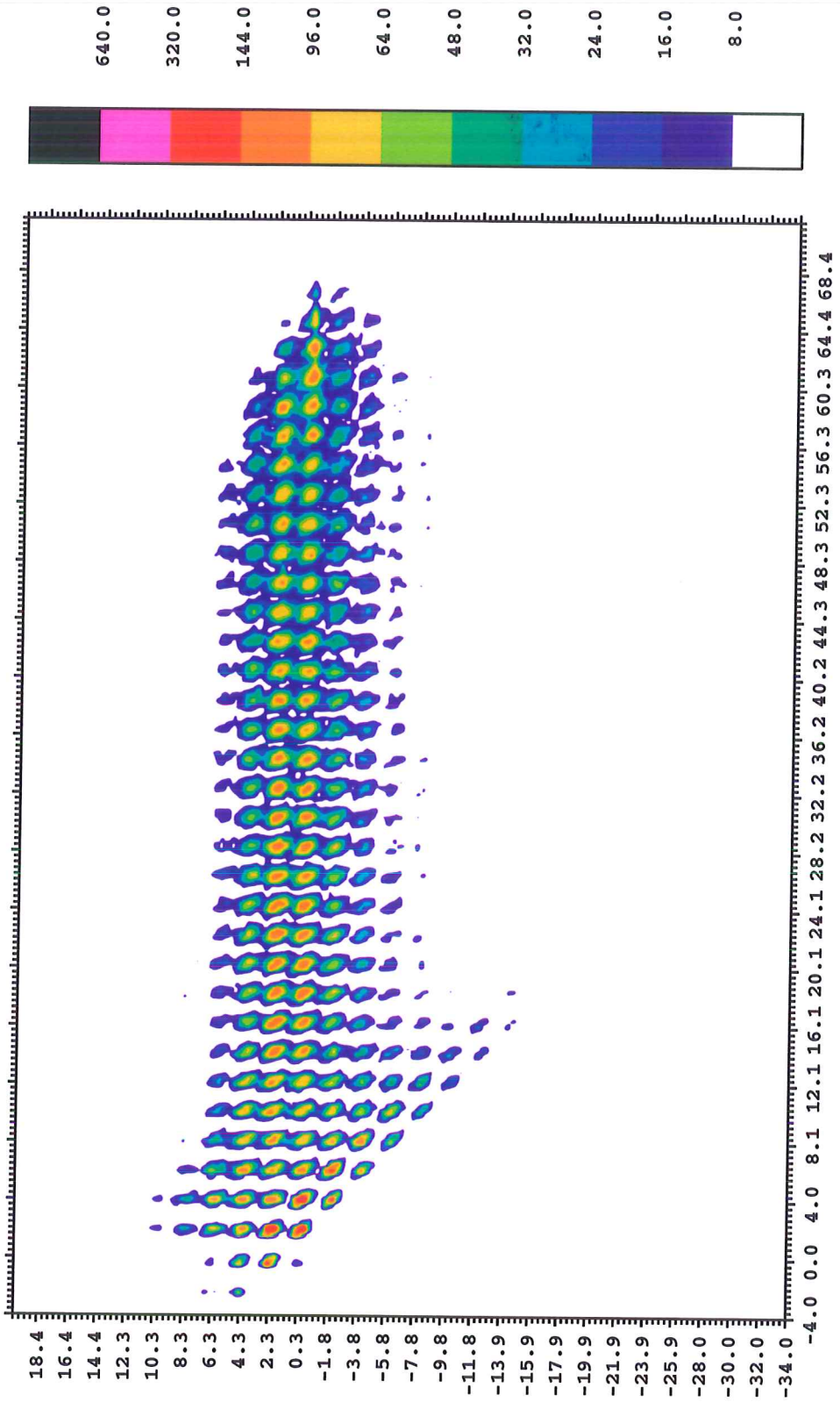

Figure 94: Atom history contour-plot for $\mathrm{IBAD_b}$. The colour scale as shown on the right of the figure indicates the number of atoms in a certain z, Δz area (here: 0.4×0.4 Å). The data is the same as in figure 53(c).

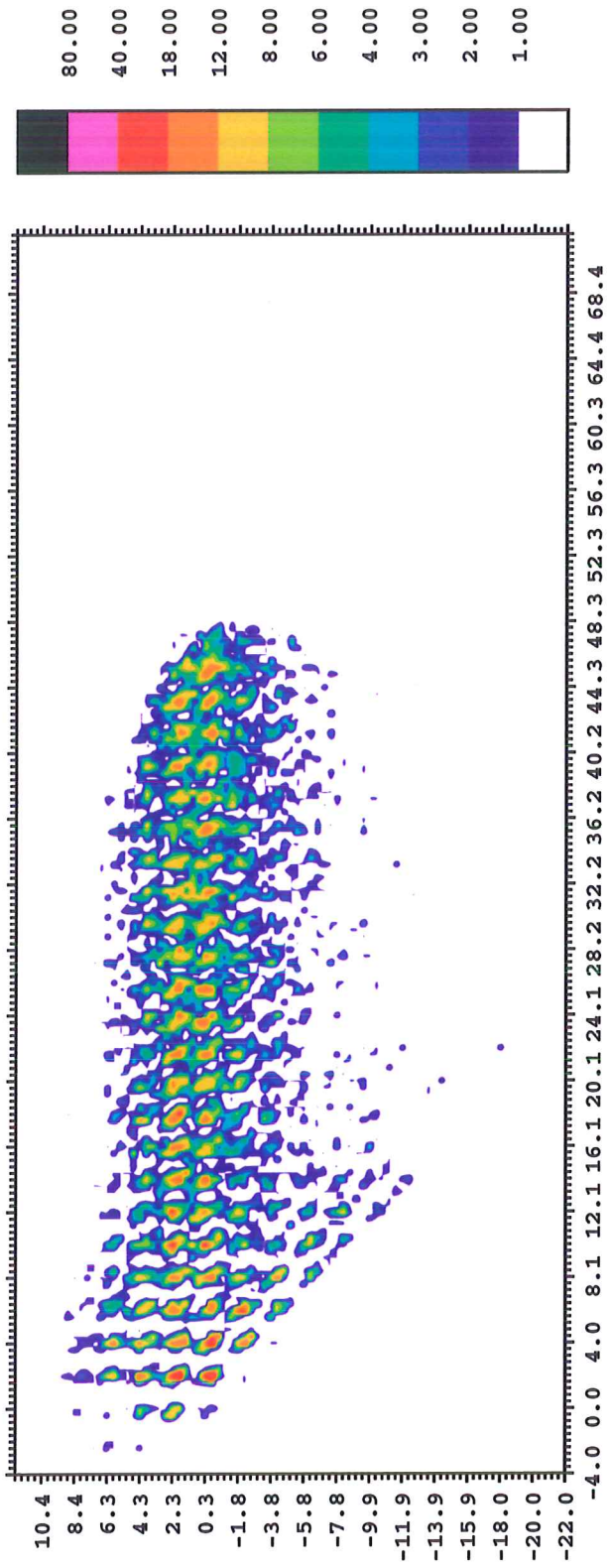

Figure 95: Atom history contour-plot for $IBAD_s$. The colour scale as shown on the right of the figure indicates the number of atoms in a certain z, Δz area (here: 0.4×0.4 Å). The data is the same as in figure 54(c).

5 Discussion

5.1 Verisimilitude of the simulations

Our Cu-Cu interaction and the derived Cu-Mo interaction reproduce several physical quantities of experimental Cu and Cu-Mo interactions well, such as the desorption energies (§4.1.6), the hcp/fcc and bcc/fcc energy differences (§4.1.5) and the melting temperature of Cu (§4.1.2), or reasonably adequate, such as the surface energies (§4.1.4) and the activation energies for bulk and surface diffusion (§4.1.7). Several less satisfactory results are found also. Below, the validity of the Cu-Cu and of the Cu-Mo interactions is discussed. Another factor in the realism of the simulations is the high temperature applied in order to activate (more) higher activation energy processes during simulation, which is discussed as well.

Validity of the Cu-Cu interaction Two main deviations are found for our Cu-Cu interaction as compared to experimental quantities. The elastic constants (§4.1.3) at low T are higher than experimental values by more than 10 %. They also show an unsurprising and physically sound trend towards lower values at higher temperatures. The deviating values of the elastic constants make looking at the parameter ℓ less straight forward, as it is highly dependent on the relative strengths of these elastic constants. Another important difference is the atomic volume, which is consistently too large, and the (volume and linear) thermal expansion, which is also too high, but not very far off when compared to other simulation values. This results in a smaller mismatch between Cu and Mo, and also introduces problems in interpreting the simulations, which are all based on the experimental room temperature volume. Below, we return to the effect of elastic constants and volume, in relation with the applied temperature. The elastic constant reported in [6] are close to (extrapolated) 0 K values, but are considerably different at 300 K, while the linear expansion coefficient is further away from the experimental values than our own. The atomic volume (at 0 K) is equal to the experimental volume (at 300 K). This indicates that obtaining an EAM interaction which reproduces all physical quantities for more than a single temperature is not trivial.

In summary, the current Cu-Cu potential is usable, but there are some issues that make using it more difficult than we would like. It would be good if we can find a way of evaluating the equations from Oh and Johnson either at 300 K, using the experimental parameters that are found at this temperature and somehow dealing with the presence of a kinetic energy in this potential, or evaluating the equations at 0 K, using experimental quantities that are "extrapolated" for use at 0 K as well, such as the elastic constants used in [45]. A possibly useful modification of the evaluation of the functions may be to explicitly fit to Ω (or $r^{eq}_{1,CuCu}/r^{CuCu}_{latt}$) and split Ω, B and G_v. This would make the result of the fit easier to evaluate. Nevertheless, our fit procedure for obtaining the potential parameters should lead to values for Ω, B and G_v (evaluated for a Cu system at 0 K) that reproduce the experimental values (at 300 K). We suspect that programming errors are the reason that this is not so.

Choice of cutoff radius Aside from the above considerations, a recent article concerned with determining the stacking-fault energy in Cu using EAM [35], warns of caution when applying finite-range potentials (which most if not all MD interactions are) to situations with large strains, as this will lead to next neighbour shells to be included/excluded. In studying Cu fcc materials in particular, the number of third and fourth neighbours may be very sensitive to the particular choice of cutoff, and could change as a result of small contractions or expansions. In our case, as the cutoff is quite close to the hcp fourth neighbour distance, a linear contraction of a less than two percent results in hcp third neighbours being taken into account. This is only a very small effect, but the energy difference between the two crystal structures is likewise small. However, against the conclusion of [35], this need not be an unphysical effect. Since a smooth cutoff is used, then these atoms have an increasingly larger effect with the increase in contraction, just like the third and second neighbour atoms, actually. This is the intended behaviour. The article further mentions the possibility of a phase transition for fcc materials at linear deformations in excess of 12 %. It is not impossible that this happens as the higher neighbour shell atoms have an increasingly stronger interaction with the "central" atom. At which linear deformation this phase transition occurs is dependent both on the form of interaction function and on the cutoff. However, the choice of this cutoff belongs in the realm of wisely constructing an interaction, so that this is just another factor to take into consideration. All of this indicates that the choice of the precise value of r_c in an EAM interaction is not an arbitrary one.

Validity of the Cu-Mo interaction In view of the fact that the geometry of the CsCl structure, which is used for fitting the only experimentally available quantity of the Cu/Mo system, is more in agreement with bcc than with fcc, the use of the (fcc) Cu-Cu fcc pair potential function as a basis for the Cu-Mo pair potential is perhaps not the best choice. Also, the shape of the potential energy of a Cu-Mo pair is odd (see figure 15). However, seeing the results (especially the desorption energy), the choice looks credible. Nevertheless, we have now had more time studying other methods of deriving a mixing-potential. As the used method is rather *ad-hoc*, we should reconsider before applying the method to future mixing systems such as the Cu-Ta interaction. Recently we found an alternative method of mixing fcc and bcc metals using EAM [16] (Ni-Cr). This method is applied to the Cu-Ta system by Heino to study the energetics and yield point of a series of Cu/Ta model interfaces [33]. He uses existing single-element Cu [54] and Ta [6] EAM potentials which are modified to provide better mixing abilities and are updated with values from [46].

The effect of usage of high deposition temperatures on ℓ The parameter ℓ gives a measure for the ability to form epitaxial relations (§2.5.1, page 34). Comparison between literature value and the value(s) found here at different temperatures indicates the influence which the use of elevated temperatures has on the observed epitaxy. The literature value for ℓ was found to be $\ell_{lit} = 5.88$ (see the end of §2.5.1). Looking again at the somewhat higher

value for ℓ that was calculated in §4.3 on page 95 for deposition at 1000 K, $\ell_{1000\text{ K}} = 5.94$ (the mismatch is reduced by 2.84 %, but Ω increases by 9 %), it is interesting to see what the values for 0 K and 300 K are. These values are:

$$\begin{aligned}\ell_{0\text{ K}} &= \frac{1.2\,\Omega_{\text{Cu}}\,(c_{11}^2 - c_{12}^2)/(2c_{11})}{Q_{surf.diff}\,r_{\text{m}}^2} \\ &= \frac{1.2 \cdot 12.0398\ \text{Å}^3 \cdot (203^2 - 142^2)/(2 \cdot 203) \times 10^9\,\text{Pa}}{0.110\ \text{eV} \cdot 0.94389^2} = 5.24\end{aligned}$$

and

$$\ell_{300\text{ K}} = \frac{1.2 \cdot 12.246\ \text{Å}^3 \cdot (198^2 - 134^2)/(2 \cdot 198) \times 10^9\,\text{Pa}}{0.110\ \text{eV} \cdot 0.94925^2} = 5.46.$$

This means that the temperature does not have a very large effect on ℓ. From these values of ℓ it would be predicted that Cu starts growing as a pseudomorphic layer for coverages of $\Theta \leq 0.57$ at 1000 K to $\Theta \leq 0.68$ for 0 K and at higher coverage switches to the NW-x orientation (see figure 10 on page 35). We find that the first monolayer largely remains pseudomorphic. We also observed that at $\Theta = 0.75$ the first plane 2 atoms appear. Note, however, that the theory behind ℓ is not really suited to sub-monolayer coverages, and that it only describes a static situation, not taking dynamics into account. Therefore, the altogether good agreement is not necessarily the definitive result. Once we have a better analysis method for our stress tensor data, it may be interesting to compare our results using the critical thickness obtained from [86]. Perhaps we might also use results from [4] to characterize the found epitaxial relationship(s).

There is no strong difference between the literature value for ℓ and our own values at low temperatures. In fact, going to a high temperature decreases the difference with the literature value, which makes the present results more comparable to experimental values.

5.2 Discussion of the obtained results

Diffusion behaviour The high diffusion of the Cu atoms both on Mo and on 1ML Cu//Mo(110) (§4.1.7) enables the film to start growing the first monolayer of Cu, and also enables the formation of island by atoms clustering together and becoming attached existing islands. The literature does not report the observed remarkable non-random walk behaviour of Cu adatoms on a Cu{111} surface at low temperature. Boisvert and Lewis [12] describe behaviour which may resemble what we found, however, the reported results are inconclusive. They do report an interesting behaviour at higher temperatures, involving Brownian motion, which may describe our high temperature results as well. However, the observed high temperature behaviour can also be explained by activation of an additional jump mode along $\{110\}_{\text{fcc}}$ described in [43]. Anyhow, the behaviour could well be the same as what was found in [12], but the explanation offered there may not be sufficient. The low temperature behaviour needs further research for a full description, and perhaps further audits of literature.

Di- and multimer diffusion is also an interesting aspect of diffusion found during initial phase of the deposition simulations. We basically observed that

the average diffusion distance of deposited atoms is much less than expected from the adatom diffusion alone (see §4.1.7 and §4.3.1). This is attributed to clustering of adatoms into larger, less mobile or even immobile, groups of atoms. For adatoms on the substrate these contain more than 4–6 atoms. On the first monolayer , 10-13 atom clusters constitute a critical nucleus for island formation.

Nanostructure and texture of the deposited films The epitaxial relation(s) observed in the Cu/Mo films are mainly NW-x, with some incoherent features, as expected from theory. The presence of a 1 monolayer pseudomorphic Cu layer, is also not unexpected, although the thickness (or lack thereof) is more controversial.

The observed change from 2-D to 3-D growth is related to the structure of this first monolayer of Cu, but what controls the change back to (more) 2-D growth is not clear. From the difference in duration of 3-D growth between large and smaller systems, we may derive that the change back depends on the lateral growth and thus on the distance between the islands.

The linear defects seen are indeed (partial) dislocations, as a comparison with [72] shows. This article compares total and partial partial dislocations in Al (fcc), using the OJ-EAM interaction (§3.1.1, and [57, 58]).

In the large systems, we observe the formation of one or two grain-boundaries, which are located more or less parallel to the shortest lateral system dimension and to a certain crystallographic direction (bcc[110]/fcc{211}). We cannot, at present, distinguish which is the determining fact. It is certainly possible that the periodicity of the box influences the shape of the grain boundaries, see §5.3.

The occurrence of the many stacking-fault defects is so well reproduced between the simulations that these should be expected to occur in experiments as well, at least qualitatively in the same amounts. The fact that we performed our simulations at 1000 K, which influences the elastic constants, and that our Cu has a somewhat lower fcc/hcp energy difference, two factors that favour partial dislocations, means that in experiments these defects may have a lower concentration.

Analysis of texture parallel to the surface shows that the crystal orientation is predominantly fcc(111) or hcp(111) for both the IBAD and the EVAP cases (with an NW-x orientation for most of the planes). From the lowest plane to the higher ones, there is a decreasing tendency for the planes to deviate (in θ away from this substrate normal) from this texture. For the smaller simulation box the structure is mainly in the fcc or hcp (344) orientation instead, probably due to restrictions brought on by the smaller box dimensions.

A remarkable thing about all deposited films is that they contain only very few, or no, point defects. The relatively high diffusion coefficients have a large influence in this respect. It may be that the presense of other, one- or two-dimensional defects suppresses point defects by capturing them. This should show up in TDS spectra.

EVAP versus IBAD From the present results we can not find the clear difference in fcc/hcp ratio that we reported in [15]. It does appear that in general the IBAD films contain more hcp, but the variations between all the films show no strong trends. This is discussed below.

A difference between the EVAP and the IBAD simulations which is clear, is that the bcc-collapse (figure 67) takes place at a higher coverage. The reason behind this is not known.

The structure has a more gradual transition from bulk bcc Mo to bulk close-packed Cu due to intermixing and due to a modified structure as compared to EVAP. This structural difference is clearly observable from the difference in structure of figures 61 (EVAP) and 62 (IBAD). IBAD results in a transition of the first Cu layer from pseudomorphic bcc(110) to a plane with higher in-plane density, approaching more closely the other Cu planes in structure and in-plane density. With IBAD, plane 2 also contains more bcc than for EVAP (figures 84 and 85, lower left picture). Between the different simulations, the mean volume per atom, however, does not vary in these two planes or in the bulk of the film (see figure 89). The mixing of the Cu and Mo atoms at the interface (table XXIII, figure 87) is also a notable effect, with Mo atoms ending up as high as in the fifth Cu layer. These three effects result in a more gradual potential energy change over the interface. EVAP leads to a weakly bound second Cu plane. Therefore, for the IBAD films, the interface adhesion properties are likely to be better, but more work is needed on this.

We have observed most of the effects that are reported for IBAD (see §2.5.3 growth, namely:

- mixing at the interface
- island break-up and, related
- a lower roughness
- an increased tendency to equilibrium, as signaled by the lower amount of threading dislocations and grain boundaries, and by the less coherent interface.

Trends in EVAP versus IBAD and in system size After seeing the initial results with two small systems ($EVAP_s$ and $IBAD_s$) we concluded that EVAP results in more hcp than does IBAD [15]. Now however, looking at figure 66 the conclusion must be that this is not true. Instead, it seems that IBAD has a relatively high fraction of hcp and EVAP has less hcp, but more importantly, the fcc/hcp balance may vary considerably in favour of either fcc or hcp. The fcc/hcp ratio from $EVAP_{b1}$ and $EVAP_{b2}$ for instance differs by more than a factor 3 (see table XXIII).

In all films, after 3-D growth has ceased, the hcp fraction first increases (figure 66). In some of the simulations it falls down again as fcc "takes over" while in other the hcp fraction's growth continues with the fcc fraction having a smaller role. It would be interesting to know whether repeating the simulations starting just after the fall down of 3-D growth reproduces this hcp fall

down/further growth or not. This would answer the question whether this behaviour is enclosed in the structure at that time or not. Also, we may need further investigate the energy difference between fcc and hcp in circumstances further away from an equilibrium bulk structure.

Comparison with TDS (simulations) The previously mentioned simulations of the first stage of TDS [19, 15] reported the presence of dislocations with a mixed edge- and screw character in the initial films (which are taken from $EVAP_s$ and $IBAD_s$). The current study determines that many planes are buckled due to partial dislocations. These partials show a mixed burgers vector by default [7]. The related defects found are, as we now know, the stacking fault defects.

The TDS simulation study finds that during He bombardment, atoms move along lines (close-packed atom rows). These lines are currently identified as dislocations. The movements take place by means of replacement collisions. Most He atoms are eventually located at the second Cu plane, which we here determined to be more weakly bound that the other planes (for EVAP), while the first plane is more strongly bound in all systems. The He bombardment of the EVAP "10 Å" film also apparently induces the bcc-collapse which normally takes place at a somewhat higher coverage. This results in an increased amount of fcc and hcp after the bombardment. This result should be contrasted with the influence of ("*in situ*") IBAD, where the bcc collapse is delayed.

As we found virtually no point defects, no He can be expected to be trapped in existing defects. The threading dislocations likely function as diffusion paths out of the films. We only have a very limited amount of experimental results. The change in structure with increasing coverage should be observable in TDS spectra, and the experimental results do indeed show a strong change with thickness [15, 19]. More research is required in order to assign the experimentally observed peaks to specific structural features, as found from simulations.

5.3 Roles of system size and of computing environment

As we have done experiments at two different system sizes for Cu on Mo, and also duplicated the EVAP run on a different machine, and with a difference in restart interval, we can compare the influence of these two computational quantities, that should yield the same results (at least statistically), as the temperature and the deposition rate, as well as the initial system before deposition, are equal. For the Cu on Cu deposition, we have simulations that are at two temperatures, but also in different systems. These are difficult to compare, but it might still be worthwhile.

Effect of processor type The one thing that is very different in comparing $EVAP_{b1}$ with $EVAP_{b2}$ and $IBAD_b$ is the amount of fcc and the roughness, which both are higher for $EVAP_{b1}$. Other factors, like the large spread in fcc/hcp ratio between all simulations, make it unlikely that this is a result from using another CPU type (and the serial or parallel version of our simulation code). The roughness seems to be related to the fcc content in $EVAP_{b1}$. A possible

influence in this respect may come from differing restart intervals (which introduces a new random number seed). On the Cray computer (see table XIV), the program is restarted after each hour of calculation, while the serial version is only occasionally restarted. The random number generator is trustworthy.

Effects of system size

Dimensional restriction The system size-effect is evident. In the smaller systems, only one island developed, the periodicity just fitting in the box. On the other hand, the larger system shows a periodicity that is, although more complex, and less symmetric, still of about the same size (see the staircases, figures 39–43). Corresponding, the very small system $\mathrm{EVAP_v}$ only shows a brief period of 3-D growth, as the allowed island size is so small that it meets its box-images within a small amount of coverage (not shown, figure 83 contains the R-curve of $\mathrm{EVAP_v}$ (dotted cyan line)). Height-height correlation data shows that in the large systems, the island "period" is about 55 Å in the bcc[110] direction (horizontal in most of the hard-ball images). The smaller box measures only 44.5 Å in this direction, while the very small system can only contain half an island period (table XIII).

The two Cu on Cu depositions both show twinning (resulting in one atomic row "missing") in the surface normal direction at low temperature, and a distortion of the planes, where one or more atomic rows are missing both in x and in y. In the smaller system this is achieved by a shear of the total plane (for all planes), while in the larger system the shear is only in parts of the planes ($k < 4$). To make this possible, these planes contain dislocations. This results in a plane that appears to be rotated rather than sheared. At high temperature, the large system ($k > 3$) has a plane density equal to that of bulk Cu at this T, while the small system has a somewhat too high density as it has less freedom to modify its plane density. At the low temperature, the structure of the small system was much more complicated and had a higher roughness but this could also result from the lower temperature of the bulk in the larger system (compare figure 24 and 25).

More atoms is more detail Part of the difference is a "better-statistics" type difference of the large systems with respect to the small ones, as shown by the Ar incorporation, Cu/Mo intermixing and surface "span", and possibly with the vacancy presence. The atom-history shows this very clearly as well, as illustrated by figures 91–95. Do note that a longer simulation time increases the absolute amount of atoms. However, these figures do also show that the behaviour is somewhat different in a more subtle manner such as the shape of the high atom count regions, which are less rounded. The distinction between statistics and modified behaviour due to size constraints is not always clear. From the various figures showing the R-curves, we see two clear effects of system size. Firstly, the 3-D growth region has more abrupt boundaries for smaller systems (figure 83, shows that this remains true also for $\mathrm{EVAP_v}$). Also, but possibly connected, the 3-D growth region's peak moves to higher coverage as

the system size increases. A second observation is that the roughness of the smaller systems after 3-D growth has subdued is much more stable than in the larger systems, and that it remains lower. This can be attributed to a down-scaling of the surface "hills" seen for instance in the staircase figures. Each hill-like feature of the large systems is one sixth to one half of the box surface, ie. 3360–10085 $Å^2$, while the smaller systems have a surface of only 2521 $Å^2$ (see table XIII, $EVAP_v$: 925 $Å^2$), so that these features can not fully develop.

Necessity of large systems Comparing the nanostructure in the films, we see that the smaller systems show a structure which is representative of what is seen in the larger systems as well, albeit with some simplifications. The very small systems do not show this structure. We can not however conclude from this that the small systems would have been sufficient. It is only in looking down from the larger systems and the features of the structures seen there, that we see the similarity. Previously, the conclusion would have been that there is considerable difference in structure between EVAP and IBAD. The larger simulations, in providing us with more complex and diverse structures, make clear that the perceived difference may be coincidental.

The higher roughness of the larger systems at high coverage is another effect which could not be found from the small systems, showing the need for the larger simulations.

6 Summary of results

6.1 New methods for analysis

In the course of this work, we have developed several new methods for analysis of the MD results, as described in §3.2.

- The local crystal geometry parameter S is not only useful by itself, but also proved very useful for indicating defects in fcc/hcp, as these are decorated by atoms with an (apparent) bcc local geometry. Dislocation lines, for instance, are indicated by ribbons of bcc atoms. See figures 69–73 (bccdot-plots), 77–81 (3D-bccdot figures) and the left-hand side of figures 63–65, 74–76, 84, 85 (the structure of a selection of planes), and other figures based on S.

- The plane filling compared to the s-o-s model, β_k (figures 50–54(b)) is a helpful quantity for studying the growth mode. Better analysis of theoretical growth modes in terms of β_k will further improve its usefulness, as is clear from pages 110, 122 and page 123. The current manner of creating the β_k-data, using a spline-fit to obtain the derivate of the plane filling introduces artifacts for very incomplete planes. This could be improved by using the available information on the shape of the plane-filling (an S-curve) in the (spline-)fit procedure.

- The atom-history logging (figures 50–54(c), figures 91–95 (contour-plots), and the text on pages 110, 161) showed considerable value in describing the out-of-plane atomic movements after deposition. It needs to be improved to provide quantitative results that are more easily interpreted. From the available data, it is possible to better measure for the lateral displacement, which is especially interesting for the first few monolayers of deposition, where diffusion and cluster mobility play a large role (see page 96).

- We have successfully utilized the δ^θ analysis (right-hand side of figures 63–65, 74–76, 84,85 and §4.3.4) for "texture" analysis. The method enables us to determine the dominant texture in the film, as well as deviations from this texture. In combination with the S analysis, this analysis method shows how the defects, such as stacking-faults and grain boundaries, are positioned and how they influence the surrounding crystal.

6.2 Inaccuracies in the performed simulations

There are two important problems with the present Cu-Cu interaction. One lies in the Cu diameter, which is about 3.7 % too large at 300 K (§4.1.1), the other lies in the elastic constants, which are up to 18 % too large at 300 K, and are even larger at 0 K (§4.1.3). The necessary elevation of the deposition temperature to 1000 K (§2.4) increases the problem of the Cu diameter as our Cu expands more than normal Cu, while Mo has a very low expansion (the Mo substrate is actually held fixed in the lateral directions), leading to a 2.8% reduced mismatch

r_m as compared to the experimental r_m at 300 K. However, the elastic constants are lower at 1000 K than at 300 K. Together, these two effects likely lead to a more easy accommodation of mismatch strains, which favours pseudomorphy and other epitaxial relations. The values of ℓ (see §5.1) indicate that this is effect is not a large (§5.1), and that, in fact, the high temperature simulations are closer to the experimental result than simulations at 300 K. Other problems are due to the limited dimensions of the systems. The possible influence of this is summarized in §6.4, below.

6.3 Observed phenomena in Cu on Mo(110) deposition

General features of Cu/Mo films Several phenomena are common to all films, independent of the applied deposition method:

- The mean atomic volume of the deposited films is 1% larger than bulk Cu at 1000 K (see tables XV and XXIII). It varies only 0.4% between the simulations. In the interface planes $k = -1$ to 4, the density is different, see figure 89.
- The film growth behaviour has several notable features (see the β_k and R data, figures 48,83, and also figures 46,47):
  - The first Cu plane forms as a pseudomorphic bcc plane. It is nearly completed before the next plane starts growing.
  - The growth mode changes to 3-D island growth after the first Cu plane is nearly completed, resulting in a high roughness of the film. This growth mode is maintained until the islands have grown together, after which the growth changes to a plane-by-plane like mode.
  - At higher thicknesses, the growth mode shows a less perfect plane-by plane growth, with a resulting increasing roughness (although still low in comparison with Mo{110} growth, see figure 83). This effect is most clear for the larger systems.
- During the 3-D growth the structure is mainly bcc with fcc/hcp "cores" in the higher planes of the islands. At higher coverage, the structure shows a sudden change, marked by a collapse in bcc content of the film and an accompanying rise in hcp (and fcc) local crystal structure (figures 66,67). The bcc regions diminish in width and become the boundaries of tiny fcc/hcp grains, and then dissolve further into more individual threading dislocations (bccdot-plots, figures 71–73 and 3D-bccdot figures, figures 77–81).
- The final films consist of bands of fcc/hcp close-packed planes separated by stacking-faults and forming a nanograined structure. The bcc atom-marked dislocation lines form one or two grain boundaries, and are present as individual threading dislocations.
- The films have a predominant $\{111\}_{fcc}$ and $\{111\}_{hcp}$ (not a close-packed plane) orientation, with deviations of 5–10° near stacking-faults. The

smaller systems have a systematic deviation from the fcc{111} orientation (EVAP: $\{344\}_{fcc}$, IBAD: $\{122\}_{fcc}$).

- The mean potential energy in the "bulk" of the films is 0.4% higher than bulk Cu at 1000 K. The energy is lower for the first film plane. For EVAP the second plane has a higher energy than other planes (§4.3.7).

- Several types of defects are found in the deposited films:

  - Interstitials (crowdions) form in the first Cu plane (EVAP: 0.6% of a monolayer , IBAD: 3.9%). For IBAD, they cluster and modify the pseudomorphic structure. The crowdions change position within the plane (EVAP: figures 56,59,61; IBAD: figures 57,60,62).
  - Only a few vacancies are found in the IBAD films, and none in EVAP (table XXIII).
  - In the large IBAD film, three Ar are incorporated, and in both IBAD films, one Ar is incorporated in the substrate (§4.3.7, figures 88 and 87).
  - A large number of threading dislocations is found, all reaching up from the interface to the surface. Some are seen in pairs, enclosing a stacking-fault, while others form grain-boundary walls. All undergo an oscillating lateral motion, with a frequency of about 15 MHz and an amplitude of 2–4 Å (see §4.3.4, page 135).
  - During the deposition the formed grain boundaries move and reshape as the grains grow, eventually forming one or two walls parallel to the smallest lateral dimension of the box (bccdot-plots, and 3D-bccdot figures).

IBAD Several features are only found for IBAD namely:

- Compositional mixing at interface
- Ar incorporation in film (all neutralized Ar atoms)
- Sputtering of Mo while the substrate is exposed to arriving ions, and sputtering of Cu during the entire deposition.

The influence of Ar atoms on the development of the films lies mainly in introducing intermixing of Cu and Mo (figure 87 in §4.3.7), and also leads to the first Cu plane changing structure at higher coverages to a structure which contains highly deformed regions. This structure functions as as an intermediate between the substrate and film structures (ie. figure 62 versus 61, and see also figure 90). Both effects result in a more diffuse/gradual interface with (likely?) better adhesion properties. Also, the energy introduced by the Ar leads to decreased islanding (see figure 48 or 83). In $IBAD_b$, only one grain boundary forms instead of two (bccdot-plots, and other figures).

Accommodation of misfit We can conclude that the misfit is accommodated by a combination of elastically strained regions and stacking defects between close-packed planes. For EVAP, the first plane is almost entirely elastically strained while for IBAD this plane contains more defects (bands of crowdions) to relieve strain. In EVAP, the misfit is accommodated mainly in plane 2, which is consequently more weakly bound. In IBAD, the more diffuse interface, spanning the top two substrate planes and at least the first two film planes, provides for a more gradual accommodation of the misfit.

6.4 Effect of system size

The effect of the system size on the results is not clearly distinguishable for all of the observed phenomena. Apart from the improved statistics due to the larger number of atoms, two significant effects are:

- the relative simplicity of the nanostructure in the smaller films (see the bccdot-plots), and
- the almost constant low roughness of the small systems up to the end of the simulation (figure 48, and §4.3.5).

The size of the hill-like features that develop at high roughness may indicate that the large systems may also somewhat limit the roughness. The grain boundaries that span the entire box (see the bccdot-plots) also indicate that the large systems do noticeably restrict the film.

6.5 Miscellaneous results

- The melting temperature of our Cu (1380 K) is close to the experimental melting temperature, being at most 30 K too high (§4.1.2). The melting temperature of the deposited films is somewhat lower. In a recent study [19], our Cu/Mo films showed surface melting above $\sim$ 1200 K. The desorption energies of 1 monolayer and 2 monolayers of Cu from a Mo{110} substrate are also in close agreement with the experimental values (§4.1.6).
- The critical nucleus for the formation of immobile clusters on Mo{110} is 4–6 atoms (figure 45). The critical nucleus for island formation on the first Cu monolayer is 12–15 atoms (see the staircases, figures 39–43).
- We found a remarkable diffusion behaviour of Cu on Cu{111}, where at low temperature, a Cu adatom shows a memory effect, moving in orbits around surface atoms §4.1.7. The high temperature behaviour is more in agreement with the literature. We were not (yet) able to determine if diffusion became dominated by Brownian motion [12], or if an additional jump event which leads to longer jumps is activated at these temperatures, as suggested in [43]. Adatom diffusion on a pseudomorphic Cu monolayer on Mo{110} involves exchange of atoms (§4.1.7, page 88 and figure 33).

7 Future work and recommendations

7.1 Recommendations

- New simulations using the current Cu (and Cu-Mo) interaction should at least be performed with systems that have an appropriate substrate lattice constant, depending on the temperature. It is therefore recommended to use pressure control, either in all three Cartesian directions or only in the lateral directions for deposition and other surface related simulations.

- For a more extensive study using Cu, it would be better to modify the Cu interaction using the experimental values that are reported in the current work. As we now have a better understanding of the issues involved, and more and better possibilities of checking the outcome, this would likely improve the real-world validity of the simulations. For a high temperature study one should consider also modifying the Mo (or another high melting temperature material) interaction in order to obtain results that are more easily translated to experimental conditions.

- It is worthwhile to investigate the energies and (relaxation) behaviour of stacking-fault defects, and the related hcp-fcc energy difference as a function of temperature, as the large amount of hcp found in the current Cu/Mo simulations suggests that this already very small energy is significantly further reduced at high temperature.

- Using the obtained results of the larger films, performing more simulations with smaller systems (possibly only for reproducing a small coverage range) could provide an improved understanding of which observed phenomena are random fluctuations and which are clear differences resulting from differing simulation conditions.

- For a further analysis of the behaviour of isolated and interacting adatoms moving over a Mo{110} or Cu/Mo{110} surface it may be interesting to use the results from [65], in which Monte Carlo simulations are used to study adatom concentrations on vicinal surfaces during epitaxial growth. Also useful in this respect may be a review article by Zangwill [85] in which he attempts to give " ... a sort of "consumer's guide" to the recent theoretical literature."

- To be able to better compare the different interfaces obtained from EVAP and from IBAD, we may consider using [50], which reports a method to characterize interface roughness based on the interface height distribution curve. This is a variation on the tools used in [62].

- To obtain a more definite answer on the adhesion properties of the films, the films can be bended to see if, and when, the film breaks loose from the substrate.

7.2 Left for further work

- A proper analysis of stresses and strains in the deposited films still needs to be done. One should aim for a better understanding of the variations in stresses from atom to atom and how the variations are influenced by the presence of the various types of defects, such as stacking-faults or dislocations and vacancies or Ar and Mo impurities in the films.

- The initial stages of the Cu deposition on Mo, up to the first monolayer, should be repeated at low temperature. This results in simulated films that more properly reflect the mismatch and strains that are present in experiments. In this stage elastic strains are very important for the resulting structure. This stage of deposition is also strongly dependent on the possibility of surface diffusion. However, this poses no problem, as the necessary processes are active even at low temperature.

- To help in investigating the behaviour of stacking-fault like defects, we should study the behaviour of a series of such defects, with various shapes and orientations. Here we can now profit from the better insight that we gained of what such defects look like, and how to introduce them in bulk crystals.

- It should be tested if the restart frequency of a simulation run affects its outcome, as each restart introduces a new random number sequence. This would indicate that we need to perform many runs with a new sequence of random numbers for reliable statistics. Until recently, we had to restart the parallel simulations after each hour of calculations, but this is no longer required.

- The roughness may be further investigated by means of the methods described in [30] for calculating the height-height correlation of a solid-on-solid model. The study finds that the positions and sizes of the islands formed during $\Theta \leq 0.5$ monolayer are highly correlated. At higher coverages, the larger roughness of the large systems as compared to small systems, as well as the much higher roughness of the $\mathrm{EVAP_{b1}}$ film may also show up in height-height correlation data.

References

[1] G. J. Ackland, G. Tichy, V. Vitek, and M.W. Finnis, *Simple N-body potentials for the noble metals and nickel*, Phil. Mag. A **56** (1987), 735–756.

[2] James B. Adams, Zhiyong Wang, and Youhong Li, *Modeling Cu thin film growth*, Thin Solid Films **365** (2000), 201–210.

[3] Rajeev Ahuja, A.B. Belonoshko, and Börje Johansson, *Melting and liquid structure of aluminum oxide using a molecular dynamics simulation*, Phys. Rev. E **57** (1998), no. 2, 1673–3844.

[4] T. Akbay, K. Aydinol, and S. Bor, *Simulation of electron diffraction patterns of alloys with oriented precipitates*, J. Appl. Cryst. **27** (1994), 379–384.

[5] M.P. Allen and D.J. Tildesley, *Computer simulation of liquids*, p. 78, Oxford Science Publications, New York, 1989.

[6] Zhang Bangwei and Ouyang Yifang, *Theoretical calculation of thermodynamic data for bcc binary alloys with the embedded atom method*, Phys. Rev. B **48** (1993), no. 5, 3022–3029.

[7] Charles S. Barret and T. B. Massalski, *Structure of metals*, third ed., Materials Science and Engineering series, pp. 384–395, McGraw-Hill Book Company, New York, 1966.

[8] M.I. Baskes, *Modified embedded-atom potentials for cubic materials and impurities*, Phys. Rev. B **46** (1992), no. 5, 2727–2742.

[9] E. Bauer and Jan. H. van der Merwe, *Structure and growth of crystalline superlattices: From monolayer to superlattice*, Phys. Rev. B **33** (1986), no. 6, 3657–3671.

[10] A.B. Belonoshko, R. Ahuja, O. Eriksson, and B. Johansson, *Quasi* ab initio *molecular dynamic study of Cu melting*, Phys. Rev. B **61** (2000), no. 6, 3838–3844.

[11] H.J.C. Berendsen, J.P.M. Postma, W.F. van Gunsteren, A. Di Nola, and J.R. Haak, *Molecular dynamics with coupling to an external bath*, J. Chem. Phys. **81** (1984), no. 8, 3684–3690.

[12] Ghyslain Boisvert and Laurent J. Lewis, *Self-diffusion on low index metallic surfaces: Ag and Au* (100) *and* (111), Phys. Rev. B **54** (1996), no. 4, 2880–2889.

[13] E.A. Brandes and G.B. Brook (eds.), *Smithells metals reference handbook*, seventh ed., pp. 61–65, Butterworth–Heineman Ltd., London, UK, 1992, Ch. 14, tables 14-1, 14-2.

[14] L.A. Bruce and H. Jaeger, *Geometric factors in f.c.c. and b.c.c. metal-on-metal epitaxy III. The alignments of* (111)*f.c.c.*-(110)*b.c.c epitaxed metal pairs*, Philos. Mag. A **38** (1978), no. 2, 223–240.

[15] Bouke S. Bunnik, Carin de Hoog, Edwin F.C. Haddeman, and Barend J. Thijsse, *Molecular dynamics study of Cu deposition on Mo and the effects of low-energy ion irradiation*, Nucl. Instr. Meth. B **accepted for publication** (2000–2001).

[16] J.K. Chen, D. Farkas, and JR Reynolds, W.T., *Atomistic simulation of an f.c.c./b.c.c. interface in Ni-Cr alloys*, Acta. mater. **45** (1997), no. 11, 4415–4421.

[17] B.M. Clemens, H. Kung, and S.A. Barnett, *Structure and strength of multilayers*, MRS bulletin **24** (1999), no. 2, 20–26.

[18] Vic Comello, *Next-generation copper ICs still need more development*, Thin-film research (1997), s3–s8.

[19] Carin de Hoog van Beynen, *Low energy He^+ ion effects in Cu films, Molecular dynamics simulation in support of thermal helium desorption experiments*, Master's thesis, Delft University of Technology, Department of Applied Physics; Section Physical and Chemical Materials Science of the Department for Material Science and Engineering, Rotterdamseweg 137, 2628 AL Delft, The Netherlands, Jul 2000, Supervisors: Dr. B.J. Thijsse, Prof. Dr.ir. T.M. Klapwijk.

[20] Mario del Popolo and Ezequil Leiva, *Embedded atom method study of Cu deposition on Ag*(111), Journal of Electroanalytical Chemistry **440** (1997), no. 1–2, 271–277.

[21] G.J. Dickins, Audrey M.B. Douglas, and W.H. Taylor, *The crystal structure of the Co-Cr σ phase*, Acta Cryst. **9** (1956), 297–303.

[22] Masao Doyama, *Simulation of dislocations and plastic deformation in nano-size single crystals*, Nanostructured Materials **9** (1997), 689–692.

[23] Masao Doyama and Y. Kogure, *Embedded atom potentials in fcc and bcc metals*, Comp. Mat. Sci. **14** (1999), 80–83.

[24] W. Eckstein, *Computer simulation of ion-solid interactions*, pp. 40, 75, Springer-Verlag, Heidelberg, 1991.

[25] S.M. Foiles, *Embedded-atom and related methods for modeling metallic systems*, MRS Bulletin **21** (1996), 24–28.

[26] H. Gades and H.M. Urbassek, *Energy deposition, reflection and sputtering in hyperthermal rare-gas yields Cu bombardment*, Appl. Phys. A **61** (1995), no. 1, 39–43.

[27] Gary S. Grest, Burkhard Dünweg, and Kurt Kremer, *Vectorized linked cell fortran code for molecular dynamics simulations for a large number of particles*, Comp. Phys. Comm. **55** (1989), 269–285.

[28] Francois Grey and Jakob Bohr, *Alternative explanation for epitaxial growth: the case of fcc(111) on bcc(110)*, Applied Surface Science **65-66** (1993), no. 1–4, 35–44.

[29] Edwin F.C Haddeman, Bouke S. Bunnik, and Barend J. Thijsse, *Thin film growth and ion-beam modification: MD simulations going beyond simple systems*, Fundamental mechanics of low-energy-beam-modified surface growth and processing (Steven C. Moss, Eric H. Chason, Barbara H. Cooper, James E. Harper, Thomas Diaz de la Rubia, and M.V. Ramava Murty, eds.), Mat. Res. Soc. Conf. Proc., vol. 585, 2000, pp. 103–108.

[30] Niaz Haider, Mark R. Wilby, and Dimitri D. Vvedensky, *Correlation length scaling during the early stages of epitaxial growth*, Mat. Res. Soc. Symp. Proc., vol. 280, 1993, pp. 135–138.

[31] H. Häkkinen and M. Manninen, *Computer simulation of disordering and premelting of low-index faces of copper*, Phys. Rev. B **46** (1992), no. 3, 1725–1742.

[32] James M.E. Harper and K.P. Rodbell, *Microstructure control in semiconductor metallization*, J. Vac. Sci. Technol. B **15** (1997), no. 4, 763–779.

[33] P. Heino, *Microstructure and shear strength of a Cu-Ta interface*, Comp. Mat. Sci. **20** (2001), 157–167.

[34] P. Heino, H. Häkkinen, and K. Kaski, *Molecular-dynamics study of copper with defects under strain*, Phys. Rev. B **58** (1998), no. 2, 641–652.

[35] P. Heino, L. Perondi, K. Kaski, and E. Ristolainen, *Stacking-fault energy of copper from molecular-dynamics simulations*, Phys. Rev. B **60** (1999), no. 21, 14625–14631.

[36] Hoedemaker, van der Kuur, Melker, and Thijsse, *Defects in thin amorphous Si films deposited with and witout Ar^+ ion assistance*, Nucl. Instr. Meth. B **127–128** (1997), 888–892.

[37] R. Hoogeveen, M. Moske, H. Geisler, and K. Samwer, *Texture and phase transformation of sputter-deposited metastable Ta films and Ta/Cu multilayers*, Thin Solid Films **275** (1996), 203–206.

[38] H.B. Huntington, Solid State Physics **7** (1958), no. 1, 214.

[39] H. Jacques and K.H. Robrock, *Mechanical relaxation effects of self-interstitial-atoms in molybdenum*, Point defects and Defect Interactions in Metals (J.I. Takamura, M. Doyama, and M. Kiritani, eds.), vol. V, 1982, pp. 159–162.

[40] R.A. Johnson, *Alloy methods with the embedded atom method*, Phys. Rev. B **39** (1989), no. 17, 12554–12559.

[41] ———, *Phase stability of fcc alloys with the embedded atom method*, Phys. Rev. B **41** (1990), no. 14, 9717–9720.

[42] Robert A. Johnson and Dirk J. Oh, *Analytic embedded atom model for bcc metals*, J. Mater. Res. **4** (1989), no. 5, 1195–1201.

[43] G.C. Kallinteris, G.A. Evanglakis, and N.I. Papanicolaou, *Molecular dynamics study of the vibrational and transport properties of copper adatoms on the* (111) *copper surface; comparison with the* (001) *face*, Surface Science **369** (1996), no. 1–3, 185–198.

[44] Janine Kardokus and Paul Silinger, *Damascus complete; Total Solutions; ECD matures; Material considerations*, European Semiconductor **Sep** (1998), 19–31.

[45] C. Kittel, *Introduction to solid state physics*, third ed., Wiley, Chichester, 1967.

[46] ———, *Introduction to solid state physics*, fifth ed., Wiley, Chichester, 1976.

[47] Peter Klaver, *A molecular dynamics study of ion beam assisted deposition of thin molybdenum films and analysis by thermal desorption spectrometry*, Master's thesis, Delft University of Technology, Applied Sciences, Section for Physical and Chemical Materials Science of the Department for Materials Science and Engineering, Rotterdamseweg 137, 2628 AL Delft, The Netherlands, Apr 1998, Supervisors: Dr. Barend J. Thijsse, ir. Leon D. van Ee.

[48] Peter Klaver, Edwin Haddeman, and Barend Thijsse, *Atomic-scale effects of sub-keV ions during growth and subsequent ion-beam analysis of molybdenum thin films*, Nucl. Instr. Meth. B **153** (1999), 228–235.

[49] Peter Klaver and Barend Thijsse, *Defect production during ion-assisted deposition of molybdenum films studied by molecular dynamics*, Mat. Res. Soc. Symp. Proc, vol. 504, Jan 1998, pp. 51–56.

[50] Su-Heng L and K. Hatalis, *A new quantitative roughness measurement and its applications in the polysilicon/silicon dioxide interface*, Mat. Res. Soc. Symp. Proc., vol. 280, 1993, pp. 111–116.

[51] Charles T. Lynch (ed.), *Handbook of materials science*, vol. I: General properties, pp. 61–65, CRC Press, Inc., 18901 Cranwood Parkway — Cleveland, Ohio 44128, 1974.

[52] M.J. Mehl and D.A. Papaconstantopoulos, *Applications of a tight-binding total-energy method for transition and noble metals: Elastic constants, vacancies, and surfaces of monatomic metals*, Phys. Rev. B **54** (1996), no. 7, 4519–4530.

[53] H. Mehrer (ed.), *Landolt-Börnstein Numerical data and functional relationships in science and technology*, New Series — Group III: Crystal and Solid State Physics, vol. 26, Springer-Verlag, Berlin, 1990.

[54] J. Mei, J.W. Davenport, and G.W. Fernando, *Analytic embedded-atom potentials for fcc metals: Application to liquid and solid copper*, Phys. Rev. B **43** (1991), no. 6, 4653–4658.

[55] J.R. Morris, C.Z. Wang, K.M. Ho, and C.T. Chan, *Melting line of aluminum from simulations of coexisting phases*, Phys. Rev. B **49** (1994), no. 5, 3109–3115.

[56] P.T. Moseley and C. J. Searbrook, *The crystal structure of β-tantalum*, Acta Cryst. B **29** (1973), 1170–1171.

[57] Dirk J. Oh and Robert A. Johnson, *Simple embedded atom method model for fcc and hcp metals*, J. Mater. Res. **3** (1988), no. 3, 471–478.

[58] ———, *Embedded atom method for close-packed metals*, Atomistic Simulations of Materials: Beyond Pair Potentials (Vaclav Vitec and David J. Srolovitz, eds.), Jan 1989, pp. 233–238.

[59] M. Paunov and E. Bauer, *An adsorption-desorption study of Cu on Mo{110}*, Appl. Phys. A **44** (1987), 201–208.

[60] R. Randler, M. Dietterle, and D.M. Kolb, *The initial stages of Cu deposition on Au(100) as studied by in-situ STM: The epitaxial growth of bcc Cu*, Zeitschrift fr Physicalische Chemie **208** (1999), 43–56.

[61] A. Robbemond, *Het maken van dunne films met behulp van ionenbundel-assistentie, bestudeerd met moleculaire dynamica*, Master's thesis, Delft University of Technology, Department of Chemical Engineering and of Materials Science and Engineering, Section Physical and Chemical Materials Science (FCM-1), Rotterdamseweg 137, 2628 AL Delft, The Netherlands, 1996, Supervisors: Dr. B.J. Thijsse, Prof. Dr.ir. A van den Beukel; in Dutch.

[62] Arie Robbemond and Barend J. Thijsse, *Ion-beam assisted deposition of thin molybdenum films studied by molecular dynamics simulation*, Nucl. Instr. Meth. B **127–128** (1997), 273–277.

[63] M. Djafari Rouhani, R. Malek, and D. Esteve, *Monte Carlo simulation of mismatch relaxation and island coalescence during heteroepitaxial growth*, Thin Solid Films **318** (1998), 61–64.

[64] Changsup Ryu, Haebum Lee, Kee-Won Kwon, Alvin L.S. Loke, and S. Simon Wong, *Barriers for copper interconnections*, Solid State Technology (1999), 53–56.

[65] Tomoya Shitara, Takashi Suzuki, Dimitri D. Vvdensky, and Tatau Nishinaga, *Adatom concentration profiles on simulated vicinal surfaces during epitaxial growth*, Mat. Res. Soc. Symp. Proc., vol. 280, 1993, pp. 131–134.

[66] F.A. Smidt, *Ion beam assisted deposition*, International Materials Reviews **35** (1990), no. 2, 61–128.

[67] P.J. Steinhardt, D.R. Nelson, and M. Ronchetti, *Bond-orientational order in liquids and glasses*, Phys. Rev. B **28** (1983), no. 2, 784–805.

[68] L.C.A. Stoop, *Misfit accomodation in epitaxial monolayers on* (111) *f.c.c. and* (110) *b.c.c. substrates IV: analytical approach to loss of complete coherence*, Thin Solid Films **94** (1982), 341–352.

[69] ———, *Misfit accomodation in epitaxial monolayers on* (111) *f.c.c. and* (110) *b.c.c. substrates IV: numerical approach to monolayers in the Nishiyama-Wassermann orientation*, Thin Solid Films **94** (1982), 353–363.

[70] L.C.A. Stoop and J.H. van der Merwe, *Misfit accomodation in epitaxial monolayers on* (111) *f.c.c. and* (110) *b.c.c. substrates II: analytical approach to monolayers in the Nishiyama-Wassermann orientation*, Thin Solid Films **91** (1982), 257–274.

[71] ———, *Misfit accomodation in epitaxial monolayers on* (111) *f.c.c. and* (110) *b.c.c. substrates III: analytical approach to monolayers in the Kurdjumov-Sachs orientation*, Thin Solid Films **98** (1982), 65–74.

[72] N.J. Tajima, T. Nozaki, T. Hirade, Y. Kogure, and Masao Doyama, *Computer simulation of creation and motion of edge dislocations in face centered crystals*, Mat. Res. Soc. Symp. Proc., vol. 365, 1995, pp. 111–116.

[73] Mark Telford, *Applied targets tantalum/copper*, European Semiconductor **Feb** (1998), 11–12.

[74] *Damascene copper making tracks*, European Semiconductor **Sep** (1997), 11–13.

[75] J. van der Kuur, E.J.W. Melker, T.P. Huijgen, W.H.B. Hoondert, G.T.W.M. Bekking, A. van den Beukel, and B.J. Thijsse, *Thin Mo films deposited and analyzed using sub-keV noble gas ions*, Mat. Res. Soc. Symp. Proc., vol. 396, 1996, pp. 587–592.

[76] Jan van der Kuur, *Defects in thin films deposited with and without ion assistance*, Ph.D. thesis, Delft Technical University, Rotterdamseweg 137, 2628 AL Delft, The Netherlands, Nov 1998.

[77] Jan H. van der Merwe, *Analytical selection of ideal epitaxial configurations and some speculations on the occurence of epitaxy I. Epitaxy with rectangular interfacial atomic meshes*, Phil. Mag. A **45** (1982), no. 1, 127–143.

[78] ———, *Analytical selection of ideal epitaxial configurations and some speculations on the occurence of epitaxy II. Epitaxy of* (111) *f.c.c. overlayers on* (110) *b.c.c. substrates*, Phil. Mag. A **45** (1982), no. 1, 145–157.

[79] ———, *Analytical selection of ideal epitaxial configurations and some speculations on the occurence of epitaxy III. Epitaxy of thin* (111) *f.c.c. films on* (110) *b.c.c. substrates by coherence*, Phil. Mag. A **45** (1982), no. 1, 159–157.

[80] D.P. van der Werf, *Helium in tungsten, a calculational approach*, Ph.D. thesis, University of Groningen Faculty of Mathematics and Natural Sciences, Nijenborgh 4, 9747 AG Groningen, The Netherlands, 1994.

[81] Leon D. van Ee, *The diffusion mechanism in amorphous Ni_81B_19 studied by molecular dynamics simulations*, Ph.D. thesis, Delft Technical University, Rotterdamseweg 137, 2628 AL Delft, The Netherlands, Nov 1998.

[82] H. Wendrock, W. Brückner, M. Hecker, T.G. Koetter, and H. Schloerb, *Room temperature grain growth in electroplated copper thin films*, Microelectronics Reliability **40** (2000), 1301–1304.

[83] Mark Winter, *Webelements*, available: http://www.webelements.com, 1993–2001.

[84] I. Yamada, T. Takagi, and P. Younger, *Handbook of thin-film deposition processes and techniques*, pp. 344–363, Noyes, Park Ridge, US, 1988.

[85] A. Zangwill, *Scaling description of sub-monolayer epitaxial growth*, Mat. Res. Soc. Symp. Proc., vol. 280, 1993, pp. 121–130.

[86] Tong-Yi Zhang, *Elastic constant effect on the critical thickness of an epilayer*, Mat. Res. Soc. Symp. Proc., vol. 365, 1995, pp. 325–329.

Summary

We study deposition of Cu on Mo(110) substrates by means of Molecular Dynamics (atomistic) simulations, using Embedded Atom Method (EAM) interactions. The Cu-Cu and Cu-Mo interactions are newly created.

Cu is an important material in current IC tecnologies, but it needs a barrier layer to prevent diffusion of Cu into the surrounding semiconductor material. Ta is one of the metals used for theser barriers. On the barrier, first a Cu "seed" layer is plasma-deposited in order to control the texture and improve adhesion. The processes involved in this are not properly known, which motivates this study. In our model system we use Mo, which is similar to Ta in many respects, to avoid the complicating factor of the β-Ta phase. The (epitaxial) growth of Cu (fcc) on Mo (bcc) is also of theoretical interest. Additional motivation comes from the large positive enthalpy of mixing of the Cu/Mo system, from which an atomically sharp interface can be expected. We study both deposition by thermal evaporation (EVAP) and Ar-ion assisted deposition (IBAD), which produces effects in many respects similar to plasma deposition.

To improve the efficiency of the simulation program, we use a Neighbour table, which has to be refreshed only at certain intervals. Despite this, the simulations can only span a very limited amount of time, so that it is necessary to use elevated temperatures as a means of activating the same processes as in a real room temperature experiment.

We have developed several new analysis methods and improved others in order to study our results in more detail. The most notable methods are: a local crystal symmetry index; a quantity which compares the plane filling to a simple solid-on-solid model; and the creation of an atom "history" in order to keep track of atomic movements after arrival in the film.

In general, the Cu-Cu interaction is found to be usable, but two aspects are not entirely accurate: the diameter of our Cu is 3.7% too large, and the elastic constants are up to 18% too large at 300 K. The Cu-Mo interaction proves to be suitable. We observed a remarkable non random-walk behaviour in low temperature diffusion of Cu adatoms on Cu(111). Apart from this, the diffusion constants are comparable to the literature values.

Deposition of Cu on Mo(110) results in a film with a nanostructure consisting of fcc{111} and hcp{111} regions, seperated by stacking-faults. The associated partial dislocations form threading dislocations and coalesce to form one or two grain boundaries. During deposition the growth mode undergoes several changes. The first monolayer exhibits a flat growth and is pseudomorphic with the substrate. As this plane nears completion, (3-D) island growth develops, which only lasts for 4–5 monolayers of coverage (15 Å). Thereafter, the growth mode changes to a plane-by-plane growth mode, accompanied by a decrease in roughness. Only in this stage does the described nanostructure fully develop.

IBAD results in a gradient in composition near the interface, and in a structure which changes more gradually from bcc at the interface to close-packed in the bulk. IBAD also results in incorporation of a few Ar atoms and leads to the formation of some vacancies. These results are summarized in section 6. Section 7 gives recommendation for future analysis of the present results and for future simulations on similar systems.

Samenvatting

We bestuderen de depositie van Cu op Mo(110) met behulp van moleculaire dynamica simulaties, en interacties gebaseerd op de "Embedded Atom Method" (ingebed-atoom methode, EAM). De Cu-Cu en Cu-Mo interacties zijn nieuw.

Cu is een belangrijk materiaal in de tegenwoordige IC technologie, echter, om te voorkomen dat Cu naar het omringende halfgeleider materiaal diffundeert is gebruik van een barrïere-laag noodzakelijk. Ta is een van de toegepaste metalen. Op de barrïere wordt via plasma-depositie een Cu "seed"-laag aangebracht met als doel de hechting te verbeteren en de structuur te kunnen sturen. De huidige studie beoogt het beperkte begrip van de betrokken processen aan te vullen. In ons modelsysteem gebruiken we Mo, een materiaal dat in veel aspecten op Ta lijkt, om de gecompliceerde β-Ta fase te vermijden. Verder is de (epitaxiale) groei van Cu (fcc) op Mo (bcc) theoretisch interessant, zeker omdat Cu/Mo een grote negatieve mengwarmte heeft, waardoor een atomair scherp grensvlak kan worden verwacht. Naast depositie door verdamping (EVAP) simuleren we ook Ar-ion geassisteerde depositie (IBAD), wat in veel opzichten een resultaat oplevert vergelijkbaar met dat van plasma-depositie.

Om de efficiency van onze simulatie-code te vergroten gebruiken we een "Neighbour table" welke met tussenpozen wordt bijgewerkt. Aangezien de simulaties desondanks slechts een relatief kort tijdsbestek bestrijken, blijkt het noodzakelijk een verhoogde temperatuur te gebruiken om dezelfde processen actief te maken als in experimenten op kamertemperatuur.

We hebben een aantal nieuwe analysemethoden ontwikkeld, en oude verbeterd, om onze resultaten diepgaander te kunnen bestuderen. De belangrijkste zijn: de kristal-symmetrie index; de vergelijking van de vlak-opvulling met het simpele "solid-on-solid" (vaste stof op vaste stof) model; en het bijhouden van een "atoom-historie" waarmee atoom bewegingen in de film worden gevolgd.

De ontwikkelde Cu-Cu interactie blijkt bruikbaar, maar voldoet niet goed op twee punten: ons Cu heeft een 3.7% te grote straal, en de elastische constanten zijn bij 300 K tot 18% te groot. De Cu-Mo interactie voldoet goed. Bij lage temperatuur diffusie van een Cu adatoom op Cu{111} vinden we een opmerkelijk, niet "random-walk" gedrag. Voor het overige stemmen de diffusieconstanten overeen met de literatuur.

De Cu/Mo depositie resulteert in een nanostructuur bestaande uit domeinen van fcc{111} en hcp{111} met daartussen stapelfouten. De partiële dislocaties die hiermee zijn geassocieerd vormen "threading" dislocaties welke groeperen tot één of twee korrelgrenzen. Gedurende de depositie verandert de groei modus. De eerste monolaag groeit als een vlakke laag en pseudomorf met het substraat. Als deze laag nagenoeg voltooid is ontwikkelt zich 3-D groei, die gedurende 4–5 monolagen aanhoudt en dan overgaat in min of meer vlakke groei. Pas in dit stadium ontwikkelt zich de eerder genoemde structuur. IBAD veroorzaakt een gradient in samenstelling over het grensvlak, en een meer geleidelijke structuurverandering van bcc substraat naar dichtst gepakte film. Verder zijn de verschillende groei modes minder scherp onderscheiden. Bij IBAD wordt tevens een (zeer klein) aantal Ar atomen ingevangen en vinden we een paar vacatures. Deze resultaten worden in sectie 6 opgesomd. In Sectie 7 doen we enkele aanbevelingen en geven we suggesties voor verdere simulaties.

Acknowlegdements

In the course of this long graduation work, I learnt a great deal about physics and doing research. I also learnt programming and using UNIX, and I discovered the GNU/Linux free software operating system. Despite several difficult periods in different stages of this work, I enjoyed my time in this section and with the faculty, and in general, I enjoyed the past period of doing research, and look forward to continue in this line of work. I believe that my feelings on this are at least partly attributable to the enthusiastic, inquiring and well informed nature of the people in this group.

I thank Edwin Haddeman, not only for the numerous occasions where his troubleshooting skills in programming and shell scripting made my life a lot easier and for his aid in improving the interpretation of my results, but also for the generally pleasant atmosphere in working next to him. His dry sense of humor was always delightful. I greatly enjoyed the congenial cooperation with Carin de Hoog and her in-depth questions about the simulated films, wich resulted in a better understanding both of her and of my own results, and also for her encouragements to put more attention into planning. I must confess that plannning is still not my best characteristic, but I have improved on this. Finally, Barend Thijsse has greatly helped me with his physical insight and imagination, and his inventiveness and enthusiasm.